



HAL
open science

Experimental study of dilute spray combustion

Antoine Verdier

► **To cite this version:**

Antoine Verdier. Experimental study of dilute spray combustion. Fluids mechanics [physics.class-ph]. Normandie Université, 2017. English. NNT : 2017NORMIR27 . tel-01821191

HAL Id: tel-01821191

<https://theses.hal.science/tel-01821191>

Submitted on 22 Jun 2018

HAL is a multi-disciplinary open access archive for the deposit and dissemination of scientific research documents, whether they are published or not. The documents may come from teaching and research institutions in France or abroad, or from public or private research centers.

L'archive ouverte pluridisciplinaire **HAL**, est destinée au dépôt et à la diffusion de documents scientifiques de niveau recherche, publiés ou non, émanant des établissements d'enseignement et de recherche français ou étrangers, des laboratoires publics ou privés.



Normandie Université

THÈSE

Pour obtenir le diplôme de doctorat

Spécialité Analyse expérimentale de la combustion

Préparée au sein de l'INSA Rouen Normandie

Experimental study of dilute spray combustion

**Présentée par
Antoine Verdier**

**Thèse soutenue publiquement le 05/12/2017
devant le jury composé de**

M. Christian CHAUVEAU	DR, Laboratoire ICARE, Orléans	Rapporteur
M. Sebastien DUCRUIX	DR, Laboratoire EM2C, CentraleSupélec, Paris	Rapporteur
Mme. Bénédicte CUENOT	Chercheur HDR, CERFACS, Toulouse	Examineur
M. Franck BEYRAU	PR, Institut für Strömungstechnik und Thermodynamik (ISUT), Magdeburg, Germany	Examineur
M. Stephane RICHARD	Ingénieur, Dr, SAFRAN HE, Pau	Examineur
Mme. Sawitree SAENGKAEW	HDR, Rainbow Vision Inc., Rouen	Membre Invité
M. Bruno RENO	PR, CORIA, INSA Rouen Normandie	Directeur de thèse
M. Gilles CABOT	PR, CORIA, Université de Rouen	Co-Directeur de thèse

Thèse dirigée par Bruno RENO et Gilles CABOT, laboratoire CORIA

Abstract

Liquid fuels are the primary energy source in a wide range of applications including industrial and residential furnaces, internal combustion engines and propulsion systems. Pollutant emission reduction is currently one of the major constraints for the design of the next generation combustion chamber. Spray combustion involves many complex physical phenomena including atomization, dispersion, evaporation and combustion, which generally take place simultaneously or within very small regions in the combustion chambers. Although numerical simulation is a valuable tool to tackle these different interactions between liquid and gas phases, the method needs to be validated through reliable experimental studies. Therefore, accurate experimental data on flame structure and on liquid and gas properties along the evaporation and combustion steps are needed and are still challenging. A joint effort between numerical and experimental teams is necessary to meet tomorrow's energy challenges and opportunities. The complexity of the real aeronautical configurations implies to study the effect of local properties in flame dynamics on a canonical configuration, which presents the essential feature of very well defined boundary conditions. This work, carried out within the framework of the ANR TIMBER project, aims to improve the understanding of two-phase flow combustion, as well as to produce an efficient and original database for the validation of the models used in LES.

Firstly, the investigations are focused on the characterization of the carrier and dispersed phases to understand the different combustion regimes present in the flame structure. An accurate and efficient technique (Instantaneous Global Rainbow Refractometry, I-GRT) is introduced for the measurement of the instantaneous fuel droplet temperature in a realistic spray flame. Simultaneously, the instantaneous flame structure is analyzed by OH-PLIF. The polydisperse spray distribution yields small droplets along the centerline axis while the majority of the mass is situated as big droplets along the spray borders. The flame structure presents a classical shape, with an inner wrinkled partially premixed flame front and an outer diffusion flame front. In the mixing zone, the fuel droplet temperature decreases to a lower equilibrium temperature close to 284 K along the centerline. The profile across the flame front presents a steep gradient that allows distinguishing the temperature of droplets situated in the burnt gases and in the fresh gases. In the burnt gases, the evaporation process occurs at an equilibrium temperature (331 K) lower than

the fuel boiling temperature.

The second phase of the research addresses the response of the flame structure to unsteady local flow properties via turbulence-flame interactions. Special attention is given to the interaction between large droplets and the reaction zone. The focus is placed on the transient phenomena that occur in a spray jet flame and, in particular, on the mechanisms governing the local extinctions. The objective of this section is to extend understanding of turbulence-flame interactions and droplet-flame interactions by combining two high-speed optical diagnostics (HS-OH-PLIF and HS-PIV). We were able to show that in the inner reaction zone, local flame extinctions are mainly controlled by the shear and by the fuel-air heterogeneities due to the evaporation of small droplets in the vicinity of the flame front. The large scales of turbulence in the shear layer play a significant role in the dynamics of these extinctions. It is also found that the large inertial droplets penetrate the base of the inner front reaching the burned gases, where they may evaporate rapidly, and disturb the outer reaction zone due to the low droplet temperature and the rich mixture in the wake of the droplets.

Finally, it was shown that the simulation of these geometries is a complex task since it requires at least (i) an accurate prediction of the fuel vapor and the thermal budget between the droplet and its gaseous surrounding through the evaporation model, and (ii) a detailed description of the combustion reactions able to predict the different modes of combustion. To meet the objectives of the international workshops on the Turbulent Combustion of Sprays (TCS), a database is given to different laboratories (CERFACS, EM2C, IMPERIAL COLLEGE and TU Delft) in order to evaluate the importance of models choices in LES results. A detailed comparison is made between numerical and experimental results. The simulation strategy strongly affects the results whether in flow properties or flame structure. From this perspective we can show the interest of the development of experimental diagnostics in order to quantify more precisely the local properties as well as the transient phenomena, such as the local extinctions that affects the production of pollutant.

Acknowledgements

Ce travail expérimental a été effectué au sein du groupe Analyses Expérimentales de la Combustion du laboratoire CORIA à Saint Etienne du Rouvray. Je tiens tout d'abord à remercier son ancien directeur M. Abdelkrim Boukhalfa de m'y avoir accueilli ainsi que Mme. Armelle Cessou pour avoir repris le flambeau et su garder un environnement propice à l'épanouissement intellectuel.

La réalisation de ce manuscrit n'est pas le fruit d'un travail solitaire mais bien celui d'une équipe unie. Le moment est venu pour moi de remercier tous ceux qui m'ont entouré durant toutes ces années.

Je tiens à remercier en premier lieu mes deux encadrants de thèse Bruno Renou et Gilles Cabot pour m'avoir fait confiance dès mon plus jeune âge. En effet, j'ai pu intégrer le laboratoire pour un stage de Licence 3 en 2012. Cette expérience fût pour moi déterminante car elle m'a permis d'écrire ces quelques lignes aujourd'hui. Je tiens vraiment à vous remercier pour votre aide et votre soutien continu tout au long de ces trois magnifiques années. J'ai apprécié la qualité de vos conseils techniques et scientifiques durant toutes les étapes de ma thèse et notamment je tiens à remercier profondément Bruno pour les corrections rigoureuses qu'il a apporté à la rédaction de ce manuscrit. Vos qualités scientifiques et humaines ont sans aucun doute contribué à la réussite de cette thèse. Les activités que nous avons partagées en dehors du CORIA m'ont permis de vous connaître dans un environnement différent et ainsi de partager d'excellents moments. Je pense évidemment aux sorties course à pied dans la forêt de Saint Etienne du Rouvray mais également au week - end que nous avons passé ensemble à la montagne.

Je remercie également les membres de mon jury qui ont accepté d'évaluer mon travail. Je remercie d'abord Christian CHauveau et Sébastien Ducruix qui ont accepté d'être rapporteurs de cette thèse, et pour leur intérêt pour les travaux de recherches effectués. Enfin, je remercie sincèrement les examinateurs de ce manuscrit pour leurs critiques constructives.

Un grand merci également à tous les membres de l'atelier : Jacky, Benjamin, Yves, Thierry, Philippe (Touti), Bruno, Ludo, Antoine, et depuis peu les deux Romains. Que dire mis à part que ce fût un réel plaisir de faire votre connaissance. Entre les discussions sur la moto GP avec Bruno, de course avec Jacky et Antoine et de pleins d'autres sujets avec vous tous. Vous m'avez beaucoup appris notamment en "bricolage" et je vous suis

reconnaissant du temps passé à mes côtés.

Rien de ce que j'ai réalisé ici n'aurait pu être envisagé sans la qualité du service de métrologie. Je tiens à remercier Franck et Carole pour leur aide tout au long de ces trois années. Merci pour votre générosité, votre joie de vivre, ainsi que votre sympathie qui permet de travailler dans des conditions formidables. Je ne peux oublier de remercier Gilles, qui en plus de ses qualités "laser", est une personne que j'ai eu la chance de côtoyer à l'extérieur et partager d'excellents moments (sportifs et festifs). Viens le temps de remercier mon "inséparable" (Alexis Vandiel) comme diraient beaucoup de personnes du laboratoire, sans lui, ma thèse aurait un tout autre aspect. Je tiens à te remercier pour ces trois années, j'ai vraiment eu de la chance de t'avoir à mes côtés durant cette thèse. Mais finalement plus que l'aspect scientifique, cette thèse m'a permis d'avoir un nouvel ami. En effet, nous avons nos habitudes : 7h30 le premier café et à midi une petite heure de course à pied. Nous avons passé d'excellents moments. J'ai connu également des moments difficiles quand j'essayais de te suivre sur un 10 km. Grâce à toi, j'ai fait des longues, très longues courses en montagne que je n'aurais jamais eu l'intention de faire.

Cette thèse n'aurait pas pu se faire sans l'aide précieuse des membres du personnel administratif et technique du laboratoire CORIA. Je tiens vraiment à remercier le service informatique et le pôle administratif. Une attention particulière est donnée pour Isabelle qui se dévoue, non sans mal, à organiser nos déplacements le mieux possible.

Je remercie aussi tout particulièrement les doctorants qui ont fait de ces années une expérience inoubliable. Une pensée particulière à mes collègues successifs de bureau : Yi, Manu, Juan Pa, mes collègues du bureau d'à côté : Erwan, Pierre, Irfan, Felix, etc. Je garderai en mémoire les nombreux échanges que l'on a pu avoir sur des sujets variés. Je tiens à remercier particulièrement Javier qui a été pour moi bien plus qu'un simple collègue, et oui encore un ami, et un ami espagnol cette fois-ci... Tu m'as fait découvrir ta culture et j'ai passé avec toi des moments inoubliables notamment lors de nos déplacements en conférences, j'en ai des souvenirs plein la tête. Je tiens à te remercier aussi pour toutes les discussions scientifiques que l'on a pu avoir mais surtout pour toutes les corrections d'Anglais que tu as pu m'apporter.

Je n'oublie pas les nombreuses autres personnes du laboratoire que j'ai côtoyé au cours de ces trois années et avec qui j'ai passé de bons moments. Je pense bien sûr aux gars du foot : Andrès, Antonio, Marcos, Thán, Guillaume, Guillaume R., Abou, Fred, Geoffrey, Thomas, FX, Julien, etc.

Enfin, je souhaite bien sûr remercier ma famille et mes amis qui m'ont toujours accompagné dans les bons moments mais surtout dans les moments difficiles. Merci à mes parents, ma sœur et mes grands-parents qui se sont toujours intéressés à ma thèse et m'ont permis d'avancer dans la vie. Une pensée va à mes grands-parents décédés pendant ces travaux et qui auraient aimé voir ce manuscrit. Ils ont toujours cru en moi et auraient été fier de ce que je suis devenu. Ce manuscrit est pour vous.

Enfin, je termine ces remerciements, par celle qui m'a donné la force d'avancer, celle qui a toujours été là pour moi, celle pour laquelle mon cœur bat et battra toujours. Mes pensées vont naturellement vers ma compagne Julie à qui je souhaite témoigner ici tout mon amour. Je ne pourrai jamais suffisamment te remercier pour ta patience, ton aide et ta compréhension dans les moments difficiles.

"Le meilleur moyen de prévoir le futur, c'est de le créer". (Peter Drucker)

A ma compagne et ma famille

Contents

List of Figures	xi
1 Introduction	1
1.1 Aircraft engines	2
1.2 Multi-physical study	4
1.3 Atomization	5
1.4 Combustion regimes	7
1.5 Applied research	8
1.6 Spray jet flame experimental configurations	13
1.7 Objectives and organization of the manuscript	16
2 Fundamentals of spray combustion	19
2.1 Droplet evaporation	19
2.2 Multi-physical study	26
2.2.1 Spray-Turbulence interactions	26
2.2.2 Turbulence-gaseous flame interactions	28
2.2.3 Spray-Flame interactions	30
2.2.4 Combustion regime	31
2.3 Conclusion	33
3 Experimental facilities and optical diagnostics	35
3.1 CORIA Rouen Spray Burner (CRSB)	36
3.1.1 Plenum and air co-flow	36
3.1.2 Liquid fuel injection	36
3.1.3 Stability diagram	38
3.1.4 Operating conditions	39
3.2 Characterization of the dispersed phase by Phase Doppler Anemometry (PDA)	40
3.3 Microscopic shadowgraphy	42
3.4 Planar Laser-Induced Fluorescence on OH radical (OH-PLIF)	44
3.4.1 Principle	44

3.4.2	Strategy for OH excitation and detection	46
3.4.3	Experimental set-up	47
3.4.4	Post-processing	47
3.5	High-Speed optical diagnostic	48
3.5.1	Experimental set-up	48
3.5.2	HS-OH-PLIF	49
3.5.3	HS-PIV	51
3.6	Conclusion	55
4	Application and development of a technique for measuring the fuel droplet temperature	57
4.1	Droplet temperature by optical measurement techniques	58
4.1.1	State of the art	58
4.2	Background on the Rainbow Refractometry Technique	59
4.2.1	Standard Rainbow refractometry	59
4.2.2	Global rainbow refractometry (C-GRT)	63
4.2.3	Instantaneous Global rainbow refractometry (I-GRT)	69
4.3	Application of C-GRT	70
4.3.1	Experimental set-up	70
4.3.2	Fuel droplet temperature measurement procedure	71
4.4	Development and application of Instantaneous Global rainbow refractometry coupled with OH Planar Laser Induced by Fluorescence (I-GRT coupled with OH-PLIF)	77
4.4.1	Experimental set-up	77
4.4.2	Studied zones	78
4.4.3	Image post-processing	79
4.5	Conclusion	79
5	Local flame structures and fuel droplet properties	81
5.1	Global appearance and behavior of the spray jet flame	82
5.2	Analysis of carrier phase and dispersed phases in Reactive Condition	83
5.2.1	Air co-flow aerodynamic	83
5.2.2	Fuel droplet properties	85
5.3	Flame structure	90
5.3.1	Inner Reaction Zone (IRZ)	90
5.3.2	Outer Reaction Zone (ORZ)	91
5.4	Stabilization of the flame base	93
5.5	Fuel droplets temperature conditioned by the distance to the flame front	94
5.6	Conclusion	98

6	Flame dynamics and local extinctions	101
6.1	Position of local extinctions	102
6.2	Analysis of joint measurements of HS-OH-PLIF and HS-PIV	103
6.2.1	Flame-turbulence interactions	103
6.2.2	Droplet-flame interactions	107
6.3	Conclusion	109
7	Comparisons Simulations / Experiments	111
7.1	Experimental and numerical analysis of a turbulent spray flame structure .	113
7.1.1	Numerical setup	113
7.1.2	Non reacting case	116
7.1.3	Reacting case	119
7.1.4	Effect of the evaporation model and the chemistry	124
7.2	6 th Workshop on measurement and computation of Turbulent Spray Com- bustion (TCS6)	125
8	Conclusion and Perspectives	137
8.1	Conclusion	137
8.1.1	Characterization of non-reactive conditions	138
8.1.2	Characterization of reactive conditions	138
8.1.3	CRSB - Flame Data Base	140
8.2	Perspectives	140
8.2.1	Database extension	140
8.2.2	Improvement of GRT technique	141
8.2.3	Extension of the experimental conditions	142
	Appendix	143
A	Analysis of ignition probability and carrier and dispersed phases in non reacting conditions	145
A.1	Optical diagnostics	146
A.1.1	Phase Doppler anemometry (PDA)	146
A.1.2	Ignition: spark induced by laser	147
A.2	Results and discussion	148
A.2.1	Flow aerodynamics - carrier phase	148
A.2.2	Flow aerodynamics - dispersed phase	148
A.2.3	Time scale analysis	151
A.2.4	Ignition probability	153
A.2.5	Flame propagation mechanisms	155
A.3	Conclusion	156

List of Figures

- 1.1 Schematic representation of the aircraft engine. 2
- 1.2 Schematic representation of the aircraft engine. 3
- 1.3 Sketch of fundamental spray-combustion processes. Extracted from [1] . . . 4
- 1.4 Schematic representation of the interactions involved in a reactive turbulent spray 5
- 1.5 Cross section of an air-blast nozzle. Extracted from [2]. 7
- 1.6 Main Characteristics of ONERA test facilities 8
- 1.7 (a) HERON test bench from CORIA. (b) HBK-S high-pressure combustion chamber test rig from DLR. 9
- 1.8 Schematic representation of the level of modeling required for each of the approaches for the example of a time signal of temperature and in spectral representation 10
- 1.9 (Snapshots of the ignition sequence: experimental direct imaging of the flame emission colored for visualization purposes (top rows) versus iso-surfaces of $T = 1781$ K colored by the axial velocity and $U = 25$ m/s in light blue extracted from the LES (bottom rows). [3] 12
- 1.10 (a) Experiments: fast visualization of the flame showing an axial propagation. (b) LES results: instantaneous snapshots of the ignition sequence visualized by the volume rendering of heat release [4]. 12
- 1.11 Burner system cross section studied by Friedman et al with all dimensions in mm. The photographs and the OH-PLIF images present the main results of this study in term of air co-flow effect [?]. 13
- 1.12 Schematic of the Sydney University spray burner [5]. 14
- 1.13 Geometry of the Delft Spray burner 15
- 1.14 Geometry of the Cambridge University swirling spray burner [6]. 16

- 2.1 Temporal and spatial temperature evolution for the 3 different types of evaporation models. 22
- 2.2 Temporal evolution of the droplet diameter squared (a) and droplet temperature (b) for decane ($T_B = 447.7K$) with various models [7]. The experimental results are from Wong and Lin [8] 23

2.3	Sketch of the heat fluxes and temperature profile in the evaporation of an isolated droplet following the infinite conductivity model (ICM). Extracted from AVBP handbook.	25
2.4	Preferential segregation of droplets. Experimental image obtained by the Mie diffusion of the droplet, with a laser sheet.	27
2.5	Combustion regime diagram demonstrating turbulent flame structure for premixed flames.	29
2.6	Representation of the different interaction levels in two-phase combustion. Right: Pre-vaporized flame. Middle: Homogeneous combustion. Left: Heterogeneous combustion. Adapted from [9]	30
2.7	Two-phase combustion regimes according to the group number G . Extracted from [10]	32
2.8	Borghi's diagram for laminar flames propagating in homogeneous and poly-dispersed droplets Extracted from [11]	32
2.9	(a) Three-dimensional diagram for diluted spray combustion. Extracted from [12]. (b) Summary of the generic flame structures. Red continuous line: premixed burning blue dashed line: diffusion burning. Adapted from [12].	34
3.1	Detail of the injection system.	36
3.2	Details of the plenum.	37
3.3	Details of the injection system.	37
3.4	Schematic representation of the Danfoss injector and photo of swirl chamber inside the injector obtained by an electronic microscope.	38
3.5	Extinction limits and operating range of the burner. The red star represents the operating point.	38
3.6	Mesh for Phase Doppler Anemometry in reacting condition with different optical diagnostics applied in the spray jet flame.	39
3.7	List of available data and optical diagnostics associated.	40
3.8	Photographs of the PDA system with the laser beam in non-reacting and reacting condition	41
3.9	Principle of the Shadowgraphy	43
3.10	Images showing the liquid sheet breakup.	43
3.11	Images showing the shape of droplets at $Z=35\text{mm}$ for different radial stations and different images at $Z=1.8$ and 2.6mm	44
3.12	Schematic illustration of a two-level energy diagram [13].	45

3.13	Experimental and theoretical laser excitation spectrum of OH molecule in a laminar burner. CH_4 , $P = 1bar$, $T = 2000K$. The fluorescence signal was obtained by averaging 150 images and by taking the mean value of a defined region of interest. The wavelength interval between two measurements was 0.01nm	46
3.14	Photograph of OH-PLIF experimental facility	47
3.15	Optical arrangement for simultaneous HS-PIV and HS-OH-PLIF measurements.	49
3.16	(a) Image filtered by NLD. (b) Comparison between raw (red line) and NLD profiles (blue line).(a) Final contour obtained by level set method. . .	50
3.17	Principle of PIV measurement.	52
3.18	Optical arrangement for HS-PIV measurements to capture the air entrainment.	54
3.19	Raw image of air entrainment obtained by HS-PIV-(B).	54
4.1	Refracted and reflected rays by a droplet.	60
4.2	Diffusion pattern for an angular range between 110 and 150 degrees, for a droplet of diameter 100 μm and with refractive index equal to 1.38.	61
4.3	Influence of the refractive index on the GRT signal	64
4.4	Spatially averaged intensity profile from the selected band extracted from C-GRT images for two positions in spray (a): $X = 0$ & $Z = 35 mm$ with $D_{10} = 10 \mu m$ (see chap:5). (b): $X = 10$ & $Z = 35 mm$ with $D_{10} = 20 \mu m$ (see chap:5)	65
4.5	Comparison between the droplet size distribution obtained by C-GRT (dotted line) and PDA (line) in two position in spray. (a): $X = 0$ & $Z = 35 mm$. (b): $X = 10$ & $Z = 35 mm$	66
4.6	Inversion methodology developed by Saengkaew [14]	67
4.7	Inversion methodology developed by Saengkaew [14]	67
4.8	Refractive index gradients at droplet surface (dm/dr^*)s as a function of time τ^* [15].	68
4.9	(a) Evolution of the droplet temperature in the cartesian coordinates system.(b) Evolution of the droplet temperature in the local coordinates system as a function of the mean progress variable. [16].	69
4.10	Global rainbow created experimentally for sixty droplets. (a) With a continuous laser. (b) With a pulsed laser	70
4.11	Optical arrangement of droplet temperature measurement obtained by C-GRT. (a): Schematic representation. (b) Photograph of the installation . .	71
4.12	C-GRT calibration with mirror methodology.	72
4.13	Mirror calibration software.	73

4.14	Recorded signal from the liquid jet.	74
4.15	Computed signal for the liquid jet.	74
4.16	Measurement grid for Phase Doppler Anemometry and Continuous Global Rainbow Technique with the mean OH-PLIF image	75
4.17	Rainbow image with associated light intensity profile	75
4.18	Software interface of inversion calculation; input parameters	76
4.19	Software interface of inversion calculation; Statistical analysis	76
4.20	Evolution of the refractive index as a function of temperature for different fluids.	77
4.21	Optical arrangement of combined OH-PLIF and C-GRT / I-GRT measure- ments	78
4.22	Studied zones for I-GRT	78
4.23	Instantaneous OH-PLIF image with the I-GRT measurement volume . . .	79
5.1	(a) Photo of the spray jet flame. (b) OH-PLIF and different zones.	82
5.2	Mean components of air velocity flow for reactive conditions with vector field obtained with configuration <i>PDA(A)</i> .(a) Mean axial velocity. (b) Mean radial velocity.	83
5.3	(a) Turbulent kinetic energy of the air in reactive conditions (k). (b) Tur- bulent Kinetic Energy profiles for different axial stations.	84
5.4	Instantaneous fluctuation velocity field	85
5.5	(a) Fuel droplet mean diameter D_{10} in reactive condition. Error bars indi- cate the RMS of the droplet size distribution (b) Pdf of droplet size fitted by Rosin-Rammler distribution	86
5.6	Radial profiles of the axial volume liquid flux for axial stations $Z = 16, 25,$ 35 and 45 mm	87
5.7	Mean components of fuel droplet velocity in reactive conditions separated in four size-classes obtained with <i>PDA(B)</i> configuration. \circ represent the $[0 - 10] \mu m$ group, \blacktriangleleft the $[20 - 30] \mu m$ group, $+$ the $[30 - 40] \mu m$ and \blacktriangledown represent the $[50 - 60] \mu m$. Black lines represent the Air velocities profiles. (a) Axial velocity. (b) Radial velocity	88
5.8	RMS of fuel droplet velocity in reactive conditions separated in four size- classes obtained with <i>PDA(B)</i> configuration. \circ represent the $[0 - 10] \mu m$ group, \blacktriangleleft the $[20 - 30] \mu m$ group, $+$ the $[30 - 40] \mu m$ and \blacktriangledown represent the $[50 - 60] \mu m$. Black lines represent the Air velocities profiles. (a) RMS of axial velocity. (b) RMS of radial velocity	89

5.9	(a) Evolution of mean droplet temperature and mean progress variable maps \bar{c} (b) Axial and radial profiles of mean temperature in the mixing zone below the stabilization point (bottom) and along the centerline axis (top). The errors bars indicate the RMS of measurement.	91
5.10	Selected images of OH-PLIF images at low repetition rate 10 Hz [17] . . .	92
5.11	(a) Spatially averaged ORZ position (black lines obtained with OH-PLIF measurements) and air entrainment streamlines with the norm of velocity ($ U = \sqrt{U^2 + V^2}$) obtained with HS-PIV-(B) configuration). (b) Schematic representation of ORZ : Generic structure of a laminar diffusion flame . . .	93
5.12	Positions of the flame base	94
5.13	Right: Instantaneous field of gaseous equivalence ratio with an isocontour of zero flame displacement speed in a vertical cut, obtained from LES. Left: PDF of gaseous equivalence ratio at two locations (S) and (S'), from LES [18].	95
5.14	Radial profiles of the mean temperature obtained by C-GRT for the non-reactive case (black) and for the reactive case (blue squares) across the flame front at $Z=35$ mm. For comparison, the mean temperature obtained by averaging instantaneous measurements by I-GRT is also reported (red triangles). The errors bars indicate the RMS of measurement.	95
5.15	Mean droplet temperature conditioned by the distance to the flame front along the axial position $Z=35$ mm and associated PDF of temperature. The error bar indicates the RMS of the distribution.	96
5.16	Mean droplet temperature conditioned by the distance to the flame front along the axial position $Z=35$ mm, for different radial measurement positions ($X=8, 10, 12$ and 14 mm).	97
5.17	Radial evolution of mean droplet diameter (green circles) at different axial stations and their mean trajectory for reactive condition (dashed line). Two instantaneous flame front are plotted (red and blue lines) with the averaged progress variable $< \bar{c} = 0.5$ (gray line).	98
6.1	Mean OH-PLIF with extinction points	102
6.2	HS-OH-PLIF series images overlaid with the fluctuation velocity field and the strain rate (SM3)	104
6.3	Schematic representation of the extinction mechanisms in the inner reaction zone.	105
6.4	Profile at $R = 16$ mm and $Z = 30$ mm. (a) Extinction occurrence temporal analysis. (b) Extinction occurrence frequency analysis	106
6.5	HS-OH-PLIF images - time separation = 0.1 ms. Extinction in the leading edge due to the droplet-flame interactions.	107

6.6	HS-OH-PLIF images - time separation = 0.1 ms. Perturbations in the outer reaction zone (ORZ) due to the droplet-flame interactions.	108
6.7	(a) Schematic representation of the droplet-flame interactions. (b) Schematic representation of a radial profile for the fuel and oxidant mass fraction and temperature in different regions. Burned Gases (BG), Fuel vapor (Fv), Drop, ORZ and Fresh Gases (FG) are respectively the burned gases, the fuel vapor, the droplet, the outer reaction zone and the fresh gases.	109
7.1	(a) View of the main part of the computational domain. (b) View of the mesh in a vertical cut.	113
7.2	Shadowgraphy images for radial profile at Z=35mm.	114
7.3	Radial profiles of (a) mean axial velocity and (b) RMS axial velocity at Z = 10, 20 and 40 mm for the carrier phase. (+) Exp; (-) LES.	117
7.4	Radial profiles of (a) mean radial velocity and (b) RMS axial velocity at Z = 10, 20 and 40 mm for the carrier phase. (+) Exp; (-) LES.	117
7.5	Mean components of fuel droplet (a) axial velocity (b) radial velocity separated in three size-classes. \triangle represent the [0 – 15] μm group, \triangle the [15 – 35] μm group, \triangle the [35 – 60] μm . Error bars are proportional to measured RMS values.	118
7.6	Radial profiles of droplet diameter at Z = 10, 20 and 40 mm for the carrier phase. (\square) Exp with error bars; (\triangle) LES.	119
7.7	Radial profiles of fuel droplet temperature at Z = 20, 30 and 40 mm. (+) Exp; (\square) LES.	120
7.8	Instantaneous visualization of the spray jet flame. LES: heat release field. EXP: OH-PLIF image	121
7.9	Instantaneous field of fuel vapor with an isocontour of heat release extracted from LES	121
7.10	(a) Field of Takeno flame index, with isoline of stoichiometric mixture fraction (white). (b) Isolines of Takeno index, corresponding to premixed flames (grey, Takeno=1) and diffusion flames (black, Takeno=-1), obtained from LES	122
7.11	Scatter-plot of temperature versus mixture fraction in a vertical plane, obtained from LES. [18]	122
7.12	Instantaneous radial profiles across the flame at Z = 30 mm: (solid line) Normalized heat release; (dashed black) Fuel vapor and (dashed gray) total fuel mass fraction (vapor + liquid); (dash-dot) Oxidizer mass fraction. [18]	123
7.13	(a) Instantaneous field of gaseous equivalence ratio with an isocontour of zero flame displacement speed in a vertical cut, obtained from LES; (b) PDF of gaseous equivalence ratio at two locations (S) and (S'), from LES. [18]	124

7.14	Contour plots of the simulated OH mass fraction together with an isoline of the stoichiometric mixture fraction highlighted in red lines and the corresponding instantaneous droplet motions. Color map indicates the droplet temperature while droplets are scaled with their sizes.	125
7.15	Liquid phase modeling for the different numerical teams.	127
7.16	Combustion phase modeling for the different numerical teams.	128
7.17	Numerical setup.	128
7.18	Radial profiles of mean axial velocity and RMS at $Z = 10, 20, 30$ and 40 mm for the carrier phase.	129
7.19	Radial profiles of mean radial velocity and RMS at $Z = 10, 20, 30$ and 40 mm for the carrier phase.	130
7.20	Radial profiles of mean axial velocity and RMS at $Z = 10, 20, 30$ and 40 mm for the dispersed phase.	131
7.21	Radial profiles of mean radial velocity and RMS at $Z = 10, 20, 30$ and 40 mm for the dispersed phase.	132
7.22	Radial profiles of mean droplet diameter (D_{10}) at $Z = 10, 20, 30$ and 40 mm.	133
7.23	Radial profiles of mean droplet temperature at $Z = 10, 20, 30$ and 40 mm.	134
7.24	Comparison of OH-PLIF images between experiment and numerical results	134
7.25	Comparison of the mean OH-PLIF images between experiment and numerical results	135
8.1	Mean NO concentration with the mean flame front position (black lines)	141
A.1	Optical arrangement for laser induced spark ignition measurements. The mesh is symmetric and just one side is represented here.	147
A.2	(a) Norm of the air velocity with vector field. (b) Turbulent kinetic energy of the air in non reacting conditions	149
A.3	(a): Fuel droplet Sauter mean diameter D_{32} in non reacting condition at $Z = 16, 25, 35$ and 45 mm). (b) PDF of droplet size for three axial station $Z = 7, 30$ and 50 mm at $R = 0$ mm.	150
A.4	Mean components of fuel droplet velocity in non reacting conditions separated in four size-classes obtained with PDA configuration. \circ represent the $[0 - 10] \mu m$ group, \blacktriangleleft the $[20 - 30] \mu m$ group, $+$ the $[30 - 40] \mu m$ and \blacktriangledown represent the $[50 - 60] \mu m$. Black lines represent the Air velocities profiles.(a) Axial velocity. (b) Radial velocity	151
A.5	RMS components of fuel droplet velocity in non reacting conditions separated in four size-classes obtained with PDA configuration. \circ represent the $[0 - 10] \mu m$ group, \blacktriangleleft the $[20 - 30] \mu m$ group, $+$ the $[30 - 40] \mu m$ and \blacktriangledown represent the $[50 - 60] \mu m$. Black lines represent the Air velocities profiles.(a) Axial velocity. (b) Radial velocity	152

A.6	Representation of evaporation rate (\dot{m}_{vapor}) as a function of axial and radial position. The surface is colored by the mean droplet diameter obtained by the PDA measurements.	153
A.7	(a) Ignition probability map with the iso-line $P_{ign} = 0.5$, which correspond to the line with a ignition probability to have 50% of successful ignition.. (b) Ignition probability plotted as a function of evaporation rate and each points are colored by the radial position.	154
A.8	High-speed recording of flame kernel development from side view. The ignition location is $R = 15mm$ and $Z = 35mm$, where ignition probability $P_{ign} = 1$	155
A.9	High-speed recording of flame kernel development from top view. The ignition location is $R = 15mm$ and $Z = 35mm$, where ignition probability $P_{ign} = 1$	156

Chapter 1

Introduction

Contents

1.1 Aircraft engines	2
1.2 Multi-physical study	4
1.3 Atomization	5
1.4 Combustion regimes	7
1.5 Applied research	8
1.6 Spray jet flame experimental configurations	13
1.7 Objectives and organization of the manuscript	16

Liquid fuels are the primary energy source in a wide range of applications including industrial and residential furnaces, internal combustion engines and propulsion systems. Pollutant emission reduction is currently one of the major constraints for the design of the next generation combustion chamber. To decrease the impact of human activities on the environment the production and use of renewable energy is, nowadays, a crucial issue. However, if the aeronautical field is not an exception in terms of stringent emissions standards, it is compulsory to use fossil fuel for aircraft propulsion. The amount of energy liberated by the chemical process of combustion is so elevated that it is impossible to replace it safely. In addition, the use of renewable fuel is more complicated due to the stringent conditions, in terms of temperature and pressure, encountered by aircraft engines. The certification of future propulsion systems using renewable fuel will therefore be difficult. Despite the fact that pollutant emissions reduction is crucial, it must not impact the safe operation of the engine. At ground level or at high altitude conditions, some events such as ingestion of ice or birds, may impact the operation of the engine and lead to the full extinction. Whatever conditions, it is then essential to ignite or re-ignite the flame in the combustion chamber as soon as possible, and safely. The current rules for the design of aircraft combustion chambers enable us to insure these safety standard, in particular for ignition and re-ignition. To ensure these objectives which are the safety and

the protection of environment, a detailed analysis and a deep fundamental understanding of the processes involved in two-phase and lean combustion are necessary.

1.1 Aircraft engines

The gas turbine engine is essentially a heat engine using air as a working fluid aid to provide thrust. To achieve this, the air passing through the engine has to be accelerated; this means that the velocity or kinetic energy of the air is increased. To obtain this increase, the pressure energy is first of all increased, followed by the addition of heat energy, before final conversion back to kinetic Energy in the form of a high velocity jet efflux.

Whatever the propulsion mode may be, we always find the following operating phases: (i) compression, (ii) combustion and (iii) expansion. In an aircraft engine, these phases are achieved with the following elements:

- Air intake
- Compressor
- Combustion chamber
- Turbine
- Exhaust

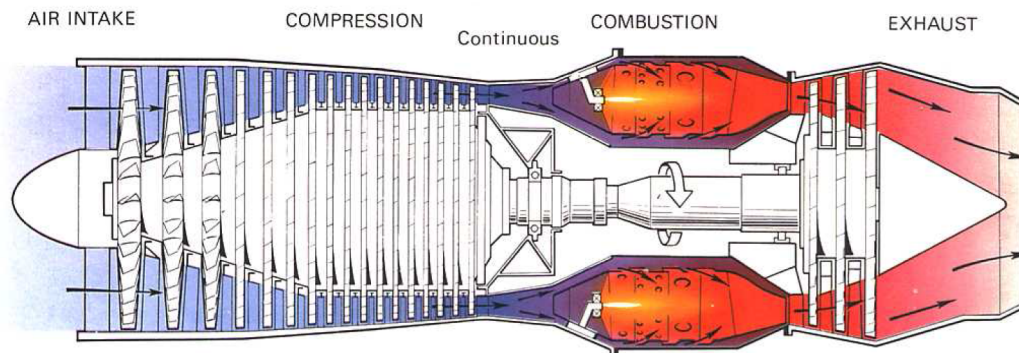


Figure 1.1: Schematic representation of the aircraft engine.

The working cycle upon which the gas turbine engine functions is, in its simplest form, represented by the cycle shown on the pressure volume diagram in fig 1.2. Point A represents air at atmospheric pressure that is compressed along the line AB. From B to C heat is added to the air by introducing and burning fuel at constant pressure, thereby considerably increasing the volume of air. Pressure losses in the combustion chambers (Part 4) are indicated by the drop between B and C. From C to D the gases resulting

from combustion expand through the turbine and jet pipe back to atmosphere. During this part of the cycle, some of the energy in the expanding gases is turned into mechanical power by the turbine; the remainder, on its discharge to atmosphere, provides a propulsive jet.

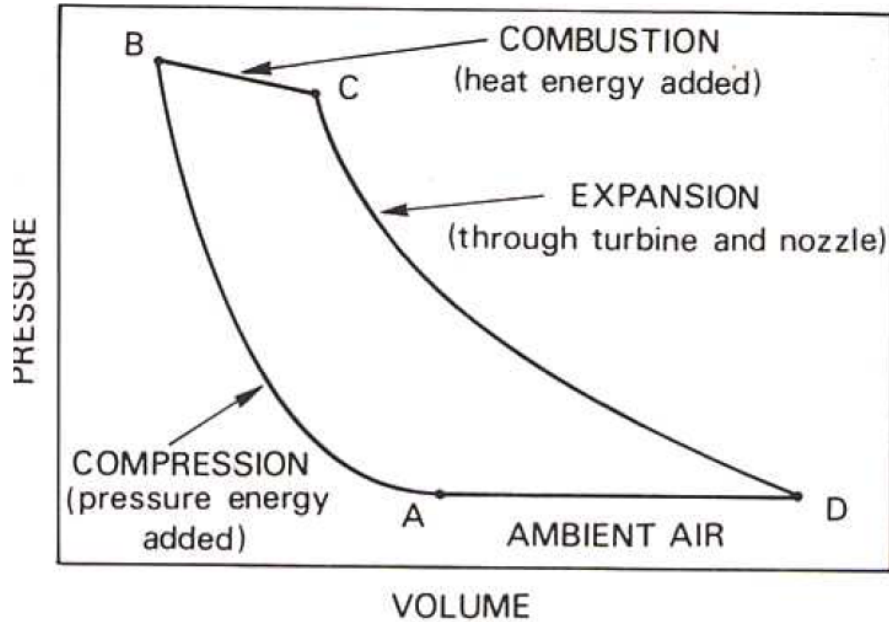


Figure 1.2: Schematic representation of the aircraft engine.

In this work, only the processes taking place in the combustion chamber are of interest, and more precisely the phenomena related to the liquid fuel spray. For this reason, the compressor and the turbine will not be taken into account. The function of the combustion chamber is to provide an enclosure in which the fuel air mixture is burnt and to deliver the gas resulting from combustion to the turbine, which corresponds to the transformation of the potential energy in the fuel into calorific energy. Although the combustion chamber has been the subject of numerous studies to improve in particular the performance of propulsion systems, today the standards are increasingly drastic. The International Civil Aviation Organization (ICAO) has promulgated regulations for civil subsonic turbojet/turbofan engines. The past decade has witnessed rapid changes both in the regulations for controlling aircraft engine emission. Indeed, the exhaust from an aircraft engine is composed of CO , NO_x , CO_2 , water vapor (H_2O) and unburned hydrocarbons (UHC). The situation in regard to compliance with the ICAO regulations is generally satisfactory for subsonic aircraft engines, due mainly to the efforts of the engine manufacturers in improving combustor design and in reducing engine specific fuel consumption. However, there is continuing pressure to reduce the NO_x emissions. To comply with this objectives, the multi-physical process occurring in aeronautical combustion is presented in the section 1.2. In the following section, the two-phase combustion is presented, from the atomization process to the different combustion regimes encountered

in real combustion chambers.

1.2 Multi-physical study

Two phase combustion comes coupled with multi-physical and chemical constraints, including atomization, dispersion, evaporation and combustion, which generally take place simultaneously or within very small regions in the combustion chambers. Compared to gas fired flames, additional complexity is added by the presence of liquid fuel droplets.

To understand the spray jet flame it is necessary to perfectly describe each step of the mechanisms, starting with the fuel droplet atomization up to the combustion regime occurring in the combustion chamber. The following illustration 1.3 shows the interacting multi-scale processes governing spray evaporation and combustion. Some of the interactions are not described in this chapter, only the interactions which can be encountered during this experimental work are now described.

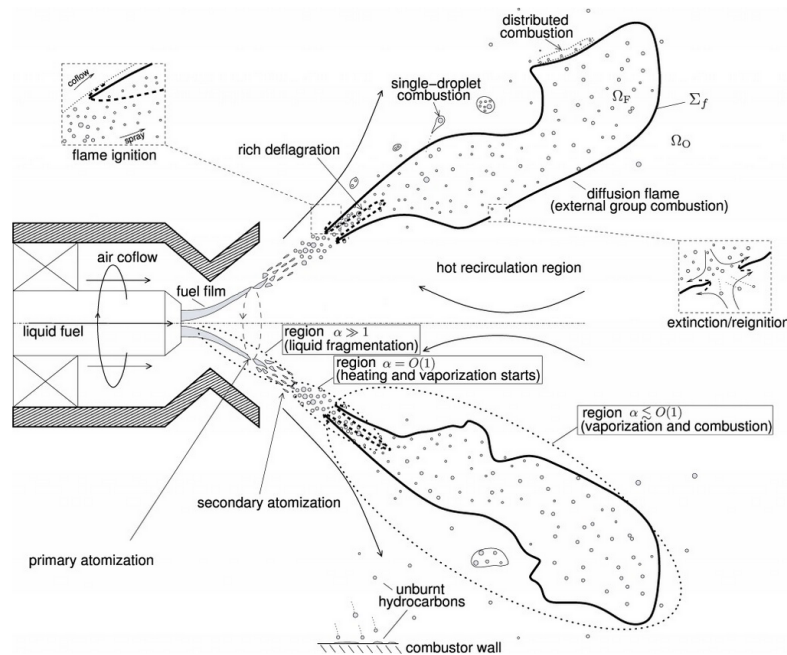


Figure 1.3: Sketch of fundamental spray-combustion processes. Extracted from [1]

The objective of modern combustors featuring low NO_x emissions is to first pre-vaporize the liquid fuel and to mix the fuel vapor, generated by the droplet evaporation. However, in most applications the time required for pre-vaporization and pre-mixing is not available. If the liquid is not perfectly pre-vaporized and pre-mixed, it will cause inhomogeneities of mixture fraction and consequently of the temperature in the flame. This will negatively affect the NO_x and soot emissions. Indeed, the addition of the droplets, by a diluted spray in a combustion chamber reveals new strong interactions, compared to pure gaseous flames, which can be summarized in fig 1.4.

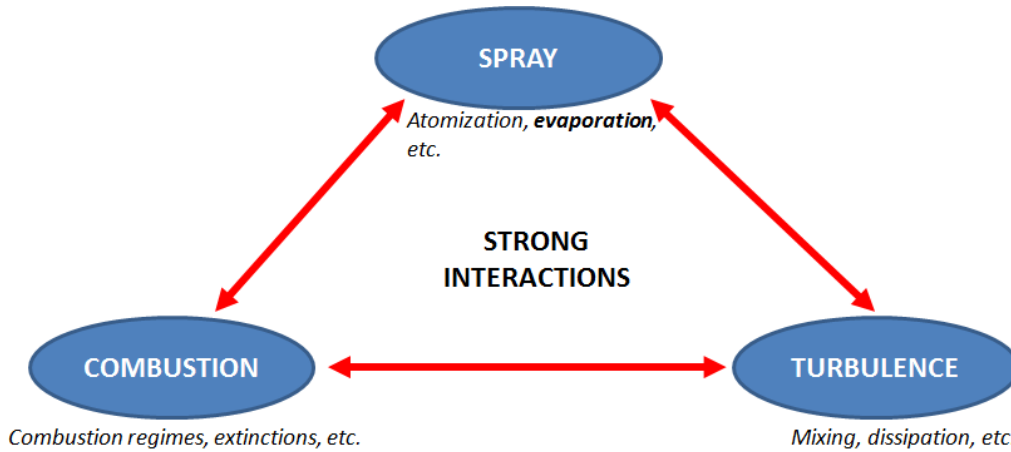


Figure 1.4: Schematic representation of the interactions involved in a reactive turbulent spray

The turbulent flow acts on the atomization and on the fuel droplet dispersion. Moreover the turbulence can amplify the droplet evaporation by forcing the exchange with the surrounding gas. The droplets can modify the local turbulence by a friction with the carrier phase. The fuel vapor production during the evaporation step leads to have, by molecular diffusion, an heterogeneous mixture fraction inside the chamber. The modification of the local mixture can have an influence on the combustion regime. Furthermore, as a result of the inhomogeneities in mixture fraction, it is very likely to encounter simultaneously several combustion regimes. Therefore, it is necessary to take into account all these phenomena simultaneously in order to understand the physical mechanisms occurring during two-phase combustion.

1.3 Atomization

The limited size of the combustion chamber implies a reduction of the spray length. To ensure this reduction, there exists a significant velocity difference between the liquid jet or sheet to be atomized and the surrounding air co-flow. The spray generated by the nozzle is characterized by droplet size and droplet velocity. An ideal atomizer would possess the following characteristics:

- Predefined uniform droplet size and velocity distribution across the spray
- High turn down ratio: The ability to provide good atomization over a wide range of liquid flow rates
- Rapid response to changes of the liquid flow rate
- No instabilities of the produced spray, neither in time nor in space

- Low power requirements and low susceptibility to blockage

Primary and secondary break-up

All atomizers have in common that the liquid sheet is generated with high velocity into the ambient air. The break-up into droplets is accomplished by the relative velocity between the liquid fragments and the air, which imposes high shear stress to the liquid surface. If the shear stress is higher than the surface tension of the liquid droplet, the break-up occurs. Therefore, high velocities are required in order to generate small size droplets at the exit of the injector. In a turbulent flow, the turbulence induced gas velocity fluctuation, which induces velocity fluctuations and pressure gradients across the droplet and may cause the droplet to disintegrate. After the primary break-up, the secondary break-up takes place if the forces acting from the outside (pressure and shear force for instance) on the droplet are larger than the interior forces due to the surface tension. The Weber (W_e) number is used to evaluate the atomization regimes and estimated with the following equation (Eq.1.1):

$$W_e = \frac{\rho U^2 L}{\sigma} \quad (1.1)$$

The weber number represents the ratio between the inertial forces of the droplet ($\rho U^2 L$) and capillary or surface tension forces (σ). This number allows us to determine the droplet capacity to resist on aerodynamic force thanks to the tension surface forces.

Air-blast atomizer

Depending on the applications, three different physical principles are used for the atomization of the liquid:

- Liquid pressure driven atomization
- Air driven atomization
- Rotary atomization

In combustion application the first two principles are mainly used, but to be consistent with the aeronautical application of this experimental work, only the air driven atomization is described.

The principle of an air-blast atomizer is the following: (i) the liquid is sprayed onto the pre-filming surface, (ii) the air flow generates shear forces in the thin liquid film, which is following towards the atomizing edge. At the exit of the injector, the disintegration of the film first into ligaments and then into droplets occurs. If the liquid flow is reduced,

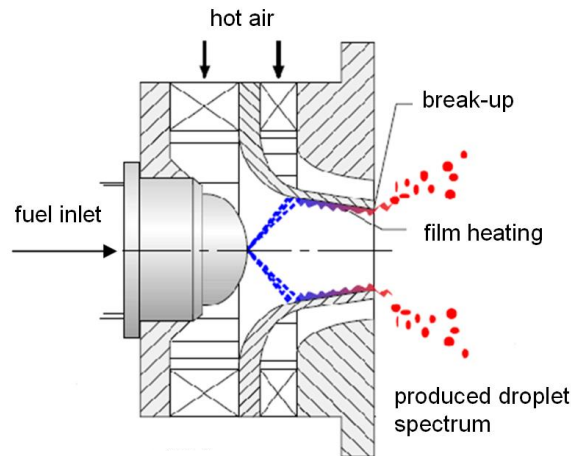


Figure 1.5: Cross section of an air-blast nozzle. Extracted from [2].

the air velocity is kept constant. The relative velocity between the liquid and air at the injector edge will be almost constant and hence also the droplet size and velocity. The major advantage of an air-blast injector is that the droplet size and velocity are unaffected by turning down the liquid flow rate. Furthermore, even at low liquid flow rate, small droplets will be produced thanks to the high relative velocity between the liquid and air.

1.4 Combustion regimes

Although all combustion processes are chemical reactions between fuels and oxidizer, the details of the processes vary greatly, so much so that we must treat them in different ways. In particular we divide combustion into two main categories, which can be encountered in aircraft engines:

- **Non-premixed combustion** In non-premixed combustion regions of fuel and oxidizer are separate, and combustion occurs on the interface between the two regions. Examples include various types of burner where a jet of fuel is injected into a region of air, and diesel combustion, where the fuel is broken up into individual droplets, and combustion can occur at the surface of the droplets.
- **Premixed combustion** In premixed combustion the fuel and oxidizer are mixed at the molecular level before combustion occurs. In such a case there are distinct regions of unburnt and burnt mixtures, separated by the flame.

In technical applications the optimum regime often lies somewhere between the two, where the fuel and oxidizer are permitted to mix partially but not completely before combustion occurs. This is known as Partially Premixed Combustion. However, in complex applications, such as in aircraft combustion chambers, all combustion regimes can be

met simultaneously. Furthermore, the two-phase combustion adds complexity in terms of combustion regime and needs to be studied in detail.

1.5 Applied research

To assist the engine manufacturers in developing high performance, low-emission combustors for engine propulsion systems, the research in experimental point of view can answer to the theoretically issue of spray combustion. Performing applied research in combustion sciences and exploratory development of combustors for gas turbine and advanced air breathing propulsion systems is becoming essential. Some experimental test bench are designed to operate in the severe conditions of pressure and temperature encountered in the ground and aeronautical gas turbines. Test facilities capable of reproducing these specific operating conditions are available at ONERA and enable subsonic air-breathing reacting flows occurring within gas turbine based aero-engines to be studied. Figure 1.6 summarizes the test facilities that are of interest in ONERA with their operating condition ranges. They are listed according to increasing thermal power supplied to the test line.

Test bench	Minimum air mass flow rate (kg/s)	Maximum air mass flow rate (kg/s)	Minimum pressure (MPa)	Maximum pressure (MPa)	Minimum air inlet temperature (K)	Maximum air inlet temperature (K)	Maximum air supply power (MW)
Microcombustion test bench*	0.0002	0.005	0.1	4	293	293	0
MERCATO	0.01	0.1	0.05	4	233	473	0.0246
EPICTETE test bench (LAERTE facility)	0.08	0.6	0.1	3	293	600	0.194
LACOM	0.1	1	0.1	50	293	900	0.68
MICADO 1 (ATD laboratories)	0.5	3	0.1	30	250	900	2.19
M1 (ATD laboratories)	0.1	4	0.05	30	250	900	2.91
MICADO 2 (ATD laboratories)	0.5	4	0.1	40	250	900	2.91

* No air preheating

Figure 1.6: Main Characteristics of ONERA test facilities

The DLR Institute of combustion technology also studied the pressurized combustion. Indeed, The Institute of HBK-S high-pressure combustion chamber test rig allows combustion processes in gas turbines to be studied under realistic conditions (Fig.1.7(b)). Moreover, a high-pressure flame system has been designed and constructed for studying nitrogen oxide formation in fuel-air combustion in NASA Langley Research Center. In Lund University, a facility is designed for study of high-pressure flames by spectroscopic methods and should also aid in the development of spectroscopic tools for high-pressure combustion environments.

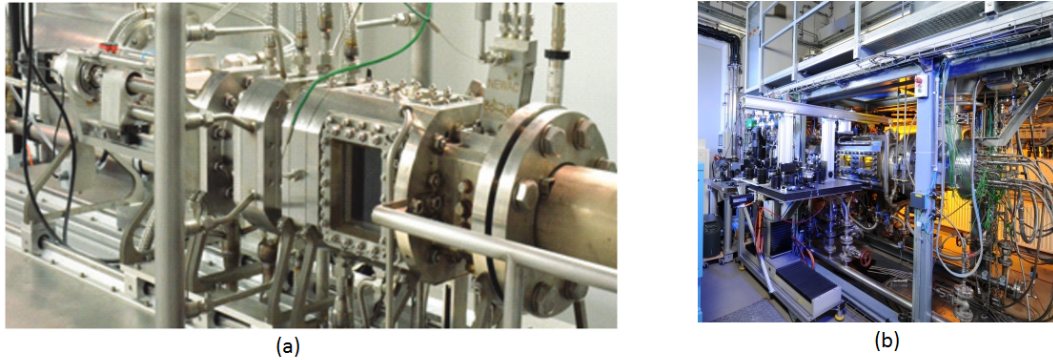


Figure 1.7: (a) HERON test bench from CORIA. (b) HBK-S high-pressure combustion chamber test rig from DLR

A new combustion chamber (HERON High prEssuRe facility for aerO-eNginEs combustion from CORIA Fig. 1.7(a)) offer a well-adapted infrastructure to the study of industrial fuel injection systems in the CORIA laboratory. The combustion chamber performances are optimized to study advanced helicopter fuel injection systems up to their nominal operating ranges and aero-engines injection systems up to 2/3 of their nominal ranges. The combustion chamber is equipped with an optical visualization module allowing optical measurements between the exit of the injection system (flame stabilization zone) and the internal wall of the combustion chamber (flame/wall interaction zone). A fuel preparation skid allows to control and to feed the fuel injection system with liquid multi-component fuels (kerosene, biofuels...) or gaseous fuel mixture (CH_4 , CO_2 , CO and H_2) with a well controlled chemical composition. From this experimental facility, a Lean-Premixed (LP) aero-engine injection system was experimentally studied using optically-based measurements. Experiments are conducted under relevant operating conditions up to 1.38 MPa and using commercial kerosene as fuel [19]. However, due to the critical condition, high pressure and temperature the optical diagnostics are more difficult to apply than on canonical configurations and several diagnostics will not be yet be performed in these conditions. Indeed, the high temperature and pressure imply having a combustion chamber structure able to support these critical conditions. In most cases, the combustion chamber have only small optical access to perform laser diagnostics. The confinement of the chamber is very important to support the load generated by the pressure.

In addition to the experiments and since the 1960s, the development of numerical methods to discretize Navier-Stokes equations and the increase in computational capabilities, have allowed the development of digital fluid mechanics. Since then, the Computational Fluid Dynamics (CFD) has taken an increasingly important part in the design of new aircraft engines, particularly in the development phases. During these phases, it is preferable from an economic point of view to use computer power than to build prototypes and then test them in order to predict their performance. One of the main reasons for the

progress made in CFDs is the understanding and prediction of turbulent flows. However, in the face of a large number of Reynolds numbers, it is difficult to solve all the dynamic scales contained in the Navier-Stokes equations. In view of these difficulties, three approaches to CFD are possible today to simulate turbulent flows. The level of modeling required for each of these methods is shown schematically in figure 1.8. In the following, a brief description of these three approaches is given.

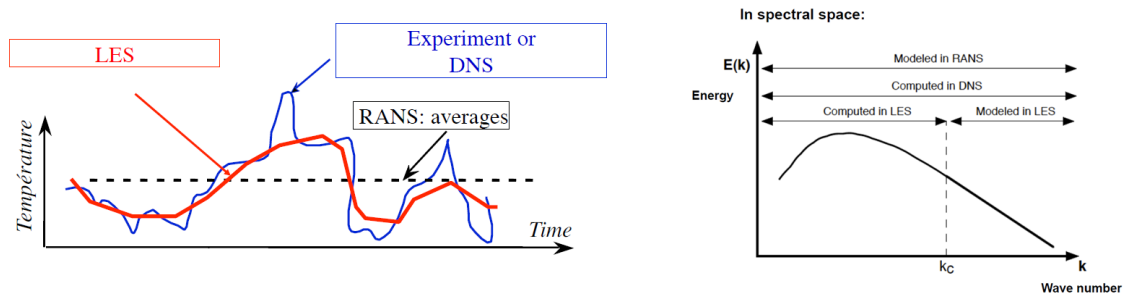


Figure 1.8: Schematic representation of the level of modeling required for each of the approaches for the example of a time signal of temperature and in spectral representation

- Reynolds Averaged Navier-Stokes : RANS

The RANS method consists of solving an average flow and modeling the turbulence fluctuations by a turbulent viscosity [20–22]. The URANS method is an unsteady extension of the RANS which solves the very large (slow) temporal fluctuations of the flow. For this, the turbulent flow is divided into two terms: one contribution linked to the mean and the other related to the fluctuations. This decomposition is called Reynolds decomposition. Consider, for instance, the Reynolds decomposition on velocity:

$$u = \bar{U} + u' \quad (1.2)$$

with $\bar{u}' = 0$

where \bar{U} represent the mean velocity and u' a fluctuation compared to the mean value. The average operator corresponds to an arithmetic mean made at any point of space and time. In real industrial applications, this is a suitable approach for the simulation of the aircraft engine, comprising the compressor and the turbine.

- Large Eddy Simulation : LES

In Large Eddy Simulation, turbulence scales smaller than mesh size are filtered and modeled while large scales containing most of the energy of the flow are fully simulated. On the other hand, this method requires a very fine discretization near a body because of the very small turbulence scales present in the thin boundary layer along the walls. Moreover, the LES allows a dynamic representation of the flow and of the large-scale unsteady

turbulent structures. In contrast, the requirement in terms of spatial and temporal resolution is much greater than for the RANS methods. Due to the unsteady nature of the phenomena occurring in the combustion chamber, LES is the most suitable approach for the simulations of this part of the engine

- Direct Numerical Simulation : DNS

The Direct Numerical Simulation (DNS) method is used to completely solve the turbulence spectrum without any modeling. This requires a sufficiently thin mesh to capture up to the smallest scale of turbulence. The exorbitant calculation cost of this method makes it inappropriate for the majority of engineering problems, but it remains essential for our fundamental understanding of the physics of turbulence. Nowadays CFD uses DNS only for the validation of numerical models in canonical test cases.

In the following two examples of the use of LES in aeronautical combustion are given:

- The first numerical study concerns the light-round, defined as the process by which the flame initiated by an ignition spark propagates from burner to burner in an annular combustor, eventually leading to a stable combustion. In a recent paper [3] the light-round simulation is performed in a spray configuration by considering liquid n-heptane injection. The LES of the ignition sequence of a laboratory scale annular combustion chamber is carried out with a mono-disperse Eulerian approach for the liquid phase description. The authors have compared the simulation results in terms of flame structure and light-round duration to the corresponding experimental images of the flame front recorded by a high-speed intensified camera and to the corresponding experimental delays (Fig.1.9).
- The design of a future aeronautical combustion chamber integrates multiple contradicting objectives such as making the combustion stage more efficient and cleaner and reducing the number of injector. The number of fuel injection systems and their spacing are crucial information which needs to be fixed. Indeed, such choices not only impact the cost and size of the combustor but they also affect the operability of the future engine. A study carried out by the CERFACS demonstrates the capacity of the LES to predict an ignition sequence [4] (Fig. 1.10). The authors performed an experimental and numerical simulation of ignition study in multi-injectors. The effect of the distance between injectors on the ignition process and a contribution of the understanding of the mechanisms driving the light-around flame propagation is provided. Comparisons between experiments and LES have shown the capability of LES to reproduce ignition sequences as well as the added value of LES in this investigation of ignition process thanks to the additional data available.

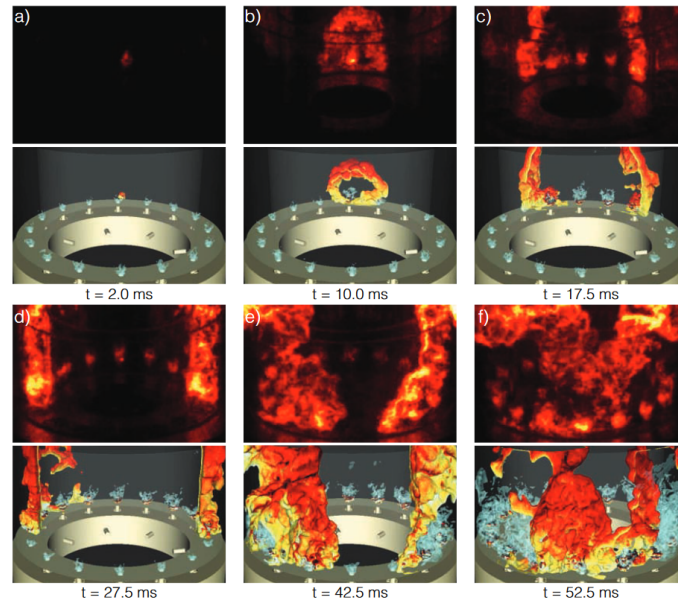


Figure 1.9: (Snapshots of the ignition sequence: experimental direct imaging of the flame emission colored for visualization purposes (top rows) versus iso-surfaces of $T = 1781$ K colored by the axial velocity and $U = 25$ m/s in light blue extracted from the LES (bottom rows). [3])

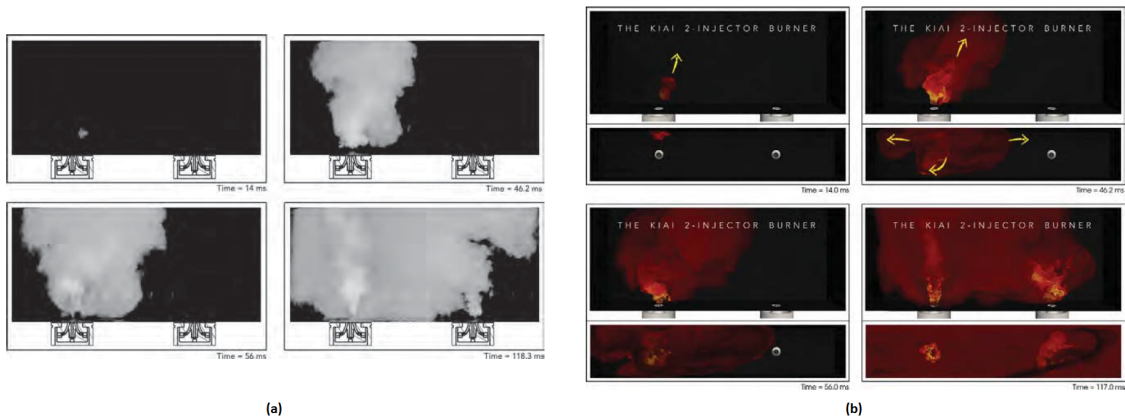


Figure 1.10: (a) Experiments: fast visualization of the flame showing an axial propagation. (b) LES results: instantaneous snapshots of the ignition sequence visualized by the volume rendering of heat release [4].

Several studies show the efficacy of the numerical simulation in the understanding of the mechanisms driving the combustion. Nowadays, the numerical results are in accordance with the experiments for the characterization of the dispersed and carrier phase. However, the prediction of flame structures is more difficult due to the complexity of the combustion models. Moreover, in real configuration, the lack of experimental data makes the task of choosing the model more difficult. It is in this perspective that the different laboratories develop experiments to be able to better understand the mechanisms of combustion. Moreover, with the development of new diagnostics, databases appear more and more. The following section gives an overview of existing databases of spray jet flame

configuration.

1.6 Spray jet flame experimental configurations

To overcome the difficulties resulting from real geometries (small optical access and measure altered by the strong conditions such as the temperature and pressure), the jet spray flame configuration is mostly experimentally investigated. This canonical configuration includes a central pressure or air-blast fuel injector, surrounded by a co-flow which may present different thermo-physical properties (composition, temperature, etc.). A flame is then stabilized downstream the injection and presents a rich variety of flame structures. In the following, some previous results available in literature are presented to give the most relevant properties of such configurations. The pioneer works of Cessou et al. [?,23,24] investigated the flame structures in the stabilization zones of a two-phase jet flame above a coaxial air-blast injector. From quantitative OH-PLIF measurements, they suggested that the flame presents a structure of two diverging and opposed diffusion-like fronts. They found also that the flame structures were strongly affected by the atomization process and the spatial distribution of fuel droplets. In their Jet Spray Flame burner operating with pressurized fuel injector and a large bluff-body, Friedmann et al. [?] showed that the spray flame had also a dual reaction zones structure with air co-flow off but a single reaction zone with air co-flow on (figure 1.11).

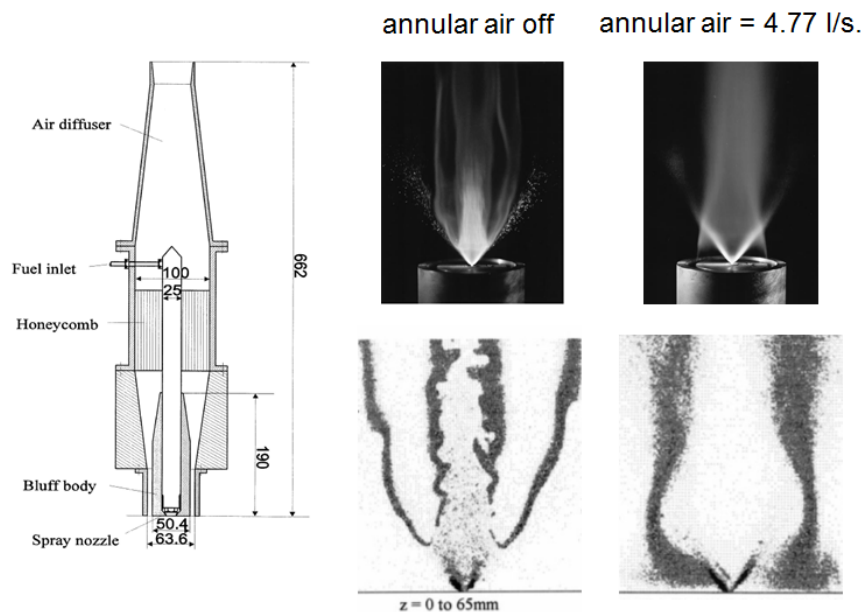


Figure 1.11: Burner system cross section studied by Friedman et al with all dimensions in mm. The photographs and the OH-PLIF images present the main results of this study in term of air co-flow effect [?].

This effect of air co-flow rate was also investigated by Marley et al. [25,26] in a spray burner operating without bluff-body, and the conclusions were somewhat different. By

using OH-PLIF measurements, they observed a double flame structure, appearing as two diverging flame fronts and consisting of an outer diffusion flame and an inner structure that transitions from mixing controlled to partially premixed combustion downstream of the leading edge. Without co-flow, the structure was modified and a double reaction zone was still observed but with an inner structure that burned intermittently with areas of local extinction occurring often at the most upstream locations near the leading edge. Cleon et al. [27] studied the effect of CO_2 dilution on a spray oxy-fuel flame in terms of flame structure and stabilization. The amount of CO_2 modified drastically the chemical time, the flame temperature, and thus the vaporization time and the size dispersion of fuel droplets. These first results highlighted the variety of flame structures associated to the burner geometry and the fuel droplets generation. Experimental works have also been conducted on more academic configurations such as counterflow flames [28]. These studies make it possible to study and isolate some physical mechanisms to facilitate understanding such as flame structure and stabilization, which can be discussed compared with the flame-spread mechanism of the droplet array with a low-volatility fuel [29].

In order to put the effort on the understanding of the droplets/turbulence/flame interactions and to improve modeling capabilities of turbulent spray reacting flows, new experimental facilities were designed in several research groups to perform extensive measurements on the disperse and carrier phase, for reactive and non-reactive conditions. Some of these recent works are coordinated by international workshops on the Turbulent Combustion of Sprays (TCS) (<http://www.tcs-workshop.org/>).

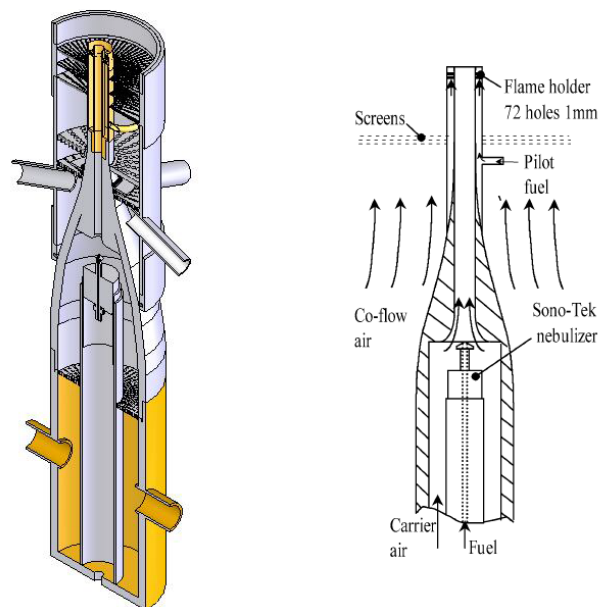


Figure 1.12: Schematic of the Sydney University spray burner [5].

Figure 1.12 presents a schematic of the Sydney Spray Burner developed by Masri and co-workers [5, 30, 31]. It consists of a piloted spray burner where fuel (acetone or ethanol) is injected by a nebulizer located upstream inside the spray nozzle in the carrier

air co-flow. The two-phase flame is stabilized by an annular pilot flame. They provided an extensive database on the phenomena of interest in dilute sprays: droplet dispersion, droplet evaporation, turbulence/droplets interaction and droplet/flame interactions. Some of the experimental conditions concern the extinction limits near the blow-off limits. Non-premixed and premixed flame characteristics are found depending on the fuel vapor pressure and the proximity to blow-off. Broad regions of OH as well as holes in the OH profile marking possible local extinction are observed. In addition, a specific study of the spray boundary conditions was made including a systematic variation of parameters leading to an extensive database useful for detailed validation studies of models in spray flames.

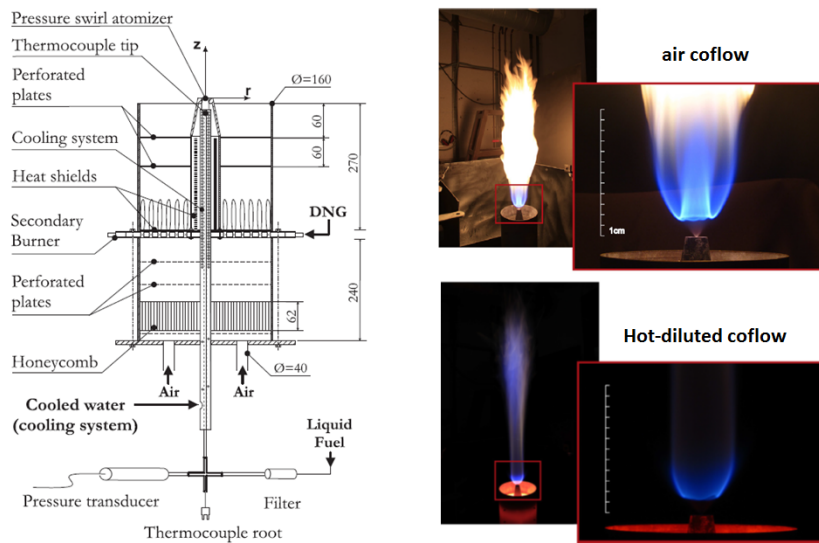


Figure 1.13: Geometry of the Delft Spray burner

The Delft Spray burner was designed by Roekaerts et al. [32,33] to study spray combustion in MILD conditions and it is represented in figure 1.13. It consists of a pressure-swirl atomizer that produces a spray of ethanol droplets issuing in a co-flow of either air or hot combustion products. Disperse and carrier phase properties were estimated by PDA measurements and a CARS system was used to evaluate the gas-phase temperature statistics. They found that both co-flow temperature and oxygen dilution lead to changes in the local flame type and strength of heat-release, even if the global double flame structure is still conserved.

Figure 1.14 shows the geometry of the Cambridge Spray Burner, updated from the gaseous bluff-body swirl burner by changing the injection system [6, 34]. N-heptane is injected through a pressure swirl hollow cone injector located within the bluff-body surrounded by a swirled air co-flow. The burner operated close to blow-off limits and specific optical diagnostics (high-speed OH-PLIF and joint PLIF measurements of CH₂O and OH) were applied successfully both to investigate the local flame structure and the reaction zones, and local extinctions holes along the flame sheet. They observed that the

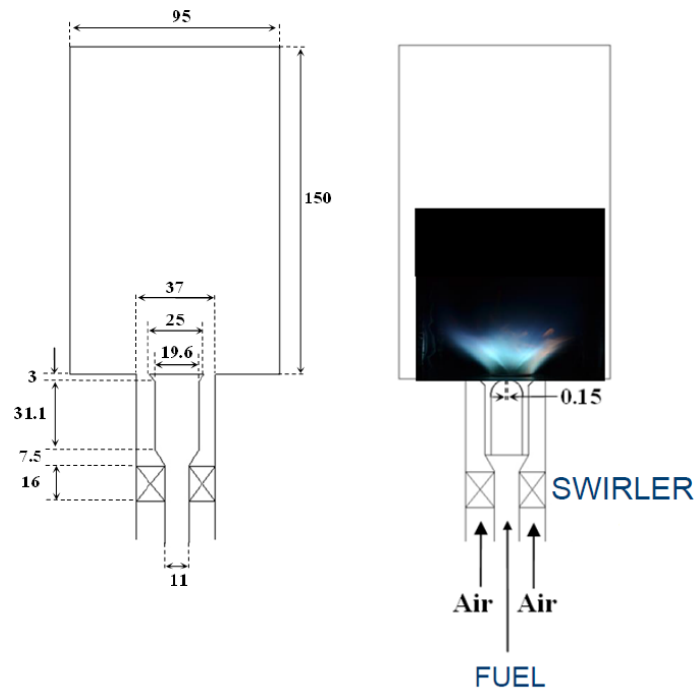


Figure 1.14: Geometry of the Cambridge University swirling spray burner [6].

flame inner branch which appears to be a diffusion flame between evaporated fuel and the recirculating air, is less prone to extinction than the outer flame branch along the shear layer. This latter may lift-off the bluff body randomly and the central part of the flame shows occasional breaks. Unfortunately, these phenomena cannot be resolved temporally with the 5 kHz system due to the fast air flow and the presence of swirl.

1.7 Objectives and organization of the manuscript

Today, to predict and understand the combustion occurring in industrial applications, particularly in aeronautical combustion chambers, numerical simulations are increasingly used. However, for the LES to be able to predict the complex phenomena occurring during the combustion of liquid fuel, it is necessary to validate the simulation codes by comparing them with experimental data. From an experimental point of view, the drastic conditions of industrial applications make it difficult to apply optical diagnostics. It is therefore important to develop a simpler configuration burner in order to fine-tune the mechanisms that take place in the combustion chamber. Previous studies, notably those of Camille Letty [35] and Armelle Cessou [?] on the study of spray flames, made it possible to understand the mechanisms of interaction between spray, turbulence and combustion. However, these experimental databases must be provided with accurate experimental data to answer the hard points of the LES, which can be summarized in the following:

- Evaporation models, strongly impact the fuel droplet temperature and the fuel vapor

available for the combustion, and consequently the flame stabilization

- Combustion models through detailed or simplified chemistry, which greatly influence the prediction of pollutant emissions
- Capacity of LES to predict the different two-phase flow combustion regime occurring simultaneously in real configuration. Moreover, the local flame extinction can be difficult to predict and depends on the use of models.

This work is carried out to:

1. Develop a new experimental facility (Chapter 3) with accurate experimental techniques able to measure on flame structure and on liquid and gas properties along evaporation and combustion steps. The first part is dedicated to present the burner, the fundamentals of the spray combustion and the optical diagnostics applied in this experimental facilities.
2. Develop and apply extensive optical diagnostic techniques such as the Phase Doppler Anemometry (PDA) and the OH Planar Laser Induced Fluorescence (PLIF). The investigations are focused on the characterization of the carrier and dispersed phases to understand the different combustion regimes present in the flame structure (Chapter 5).
3. Develop and apply a new technique (Global Rainbow Technique GRT) able to measure the fuel droplets temperature in a complex configuration and in real spray reacting conditions (Chapter 4).
4. Perform High Speed optical diagnostics (PIV and OH-PLIF) simultaneously to study the response of the flame structure to unsteady local flow properties via turbulence-flame interactions (Chapter 6).
5. Provide a reliable database to meet the objectives of the international workshops on the Turbulent Combustion of Sprays (TCS). The comparisons between different laboratories (CERFACS, EM2C, IMPERIAL COLLEGE and TU Delft) and our experimental results are presented in Chapter 7 in order to evaluate the importance of model choices in LES results.

Chapter 2

Fundamentals of spray combustion

Contents

2.1	Droplet evaporation	19
2.2	Multi-physical study	26
2.2.1	Spray-Turbulence interactions	26
2.2.2	Turbulence-gaseous flame interactions	28
2.2.3	Spray-Flame interactions	30
2.2.4	Combustion regime	31
2.3	Conclusion	33

Chapter 1 illustrates that several spray jet flame databases appear to describe the different mechanisms occurring in two phase combustion. The strong interactions between the carrier and dispersed phases implies understanding in their simplest configuration, the main mechanisms such as the droplet evaporation and the different combustion regime. This chapter is organized as follow: (i) the droplet evaporation model is given to explain two different models mainly used in LES. (ii) The different combustion regimes that can be encountered in a configuration are described.

2.1 Droplet evaporation

Predictive models of heating and evaporation of fuel droplets is of great importance in many energy systems involving spray combustion. In a general, the liquid fuel atomization creates multiple droplets of different sizes, where droplet-to-droplet interactions play a significant role in the evaporation process. The complexity of real configurations makes it difficult to develop models to study the evaporation in a real spray. Indeed, the majority of evaporation models used for real combustion chamber calculations do not take into account its interactions. The modelings of heating and evaporation use in LES

are widely available in literature [36–41]. Some previous theoretical [11, 42] and experimental [43, 44] studies were performed in similar conditions to those encountered in real application. However, to validate the numerical models, it is necessary to simplify and limit the uncontrolled interactions that can be encountered in a spray. This approach is related to studying the evaporation of a single droplet, under different conditions. The first experimental facility is the suspended evaporating droplet. Several studies of droplet evaporation are carried out in convective streams [45–47] or non-convective streams at normal gravity. However, to simplify the model, and to guarantee the spherical symmetry of the droplet, some experimental studies performed droplet evaporation under micro-gravity conditions [48–51]. The evaporation of an isolated droplet in different surrounding conditions is a process involving mass, momentum and heat transfers in both gas and liquid phases, which couple at the interface. These fundamental studies provide the physical basis for the understanding of evaporation process in order to move forward in more complex spray configurations. However droplets in real aeronautical spray applications are surrounded by neighbors which influence the evaporation rate. In order to study these interactions, theoretical and experimental investigations have been performed recently. Castenet et al. [52] studied the interaction processes that affect the heat and mass transfers in a chain of periodically-arranged monodisperse droplets by experimental and numerical approach.

To demonstrate the importance to study the droplet evaporation process, an overview of the study of Miller et. al [7] is given. In this work, a variety of liquid droplet evaporation models, defined by three types of models described in the following, are evaluated through comparisons with experiments.

Type	Model	Name
Type 1	M1	Classical rapid mixing
Type 1	M2	Abramzon-Sirignano
Type 2	M3	Mass analogy Ia
Type 2	M4	Mass analogy Ib
Type 2	M5	Mass analogy IIa
Type 2	M6	Mass analogy IIa
Type 3	M7	Langmuir-Knudsen I
Type 3	M8	Langmuir-Knudsen II

Table 2.1: Nomenclature of models studied in the paper [7].

The droplet evaporation model given in table. 2.1 can be classified into the following three groups with increasing complexity. For each groups, the evaporation models are globally described and the main assumptions are given.

- TYPE 1: The fuel droplet temperature is kept constant along the evaporation process. Figure 2.1 illustrates that the droplet temperature is uniform inside the

droplet and constant with the time. Moreover, the different models of type 1 assume the fuel vapor diffusion in carrier phase to be spherically symmetric. The first model described in table. 2.1, called classical rapid mixing by the authors [7] is also referred to as the D^2 law and assumes a constant droplet temperature and include the quasi-steady assumption with infinite conductivity model or the rapid mixing model ($T = \text{cste}$). Then Model M2 (Abramzon and Sirignano) examines the rapid mixing model including evaporation corrections on heat and mass transfer, such as the effects of Stefan flow for instance.

- TYPE 2: Figure 2.1 shows that the temperature is still uniform inside the droplet but its depends on time. It is assumed that the droplet is heated up to its boiling temperature and then evaporates. All energy transferred from the ambience to the droplet is used for evaporation. Compared to the type 1, recent models [53, 54] introduce correction factors in the spherically symmetric model for the fuel vapor diffusion. They include the effect of convection around the droplet to obtain the interaction between the external flow and the fuel vapor around the droplet, generated by the evaporation process. Models M3-M6 are all variations of a basic heat-mass transfer analogy model which can be derived directly from the vapor fraction boundary condition at the surface of the droplet. These models are assumed as TYPE 2.
- TYPE 3: In this kind of evaporation models and in addition to the temporal evolution of the droplet temperature, the gradient temperature inside the droplet is taken into account (Fig. 2.1). There are several techniques to solve these models. For instance, the resolution of the Navier Stokes equations inside and outside the droplet allows to precisely determine the droplet temperature in a given surrounding. However, it is important to note that this models is computationally very expensive and so, rarely used in LES. In the paper of Miller [7] model M7 and M8 are of TYPE3 and differ in the equilibrium assumption. Indeed, the non-equilibrium evaporation law, based on the Langmuir-Knudsen law incorporates droplet temperature non-uniformity.

Finally, the first models (M1 to M6) are considered as transient classical models with heat-mass transfer analogy, whereas, the two last models (M7 and M8) are two non-equilibrium models based on the Langmuir-Knudsen evaporation law. The difference between the eight models resides in the calculation of the heat and mass transfer terms. A brief description of the various models were just given, but the readers can be find additional details in [7].

Figure 2.2 presents the temporal evolution of the droplet diameter squared and the droplet temperature for decane droplet at the following initial conditions: the surrounding

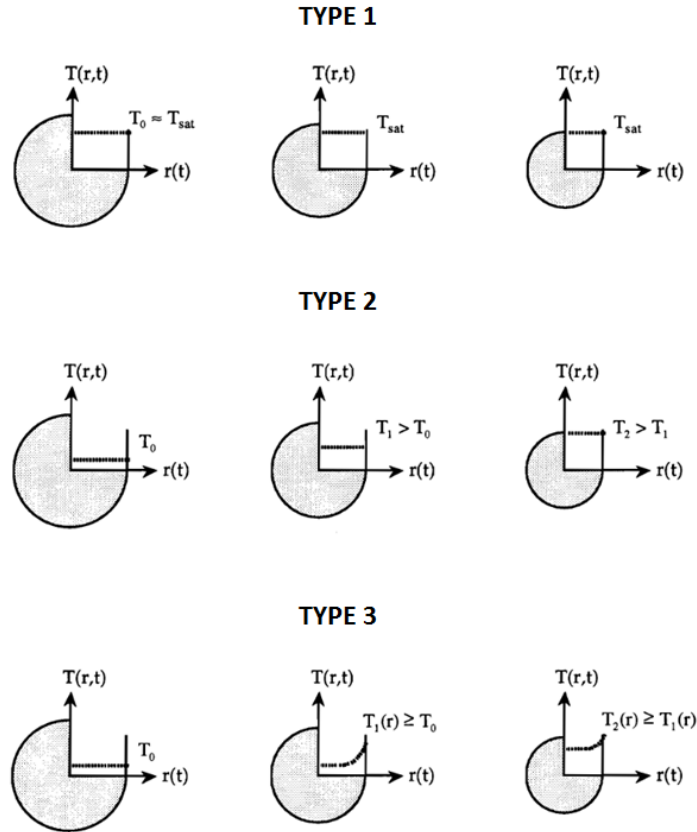


Figure 2.1: Temporal and spatial temperature evolution for the 3 different types of evaporation models.

temperature is 1000 K, the initial droplet diameter is 2.0 mm with an initial temperature of 315 K and the Reynolds number is equal to 17. This figure presents a strong divergence between the numerical and the experimental results, particularly in terms of fuel droplet temperature evolution. In comparison with most used in large eddy simulation, the classical rapid model (M1) gives a difference around 60 K with the experiments on the wet bulb temperature. This study highlights the importance of the model choice in terms of fuel droplets temperature and indirectly, on the flame structure, which will be driven by the amount of available fuel vapor. Indeed, the conclusion of this study is on the difficulty in finding the best evaporation model in a simplified configuration, where one isolated droplet is computed. However, in realistic configurations, such as in internal engine or aeronautical combustion chamber, the entirety of the spray droplets must be simulated and requires massive computations. These computational costs make that in real and complex applications the LES always uses a type 1 or 2 evaporation model. That's why, in the following of this section, two classical models (Spalding and Abramzon-Sirignano) of an isolated droplet evaporation, which are mainly used in LES are presented.

During the droplet evaporation, different processes are acting simultaneously:

- Heat transfer between ambient gas and droplet by convection, conduction and ra-

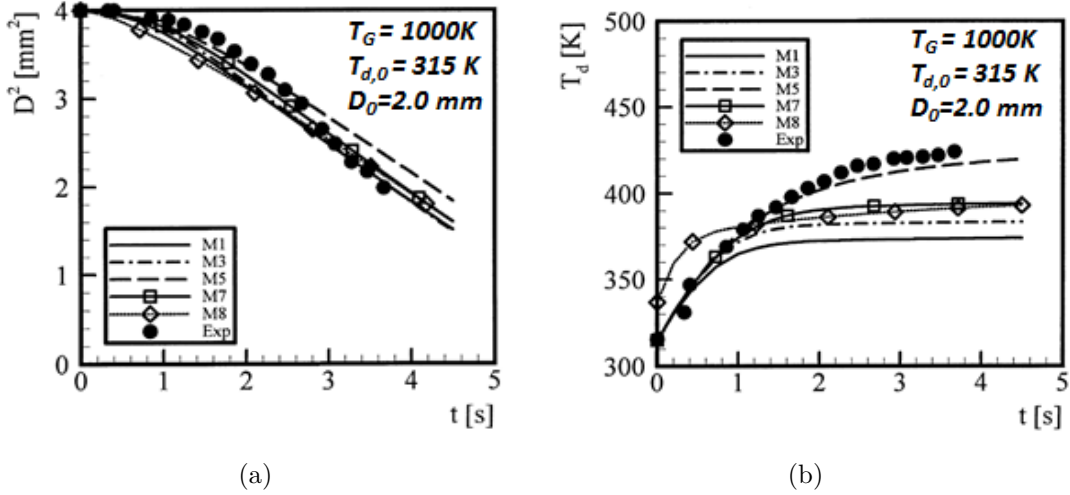


Figure 2.2: Temporal evolution of the droplet diameter squared (a) and droplet temperature (b) for decane ($T_B = 447.7K$) with various models [7]. The experimental results are from Wong and Lin [8]

diation.

- Mass transfer between ambient gas and droplet by advection and diffusion.
- Heat transfer inside the droplet by convection and conduction.
- Phase change at the droplet surface.

The Spalding model has different assumptions and the system of equations describing the evaporation can be solved analytically. (i) the droplet is assumed to be perfectly spherical and isolated, which makes it possible to neglect the interactions with neighboring droplets. (ii) the temperature inside the droplet is uniform, because the thermal conductivity inside the droplet is considered infinite. (iii) the Spalding model [55] assumes the fuel vapor diffusion in carrier phase to be spherically symmetric. The Clausius-Clapeyron law can be used to calculate the fuel gaseous mass fraction Y_F at the interface between the droplet and the surrounding gas.

Now the equations of conservation for momentum (Eq.2.1), species (Eq.2.2) and energy (Eq.2.3) can be written between the surface of the droplet (noted ζ) and the surrounding gas (noted ∞).

$$\rho U r^2 = \frac{\dot{m}_F}{4\pi} \quad (2.1)$$

$$\rho U r^2 \frac{dY_F}{dr} = \frac{d}{dr} \left(r^2 \rho D_F \frac{dY_F}{dr} \right) \quad (2.2)$$

$$\rho U r^2 \frac{dC_P T}{dr} = \frac{d}{dr} \left(r^2 \frac{\lambda}{C_p} \frac{dC_P}{dr} \right) \quad (2.3)$$

where u represents the droplet surface regression velocity, r the radial position, \dot{m}_F the fuel vapor production at the surface, Y_F the fuel mass fraction and D_F , the thermal diffusivity.

By integrating the equation 2.2 two times, the evaporation rate of an isolated droplet (\dot{m}_p) can be extracted.

$$\dot{m}_p = \frac{dm_p}{dt} = -\pi Sh d_p \rho D_F \ln(1 + B_M) \quad (2.4)$$

The ratio between the mass transfer by convection and by conduction is represented by the Sherwood number (Sh). The Spalding number (B_M) shows the difference in term of fuel mass fraction between the droplet interface and the infinite and is calculated by the following equation 2.5:

$$B_M = \frac{Y_{F,\zeta} - Y_{F,\infty}}{1 - Y_{F,\zeta}} \quad (2.5)$$

The conditions at the surface of the droplet and at infinity determine the evaporation rate. Moreover, the Clausius-Clapeyron relation allows us to calculate the conditions at the surface of the droplet.

$$X_{F,\zeta} = \frac{P_{cc}}{P} \exp\left(\frac{W_F L_v(T_{ref})}{R} \left(\frac{1}{T_{cc}} - \frac{1}{T_\zeta}\right)\right) \quad (2.6)$$

Where p_{cc} and T_{cc} are reference of pressure and temperature respectively, which correspond to a point in the saturation curve. W_F is the fuel molar mass, R is the perfect gas constant. L_v is the latent heat of evaporation at the reference temperature T_{ref} .

The decrease of the droplet diameter is directly related to the evaporation rate, and the mass evolution of the droplet is described by the law of d^2 .

$$\dot{m}_p = \frac{d}{dt} \left(\frac{4}{3} \pi \rho_l r_p^3 \right) \quad (2.7)$$

Using the Eq. 2.4 with the Eq. 2.7, the d^2 law can be obtained:

$$d_p^2 = d_{p,0}^2 - \frac{8\rho_g D_F}{\rho_g} \ln(1 + B_M) t \quad (2.8)$$

The temperature inside the droplet is assumed to be equal to the temperature at the surface. By applying an energy balance on the droplet, the temperature can be obtained and an illustration of the temperature profile is represented in Fig. 2.3

$$\frac{d}{dt} (m_p h_{s,p}(T_p)) = \Phi_l^c + \Phi_l^{ev} \quad (2.9)$$

The l and g represent the heat flux toward the droplet and toward the gas respectively. Φ_l^c and Φ_l^{ev} are the heat flux by conduction and the enthalpy flux by the phase change. The equilibrium assumption at the interface allow to write the thermal balance at the

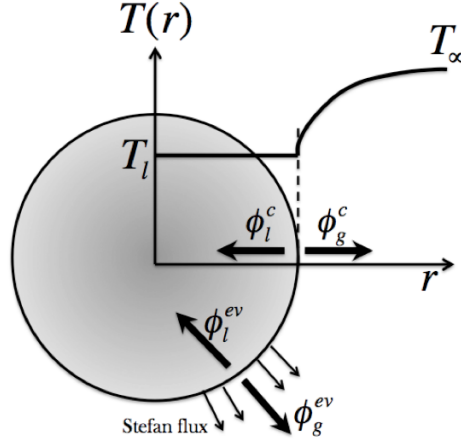


Figure 2.3: Sketch of the heat fluxes and temperature profile in the evaporation of an isolated droplet following the infinite conductivity model (ICM). Extracted from AVBP handbook.

droplet surface:

$$\Phi_l^c + \Phi_l^{ev} = \Phi_g^c + \Phi_g^{ev} \quad (2.10)$$

From the heat latent, the flux Φ_l^{ev} and Φ_g^{ev} can be determined

$$\Phi_g^{ev} + \Phi_l^{ev} = -\dot{m}_v L_v(T_\zeta) \quad (2.11)$$

By integrating the Eq. 2.3 two times, Φ_g^c can be calculated:

$$\Phi_g^c = \pi \lambda d_p Nu (T_\zeta - T_\infty) \frac{\ln(B_T + 1)}{B_T} \quad (2.12)$$

where, B_T is the Spalding number for the temperature. This quantity can be linked with the Spalding number for the mass B_M , where Le_v is the Lewis number and Nu the Nusselt number.

$$B_T = (1 + B_M)^{\frac{Sh}{Nu Le_v}} - 1 \quad (2.13)$$

In the Spalding model, the properties of diffusive transport are assumed constant. The composition and temperature of the mixture in the film are evaluated by interpolation between the values at the droplet surface and the condition in the far field using the 1/3 law [7]. It is calculated as the following equation:

$$T_i = \frac{2}{3} T_\zeta + \frac{1}{3} T_\infty \quad (2.14)$$

$$Y_{F,i} = \frac{2}{3} Y_{F,\zeta} + \frac{1}{3} Y_{F,\infty} \quad (2.15)$$

The Spalding model is based on the evaporation of an isolated droplet at rest. However, in real configuration, the relative flow around the drop induces the presence of a boundary layer. To take into account this interaction in the evaporation model, the correlation of Ranz-Marshall propose to modify the Sherwood and Nusselt number as the following:

$$Sh = 2 + 0.55Re_p^{\frac{1}{2}}Sc_v^{\frac{1}{3}} \quad (2.16)$$

$$Nu = 2 + 0.55Re_p^{\frac{1}{2}}Pr_v^{\frac{1}{3}} \quad (2.17)$$

To continue to improve the evaporation model, Abramzon and Sirignano [53] propose to take into account the convective boundary layer, which allow to define a thermal and mass thickness within the boundary layer by including two correction factors F_M and F_T

$$F_M = (1 + B_M)^{0.7} \left(\frac{\ln(1 + B_M)}{B_M} \right) \quad (2.18)$$

$$F_T = (1 + B_T)^{0.7} \left(\frac{\ln(1 + B_T)}{B_T} \right) \quad (2.19)$$

Thanks to these two correction factors, the corrected Nusselt and Sherwood number are:

$$Sh^* = 2 + \frac{Sh - 2}{F_M} \quad (2.20)$$

$$Nu^* = 2 + \frac{Nu - 2}{F_T} \quad (2.21)$$

2.2 Multi-physical study

2.2.1 Spray-Turbulence interactions

The mutual interactions between the turbulence and the spray are recently described by Balachandar et al. [56]. The modulation intensity of the turbulence by the droplets depends on the number and the droplet size. Indeed, the modulation of turbulence is double. First the droplets decrease the local turbulent kinetic energy by friction at the droplet surface. The turbulent kinetic energy is dissipated at the surface of the droplet. On the contrary, in the wake of droplets the local turbulent kinetic energy can be increased by the formation of vortices. Furthermore, the turbulence can affect the droplet size distribution. Indeed, the preferential segregation of fuel droplets depends mainly on the turbulence-spray interaction. These interactions have been studied experimentally [57,58] and numerically [59–61].

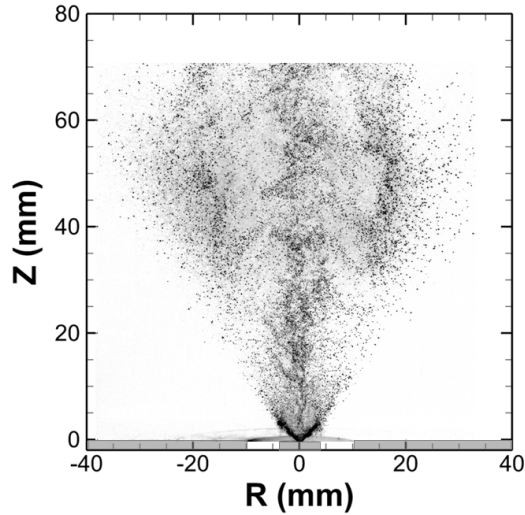


Figure 2.4: Preferential segregation of droplets. Experimental image obtained by the Mie diffraction of the droplet, with a laser sheet.

In a turbulent gas flow, the droplets are exposed to turbulent velocity fluctuations. Depending on the inertia of the droplet, it will be able or not to follow the turbulent velocity fluctuations. Obviously, a large droplet will respond less to turbulent velocity fluctuations than a smaller one. From the equation of droplet motion, the droplet response to the velocity fluctuations can be deduced.

$$\frac{d\vec{u}_d}{dt} = -18 \frac{\mu_g}{\rho_d D_d^2} (\vec{u}_g - \vec{u}_d) \quad (2.22)$$

The characteristic time $\tau_p = \frac{\rho_d D_d^2}{18\mu_g}$ represents the relaxation time. It is the time that droplets need to adapt themselves to the new ambient air velocity after a sudden change. The droplets with a large relaxation time τ_p will need more time to follow turbulent velocity fluctuations than droplets with smaller τ_p . For further analysis, the relaxation time can be compared to a characteristic time of the flow and a new adimensional number can be created: Stokes number. The Stokes number S_t allows us to describe the inertia of the droplet compared to the carrier phase, which can be more or less turbulent.

$$S_t = \frac{\tau_p}{\tau_f} \quad (2.23)$$

S_t represents the ratio between the relaxation time of the droplet and a characteristic time of the flow, which generally is the Kolmogorov scale. They are two limiting cases:

- $S_t \ll 1$: The droplet will follow perfectly the fluctuations of the gas flow. The relaxation time of the droplet is small compared to the time scale of the smaller turbulence scale (Kolmogorov)
- $S_t \gg 1$: The droplet will hardly follow the fluctuations of the gas flow. The

relaxation time is large compared to the komolgorov time scale. This is typically the case for large droplets with ballistic trajectories.

2.2.2 Turbulence-gaseous flame interactions

Turbulent combustion results from the two-way interaction of turbulence and chemistry.

- Flame impact on the turbulence. When a flame interacts with a turbulent flow, either the mechanisms can (i) generate turbulence, called "flame-generated turbulence", or (ii) it damps turbulence by relaminarization due to the high temperature.
- Turbulence impact on the flame structure. The turbulence can alter the flame structure by wrinkling and straining processes [62–64], enhancing the chemical reaction, but also from critical value of turbulence inhibiting it and leading to flame quenching.

Damköhler [65] is the first to describe the turbulent combustion and to introduce wrinkling as the one of the main mechanisms controlling the effect of turbulence on flame fronts. To understand the interactions between the combustion and the turbulence, it is necessary to compare different time scales. The Damköhler et Karlovitz number are used to describe the flame-vortex interactions.

$$Da = \frac{\tau_f}{\tau_c} = \frac{l_t/u'}{\delta/s_L^0} \quad (2.24)$$

$$Ka = \frac{\tau_c}{\tau_k} \quad (2.25)$$

The Damköhler number Da is defined for the largest eddies and corresponds to the ratio between the integral time scale τ_t and the chemical time scale τ_c . The smallest eddies are represented by the Karlovitz number Ka and it is the ratio of the chemical time scale τ_c to the Kolmogorov time τ_k .

- For $Da \ll 1$, the chemical time is larger than the turbulent times. The mixing between the fresh gas and the burned gas is made by the turbulence, whereas the overall reaction rate is controlled by the chemistry. For these specific values of Da , all turbulent time scales are smaller than the chemical time scale. This regime is called Well stirred reactor.
- On contrary, for $Da \gg 1$, the chemical time scale is shorter than the integral turbulence time. In this case, the flame structure is not affected by the turbulence, and the burning rate is similar to that obtained in laminar flame. This regime is called flamelet and the turbulence can wrinkle the flame front.

Different authors, such as Borghi [11] or Peters [66] use these characteristics times to explain the premixed turbulent combustion regimes in diagrams (Fig.2.5).

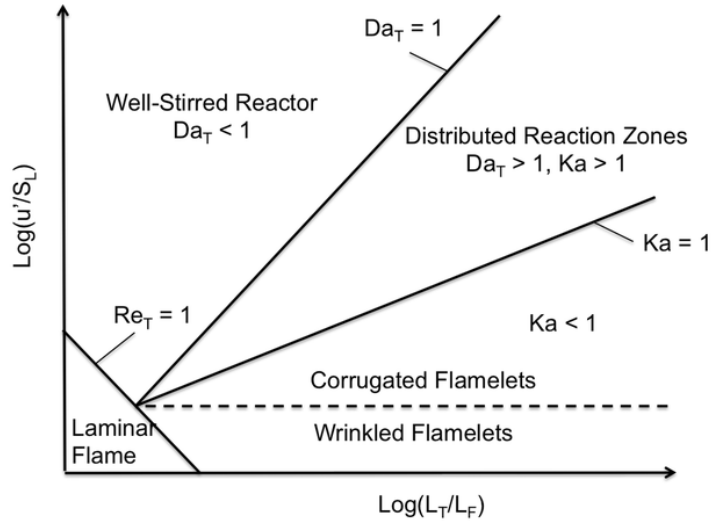


Figure 2.5: Combustion regime diagram demonstrating turbulent flame structure for premixed flames.

Figure 2.5 displays the various combustion regimes identified in terms of length (l_t/δ) and velocity (u'/s_L^0) ratios.

- When the Reynolds number is below the unity, the regime for the premixed combustion is laminar. However, for the other four regions, the regime is turbulent
- When the Karlovitz number (Ka) is below 1, the flame thickness is smaller than the smallest turbulent scale. Moreover, all turbulent time scales are smaller than the chemical time scale. In this condition, the flame front is thin, close to a laminar flame and wrinkled by the turbulence. This flamelet regime can be divided into 2 regions: (i) Wrinkled flamelet regime, which corresponds to conditions where the turbulent motion is too low to wrinkle the flame front. In this configuration the flame is slightly wrinkled and the structure is similar to that obtained in laminar regime. (ii) Corrugated flamelet regime. In this situation, the flamelet regime is still valid but the larger turbulent structures become able to interact with the flame front, which can lead to the formation of pockets of fresh or burnt gases.
- Distributed reaction zones also called thickened flame regime. This regime occurs when $Ka > 1$ and $Da > 1$. During this regime the turbulent integral time scale is still larger than the chemical time scale but the Komolgorov scales are smaller than the flame thickness and are able to disturb the flame front until to reach the flame quenching if the stretch becomes larger than a critical value.
- For Damköhler number below one, the chemical time is larger than the turbulent motion. The mixing is very fast and the reaction rate is limited by the chemistry.

The other important turbulence-flame interactions results in the possibility to extinguish the flame by high turbulence intensity. Indeed, the flame quenching occurs when a flame front is submitted to external perturbation, such as heat losses or sufficiently strong aerodynamic stretch to decrease the reaction rate. Note that the decrease of the reaction rate can be caused either by thermal quenching due to the flame-wall interactions and by the low fuel droplet temperature or by strain quenching. When the local stretch induced by turbulent motions on the flame front becomes higher than a critical value, the flame is quenched. At a given location, the combustion is altered and the fresh reactants diffuse into the products without combustion.

2.2.3 Spray-Flame interactions

As described below, the evaporation process is a complex phenomenon and the fuel vapor generated depends on many parameters. In this point of view, the two phase flow combustion can be classified following the interaction levels (fig.2.6).

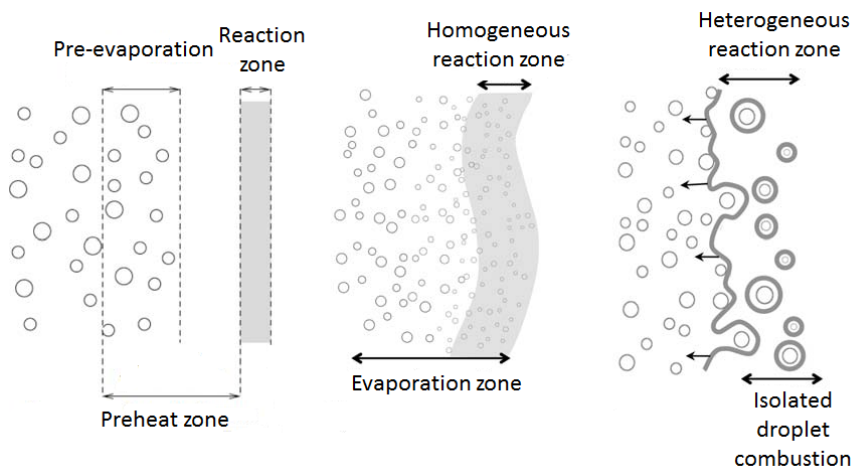


Figure 2.6: Representation of the different interaction levels in two-phase combustion. Right: Pre-vaporized flame. Middle: Homogeneous combustion. Left: Heterogeneous combustion. Adapted from [9]

Figure 2.6 displays that according to the local conditions, the combustion occurs, either after the complete droplet evaporation, or inside the spray. The ratio between the evaporation time and the droplet relaxation time determines the spray-flame interactions.

- Combustion after the complete droplet evaporation. In this configuration the droplet evaporation is completed, which leads us to have a pure gaseous mixture at the flame front location. This typical spray flame is observed only for small and homogeneous droplets with low density.
- Homogeneous two-phase combustion. The flame front is continuously supplied by a

dense and homogeneous spray of droplets. The evaporation is not complete before reaching the reaction zone, some droplets interact with the flame front.

- Heterogeneous two-phase combustion. Here, the presence of droplets strongly affect the flame front, by an important wrinkling. Moreover, some of the largest droplets can cross the reaction zone and burn in different combustion regimes, which will be described in the following section.

The spray-flame interactions can be also described by the different combustion regime encountered in spray combustion. In the following section, the specific combustion regimes are developed to continue and strengthen the explanation of the fundamentals of spray combustion.

2.2.4 Combustion regime

Chiu et al. [10] was the first to propose a classification of the spray flames. It consists in determining the flame structure propagating through a droplet spray inside a pre-heated fuel at rest. A group number denoted G is used to classify the combustion regimes. This number G represents the ratio of the characteristic velocity of evaporation to the temperature diffusion velocity. Candel et al. [67] give the number of group (G) as a function of two parameters (Eq.2.26): the total number of droplets N and the separation parameter S , which is the ratio of the mean inter-droplet distance δ_s to the radius of the flame $\delta_{r,f}$ surrounding the single droplet.

$$G \approx 5 \frac{N^{2/3}}{S} \quad (2.26)$$

If the separation number decreases, there is a point where the flame topology changes to a individual combustion regime to a group regime. By fixing S and varying N , two principal modes for spray flame can be identified in figure 2.7.

The first case corresponds to $G \gg 1$. The temperature diffusion inside the cloud is impossible, because the droplets are too close to one another ($Y_F \gg Y_{F,lim}$). In this configuration, only an external fuel vapor layer is present. The flame is positioned at the border of the droplet cloud. In the second case, $G \ll 1$, which implies that the drops are sufficiently far from each other for the hot gas to penetrate into the cloud. During this process each droplet evaporate individually and the combustion occurs around each droplet. Chiu et al [10] introduced new combustion regimes. The first mode is qualified to external mode and the second on to internal mode. In order to take into account the effect of surrounding flow, the initial classification of Chiu et al was completed by Borghi et al. [11,68]. They introduced three other parameters, which are δ_f the flame thickness, τ_f the characteristic time for combustion and τ_v the mean evaporation times of droplets.

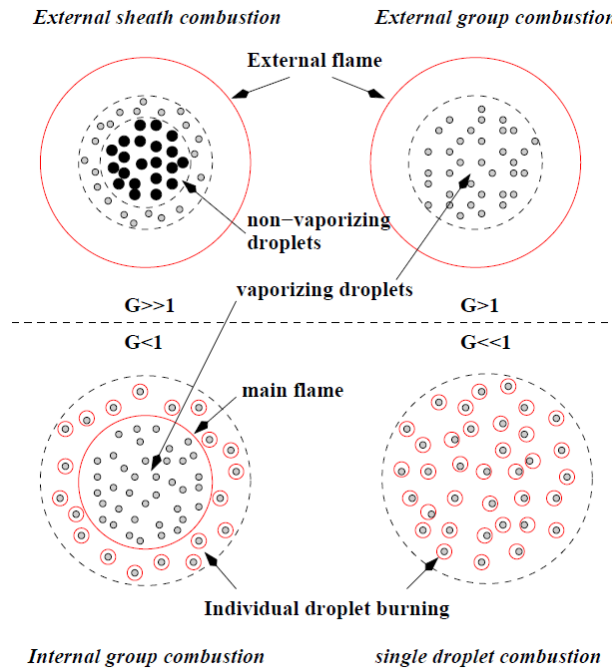


Figure 2.7: Two-phase combustion regimes according to the group number G . Extracted from [10]

If $\tau_f \gg \tau_v$, the droplets evaporate very rapidly and combustion occurs according to a premixed regime, whatever the distance between the drops and δ_f .

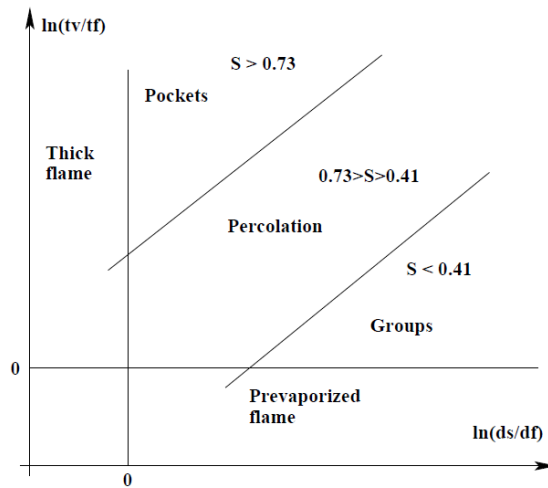


Figure 2.8: Borghi's diagram for laminar flames propagating in homogeneous and poly-dispersed droplets. Extracted from [11]

Figure 2.8 displays the combustion regime proposed by Borghi et al. The arrangement of the droplets, which can be random, requires dividing the mist of drops into 3 categories:

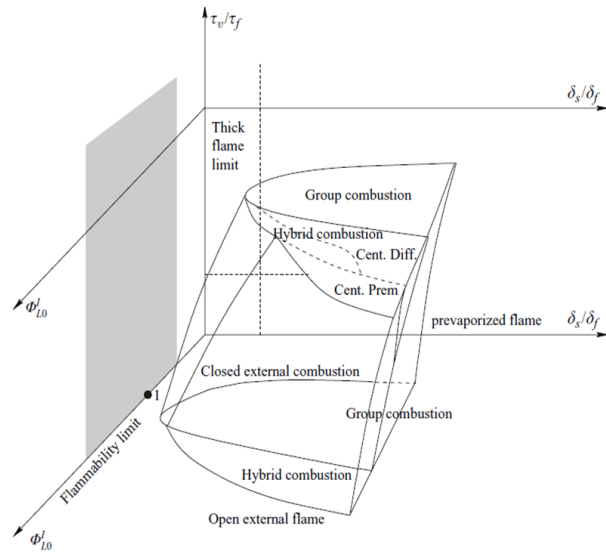
- $S < 0.41$: The spacing between the drops is sufficient for some droplets to burn individually.

- $0.41 < S < 0.73$: The presence of gas pockets as well as agglomeration of droplets are observable. The spray is constituted by dense and diluted zones.
- $S > 0.73$: The combustion is difficult due to the droplet concentration.

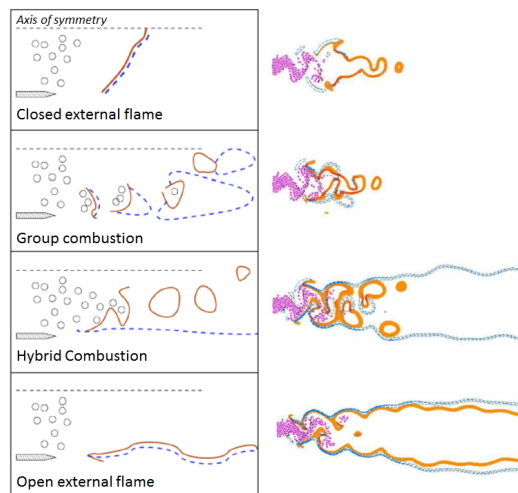
Reveillon et al [12,69] recently made an improvement on the two previous approaches. Indeed, it is important to recall that the last approaches proposed by Chiu and Borghi are based on two strong assumptions: (i) The flow is initially at rest and (ii) the notion of equivalence ratio is not take into account. From the numerical results and the comparisons with the experimental work of Cessou [?], three categories for combustion regime are given by Reveillon et al (fig.2.9.)the external combustion regime are observed when the equivalence ratio is maximum. The group combustion regime reveals that droplets form a rich zone, where the combustion occurs first in premixed and then in diffusion. When the equivalence ratio increases the hybrid combustion regime can be found. In this configuration, the groups of droplets burn in premixed but the high equivalence ratio limits the percolation of the diffusion flame inside the droplet spray.

2.3 Conclusion

This chapter gives an overview of the complexity of the spray combustion. To understand the spray jet flame it is necessary to perfectly describe each step of the mechanisms, starting with the fuel droplet atomization up to the combustion regime occurring in the combustion chamber. This illustration shows the interacting multi-scale processes governing spray evaporation and combustion. Some of the interactions are not described in this chapter, such as the droplet-wall interactions because in this work the experimental facility is composed of an open burner, without confinement. Lean combustion implies lower flame temperature and velocities leading to more unstable flames. Experimental and numerical investigations are necessary in order to further describe the mechanisms involve in two-phase combustion. In the perspective of moving forward into more complex configurations, where real combustors exhibit two-phase complex flows with strongly varying local properties, it is necessary, firstly, to study a canonical configuration.



(a)



(b)

Figure 2.9: (a) Three-dimensional diagram for diluted spray combustion. Extracted from [12]. (b) Summary of the generic flame structures. Red continuous line: premixed burning blue dashed line: diffusion burning. Adapted from [12].

Chapter 3

Experimental facilities and optical diagnostics

Contents

3.1	CORIA Rouen Spray Burner (CRSB)	36
3.1.1	Plenum and air co-flow	36
3.1.2	Liquid fuel injection	36
3.1.3	Stability diagram	38
3.1.4	Operating conditions	39
3.2	Characterization of the dispersed phase by Phase Doppler Anemometry (PDA)	40
3.3	Microscopic shadowgraphy	42
3.4	Planar Laser-Induced Fluorescence on OH radical (OH-PLIF)	44
3.4.1	Principle	44
3.4.2	Strategy for OH excitation and detection	46
3.4.3	Experimental set-up	47
3.4.4	Post-processing	47
3.5	High-Speed optical diagnostic	48
3.5.1	Experimental set-up	48
3.5.2	HS-OH-PLIF	49
3.5.3	HS-PIV	51
3.6	Conclusion	55

This section is dedicated to the description of the burner, the operating conditions and the optical diagnostics applied during the experiments. Moreover, the methods to extract results from images are also presented.

3.1 CORIA Rouen Spray Burner (CRSB)

The CRSB burner presented in this section is dedicated to the study of spray combustion, from the carrier and dispersed phase characterization to the flame structure and stabilization mechanisms. It is based on the geometry of the gaseous KIAI burner [70]. In figure. 3.1, R and Z represent the radial and axial coordinates, respectively. As shown in figure 3.1, the burner is composed of 2 distinct parts (the plenum with the air co-flow and the fuel injection system) which will now be detailed.

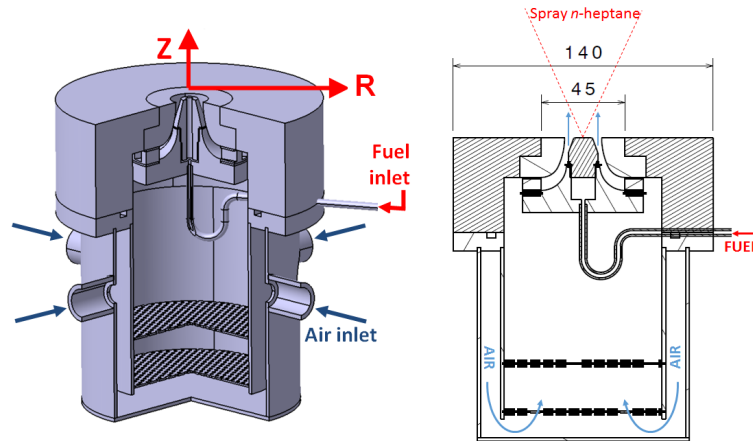


Figure 3.1: Detail of the injection system.

3.1.1 Plenum and air co-flow

Air is injected in the plenum by 4 perpendicular air inlets located in the external side of a double wall plenum. The plenum was modified compared to the gaseous version in order to remove the azimuthal velocity at the burner exit. Indeed, it was shown by [70] that with one tangential air admittance, the azimuthal velocity is around 2 m.s^{-1} at the burner exit. Then, air flow rises towards the center of plenum, where it passes through 2 multi-perforated plates and then feeds the injection system. The goal of these two plates is to remove the large turbulence scales and to suppress the residual azimuthal velocity component.

3.1.2 Liquid fuel injection

The injection system is designed to inject liquid fuel and air stream within the combustion chamber (3.3). It is composed of a simplex fuel injector and an external annular, non-swirling air co-flow. The latter is equipped with 18 radial vanes with 0 degree angle. The air-flow is then guided by a convergent and arrives around the fuel injector. With an open burner configuration, the air co-flow presents the same behavior as an annular free jet.

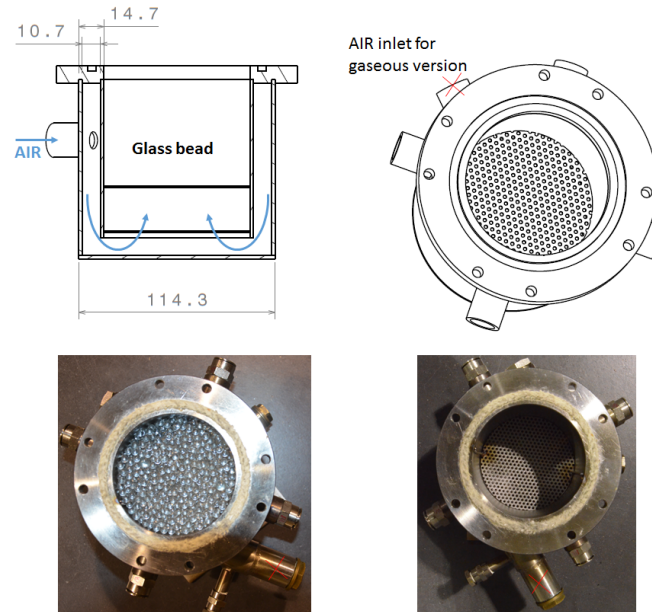


Figure 3.2: Details of the plenum.

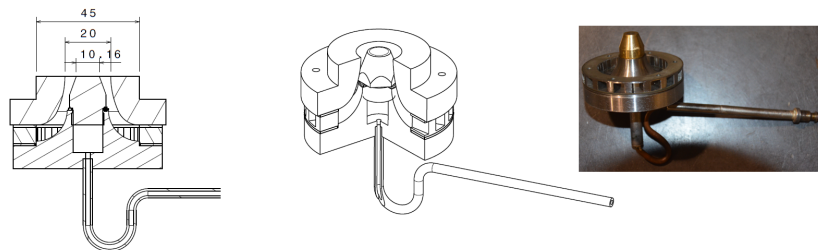


Figure 3.3: Details of the injection system.

Fuel injection is performed by a commercial pressurized swirl injector and is illustrated in Fig.3.4. *N*-heptane enters through the injector filter and continues through the bottom screw and its side holes. From there, the fuel runs along the side of the cone and into the cone slots. When the fuel, under high pressure, is forced through the cone slots it enters the swirl chamber. On its way through the cone slots some of the fuel pressure is converted into rotational energy. In the swirl chamber, the fuel gains strong rotary motion and a rotating *n*-heptane film is formed which moves towards the nozzle orifice. The velocity of the liquid film is so high that a tube of liquid is formed in the nozzle orifice. With the help of that part of the pressure not converted into rotational energy the liquid tube is forced through the nozzle orifice. On being propelled from the orifice, the liquid tube is expanded so much that it breaks up into very small fuel droplets with a hollow cone shape.

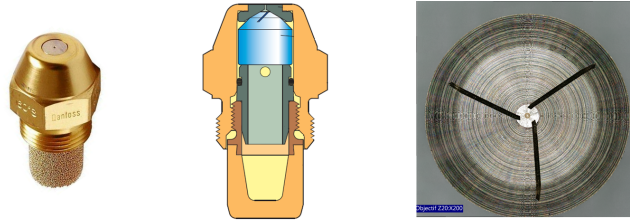


Figure 3.4: Schematic representation of the Danfoss injector and photo of swirl chamber inside the injector obtained by an electronic microscope.

3.1.3 Stability diagram

The stability diagram is studied to understand the effect of the mass flow rates on the stability of the burner and to choose the operating condition for the study. The flame blow-off limit is obtained by the following procedure: for a given air mass flow, the fuel mass flow is reduced (from the stabilized flame) until the flame extinction is observed. Moreover, the global appearance is given for the different zones to describe the stability and the instabilities of the spray flame. Figure 3.5 shows the effect of mass flow rate of the air co-flow on the flame extinction limits. We can see that the latter is proportional with the air mass flow. The mass flow rate of the air co-flow has an impact on the lift-off height and on the flame length. The higher the air velocity, the greater the lift height. The operating point, corresponding to the red star, is chosen to obtain a stable and symmetric flame with a lean combustion regime. The mass flow rate chosen for this work (air: $6 \text{ g}\cdot\text{s}^{-1}$ and $0.28 \text{ g}\cdot\text{s}^{-1}$ for the *n*-heptane) lead to a global equivalence ratio equal to 0.7. Furthermore, figure 3.5 illustrates the non-sooting and sooting reaction zones present in this spray jet flame configuration.

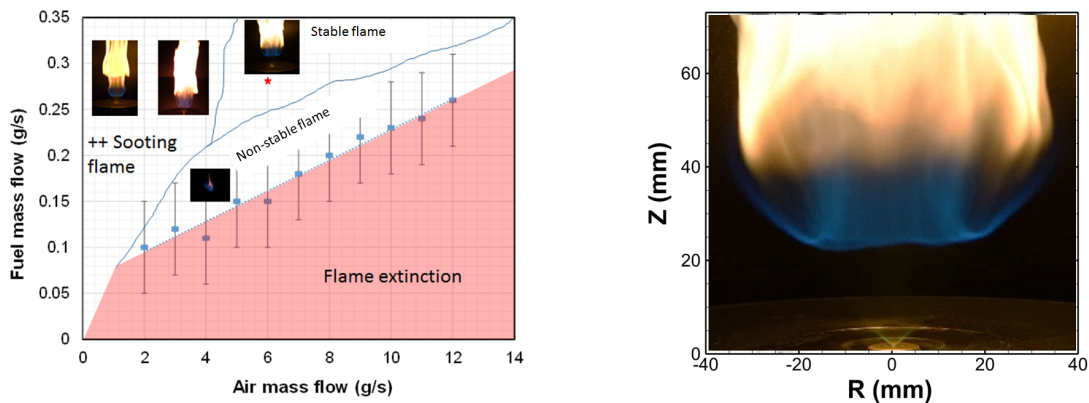


Figure 3.5: Extinction limits and operating range of the burner. The red star represents the operating point.

3.1.4 Operating conditions

Experiments are carried out in an atmospheric and open burner based on the geometry of the gaseous KIAI burner [70] (Fig. 3.1). The flow controllers are checked before each measurement campaign by a certified calibration bench. Air and liquid fuel (*n*-heptane) mass flow rates are controlled by thermal and Coriolis mass flow controllers. The operating conditions are summarized in 3.1. Inlet conditions of air and fuel are 6 g.s^{-1} ($T = 298 \pm 2 \text{ K}$) and 0.28 g.s^{-1} ($T = 298 \pm 2 \text{ K}$) respectively.

	Air co-flow	Fuel (<i>n</i> -heptane)
Mass flow (g.s^{-1})	6	0.28
Temperature (K)	298 ± 2	298 ± 2

Table 3.1: Experimental operating conditions.

A special effort is made to collect and compile the best possible experimental results useful for model validation. In this regard, several optical diagnostics were applied to define the CRSB burner. The local properties of the flow are measured by phase Doppler anemometry (PDA) obtaining size-classified velocity data for fuel droplets and velocity data for the air. The settings are adjusted in order to measure the dispersed and carrier phase in reacting conditions. The global flame structure is investigated by OH-PLIF imaging at small repetition rate (10 Hz). High Speed OH-PLIF (HS-OH-PLIF) and High-Speed PIV (HS-PIV) techniques are applied simultaneously. The temporal and spatial flame front positions and associated with instantaneous velocity are obtained in order to study the transient phenomena, such as extinctions. Fig. 3.6 shows the mesh for the optical diagnostics. To optimize the spatial resolution, the field of view concerning the HS-OH-PLIF is smaller than the typical OH-PLIF.

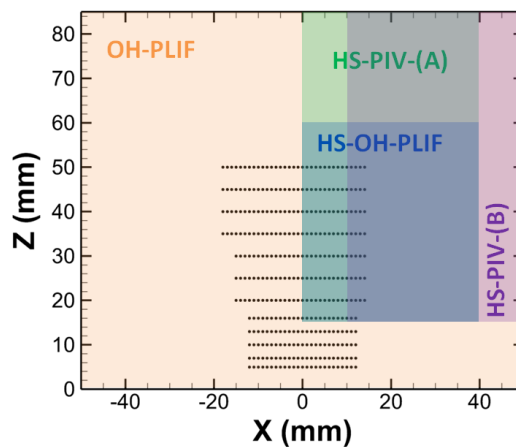


Figure 3.6: Mesh for Phase Doppler Anemometry in reacting condition with different optical diagnostics applied in the spray jet flame.

Figure 3.7 presents a list of available data. Each optical diagnostics were applied in the CRSB burner.

Type of data (raw and post-processed)	Technique	Conditions	Mesh
<i>Fuel droplet/ligaments and conical sheet images</i> <ul style="list-style-type: none"> - Height of atomization - Droplet sphericity 	Microscopic shadowgraphy	NR	7*5 mm and 2.4*1.8 mm
<i>Air velocity</i> <ul style="list-style-type: none"> - X and Z components - 40 000 samples or 30 s acquisition time 	PDA	R/NR	Z mini = 5 mm Z maxi = 50 mm
<i>Fuel droplet velocity</i> <ul style="list-style-type: none"> - X and Z component - 40 000 samples or 30 s acquisition time - Conditional average with the droplet diameter. 	PDA	R/NR	Z mini = 5 mm Z maxi = 50 mm
Fuel droplet distribution size (histograms) and associated statistics (D_{10} , D_{32})	PDA	R/NR	Z mini = 5 mm Z maxi = 50 mm
<i>Flame shape</i> <ul style="list-style-type: none"> - OH instantaneous field - Lift height (averaged and Rms) - Radial location of lift (averaged and Rms) 	OH-PLIF	R	Figure 2
<i>Fuel droplet temperature</i> <ul style="list-style-type: none"> - Temporal average over 400 recordings - Spatial average for all the droplets contained within the measurement volume 	C-GRT	NR/R	Z mini = 20 mm Z maxi = 70 mm
<i>Fuel droplet temperature</i> <ul style="list-style-type: none"> - Instantaneous measurement (few ns) - Spatial average for all the droplets contained within the measurement volume (0.92 mm³) - Data coupled with OH-PLIF measurements in order to provide temperature data conditioned to the flame front location 	I-GRT	R	Radial profile at Z=35 mm
<i>Dynamics of flame shape</i> <ul style="list-style-type: none"> - Temporal evolution of 2D OH fields (10 kHz) - Qualitative fuel droplet-reaction zone interactions - Extinction phenomena - Re-ignition phenomena 	HS-OH-PLIF	R	Figure 3.6
<i>Ignition probability map</i> <ul style="list-style-type: none"> - Laser ignition - Constant energy - Statistics over 30 trials - Visualization of the kernel flame development until flame stabilization 	Laser induced spark ignition	NR	Z mini = 5 mm Z maxi = 45 mm

Figure 3.7: List of available data and optical diagnostics associated.

3.2 Characterization of the dispersed phase by Phase Doppler Anemometry (PDA)

Droplet size and velocity were measured by a commercial PDA system (DANTEC) operating in DUAL mode. An argon laser provides green (514.5 nm) and blue (488 nm) beams

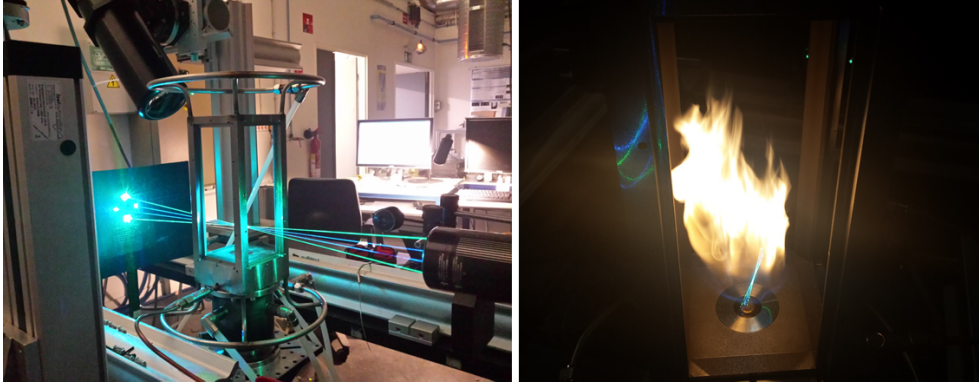


Figure 3.8: Photographs of the PDA system with the laser beam in non-reacting and reacting condition .

(3.8). Beam spacing is 50 mm ; transmitting and receiving lenses focal lengths are 350 mm and 310 mm , respectively. The off-axis angle of the receiving optics is 50 degrees (in front scattering position), not far from the Brewster angle which, in parallel polarization, enhances the refracted light detection over the reflected light. The used aperture mask allows a detection diameter range of $139\text{ }\mu\text{m}$. The measurement volume can be approximated by a cylinder of $120\text{ }\mu\text{m}$ in diameter and $200\text{ }\mu\text{m}$ in length. At each measurement location, data sampling was limited to 40,000 *droplets* or to 30 *s* of measuring time, allowing converged statistics of size-classified data. Several parameters such as sphericity or droplet concentration control the quality of the measurement. The PDA system gives time like distributions in speed and size. In the case of a sparse spray, drops with a well-defined smooth surface (also known as sphericity) and diameters above $3\text{ }\mu\text{m}$, PDA gives very good results. On the other hand, in the case of a dense spray, several particles may be present in the measurement volume, the recorded signal is then not validated. In addition, when the length of the environment to be crossed or the number of drops is important, the risks of multi-scattering increase. For a standard configuration, assuming a mean refractive index for post-processing introduces a slight error in determining the diameter. In reacting conditions this assumption can be critical because the droplets temperature increases which has the effect of reducing the refractive index. As described before, high-density regions lead to a decrease in validation due to signal rejection when more than one droplet at a time was present in the measurement volume. In this study, a decrease on the validation was observed below $Z = 10\text{ mm}$ and it becomes unsatisfactory below $Z = 7\text{ mm}$ in the dense region of the spray. To be consistent with the validation criteria, only the results for axial station upper than $Z = 10\text{ mm}$ are presented in the following. The gain and voltage in the photomultipliers (PMs) were adjusted so as not to saturate the anode currents in order to correctly detect the dispersed phase or the carrier phase. The carrier phase velocity measurements were performed, in presence of the dispersed phase, by seeding the air with $2\text{ }\mu\text{m}$ olive oil droplets and increasing the gain and voltage in the

PDA(A)). In this configuration the collection system was adapted to measure particles with a diameter smaller than $2 \mu m$. PDA(A) configuration allows us to detect the air seeding and small fuel droplets $D_{10} \leq 2 \mu m$, which follow perfectly the air velocity due to their low Stokes number. Both phases were measured in reactive conditions. The size and velocity of the dispersed phase were also measured without seeding, in order to characterize the droplet properties such as size distribution and classified-size velocities. The PDA configuration and the gain and voltage of the PDA were adjusted to detect all the sizes present in the spray ($2 \leq D_{10} \leq 80 \mu m$) (configuration: PDA(B)). Mean velocity and diameter values, presented in the next figures, were calculated with a minimum of 500 droplets. Cylindrical coordinates were considered: U_z represents the axial velocity following the Z-direction and U_r stands for radial velocity.

3.3 Microscopic shadowgraphy

The shadowgraphy arrangement depends on the change in the light intensity arising from beam displacement from its original path. When passing through the test field under investigation, the individual light rays are refracted and bent out of their original path. The rays traversing the region that has no gradient are not deflected, whereas the rays traversing the region that has non zero gradients are bent up. Figure 3.9 illustrates the shadowgraphy effect using simple geometric ray tracing. Here a plane wave traverses a medium that has a nonuniform index of refraction distribution and is allowed to illuminate a screen. The resulting image on the screen consists of regions where the rays converge and diverge; these appear as light and dark regions respectively. It is this effect that gives the technique its name because gradients leave a shadow, or dark region, on the viewing screen. A particular deflected light ray that arrives at a point different from the original point of the recording plane should be traced. It leads to a distribution of light intensity in that plane altered with respect to the undistributed case.

Shadowgraphy is applied to validate the droplet sphericity and concentration and to show the liquid break up mechanisms. The field of view is adapted to different zones in spray, close to the nozzle and far away in order to validate the droplet sphericity. In a pressure-swirl spray nozzle, the stationary core induces a rotary fluid motion which causes the swirling of the fluid in the swirl chamber, that give it high angular velocity, thereby creating an air-cored vortex. Under both axial and radial forces the fuel emerges through the orifice in the form of a hollow cone. Figure 3.10 show liquid emerging from the atomizer and sinuous waves (starting near the orifice) are observed. The underlying breakup mechanism are the shear forces between the air and the liquid fuel ejected from the nozzle.

The disintegration occurs in three steps (Fig. 3.10): (i) the liquid is stripped from the atomizing edge by the shear stress imposed by the air flow. The liquid is then separated

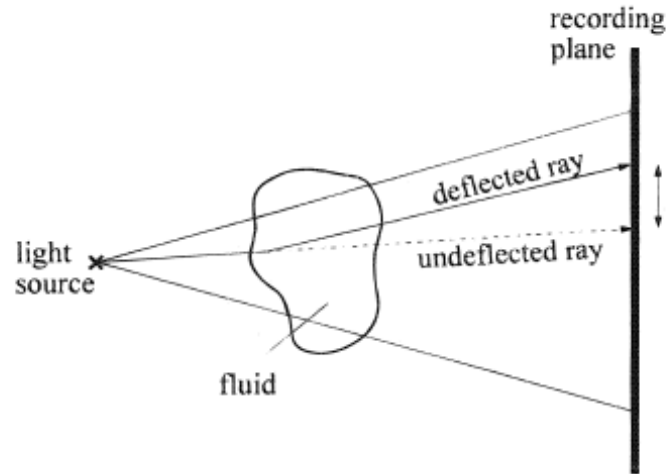


Figure 3.9: Principle of the Shadowgraphy

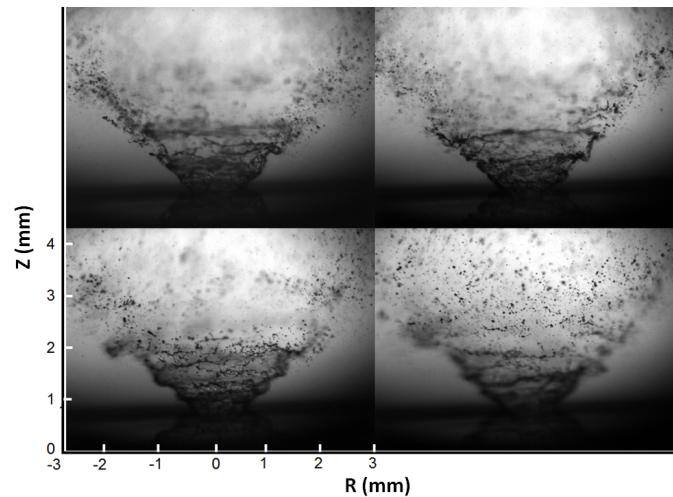


Figure 3.10: Images showing the liquid sheet breakup.

from the pre-filming surface and ligaments are formed. (ii) Depending on their shape and size the ligaments will undergo further disintegration. (iii) The ligaments start to contract themselves into droplets. As the droplets resulting from primary break up are large enough, and the relative velocity between the droplet and the air is high enough, secondary break up occurs. this mechanism of a droplet takes place if the forces acting from the outside on the droplet are larger than the interior force due to the surface tension. The outer forces may be pressure forces, shear forces induced by gas flow around the droplet, the inertia of the droplet, etc.

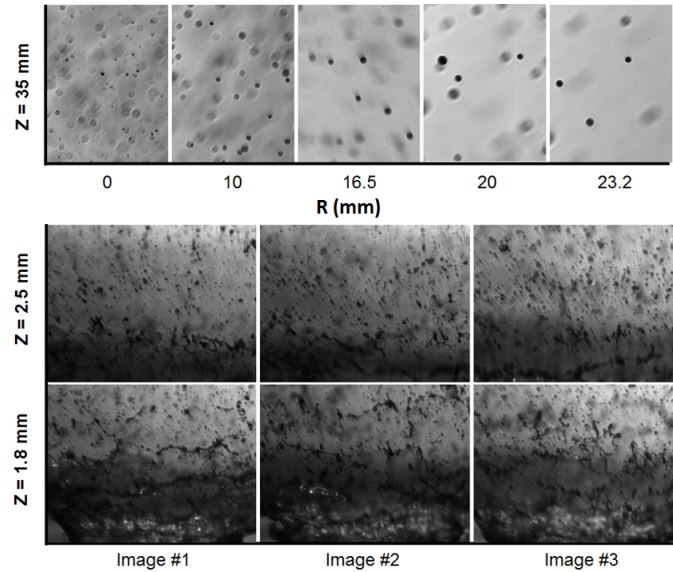


Figure 3.11: Images showing the shape of droplets at $Z=35$ mm for different radial stations and different images at $Z=1.8$ and 2.6 mm.

3.4 Planar Laser-Induced Fluorescence on OH radical (OH-PLIF)

This section presents an overview of the application of fluorescence technique in CRSB but more information can be found in [71–73] for the theory approach of this technique. In this work, OH-PLIF was performed to obtain qualitative information on the OH signal. Indeed, the OH radical is the most commonly used flame front indicator. This radical is one of the most important intermediate species present during the combustion between fuel and air. OH is formed by fast two-body reactions and then consumed by slower three-body recombination reactions [74].

3.4.1 Principle

Fluorescence denotes the radiation emitted by an atom or a molecule when relaxed by spontaneous emission of a photon from a higher to a lower energy level. The fluorescence is based on the quantum mechanics and it assumes that energy levels associated to a molecule are quantized, each quantum state has one quantum number, angular momentum and energy and are described by the following equation 3.4:

$$E_{int} = E_{vib} + E_{rot} + E_{elec} \quad (3.1)$$

where E_{int} , E_{vib} , E_{rot} and E_{elec} are respectively the internal energy of the molecule, the vibrational energy, the rotational energy and the electronic energy respectively. As

energy levels are quantized only exciting the molecules with specific wavelength results in fluorescence. The energy absorbed or emitted by photons during the fluorescence is expressed with the law of Planck (Eq.3.2).

$$\Delta E = h\nu \quad (3.2)$$

with h is the constant of Planck and ν is the frequency of the photon.

In a laser-induced fluorescence process, the upper energy level is populated using laser excitation with a wavelength tuned to a resonance between the excited state and a discrete lower state. After excitation, the laser populated upper state may undergo a number of subsequent processes, which can be defined by a two level model. The latter, shown in figure 3.12, explains the different transfer modes between the lower energy state E_1 and the upper energy state E_2 .

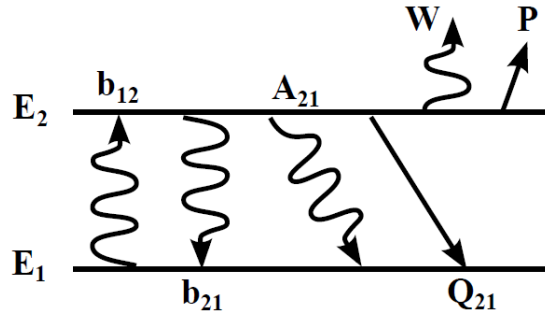


Figure 3.12: Schematic illustration of a two-level energy diagram [13].

The absorption rate induced by the laser source is represented by b_{12} and b_{21} marks the stimulated emission rate which goes directly to the lower state. The rate of spontaneous emission (A_{21}) represents the fluorescence signal captured by the camera and Q_{21} Corresponds to the collisional quenching. This term represents the de-excitation that the molecule undergoes based on inelastic collisions with other molecules. W is the photoionization, and P is the predissociation. The last two processes are generally negligible. Assuming the fluorescence is emitted equally over 360 degrees, the total number of photons N_p detected by the camera detector from the collection volume V is given by Eq 3.3:

$$N_p = \eta \frac{\Omega}{4\pi} f_1(T) \chi_m n V B_{12} E_v \frac{A_{21}}{A_{21} + Q_{21}} \quad (3.3)$$

η is the transmission efficiency of the collection system, Ω is the solid angle of collection, $f_1(T)$ is the fractional population of the lower coupled state, χ_m is the mole fraction of

the absorbing state, n is the total gas number density and E_v is the spectral fluence of the laser. The term $\frac{A_{21}}{A_{21}+Q_{21}}$ is called the Stern-Volmer factor or fluorescence yield. It is generally much smaller than 1 as $A_{21} \ll Q_{21}$.

3.4.2 Strategy for OH excitation and detection

The strategy for the excitation must be defined before performing experiments. The laser is tuned to a specific wavelength and the output laser beam goes through a controlled volume with enough molecules of interest in order to obtain a homogeneous concentration. The fluorescence S_F is collected on the intensified camera. The laser excitation spectrum of the OH radical is determined by performing this procedure for several laser wavelengths. The experimental excitation spectrum is compared with the simulated spectrum using the software LIFBASE representing the OH theoretical excitation spectrum (fig 3.13).

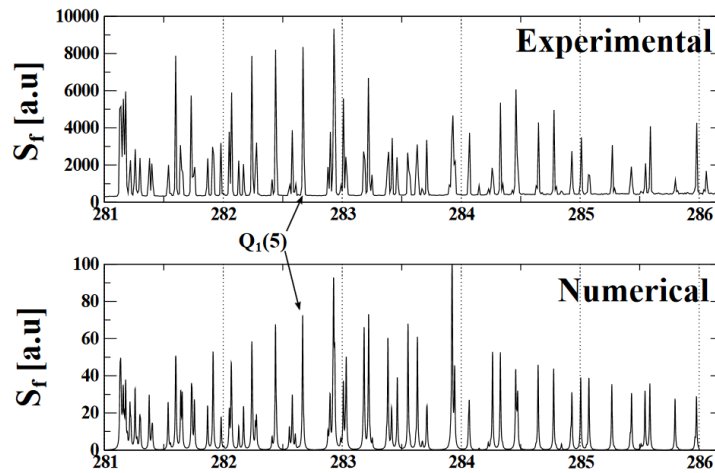


Figure 3.13: Experimental and theoretical laser excitation spectrum of OH molecule in a laminar burner. CH_4 , $P = 1bar$, $T = 2000K$. The fluorescence signal was obtained by averaging 150 images and by taking the mean value of a defined region of interest. The wavelength interval between two measurements was 0.01nm

The methodology to optimize the fluorescence signal is the following: First, it is important to set the correct wavelength in order to get a good intensity of the fluorescence signal compared to the experimental conditions. According with Bresson [75], the $Q_1(5)$ transition of the $A^2\Sigma^+(v' = 1) \leftarrow X^2\Pi(v'' = 0)$ band of OH at $\lambda = 282.665 \text{ nm}$ seems to be advantageous. The benefits of this transition have already been demonstrated by several studies [76]. To record images with a large signal-to-noise ration, a broadband collection strategy is adopted for the fluorescence signal. The spectral filter is chosen to not overlap the excitation wavelength with the collected band. Background noise arising from elastic scattering by the droplets is reduced with two high-pass optical filters (Schott WG295). The OH-PLIF signals are collected using a broadband collection strategy from 308 to 330 nm with a band-pass filter (Schott UG11).

3.4.3 Experimental set-up

The global flame structure was investigated by OH-PLIF imaging at low repetition rate (10 Hz). A Nd:YAG.laser operating at 532 nm was used to pump a tunable dye laser (Quantel TDL90). The excitation wavelength was tuned to the $Q_1(5)$ transition of the $A^2\Sigma^+(v' = 1) \leftarrow X^2\Pi(v'' = 0)$ band of OH at $\lambda = 282.665 \text{ nm}$. The thickness of the laser sheet is about $300 \mu\text{m}$ and the resultant output pulse energy is 30 mJ per shot in the probe volume. The collection system consisted of an ICCD camera (PIMAX 4, Roper Scientific, 1024×1024 pixels²) equipped with UV lens (f/2.8). The field of view was $112 \times 112 \text{ mm}^2$ leading to a magnification ratio of $4.52 \text{ pix} \cdot \text{mm}^{-1}$. A broadband collection strategy from 308 to 330 nm with a band-pass filter (SCHOTT UG11) was adopted and a high-pass filter (SCHOTT WG295) was used to reduce Mie scattering from the fuel droplets.



Figure 3.14: Photograph of OH-PLIF experimental facility

3.4.4 Post-processing

A pre-processing is applied to normalize raw images and can be divided into two steps. First, it is the background correction which allow us to subtract the reflexions and electronic noise from the camera intensifier by averaging 500 images, recorded when the experiment is switched off but with the laser beam. Due to the non-homogeneous energy distribution in the laser beam, the signal fluorescence is artificially modulated. It is possible to have access to the mean laser sheet profile, to correct these spatial energy variations, by filling a region of acetone vapor and by averaging 1000 images. Finally, the pre-processing steps can be summarized with the following equation:

$$I_{corrected} = \frac{I_{raw} - \overline{I_{noise}}}{I_{laser} - \overline{I_{noise}}} \quad (3.4)$$

Where $I_{corrected}$ is the corrected images, I_{raw} is the raw images, $\overline{I_{laser}}$ is the mean laser profile and $\overline{I_{noise}}$ is the mean background image

3.5 High-Speed optical diagnostic

This section describes the high speed measurements used to characterized the flame dynamics. Temporal and spatial flame front positions and associated instantaneous flow field are obtained by high-speed OH-PLIF at 10 kHz repetition rate combined with high-speed PIV at 5 kHz . With the improvement of the laser and camera [77] high speed diagnostics can temporarily resolve the scalars in turbulent flows. These efforts have yielded a greater understanding of dynamic turbulent flame behavior through tracking the temporal evolution of transient phenomena such as local extinction, auto-ignition and turbulence-chemistry interactions [78, 79] Besides, the previous work on the extinction phenomena, in a turbulent spray jet flame the situation is more complex and an understanding of extinction mechanisms needs to be gained

3.5.1 Experimental set-up

This section describes the dual measurement technique for the apparatus and setup presented in 3.15. Temporal and spatial flame front positions and associated instantaneous flow fields were obtained by High-Speed OH-PLIF at 10 kHz combined with High-Speed PIV at 5 kHz . A schematic of the high-speed imaging set-up is shown in Fig. 3.15. Concerning the HS-OH-PLIF, a Nd:YAG.laser operating at 532 nm (104 W) was used to pump a tunable dye laser (Sirah Credo). The excitation wavelength was tuned to the $Q_1(5)$ transition of the $A^2\Sigma^+(v' = 1) \leftarrow X^2\Pi(v'' = 0)$ band of OH at $\lambda = 282.671 \text{ nm}$. The resultant output pulse energy was 380 μJ per shot in the probe volume. The beam was then expanded to 40 mm in height using a set of fused silica lenses ($f_1 = 1000 \text{ mm}$, $f_2 = -20 \text{ mm}$, $f_3 = 500$) mm . Due to the low energy delivered, the detection system consisted of a CMOS-camera Photron Fastcam SA5 mounted with an external image intensifier (High Speed IRO, LaVision). The camera was operated at a repetition rate of 10 kHz with an array of $896 \times 848 \text{ pix}^2$ and a magnification ratio of 20.41 pix.mm^{-1} . The intensifier delay (26 ns) and gate (500 ns) were set to optimize the signal to noise ratio. Two high-pass optical filters (SCHOTT WG295) were used to reduce background noise due to elastic scattering by the droplets. The camera on-board memory can hold over 7500 frames, corresponding to an acquisition time of 750 ms . The OH-PLIF signal was collected within the 308 to 330 nm range using a band-pass filter (SCHOTT UG11). Moreover, the laser sheet profile was taken into account and corrected by filling a quartz vessel placed on the test facility with a homogeneous air-acetone mixture.

Image processing tools including non-linear filtering [80] and active contour detection implemented in a level-set method [81] were developed to extract flame front contours and are presented in the following section.

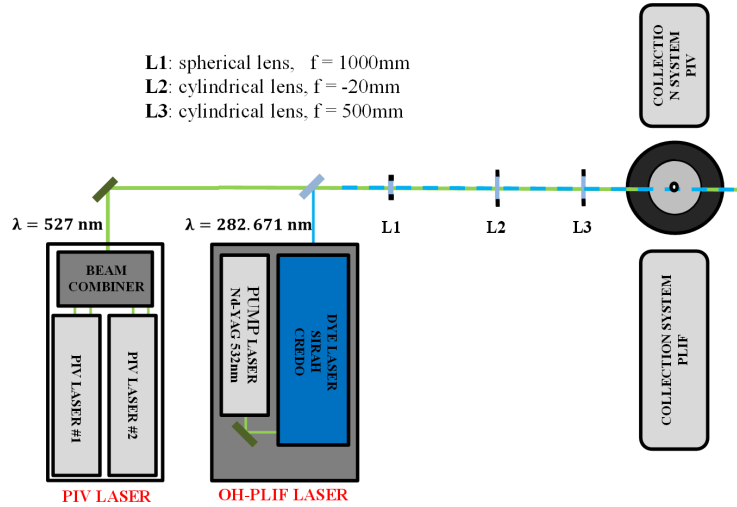


Figure 3.15: Optical arrangement for simultaneous HS-PIV and HS-OH-PLIF measurements.

Table 3.2 summarizes the experimental configuration for the simultaneous high speed diagnostics.

Diagnostic (-)	Acquisition Rate (kHz)	Resolution (pix^2)	Magnification ratio (mm/pix)	ROI LxH (mm)
HS-OH-PLIF	10	896x848	0.0527	40x45
HS-PIV	5	1280x800	0.049	40x65

Table 3.2: Experimental parameters for high speed measurements.

3.5.2 HS-OH-PLIF

Turbulent combustion is non-periodic and is characterized by a time-dependent coupling between turbulent fluid mechanics and finite-rate flame chemistry. Because turbulent combustion processes are highly transient, information is needed that is resolved in both space and time. For measurements at high frame rates ($\gg 1\text{kHz}$), though, the difficulty typically is the low pulse energy from high repetition rate lasers. Because of the low pulse energies available from commercial high-repetition rate laser systems and the difficulties of pumping conventional dye laser systems at high repetition rates, only OH PLIF (due to its high concentrations in flames) has been successfully demonstrated for monitoring a reactive scalar. However, even if the high OH concentration is present, the signal-to-noise ratio is low and a performing image-processing tool is necessary to extract various infor-

mation from the images, such as the OH gradient to define the flame contour for instance.

- Data processing

The huge amount of data resulting from high-speed imaging, needs to be developed an automatic image-processing tool. The pre-processing developed before is applied to normalize raw images. However, due to the difficulty to applied OH-PLIF at high repetition rate, an image-processing tool was developed by Erwan Salaün in the CORIA combustion team. The image-processing tool is applied to automate the flame front detection with a Non Linear Diffusion (NLD) filter to reduce the level of noise and to preserve gradients in the images. The method is based on the original approach formulated by Perona and Malik [82] and has several advantages: Noise is smoothed locally, whereas little or no smoothing occurs between image objects which enhance the local edges [80, 83].

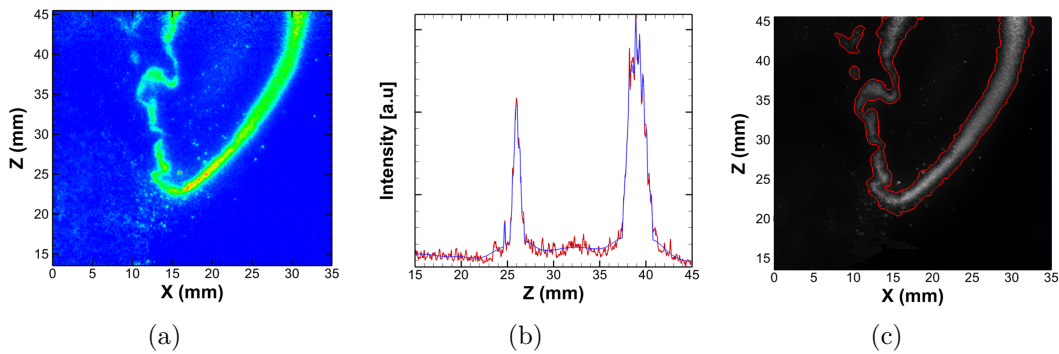


Figure 3.16: (a) Image filtered by NLD. (b) Comparison between raw (red line) and NLD profiles (blue line). (c) Final contour obtained by level set method.

Perona and Malik [82] proposed to smooth the image with a scalar-value diffusion function and to resolve the solution of the diffusion equation Eq. 3.5 where ∇u is the gray image and g is a scalar-value function.

$$\partial_t u = \text{div}(g(|\nabla u|^2)\nabla u) \quad (3.5)$$

The diffusivity function g is a monotonically decreasing function which is responsible for the edge preservation. Perona and Malik [82] proposed the following diffusivity function:

$$g(|\nabla u|^2) = \frac{1}{1 + \frac{|\nabla u|^2}{\lambda^2}} \quad (3.6)$$

In the present experimental study a NLD filter with this diffusivity function (Eq. 3.6) is applied and demonstrates a good ability to preserve the flame front edges without artificial shifting in position. Figure 3.16 show the different NLD filter results with a contour

detection marked by the red line in the last picture.

- Contour Detection

Once the raw data were filtered, flame contours were extracted by an active contour model implemented in a level set method. The latter for capturing moving fronts was introduced by Osher and Sethian [81]. To track the flame front, it was necessary to use a Eulerian method (Level set) to capture the topological changes in time of the flame front structure. The method used in this work is a geodesic region-based level set segmentation method. In a geodesic active contour (GAC), introduced by Caselles et al. [84], the basic idea is to start with a curve around the object to be detected. Then the curves move towards the boundary object. Image gradients were used to construct the stopping function g .

$$\frac{\partial \Phi}{\partial t} = \underbrace{\nu g(x, y) |\nabla \Phi| \operatorname{div} \left(\frac{\nabla \Phi}{|\nabla \Phi|} \right)}_{\text{internal forces}} + \underbrace{kg(x, y) |\nabla \Phi|}_{\text{external forces}} \quad (3.7)$$

where ν, g and k are a weight factor, the stopping function and a constant respectively. The main procedures of the proposed algorithm are summarized as follows:

1. Initialize the level set function with an initial contour

The signed distance function was applied between each of the pixels of the filtered image and the initial contour, which allows us to obtain the level set $\Phi(x)$. In the interior region $\Phi(x) < 0$, and for the outer region $\Phi(x) > 0$.

2. Application of Geodesic active contour model

The first initial contour was then moved by image driven force boundaries of the desired objects. In this study two types of force were considered internal and external forces.

- The internal forces were designed to keep the model smooth during the deformation process.
- The external forces were defined to move with the normal direction the level set function ($\Phi(x)$) toward the object boundary.

3. Check whether the evolution of the level set function has converged.

A convergence criteria was applied in term of pixels displacement between the calculation of $\Phi(x)$ and $\Phi(x) + \Delta t$.

3.5.3 HS-PIV

To obtain instantaneous velocity fields, high speed PIV was applied at 5 kHz. The PIV measurement allows us to determine 2D velocity fields. This diagnostic consists of

recording, with a CCD camera, two successive images separated by time interval Δt , which depends on the experimental configurations (i.e flow velocity, magnification ratio). The signal recorded by the camera corresponds to the Mie scattering of particles illuminated by a thin laser sheet. Note that the PIV measurement does not calculate velocity of individual particles but only for a group of particles. Knowing the displacement of particles and the Δt , a velocity vector is calculated for each interrogation window as the following equation:

$$u = \frac{\Delta x_t^{t+\Delta t}}{\Delta t} \quad (3.8)$$

where $u, \Delta x_t^{t+\Delta t}, \Delta t$ are the velocity vector estimated in one interrogation window, the statistical displacement of particles, and the time between the two images recorded, respectively. The cross-correlation method and the position of the correlation peak [85] was used to determine the statistical displacement of particles in all interrogation windows. Figure 3.17 presents a schematic representation of principle of PIV measurements including the cross-correlation method.

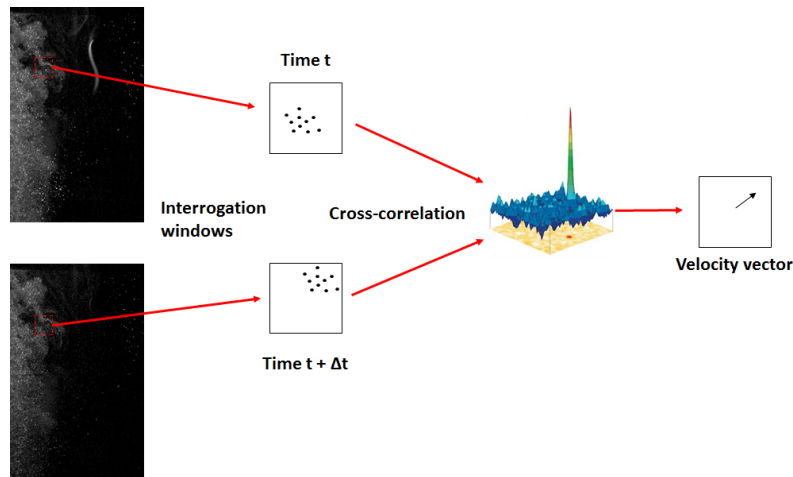


Figure 3.17: Principle of PIV measurement.

Although PIV relies on a simple principle, care should be taken in its practical implementation in order to obtain reliable measurements and reduce the uncertainties. Particular attention should be paid to the different parameters that can bias the PIV technique. The final velocity vector field can be affected by the size of the interrogation window, the out-of-plane particle motion, the signal-to-noise ratio and the flow seeding [?, 86, 87].

- Concerning the particle seeding, the PIV assumes that particles are ideal flow tracers. It means that the particles must accurately follow the flow without being intrusive.
- The pixel discretization implies an uncertainty of 0.5 pixel on the final peak location. To obtain a sub-pixel accuracy, several methods were developed.

- Presence of dispersed phase in the flow. In our configuration, the aerodynamic of the flow is measured in nominal condition (with droplets). Preliminary tests, such as the comparison between PIV with and without the dispersed phase, demonstrate the capability of PIV to measure the carrier phase velocity in the presence of spray. Indeed, in this configuration, the poly-disperse spray distribution yields small droplets along the centerline axis while the majority of the mass is located as large droplets along the spray borders. The very small droplets in the center have a Stoke Number $\ll 1$, which implies that these droplets follow perfectly the co-flow of air. Concerning the large inertial droplets, they are located outside the co-flow of air and have a velocity enough to be tracked by the Δ_{PIV} imposed to capture information in the center of the spray. It is important to keep in mind that the velocity vector fields presented in the following analysis are the results of droplet and particles seeding velocity. Effectively, some uncertainties can be added due to the difference in droplet and particle seeding size.

Air co-flow velocities: HS-PIV-(A) configuration

In order to obtain instantaneous velocity fields corresponding to the CRSB burner, high speed PIV with 5 *kHz* repetition rate was applied. A double cavity (Nd:YLF Laser Darwin Dual quantronix) operating at 527 *nm* gave two laser beams separated by $\Delta_{PIV} = 10 \mu s$. Zirconium oxide (ZrO_2) particles are used to seed the air co-flow (configuration: HS-PIV-(A)). The Mie scattering signal from droplets and ZrO_2 is collected with a Phantom V2512 camera equipped with a Nikon f/1.4 50 mm objective with a 1280x800 pix^2 resolution leading to a magnification ratio equal to 0.0527 $\text{mm}\cdot\text{pix}^{-1}$. Special attention must be paid on the diameter of ZrO_2 particles, which must be sufficiently small to follow the air flow fluctuations. A same post-treatment (Dynamics Studio software) is applied on images (HS-PIV-(A) and HS-PIV-(B)) with a cross-correlation algorithm with a window size of 32x32 pix^2 and a 50% overlap. A coherent filter is applied to correct isolated false vectors.

Air entrainment: HS-PIV-(B) configuration

In this study, attention is paid to the air entrainment by the air co-flow. To capture slow air entrainment velocity, the HS-PIV is adjusted (configuration: HS-PIV-(B), $\Delta_{PIV} = 400 \mu s$). Figure 3.18 presents the experimental facility of the HS-PIV-(B) configuration in order to obtain the air entrainment. The laser and the different lenses use configurations which are identical to HS-PIV-(A). However, a box is installed to create a containment area. The dimensions of the latter are sufficiently large to avoid perturbations caused by the confinement. The ambient air is seeded by a glycol mist with a

spectacle smoke machine. The velocity of the air-entrainment is much lower than in the air co-flow jet, which requires increasing the time between the two laser pulses.

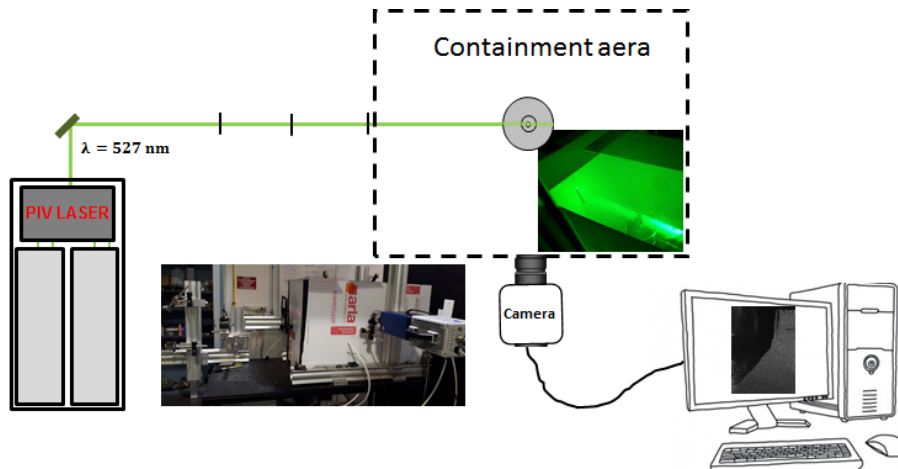


Figure 3.18: Optical arrangement for HS-PIV measurements to capture the air entrainment.

Figure 3.19 shows an instantaneous image obtained by HS-PIV in configuration (B). The field of view is moved towards the higher value of the radial coordinates as it is presented in fig 3.6. The gray part of the image represents the seeding, whereas the black part represents a hot region where the mist of glycol is completely evaporated. The interface between the black and the gray region can be interpreted as an isotherm of glycol evaporation. Close to the radial position $X = 10 \text{ mm}$, the image shows the Mie diffraction due to the interaction between the laser and the *n*-heptane droplets.

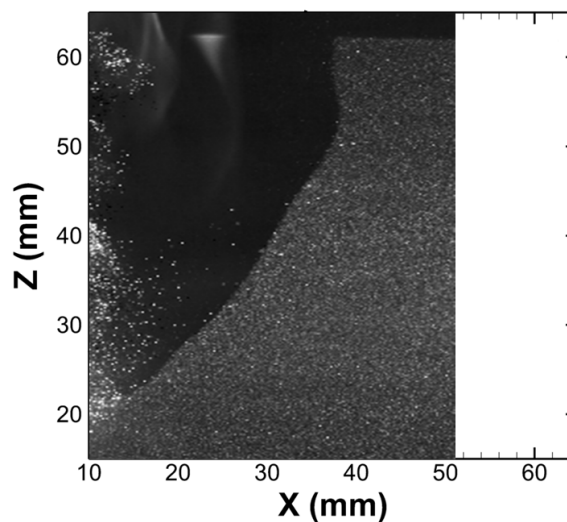


Figure 3.19: Raw image of air entrainment obtained by HS-PIV-(B).

3.6 Conclusion

This chapter presents the burner and the basic optical diagnostics used in this work to complete the knowledge on the spray combustion. As was explained during the introduction, canonical configurations with well-defined boundaries condition allow to compare and test different models necessary in large eddy simulation. In this work, the *n*-heptane is used as liquid fuel to facilitate the comparisons with simulations. Indeed, *n*-heptane presents many advantages:

- Volatility: From an experimental point of view, it is easier to use a fuel with a good volatility to avoid preheating.
- Evaporation modeling: *n*-heptane is assumed to be a mono-component, and the comparison with LES was easier, such as the studies of the evaporation model effect on flame structure. Indeed, there are more numerical models for the mono-component fuels than for poly-component fuels. Moreover, thermal, chemical and thermodynamical properties of *n*-heptane are validated, which avoids the ambiguities during the comparisons.
- Combustion modeling: *n*-heptane has been extensively studied in LES. For the combustion models, there is many approach such as the detailed chemistry, the reduced chemistry (ARC) or the global chemistry. The difference of the combustion models in flame structure is illustrated by in Chapter 7.

Concerning the burner, an industrial simplex fuel injector is used in order to reproduce the spray topology, such as the heterogeneous repartition of fuel droplet observed in a real combustion chamber. However, a choice was done to used a non swirling air co-flow to globally control the 2D average turbulence during the combustion. In a global objective to describe the spray properties, the experiments also include measurements of droplet size and velocity by Phase Doppler Anemometry. Note that the PDA was performed by my colleague Javier Marrero-Santiago. To characterize the lifted-flame structure, a classic Planar Laser Induced is used. Moreover, an accurate and efficient technique (Instantaneous Global Rainbow Refractometry, I-GRT) is introduced for the measurement of the instantaneous fuel droplet temperature in a realistic spray flame. Simultaneously, the instantaneous flame structure is analyzed by OH-PLIF. The description of this technique is now described in Chapter 4

Chapter 4

Application and development of a technique for measuring the fuel droplet temperature

Contents

4.1	Droplet temperature by optical measurement techniques . . .	58
4.1.1	State of the art	58
4.2	Background on the Rainbow Refractometry Technique	59
4.2.1	Standard Rainbow refractometry	59
4.2.2	Global rainbow refractometry (C-GRT)	63
4.2.3	Instantaneous Global rainbow refractometry (I-GRT)	69
4.3	Application of C-GRT	70
4.3.1	Experimental set-up	70
4.3.2	Fuel droplet temperature measurement procedure	71
4.4	Development and application of Instantaneous Global rainbow refractometry coupled with OH Planar Laser Induced by Fluorescence (I-GRT coupled with OH-PLIH)	77
4.4.1	Experimental set-up	77
4.4.2	Studied zones	78
4.4.3	Image post-processing	79
4.5	Conclusion	79

The spray jet flame has been already experimentally investigated by many studies on the flame structure [?, 88, 89] or on the stabilization of the leading edge [25, 27]. However, one of the fundamental aspects to consider in two-phase flow combustion is the heat transfer between the liquid and the gas phase that necessarily occurs during the vaporisation

and combustion processes. This requires a reliable experimental technique able to measure the fuel droplet temperature. Unfortunately, there are few techniques that are able to accurately measure droplet temperatures. In the present work, fuel droplet temperatures are obtained by Global Rainbow Refractometry Technique (GRT). In the following, we will first present the state-of-the-art of the available experimental techniques. Next, the GRT will be presented by the description of the experimental set-up, the principle of the technique, and the post processing enabling to obtain the fuel droplet temperature.

4.1 Droplet temperature by optical measurement techniques

4.1.1 State of the art

The characterization of droplet temperature is still challenging compared to the techniques used to measure the size and the velocities of the droplets, which are referenced in the literature. A review of the state of the art for fuel droplet temperature measurements was recently carried out by Lemoine and Castanet [90]. This paper provides a review of the main techniques available to optically measure the temperature of single droplets and sprays. Most of the techniques used to extract the droplet temperature are based on phenomena related to light interaction with matter. Indeed, some methods use the properties of the light scattering by the droplet, but other methods, such as the photoluminescence, phosphorescence or fluorescence use the signal evolution with temperature and composition. Other techniques can be cited including Raman scattering, thermographic phosphors or infrared thermography. The laser induced fluorescence technique needs to add an organic dye into the liquid. The dye is chosen by its high sensitivity of the fluorescence signal with the temperature. In most cases, a laser with a specific wavelength is used to populate the excited state. The fluorescence signal is the consequence of the spontaneous relaxation of molecular species after these have been excited by the laser. The main drawback of the fluorescence is that, the technique provides indirect measurements. For instance, fluorescence requires calibrations of the signal, such as the shape of spectral lines, lifetime or intensity, as a function of the parameters of interest for quantitative measurements. In addition, a change in the intensity of the signal does not necessarily result from variations in the droplet temperature. Other measurement techniques are based on elastic or inelastic light scattering. The most used is the global rainbow refractometry technique (GRT) and it is based on the features of the light scattered by the droplets, and more precisely on the angular position of the rainbow, which is very sensitive to the refractive index, and thus, to the droplet temperature.

Note that the first attempt to rationally explain the appearance of the rainbow was probably that of Aristotle. He proposed that the rainbow was actually an unusual kind

of reflection of sunlight from clouds. After the conjecture of Aristotle, it took almost 17 centuries before significant progress was made by Theodoric. He suggested that each droplet was individually capable of producing a rainbow. Then, Descartes showed that the rainbow was made of rays that enter in a droplet and are reflected once from the inner surface. The secondary bow consists of rays that have undergone two internal reflections. These considerations are still applicable and the explication of the GRT can be made by the Descartes relations. Nowadays, the GRT has been used by several teams ([91–94]). One can notice the pioneer works of Sankar et al. [93, 95] on the simultaneous measurement of size, velocity and temperature of fuel droplets by coupling PDA with Rainbow Thermometry. Introduced by Roth et al. [92] in the standard configuration and later extended to the global configuration by Van Beeck et al. [91], GRT has a large potential of application in real sprays. In a recent work [16], this technique was successfully applied on a two-phase V-shaped flame and the evolution of the mean fuel droplet temperature across the mean flame brush was reported for different levels of flow turbulence. In this work, the GRT is used to extract the fuel droplet temperature in a more complex spray in non-reacting and reacting conditions.

4.2 Background on the Rainbow Refractometry Technique

In this section, the background of the Rainbow Refractometry Technique is given. First, the standard configuration, which considers the interaction of one ray with one droplet is presented. Then, the effect of a cloud of droplets is illustrated in the Global Rainbow Refractometry configuration.

This technique is based on the theory of light diffusion through liquid droplet. Two approaches are possible to extract the refractive index:

- (i) To approximate the incident beam by a series of rays, and to calculate the refracted and reflected light by the droplet with the Snell-Descartes relation and the Fresnel law.
- (ii) To solve the exact Maxwell's equation with the appropriate boundaries conditions.

4.2.1 Standard Rainbow refractometry

Principle

A preliminary analysis can be obtained by applying the laws of refraction and reflection to the path of a ray through a droplet. The main assumption is that the droplet is perfectly spherical. All directions are considered equivalent and only one significant variable is present: the displacement of the incident ray from an axis passing through the center of the droplet. This is called the impact parameter and is equal to zero when the ray coincides with the central axis and equal to the radius of the droplet when the ray is

tangential. Figure 4.1 illustrates the path of a ray through a droplet. At the surface of the droplet, the incident ray is partially reflected, and this reflected light is identified as the scattered rays $P = 0$ in Fig. 4.1. The remaining light is transmitted into the droplet with a change in direction caused by a change in the refractive index between the droplet and the surrounding. At the next surface encountered, the ray is again partially transmitted ($P = 1$) and partially reflected. At the next boundary, the reflected ray is again split into reflected and transmitted components, and the process continues indefinitely. Thus, the droplet gives rise to a series of scattered rays with a rapid decrease of intensity. Rays ($P = 0$) represent direct reflection by the droplet. Rays ($P = 2$) are those that escape the droplet after one internal reflection and they make up the primary rainbow. The $P = 3$, having undergone two reflections, give rise to the secondary bow.

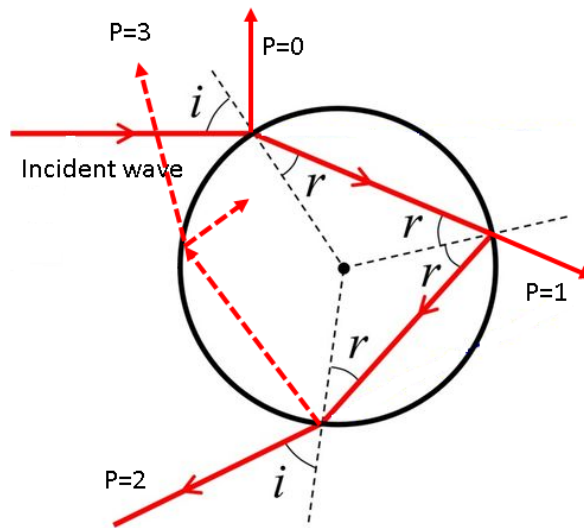


Figure 4.1: Refracted and reflected rays by a droplet.

Figure 4.2 represents a classical scattering pattern around the rainbow angle. This profile corresponds to a spherical and transparent droplet with a diameter $D = 100 \mu m$ and a refractive index $n = 1.38$. The primary rainbow is created by the rays $P=2$. Note that the Alexander dark band, where the light intensity is very low compared to the first and second rainbows, is mainly dominated by external reflection. Concerning the primary rainbow, the signal presents a principal peak followed by a succession of peaks with lower intensities. On these peaks, we can observe high frequency structures, called "ripples". These fringes are caused by the interferences between the light directly reflected at the surface of the droplet and the light internally reflected.

Theory for signal post-processing

In Standard global refractometry, the signal can be analyzed by one of these theories:

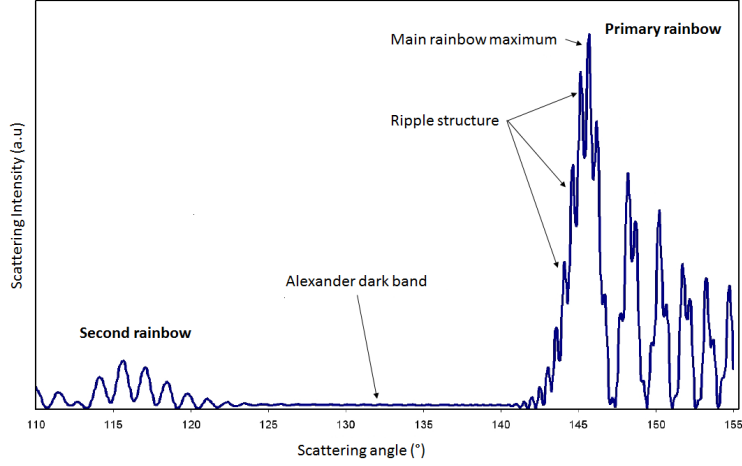


Figure 4.2: Diffusion pattern for an angular range between 110 and 150 degrees, for a droplet of diameter $100 \mu\text{m}$ and with refractive index equal to 1.38.

(i) Geometrical theory, (ii) Airy theory, (iii) Lorenz-Mie theory, (iv) Debye theory and (v) Nussenzveig theory. A detailed explanation of the mathematical models of light diffusion by a spherical droplet is not provided here, but the readers can find additional information in different theses [14, 96]. To explain the analysis principle of this typical signal (Fig. 4.2), it is usual to use the geometrical theory based on the Descartes theory of rainbows. The angular position Θ_{rg} of the first rainbow is given by the minimum of scattering angle of rays (order two $P=2$).

The angular position of the different rainbows are given by the Eq. 4.1:

$$\Theta_{rg} = 2 \left(P \cos^{-1} \left(\frac{1}{N} \sqrt{1 - \frac{N^2 - 1}{p^2 - 1}} - \sin^{-1} \sqrt{1 - \frac{N^2 - 1}{p^2 - 1}} \right) \right) \quad (4.1)$$

where N is the refractive index of the droplet and p is the order number of the scattered rays contributing to the rainbow. The dependence of the rainbow position on the refractive index is independent of the size and depends only on the refractive index. From the calculation of Θ_{rg} , it is possible to extract the mean refractive index. However, this geometrical approach is only accurate in the range of a millimeter and for larger droplet diameters. Indeed, some deviations can occur on the angular position of the rainbow for smaller droplets.

This approach can be improved to extract the refractive index for smaller droplets. A modification of Descartes theory was made by Airy. He proposed a new equation (Eq.4.2) to determine the angular position of the different rainbows.

$$\Theta_{ra} = \Theta_{rg} + \frac{1.0845}{\sqrt{\frac{N^2 - 1}{p^2 - 1}}} \left(\lambda^2 \frac{\sqrt{1 - \frac{N^2 - 1}{p^2 - 1}}}{64 a^2} \right)^{1/3} \quad (4.2)$$

where Θ_{rg} is the rainbow position according to the Descartes theory, λ is the wave-

length and a is the droplet radius. Note that with the Airy theory, the scattering intensity depends on the droplet diameter to the power of $7/3$ [14]. However, the Airy theory does not describe all the rainbow structures and the high frequency oscillations are not predicted.

The most powerful tool to describe the scattering of a plane wave by a spherical droplet implies an analytical resolution of the Maxwell's equations. The Lorenz-Mie theory allows to calculate the exact position of light around the rainbow angle and takes into account all types of interactions. The approach developed by Nussenzveig is similar and as precise as the Lorenz-Mie theory but the computation is about 300 times faster. This method will be used for the Global rainbow refractometry configuration.

In the Nussenzveig theory, it introduces one formula for each rays, but in the methodology developed by Dr. Saengkaew, the interest is limited to the rays $P = 0$, $P = 1$ and $P = 2$ [14]

$P = 0$: Nussenzveig introduces an equation to describe the reflected ray. The complex amplitude of the light externally reflected by the spherical droplet is given by:

$$f_{reflexion}(\alpha, \Theta) = -d \left(\frac{\sqrt{N^2 - \cos^2(\Theta/2)} - \sin(\Theta/2)}{\sqrt{N^2 + \cos^2(\Theta/2)} + \sin(\Theta/2)} \right) \exp(-2 i \alpha \sin(\Theta/2)) \left(1 + \frac{i}{2\alpha} \left(\frac{1}{\sin^2(\Theta/2)} - \frac{2N^2 - \cos^2(\Theta/2)}{(N^2 - \cos^2(\Theta/2))^{3/2}} + O(\alpha^{-2}) \right) \right) \quad (4.3)$$

where α is the size parameter equal to $\alpha = \frac{\pi d}{\lambda}$, d , is the droplet diameter, λ is the wavelength of the incident beam and Θ is the scattering angle define as the angle between the ray $p=1$ et $p=2$.

For $p = 1$, Nussenzveig introduces a formula to describe the twice refracted ray.

$$\begin{aligned}
 f_{reflexion}(\alpha, \Theta) = & -\frac{d}{2} \frac{2 N^2}{(N^2 - 1)^2} \frac{[(N \cos(\Theta/2) - 1)(N - \cos(\Theta/2))]^{3/2}}{(\cos(\Theta/2))^{1/2}} \frac{\exp(2 i \tau \alpha)}{\tau^2} \\
 & \left(1 - \frac{i \tau}{16 \alpha (N \cos(\Theta/2) - 1)} \left(\frac{2(N \cos(\Theta/2) - 1)}{N \sin(\Theta/2)} \right) \right) \\
 & \left(\cos \Theta - \frac{(N \cos(\Theta/2) - 1)(N \cos(\Theta/2))}{2 \tau^2 \sin(\Theta/2)} \right) \\
 & - \frac{9}{1 - \chi} + 15 \chi - 6 + 8(\chi - 1) \left(\chi^2 + \frac{5}{8} \chi + 1 \right) \frac{N^2 \sin^2(\Theta/2)}{(N \cos(\Theta/2) - 1)^2} + O(\alpha^{-2})
 \end{aligned} \tag{4.4}$$

where $\tau = (1 - 2N \cos(\Theta/2) + N^2)^{1/2}$ and $\chi = \frac{N \cos(\Theta/2) - 1}{N(N - \cos(\Theta/2))}$.

Concerning the first rainbow ($p=2$) modeling, the mathematical equations are more complex and are not described here. The readers can find the equations in [14].

Effect of the droplet temperature and droplet size on the rainbow signal

Figure 4.3 shows that a variation in the refractive index inside the droplet (ie. temperature), implies an global offset of the GRT signal. It was shown that the signal frequency can give an approximation of the droplet size [14]. The higher the frequency, the larger the droplet diameter. Considering one droplet, the externally reflected light interferes with refracted light creating high frequency fringes (ripple). The ripple structures are very sensitive to any change (size, refractive index, shape). The angular location of the rainbow is very sensitive to the droplet refractive index, and then, to the droplet temperature.

4.2.2 Global rainbow refractometry (C-GRT)

Compared to the standard configuration, the global rainbow technique is based on the analysis of the light scattered around the rainbow angle due to an assembly of droplets. Generally, this technique uses the same physical principle as rainbow refractometry. Nevertheless, the recorded light is not issued from one droplet but corresponds to collaborative scattering of a large number of droplets. Indeed, in industrial applications, the droplet concentration differs in space and in time. In this spray jet flame configuration, the droplet concentration is assumed to be constant with time but depends on the region of spray (see

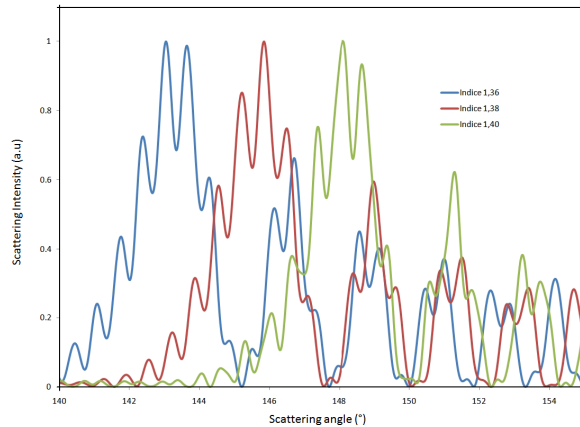


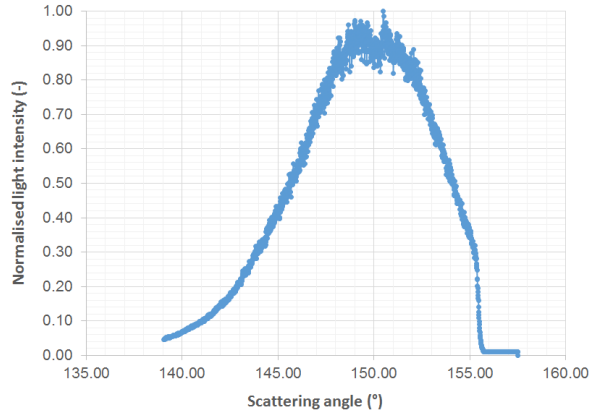
Figure 4.3: Influence of the refractive index on the GRT signal

Chapter 5). The recorded light is issued from all droplets contained in the measurement volume and accumulated during the exposure time of the camera. It is important to note that the refractive index measured is a double average, in space (many drops) and in time (camera exposure).

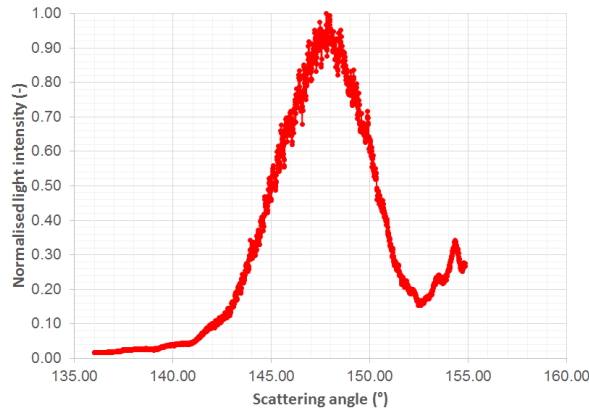
Figure 4.4 presents two intensity profiles extracted from the experimental images for two radial positions in the spray. The global rainbow signal presents a smooth shape induced by the contribution of all individual Rainbow patterns from each individual droplet. The Global Rainbow Technique removes two main disadvantages of Standard GRT :

- The addition of a large number of droplets removes the ripple structure. From 1000 droplets contained in the measurement volume, it was shown by Saengkaew [14] that the signal is smoothed.
- No effect of non spherical droplets: for non spherical droplets, if the orientation of the droplets in the spray can be assumed to be described by a random law, the contribution will be only a uniform background.

As for the rainbow for one droplet, the global rainbow pattern also depends on the droplet size distribution and the refractive index. The position of the first rainbow (peak) is greatly influenced by the value of the refractive index, whereas the shape of the curve is imposed by the size distribution [94,97]. Indeed, the profile in Fig. 4.4 at $X = 0$ & $Z = 35$ mm is larger than the profile at $X = 10$ & $Z = 35$ mm. This can be explained by the difference on the mean diameter. Moreover, the position of the peak is different on the two images and results in a difference between the mean refractive index value. It means that, for both positions in spray, the mean droplet temperature is different (see Chapter 5). The precision on the refractive index varies between 10^{-3} and 10^{-4} and the technique is able to estimate correctly the droplet size distribution. Figure 4.5 compares the droplet size distribution obtained with the C-GRT (dotted line) and the results obtained with the



(a)



(b)

Figure 4.4: Spatially averaged intensity profile from the selected band extracted from C-GRT images for two positions in spray (a): $X = 0$ & $Z = 35$ mm with $D_{10} = 10$ μm (see chap:5). (b): $X = 10$ & $Z = 35$ mm with $D_{10} = 20$ μm (see chap:5)

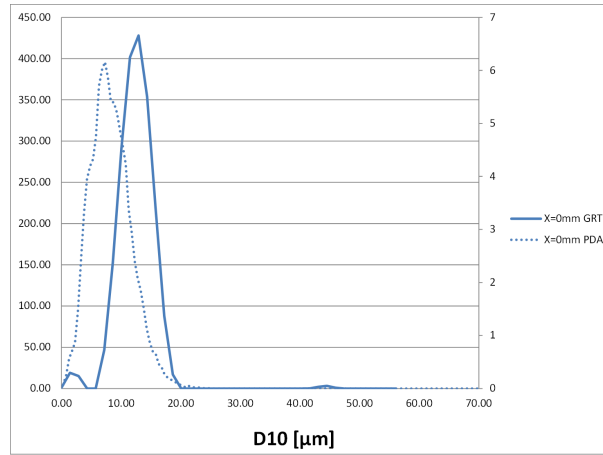
Phase Doppler Anemometry for two positions in spray. A globally good agreement can be found between the two approaches.

Global Rainbow processing

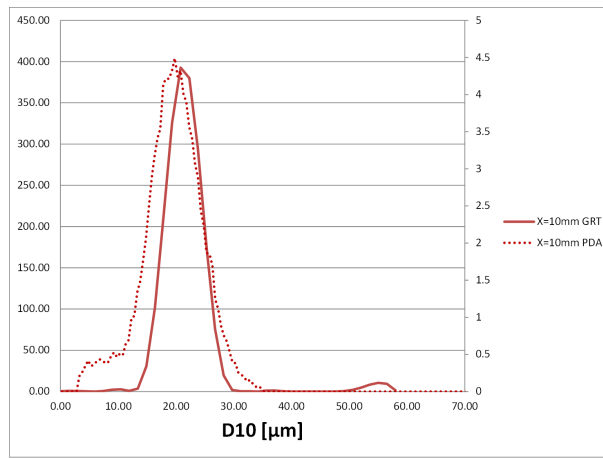
The processing tool was developed by Saengkaew and Grehan from the CORIA laboratory [14]. Figure 4.7 presents the methodology of the post-processing tool. The following description is extracted from the thesis of Saengkaew [14] and the readers will find more details namely on the validation on this processing in the thesis.

The methodology can be divided into 3 successive steps:

1. The user is asked to indicate the wavelength of the laser, the limits of the refraction angles (Θ_{min} and Θ_{max}), as well as the limits and the computation step of the assumed size distribution (d_{min} and d_{max}). The intensity matrix, A , is then calculated by the Nussenzveig theory and the least square method. The global rainbow pattern can be seen as a vector I of dimension m which describes the collected intensity for each pixel (collecting angles). This vector is equal to the product of a matrix A by a



(a)



(b)

Figure 4.5: Comparison between the droplet size distribution obtained by C-GRT (dotted line) and PDA (line) in two position in spray. (a): $X = 0$ & $Z = 35$ mm. (b): $X = 10$ & $Z = 35$ mm

vector B . The vector B , of dimension n , represents the size distribution histogram in n classes while the matrix A , of dimension $m.n$ represents the scattering of the droplets. The lines of A correspond to a scattering direction while the columns of A correspond to one droplet size class. Then the elements A_{ij} represents the scattered intensity in the direction Θ_i of the droplet of size d_j .

The elements of the matrix A can be computed by any light scattering theory by using the Nussenzveig's theory with correcting coefficients. Since A and I are known, the size distribution can be extracted, by solving the previous equation.

2. The rainbow signal from the calculated distribution is compared to the experimental signal.
3. In case of disagreement, the user is asked to go back to point 1 to change parameters in order to minimize the distance between the recorded and the computed global

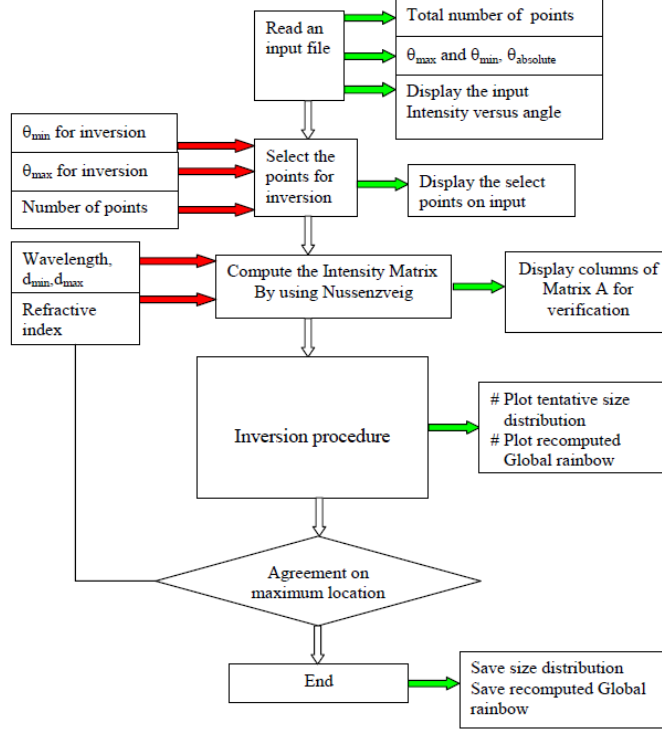


Figure 4.6: Inversion methodology developed by Saengkaew [14]

$$\begin{bmatrix} A(\theta_1, d_1) & A(\theta_1, d_2) & A(\theta_1, d_3) K A(\theta_1, d_{nb_point}) \\ A(\theta_2, d_1) & A(\theta_2, d_2) & A(\theta_2, d_3) K A(\theta_2, d_{nb_point}) \\ A(\theta_3, d_1) & A(\theta_3, d_2) & A(\theta_3, d_3) K A(\theta_3, d_{nb_point}) \end{bmatrix} \begin{bmatrix} b(d_1) \\ b(d_2) \\ b(d_3) \end{bmatrix} = \begin{bmatrix} I_1 \\ I_2 \\ I_3 \end{bmatrix}$$

$$A(\theta_{nb_angular_point}, d_1) K A(\theta_{nb_angular_point}, d_{nb_dia_point}) * b(d_{nb_dia_point}) = I_{nb_angular_point}$$

Figure 4.7: Inversion methodology developed by Saengkaew [14]

rainbow distribution. Otherwise, the diameter distribution and the refraction index are saved.

Accuracy of the global rainbow refractometry

The accuracy of these measurements (GRT) must be discussed as well as the limitations of the techniques.

First, it has to be noted that the temperature obtained from GRT measurements is weighted by the size of the droplets following a $d_p^{7/3}$ law [98], where d_p is the fuel droplet diameter. Indeed, when the droplet size is larger than the wavelength, the total scattered intensity is proportional to d_p^2 but, according to Adam (2002) [99], in the framework of geometrical optics, a rainbow ray is a ray of minimum deviation. The significant feature of this geometrical system is that the rays leaving the drop are not uniformly spaced: those near the minimum deviation angle are concentrated around it, whereas those deviated by larger angles are spaced more widely (see [99] p.235). It is possible to demonstrate that

this concentration of rays is proportional to $d_p^{7/3}$. This means that the measured average temperature is closer to that of the largest droplets crossing the measurement volume. In this experiment, the droplet size distribution obtained by PDA can be used to evaluate this contribution. The spray is polydisperse in space, with the largest droplets at the borders and the smallest droplets located in the center (5). However, for a given location, the spray is less polydisperse. Consequently, the bias is limited in our measurements.

Secondly, GRT is based on the refractive index homogeneity assumption (temperature homogeneity) throughout the entire droplet, which must be discussed when the fuel droplet crosses the flame front. The temperature homogeneity in a droplet is reached when its thermal relaxation time τ_T is much smaller than its characteristic time of transit in the flame. It was shown by Anders et al [15] that the influence of refractive index gradient inside the droplet on the GRT measurements vanishes practically when the dimensionless time $\tau^* = \frac{t}{\tau_T}$ is larger than 0.4 (Fig. 4.8).

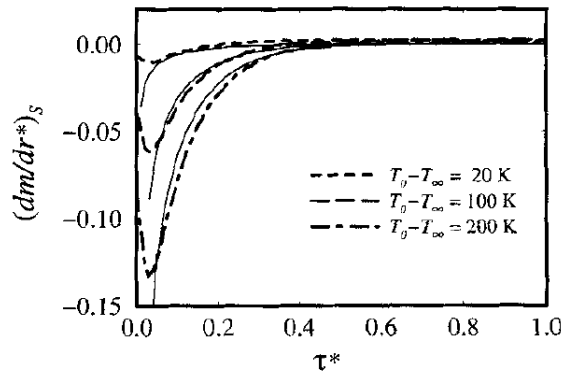


Figure 4.8: Refractive index gradients at droplet surface $(dm/dr^*)_s$ as a function of time τ^* [15].

For moving non-evaporating droplets, heat-transfer equations lead to Eq.4.5,

$$\tau_T = r_p^2 \frac{\rho C}{k} \frac{1}{\chi} \quad (4.5)$$

where r_p , ρ , C , k are the radius, density, heat capacity and thermal conductivity of the droplet. χ is the factor taking into account the increase of convective effect inside the droplet induced by the surface friction. χ depends on the Peclet number of the liquid phase [53]. In the inner reaction zone, mainly characterized by small droplet diameters ($D_{10} < 20 \mu m$), the corresponding internal temperature equilibrium time ($0.4\tau^*$) is lower than 0.1 ms. The analysis of PDA results gives a transit time of about 0.1 ms, assuming that droplets cross the flame front characterized by a typical flame thickness of 1 mm at the velocity of 10 m/s. The hypothesis is confirmed by comparing the latter to the internal temperature equilibrium time ($0.4\tau^* < 0.1 ms$).

In the following, some results of GRT are presented to show the ability of this technique to perform measurements in reacting conditions. In a recent work [16], this technique was successfully applied on a two-phase V-shaped flame and the evolution of the mean fuel droplet temperature across the mean flame brush was reported for different levels of flow turbulence.

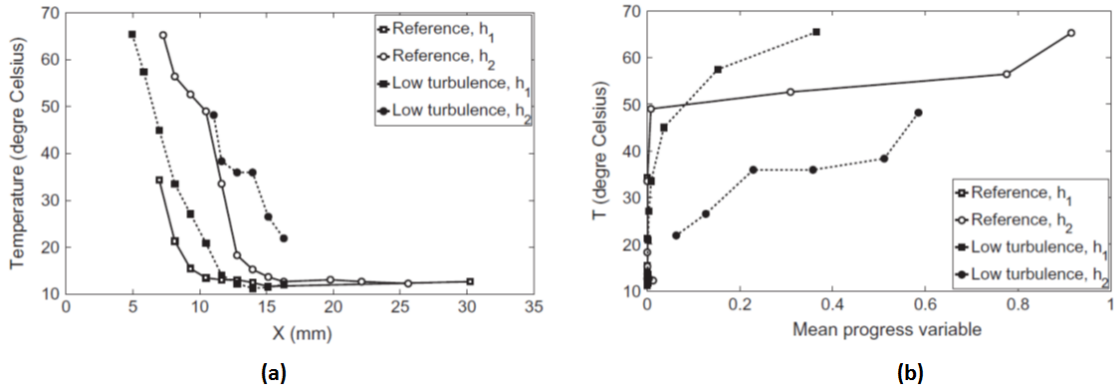


Figure 4.9: (a) Evolution of the droplet temperature in the cartesian coordinates system. (b) Evolution of the droplet temperature in the local coordinates system as a function of the mean progress variable. [16].

The evolution of the fuel droplet temperature in the vicinity of the flame front (fig.4.9) was determined through the global rainbow technique. The authors show that this technique is able to provide a quantitative measurement of the mean fuel droplet temperature in a measurement volume.

4.2.3 Instantaneous Global rainbow refractometry (I-GRT)

The major difference between global rainbow signal recorded under continuous illumination or pulsed illumination is that under pulsed illumination the light scattered by the different droplets interfere together. Then it is not enough to sum up the intensity of scattered light, the amplitude of the light scattered by each of the droplets located inside the control volume must be added together before to compute the intensity. In a conference paper (Measurement of droplets temperature by using a global rainbow technique with a pulse laser) during ILASS2010 conference Saengkaew et al. studied the possibility to use a pulse laser in the Global Rainbow Refractometry.

The major difference between a global rainbow signals recorded with a continuous laser and those generated by a pulsed laser is that under pulsed illumination, the light rays scattered by the different droplets interferes with each other. With a pulse laser, fringes are created by the interferences between the light scattered by the different droplets as it was shown in figure 4.10. In a recent paper [100], the authors studied the impact of the post-processing on the results. It seems that the use of the post-processing described in

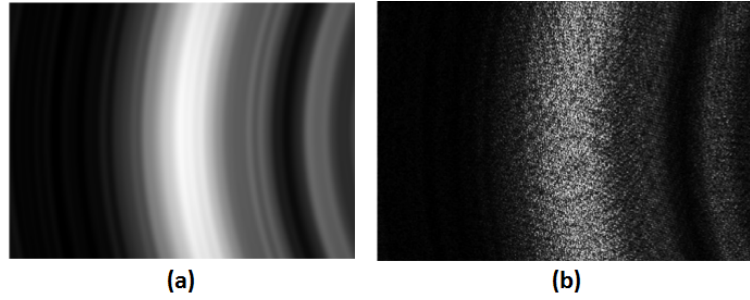


Figure 4.10: Global rainbow created experimentally for sixty droplets. (a) With a continuous laser. (b) With a pulsed laser

the C-GRT configuration yields the refractive index value and the size distribution with nearly the same accuracy (as for continuous laser). The short time measurements (10 ns) implies to have only few droplets in the measurement volume. In these cases, the refractive index measurement accuracy is on the third digit corresponding to less than $2^{\circ}C$ for fuel liquids.

4.3 Application of C-GRT

In the following section, the experimental setup and the test procedure are described. Note that the C-GRT was applied in this spray jet flame under reacting and non reacting conditions.

4.3.1 Experimental set-up

The Continuous Global Rainbow Refractometry Technique (C-GRT) system is similar to that of Letty et al. [16]. A continuous Nd:YAG ($\lambda = 532nm$) laser illuminates the spray. A first lens ($f_1 = 150mm$) collects the light scattered by the droplets at the Rainbow angle $\Theta \in [140 - 155]^{\circ}$. In the image plane, a 3 mm slit (s_1) is used to define the measurement volume. The first lens is adjusted with respect to the desired scattering angle. A second lens ($f_2 = 200mm$) creates the image of the focal plane of the first lens on a screen. The signal is recorded on a CCD camera (LaVision Imager ProX 4M camera) coupled with a 85 mm lens. The exposure time is adjusted to maximize the signal to noise ratio and it is near to 400 ms. As described in the previous section, the temperature measurement by C-GRT is an indirect measurement: the technique allows us to extract the refractive index of the droplet and then deduces the droplet temperature using a correlation (Eq.4.6). The steps of the procedure adopted for the temperature measurement are detailed below.

and its location on the CCD array. This is very important for the measurement precision since the refractive index depends on the absolute scattering angle. The calibration must be done with great precision and before every series of measurements. To increase the confidence in our experimental results, two calibration methods are used to validate the adapted methodology. Initially, particular attention is paid to the optical alignment, and the laser beam must be perfectly horizontal. Next, the first lens (f_1) is placed so that the angle around the position of the rainbow makes possible to collect all the light coming from the droplet-laser interaction. In our burner, the characterization of the fuel droplet temperature in reacting and non-reacting conditions is important for the comparison with the numerical results. The system must be able to measure the refractive index for the fuel droplet temperatures between $278K$ (evaporative cooling in Non Reacting Conditions NRC) and $363K$ in Reacting Conditions (RC). The lens (f_2) is positioned so that the entire focal plane is visible by the camera sensor. The mirror calibration needs to use a mirror mounted on an angular displacement with high precision, in order to obtain the relationship between the scattering angle and its location on the camera CCD array. The mirror must be placed in the optical alignment of the laser. The specific angle Θ_0 represents the perfect reflexion of the laser beam in the mirror and corresponds to an angle equal to zero. The calibration is obtained by varying the angle of the mirror as shown in figure 4.12.

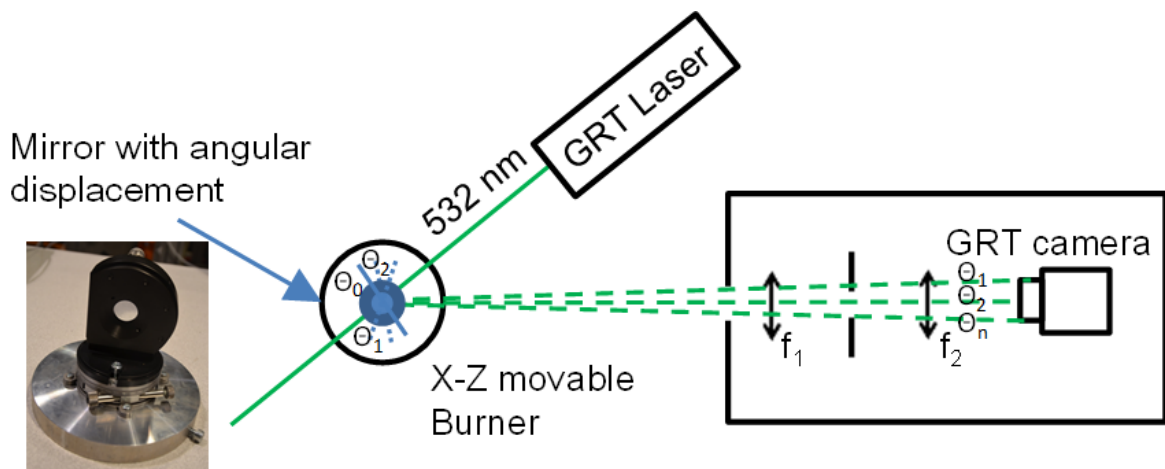


Figure 4.12: C-GRT calibration with mirror methodology.

In this way, we obtained for each angle ($\Theta_1, \Theta_2, \Theta_n$) the laser reflexion image on the camera CCD. The laser intensity must be decreased significantly using filters in order to protect the camera from too high intensity, making sure that the beam is not deflected. The relation obtained is a positive linear equation. The modeling is carried out by the software developed at CORIA by Saengkaew during her thesis [14]. Figure ?? shows an image obtained on the camera when the laser beam is reflected on the sensor. We can

also observe the set of experimentally points used to determine the relationship between pixels and angles.

A different calibration procedure used in the work of Letty [35], was also performed in order to validate the mirror-calibration. Provided that the rainbow technique is based on the measurement of the absolute location of the light scattered around the rainbow angle, it is essential to know the absolute angular location of each pixel of the camera. The light scattered by a liquid jet is recorded by the camera. The liquid jet is assumed to be perfectly characterized in size and refractive index. A shadowgraphy technique is applied to extract the diameter of the jet, and a thermocouple allows to obtain its temperature just before the injection. After that, the scattered light is computed for the same size and refractive index. Then the relationship between pixels and angles is obtained by identifying the position of the maximum intensity of each peak [14].

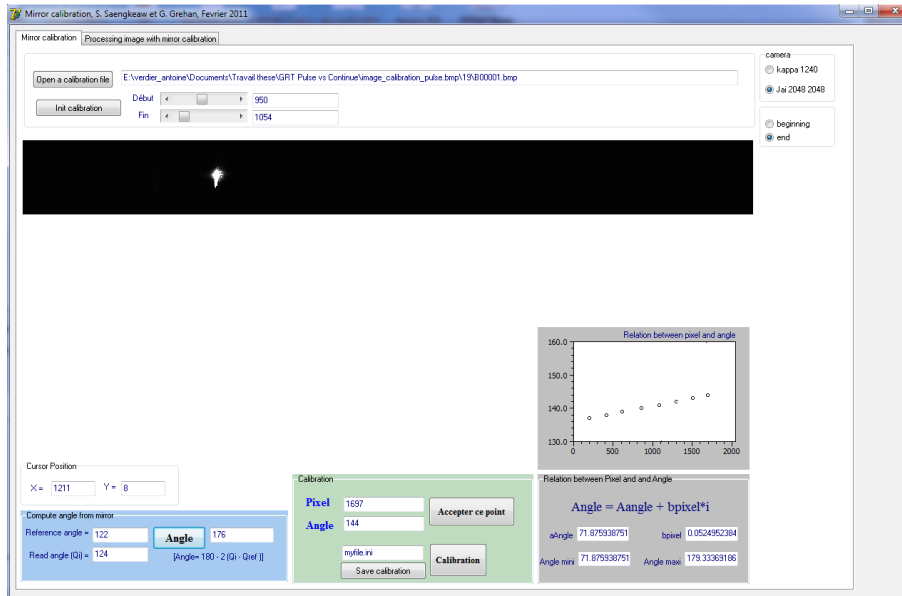


Figure 4.13: Mirror calibration software.

The light distribution scattered by the liquid jet is recorded as shown in fig.4.14. The raw recorded scattered light signal is illustrated by the red line, while the green line is the filtered signal used to facilitate the localization of the maximum of each peak as displayed by the yellow points. The same liquid jet properties are used to compute the numerical scattered light distribution (fig.4.15).

The position of the maximum intensity is then identified of each peak from the recorded and computed signals to extract the relationship between angles and pixels, as shown in fig.4.15.

To conclude on the calibration, a very good agreement is found for the both calibration, however the jet-calibration needs to implement a complex system..

- Image post-processing

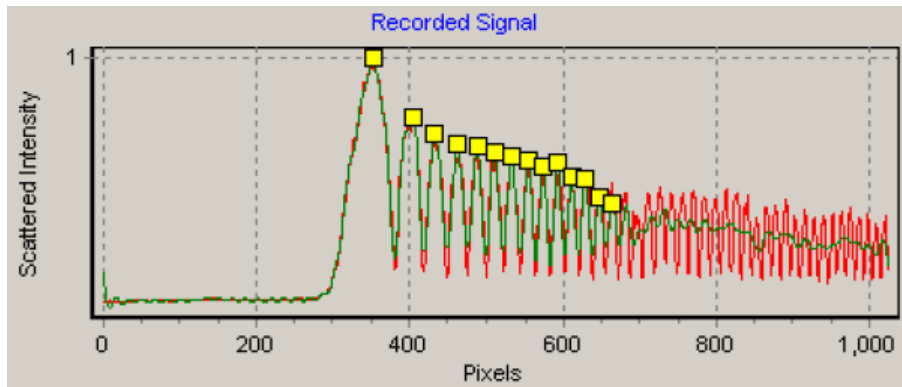


Figure 4.14: Recorded signal from the liquid jet.

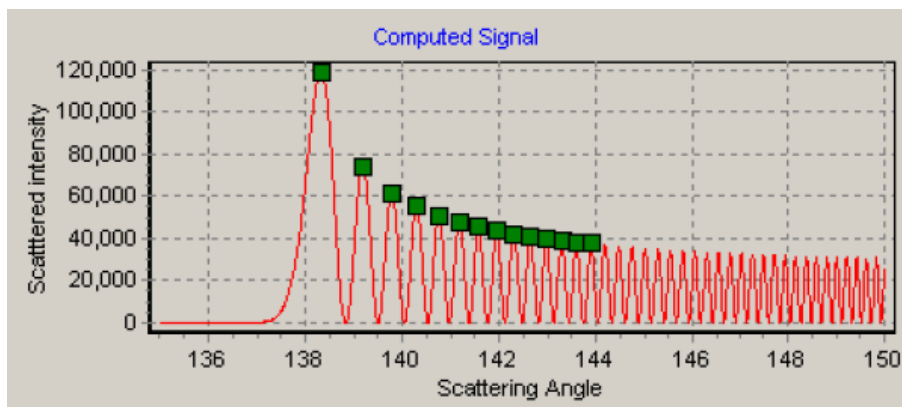


Figure 4.15: Computed signal for the liquid jet.

The C-GRT measurement is applied in the spray at different axial and radial positions. Due to the sensibility of the technique, the optical alignment cannot change during experiments. To perform the C-GRT measurements following the mesh presented in Fig. 4.16, the burner is equipped with three micro-metric displacements (R,Y,Z) to control the position of the measurement volume. Figure 4.16 presents the measurement mesh for PDA and C-GRT. Red points represent the temperature measurements, while the yellow points indicate the droplet size and velocity. To be consistent in the analysis of the results, the C-GRT is applied in the same positions as the droplet size and velocities measurements (PDA). For each measurement position, 400 images are recorded and statistics of the mean and RMS are provided.

The raw Rainbow images are post-processed following the Nussenzweig theory. First, an integration zone must be defined to apply the post-processing. This zone is used to extract an average profile of the light intensity. To perform the analysis on the raw images, an integration of 100 lines of pixels is performed to smooth the signal. The spatial average is limited to 200 lines of pixels to decrease the noise of the signal, but keeping the curvature of the rainbow signal. Note that, it is usual to define the integration zone in the same region of the camera where the calibration was done. Figure 4.17 presents a raw rainbow image, with the associated light intensity profile, which is integrated on 100

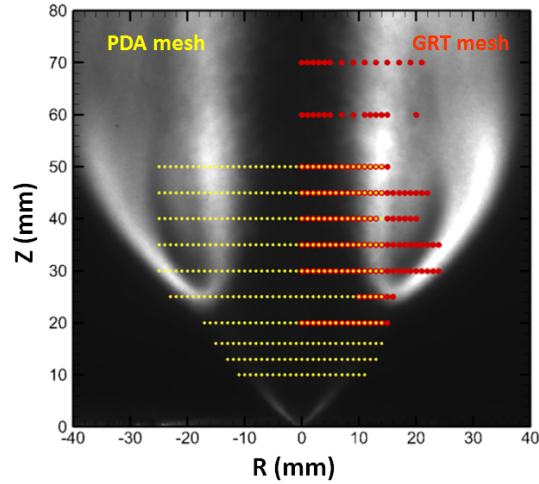


Figure 4.16: Measurement grid for Phase Doppler Anemometry and Continuous Global Rainbow Technique with the mean OH-PLIF image

lines of pixels (blue rectangle).

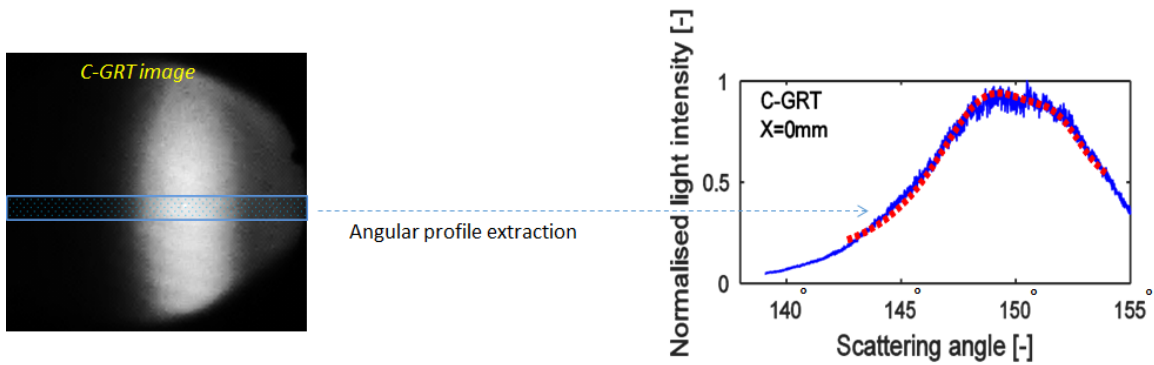


Figure 4.17: Rainbow image with associated light intensity profile

The calibration file is then implemented in the software to extract the angle / pixel relationship. On the software, the user must select the angular range in which the inversion calculation is to be carried out, the number of points to be taken into account in the calculation, the wavelength of the laser and the order of magnitude of the diameter of the smallest and largest droplets.

The post-processing is an automatic tool, which allows to extract from the raw images the average refractive index of the drops contained in the measurement volume, as well as a distribution of droplet sizes (fig. 4.18). When the input parameters are chosen, the tool reads all the images and makes a statistical analysis of the results such as the mean and the distribution of the refractive index for all images 4.19. To conclude, the user can be easily obtain the fuel droplet temperature with Eq. 4.6

It is important to keep in mind that since the refractive index changes with temperature for pure liquids, the temperature can be determined by a experimental correlation of

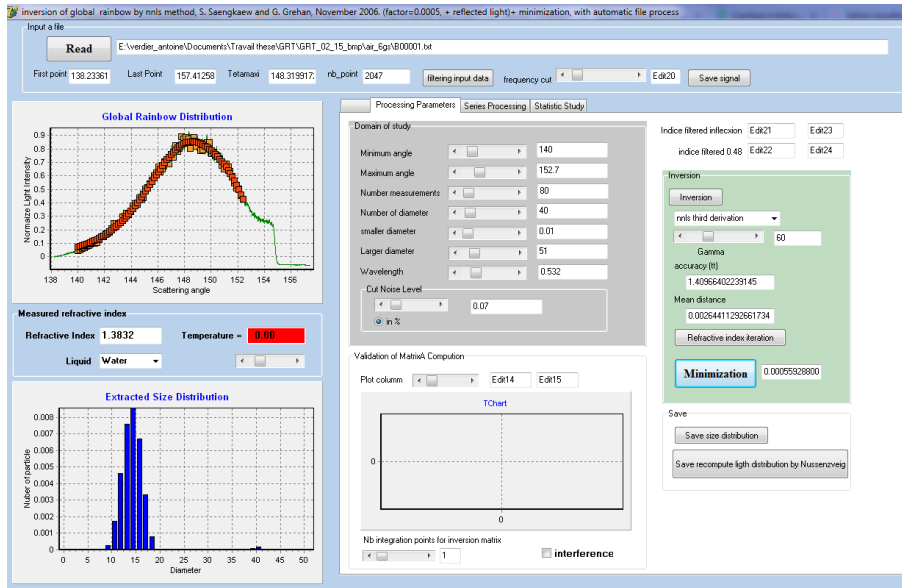


Figure 4.18: Software interface of inversion calculation; input parameters

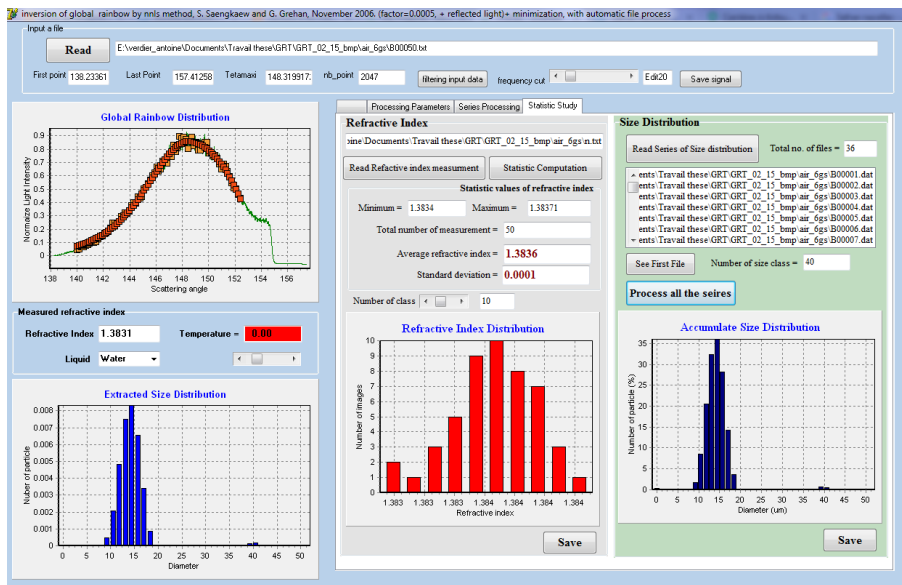


Figure 4.19: Software interface of inversion calculation; Statistical analysis

the form $T = a_n \cdot n + b_n$ 4.20. Finally, for n -heptane, the correlation between the refractive index and the temperature is given by the following equation: [102]

$$n = 1.4000 - 4.9844 \cdot 10^{-4} \cdot (T - 273.15) \quad (4.6)$$

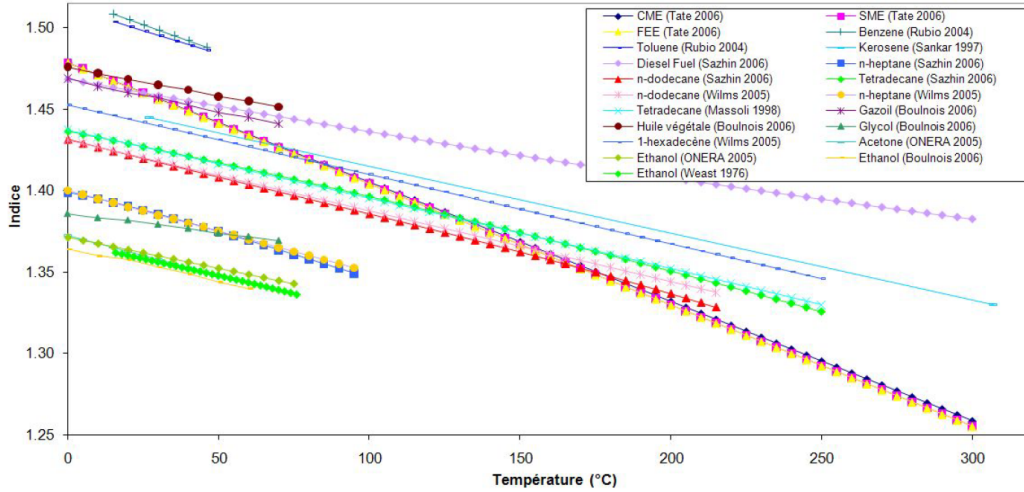


Figure 4.20: Evolution of the refractive index as a function of temperature for different fluids.

4.4 Development and application of Instantaneous Global rainbow refractometry coupled with OH Planar Laser Induced by Fluorescence (I-GRT coupled with OH-PLIH)

The recording time for one global rainbow image is typically equal to 400 ms in this configuration. These typical measurements are not resolved enough in time to follow fast variations of spray characteristics in unsteady flows. One of the added values of this study is the development and the application of the Instantaneous GRT (I-GRT) coupled with OH-PLIF measurements in order to provide new insight on the droplet temperature evolution in the vicinity of the flame front. This study is based on the encouraging results obtained by Letty et al [16] on the average conditioning of the fuel droplets temperature by the average position of the flame front. In this work, the continuous laser used in C-GRT was substituted by a pulsed Nd-YAG laser, to instantaneously measure the fuel droplet temperature contained in the measurement volume. In this experimental configuration the local and instantaneous measurement of the droplets within the measurement volume can be conditioned with the flame front position (distance to the flame front).

4.4.1 Experimental set-up

The Instantaneous Global Rainbow Refractometry Technique (I-GRT) system is carried out by substituting the continuous laser by a pulsed Nd-YAG laser (10 Hz, beam diameter = 4 mm). Temperature measurements are synchronized with OH-PLIF in order to simultaneously record the 2D flame structure and the droplet temperature within a mea-

surement volume located in the PLIF plane. Figure 4.21 presents the optical arrangement of the combined OH-PLIF and C-GRT / I-GRT measurements.

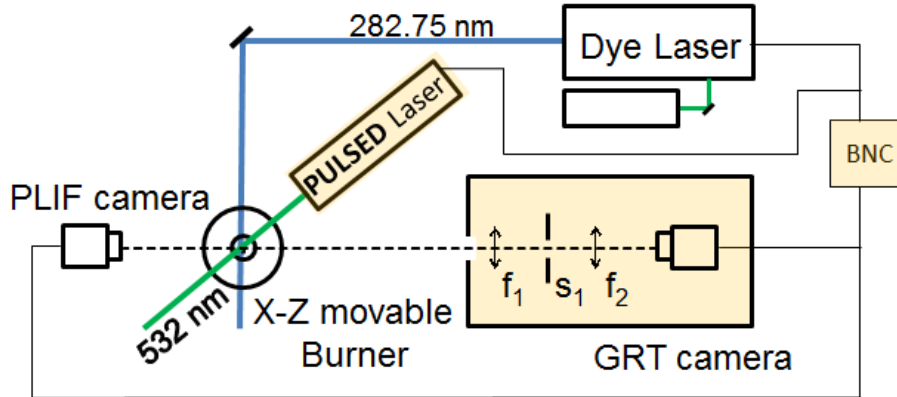


Figure 4.21: Optical arrangement of combined OH-PLIF and C-GRT / I-GRT measurements

4.4.2 Studied zones

Figure 4.22 shows the different studied zones, where I-GRT coupled with OH-PLIF was applied. Three characteristic zones are studied for one axial station $Z = 35$ mm:

- Fresh gases: represented by a mean progress variable equal to 0.05. The I-GRT measurement volume is placed in $R = 8$ mm.
- Flapping zone: represented by a mean progress variable equal to 0.45 and 0.80. Two radial positions are studied ($R = 10$ and 12 mm) due to the turbulent flame front.
- Burnt gases: represented by a mean progress variable equal to 1.00. In a radial position equal to $R = 14$ mm, the I-GRT measurement volume is always in a hot region between the two reaction zones (see Chapter 5)

Flow state	Mean progress variable $\langle C \rangle$	Zone	Absolute Position R [mm]
Fresh gases	0.05	A	8
Flame flapping zone	0.45	B	10
	0.80		12
Burnt gases	1.00	C	14

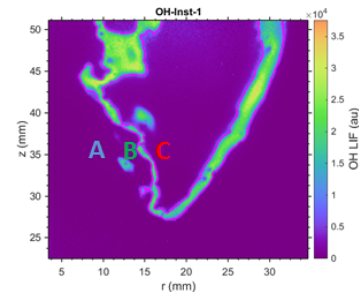


Figure 4.22: Studied zones for I-GRT

For each position of the I-GRT measurement volume, 100 images are recorded for I-GRT and OH-PLIF.

4.4.3 Image post-processing

The image post-processing concerning the I-GRT is described before in the chapter. Note that the same procedure as in C-GRT is used. Moreover, the flame front are detected by applying a threshold method in order to extract the distance between the flame front detected and the measurement volume. The goal is to provide droplet temperature conditioned by the distance to the flame front (fig. 4.23). An automatic tool is developed to extract the distance between the I-GRT measurement volume, which is kept in the same position during all experiments and the flame front position.

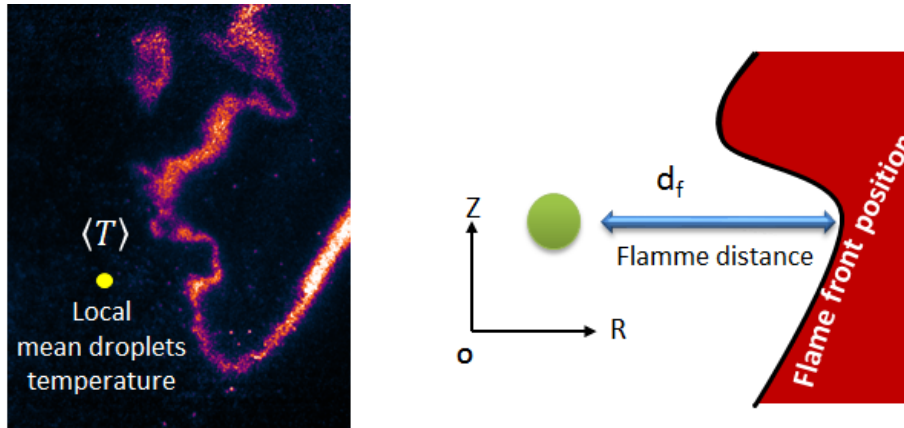


Figure 4.23: Instantaneous OH-PLIF image with the I-GRT measurement volume

4.5 Conclusion

In this chapter, the technique for measuring the fuel droplets temperature is presented. The Global Rainbow Technique is used to extract the mean n -heptane droplet temperature from the measurement of the droplet refractive index. The previous chapter 1 and 2 show the importance and the difficulty to predict the evaporation in a real application. The measurement of the fuel droplet temperature is a great importance to validate the evaporation model used in LES. However, we showed that there are few techniques available to measure the droplet temperature, in particular in reacting conditions. In the CORIA laboratory, a partnership with Dr Grehan and Dr Saengkaew was set up to apply the GRT on a complex configuration. This study was conducted using the knowledge and the experiment of Dr. Grehan and Dr. Saengkaew. A previous joint study [16] has shown the ability of the GRT to obtain temperature results in complex configurations. The goal here is to developed and apply an accurate and efficient technique (Instantaneous Global Rainbow Refractometry, I-GRT) for the measurement of the instantaneous fuel droplet temperature in a realistic spray flame, conditioned by the flame front position. In this work, this new coupled technique I-GRT/OH-PLIH is applied in non reacting and

reacting conditions. The next chapter is dedicated to the local flame structures and fuel droplet properties in reacting conditions.

Chapter 5

Local flame structures and fuel droplet properties

Contents

5.1	Global appearance and behavior of the spray jet flame	82
5.2	Analysis of carrier phase and dispersed phases in Reactive Condition	83
5.2.1	Air co-flow aerodynamic	83
5.2.2	Fuel droplet properties	85
5.3	Flame structure	90
5.3.1	Inner Reaction Zone (IRZ)	90
5.3.2	Outer Reaction Zone (ORZ)	91
5.4	Stabilization of the flame base	93
5.5	Fuel droplets temperature conditioned by the distance to the flame front	94
5.6	Conclusion	98

As described in chapter 2, the turbulence-droplet-flame interactions can lead to complex flame structures. Moreover, two phases combustion carries coupled multi-physical and chemical constraints. Due to the complexity of these multi-physical phenomena, it is essential to accurately develop and validate the numerical models for numerous practical combustion applications with accurate experimental data. To characterize the flame structure in a spray configuration, it is necessary to measured the carrier phase and the fuel droplet properties, which strong influence the combustion regime by evaporation rate and mixing. This chapter is dedicated to highlight the local flame structure observed in the Coria Rouen Spray Burner by measuring the air co-flow aerodynamics and the fuel droplets properties such as the size distribution, the velocities and the fuel droplet temperature, which is the novelty of this study.

This chapter is organized as follow: First we described the global appearance and behavior of the spray jet flame and we extracted information about the local flow properties, concerning the carrier and the dispersed phases. Then the local flame structure is analyzed by OH-PLIF measurements, to illustrate the combustion regime occur in the Inner Reaction Zone (IRZ) and Outer Reaction Zone (ORZ). To conclude this chapter, the fuel droplets temperature conditioned by the distance to the flame front is presented.

5.1 Global appearance and behavior of the spray jet flame

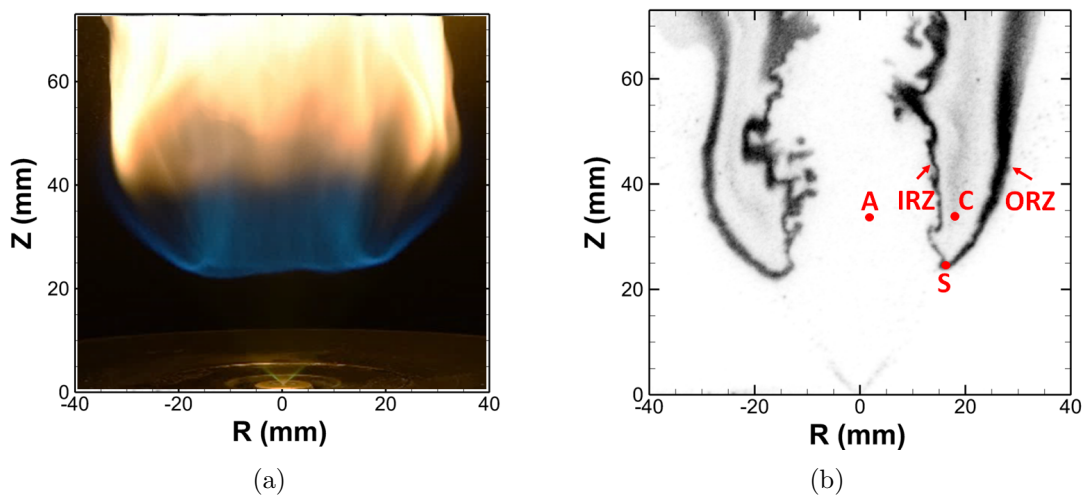


Figure 5.1: (a) Photo of the spray jet flame. (b) OH-PLIF and different zones.

Figure 5.1 presents a picture of a spray jet flame and an typical instantaneous OH-PLIF image at low repetition rate. The image shows three distinct zones including a region with no visible flame luminescence (center of spray and below the flame leading point) and two reaction zones, a bluish flame for axial stations lower than 40 mm and a yellow zone farther downstream. The global flame shape and the lift height of the flame stabilized downstream the fuel injector are conditioned by air flow rate, spray properties (droplets velocity and size) and global equivalence ratio. The asymmetric flame with a classical double structure is illustrated by the OH-PLIF recording where five different zones (A , IRZ , C , ORZ and S) are reported. The overall shape of the flame exhibits two branches corresponding to an inner and an outer reaction zone, IRZ and ORZ respectively, sharing a common flame base (S). This flame structure results from the spray heterogeneity in size [25, 33] imposed by the pressure fuel injector technology. The large droplets spread into the outer part of the air co-flow corresponding to the ambient air and the small droplets are mainly located in the centerline in the mixing zone (A). Indeed, in this region, the very small droplets represent only a small quantity of the liquid

mass and undergo a slow evaporation, leading to lean heterogeneous mixture, close to the lean flammability limit [18].

5.2 Analysis of carrier phase and dispersed phases in Reactive Condition

5.2.1 Air co-flow aerodynamic

Figure 5.2 presents a map of the two mean velocity components (axial and radial) of the carrier phase obtained by PDA in configuration PDA(A). Two important features are illustrated in the mean velocity fields. Consistent with earlier works [?, 27, 32, 103], the mean axial co-flow velocity provides two peaks at the exit of the injector. Further downstream ($Z > 25 \text{ mm}$), the co-flow air jets merge to form a unique larger jet with a flat axial velocity profile. Note that the air co-flow jet also generates radial velocities, approximately 5 times smaller than the axial velocities at $Z = 10 \text{ mm}$, which rapidly decrease down to zero at $Z = 25 \text{ mm}$.

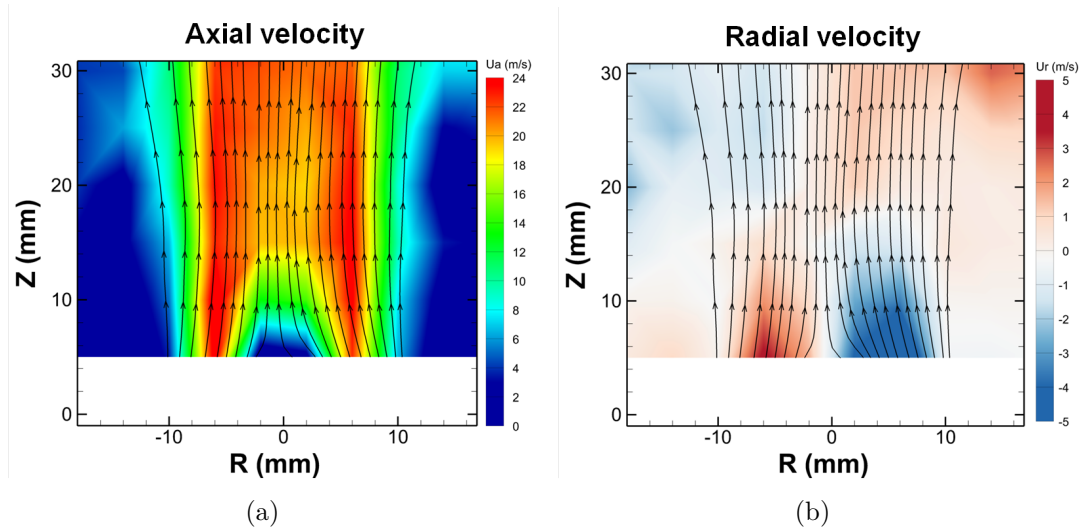


Figure 5.2: Mean components of air velocity flow for reactive conditions with vector field obtained with configuration $PDA(A)$. (a) Mean axial velocity. (b) Mean radial velocity.

Velocity fluctuations are expressed in Fig. 5.3 in terms of the turbulent kinetic energy k . Isotropy along the two directions perpendicular to the Z -axis is assumed and turbulent kinetic energy (k) is calculated following Eq. A.2

$$k = \frac{1}{2} \left(\overline{(u'_z)^2} + 2 * \overline{(u'_r)^2} \right) \quad (5.1)$$

The annular air co-flow discharging into the ambient air creates a shear layer at the interface between the high air co-flow velocity and the ambient air inducing turbulence

with large scale structures. This phenomenon is highlighted in the movie given as supplementary material 1. The quiescent ambient air is accelerated radially towards the centerline whereas a portion of the air jet loses some momentum. Figure 5.3(b) represents different Turbulent Kinetic Energy profiles for three axial stations. The maximum turbulent energy ($\approx 40 \text{ m}^2.\text{s}^{-2}$) is found at low axial stations, in the region where the air enters the chamber. The turbulent kinetic energy does not follow the same pattern as the axial velocity, with peaks diffusing radially with increasing axial stations. Given that velocity fluctuations enhance mixing and that all droplets enter the region of maximum k directly after atomization, their trajectories will be strongly influenced by the airflow velocities resulting in a heterogeneous droplet size distribution.

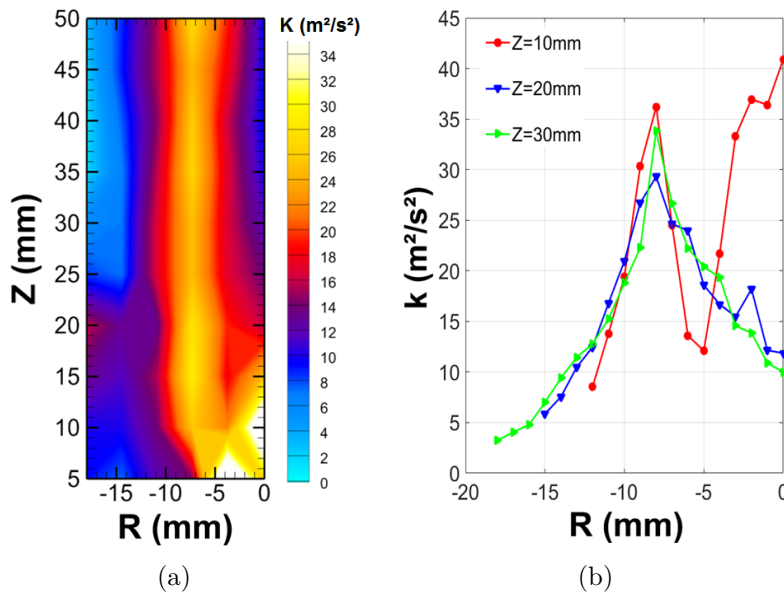


Figure 5.3: (a) Turbulent kinetic energy of the air in reactive conditions (k). (b) Turbulent Kinetic Energy profiles for different axial stations.

Averaged results enable to have an overview of the flow topology and put forward main zones of the flow in terms of velocity, turbulence and mixing. However, free jet have transient behaviors and it is compulsory to improve the analysis done by investigating instantaneous flow fields to analyze for instance the turbulence-flame interactions.

Figure 5.4 presents four instantaneous velocity fields captured in different times. Note that the velocity vectors are colored by the norm of velocity fluctuation computed as $\|U'\| = \sqrt{u'^2 + v'^2}$, where u' is estimated from the difference between the local velocity vector u and the local mean velocity vector U and respectively for the radial velocity (v'). The maximum value of $\|U'\|$ is around $12 \text{ m}.\text{s}^{-1}$ and appears intermittently in the shear layer, where turbulent kinetic energy is important. These fluctuations are representative of the turbulence large scales creating in a free jet, where strong velocity gradients are present at the interface between the air jet and the ambient air.

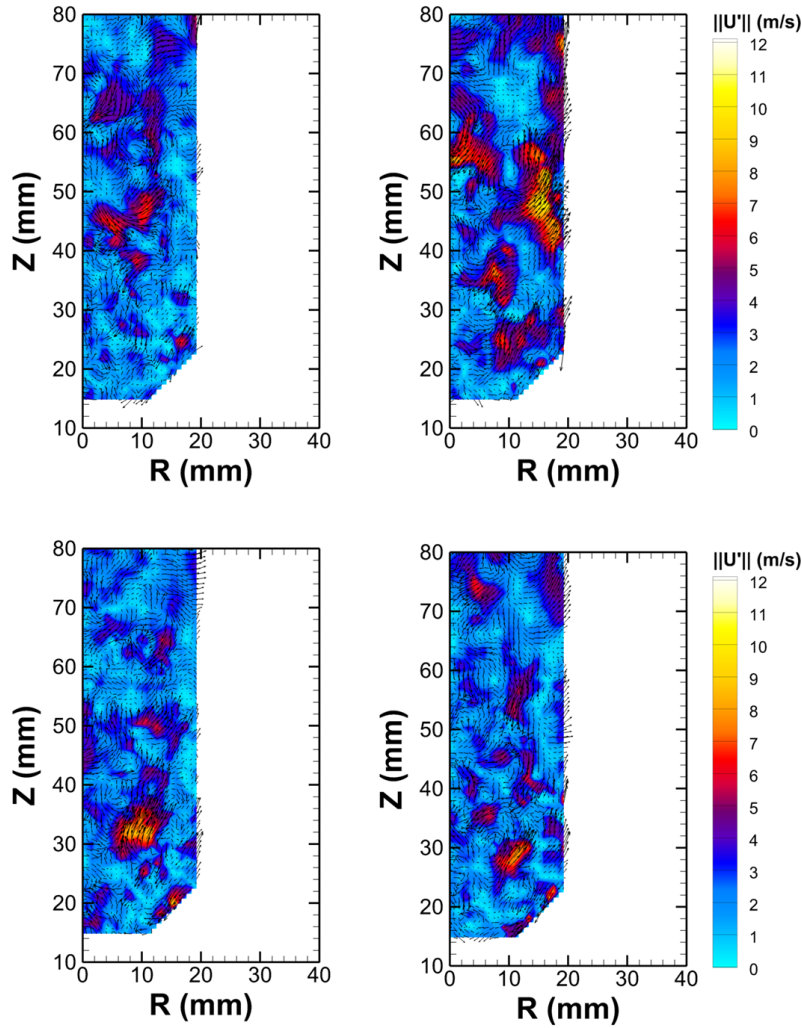


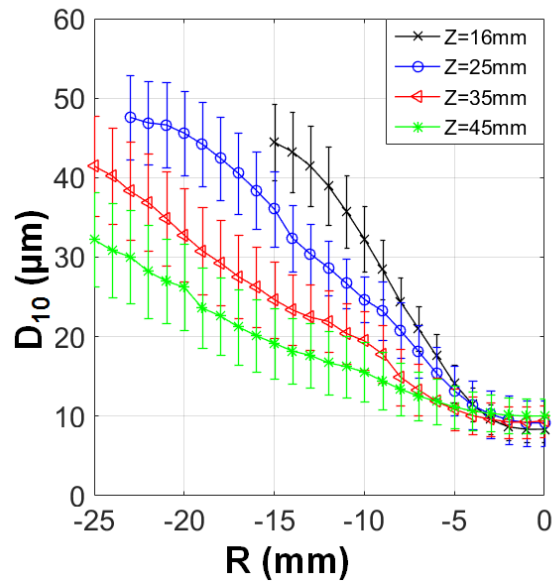
Figure 5.4: Instantaneous fluctuation velocity field

5.2.2 Fuel droplet properties

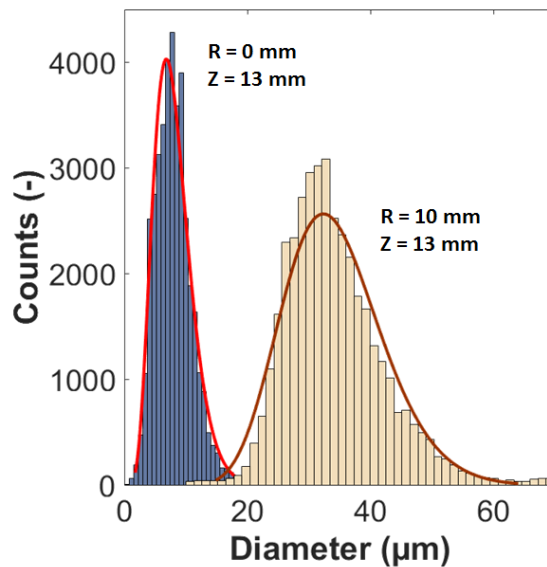
Spray distribution

The fuel spray presents a complex heterogeneous distribution, with droplet sizes ranging from 2 to 80 μm . Profiles of the mean diameter (D_{10}), at four axial stations, $Z = 16, 25, 35$ and 45 mm are represented in Fig. 5.5. The mean diameter profiles grow radially from the center towards the borders (from 5 to 50 μm) and vary significantly with Z due to the evaporation process. Droplets are expelled from the atomizer under a cone with an 80 degrees opening, following a direction that will force them to suddenly interact with the air co-flow. The central region contains a very low quantity of small droplets due to the centrifugal movement imposed by the swirling liquid injection inside the atomizer. The smallest droplets resulting from the liquid jet breakup are responsive to the air velocity field and follow the flow due to their small Stokes number. Furthermore, in this region, the very small droplets represent only a small quantity of the liquid mass and undergo a

slow evaporation, leading to lean heterogeneous mixture, close to the lean flammability limit [18]. However, larger droplets with higher Stokes number are less affected by the aerodynamic conditions and follow ballistic trajectories. It is worth noting also that the droplet size distributions are well represented by Rosin-Rammler distributions everywhere, as illustrated by Fig. 5.5.



(a)



(b)

Figure 5.5: (a) Fuel droplet mean diameter D_{10} in reactive condition. Error bars indicate the RMS of the droplet size distribution (b) Pdf of droplet size fitted by Rosin-Rammler distribution

In spray jet flame it is interesting to estimate the flux in order to predict the fuel vapor localization generated during the evaporation process. Figure 5.6 presents the result for

the same previous axial stations ($Z = 16, 25, 35$ and 45 mm). The dual mode of the PDA system allows to compute the liquid volume flux for each vector components. Its measure is based on the count of the number and size of droplets passing through a reference area, noted $A(d_i, \gamma_i)$ per unit time. The liquid volume flux is computed for the component of the probe in the z-direction (main direction of the flow)

The central region contains only small flux values due to the small droplet diameter ($D_{10} = 10\mu\text{m}$) and the low droplet detection frequency. However, large droplets, which supply the major quantity of mass are indicate by a peak in the flux profiles. The decrease of flux with axial stations is representative of the droplet evaporation and a droplet diameter diminution. For the heights equal to $Z=16$ mm and $Z=25$ mm (below the flame stabilization), the flux profiles show a peak, which corresponds to a balance between the larger droplets and the droplet detection frequency. Indeed, from $R>15$ mm even if the droplets diameter is bigger than lower radial stations, the droplet detection frequency is very small, which implies few droplets in the spray.

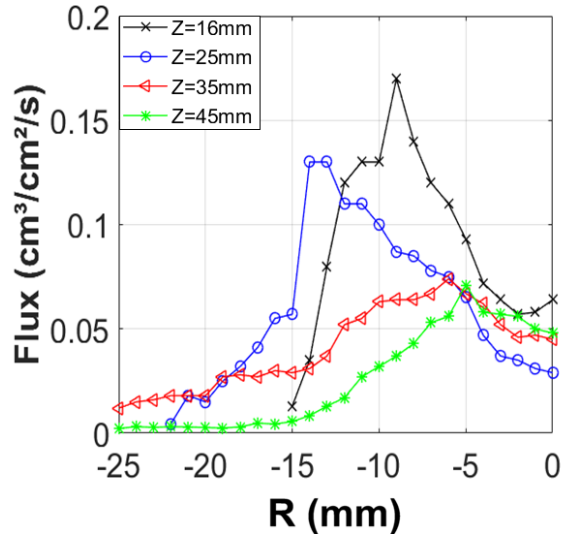


Figure 5.6: Radial profiles of the axial volume liquid flux for axial stations $Z = 16, 25, 35$ and 45 mm

Velocities by size-classes

To illustrate more precisely the droplets behavior, they are initially divided into 7 size-classes. The two mean velocity components are shown in Fig. 5.7 for 4 of the different size classes described above. The behavior of the $[60 - 70]$ group is very close to that of the $[50 - 60]$ group but, since they contain less droplets, they are not presented.

Values for the last two groups ($[30 - 40]$, $[50 - 60]$) are not shown in the central region because less than 500 droplets were detected per point. This minimum droplet number is chosen after a convergence study. The minimum droplet number depends on the position

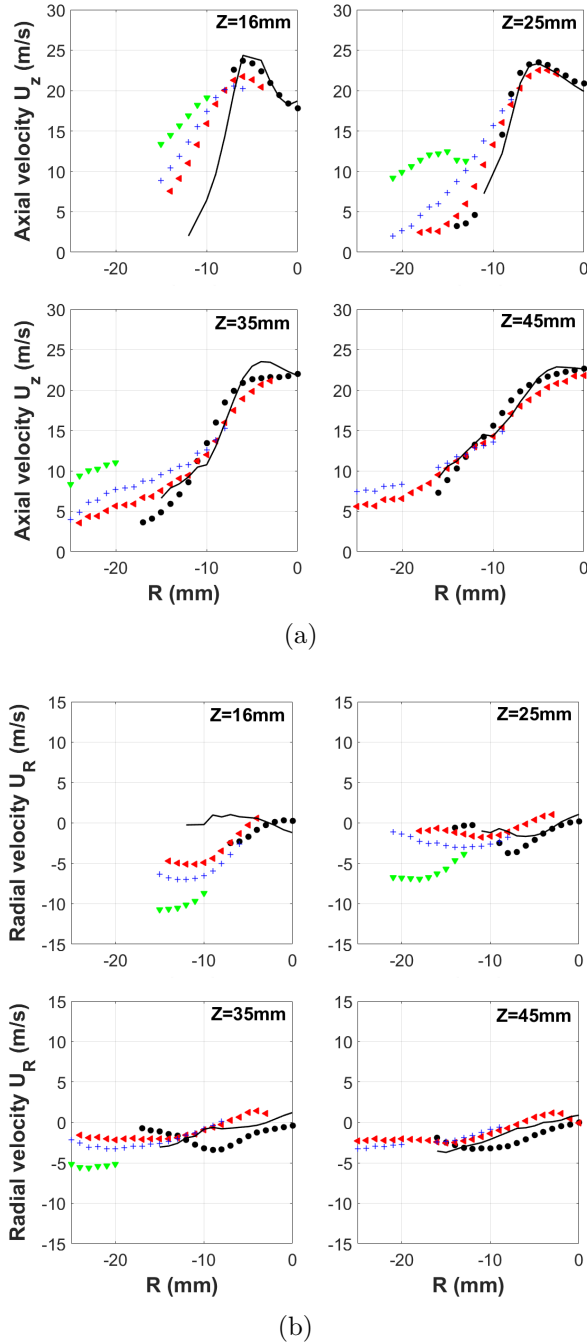
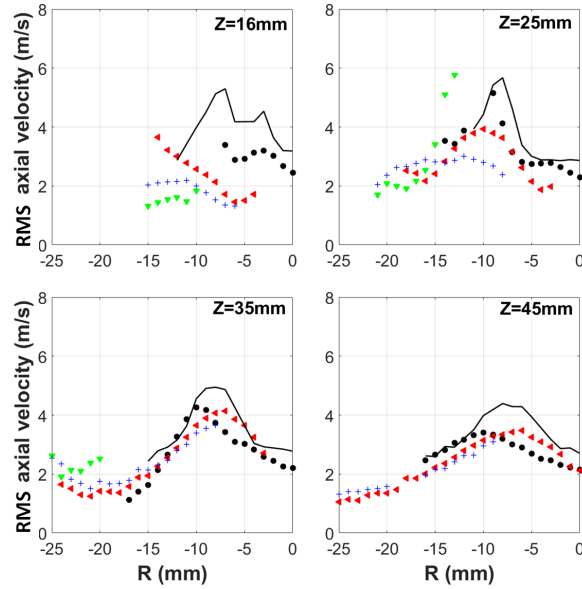


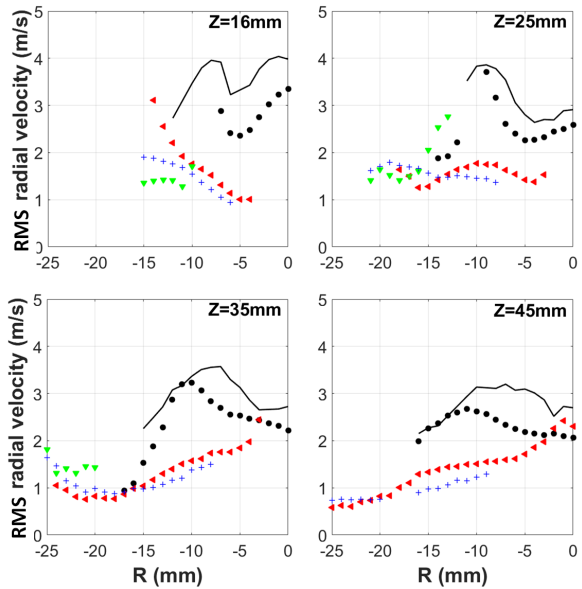
Figure 5.7: Mean components of fuel droplet velocity in reactive conditions separated in four size-classes obtained with PDA(B) configuration. \circ represent the $[0 - 10] \mu m$ group, \triangleleft the $[20 - 30] \mu m$ group, $+$ the $[30 - 40] \mu m$ and ∇ represent the $[50 - 60] \mu m$. Black lines represent the Air velocities profiles. (a) Axial velocity. (b) Radial velocity

in the spray and the aerodynamics. An acceptable convergence value is reached for every position in the spray for a minimum of 500 droplets. Fig. 5.7(b) shows that droplets are ejected from the nozzle with strong radial velocities. At the first axial station, the three groups have important radial velocities ($\approx 10 m.s^{-1}$) but farther downstream small droplets adapt their velocity to the airflow. Big droplets follow more ballistic trajectories

and continue to present radial centrifugal velocities until $Z = 35 \text{ mm}$. When overlapped to the air stream, droplet axial mean velocities are smaller for the spray than for the air, and consequently, small droplets are strongly accelerated by the co-flow while big droplets continue flying at smaller velocities until farther downstream. When fuel droplets exit the high air velocity region, they find a quiescent area where they can decelerate.



(a)



(b)

Figure 5.8: RMS of fuel droplet velocity in reactive conditions separated in four size-classes obtained with PDA(B) configuration. \circ represent the $[0 - 10] \mu\text{m}$ group, \triangleleft the $[20 - 30] \mu\text{m}$ group, $+$ the $[30 - 40] \mu\text{m}$ and ∇ represent the $[50 - 60] \mu\text{m}$. Black lines represent the Air velocities profiles. (a) RMS of axial velocity. (b) RMS of radial velocity

Concerning the velocity fluctuations, (Fig. 5.8), small droplets are more affected by the

shear layer and the coherent structures generated by the air co-flow turbulence. Near the radial station $X = 10 \text{ mm}$, in the region where the turbulent kinetic energy is maximum and for axial stations where large turbulent scales are fully developed, the RMS for radial velocities is maximum.

Mean fuel droplet temperature evolution

In the following, the C-GRT results are discussed in order to obtain a preliminary analysis of the spatial distribution of the mean fuel droplet temperature. Figure 5.9 (a) shows the radial evolution of mean temperature for different axial locations. Each dot corresponds to an average temperature obtained from 400 recordings with a camera aperture time of 400 ms . This temperature map can be analyzed according to 3 different zones. In the mixing zones (A), C-GRT results indicate that the liquid fuel droplet temperature is close to the fuel injection temperature, and decreases from 298 K to 284 K along the centerline axis ($X = 0 \text{ mm}$), and from 298 K to 279 K for a radial profile ($Z = 20 \text{ mm}$) below the flame stabilization point (5.9 (b)). This cooling effect comes from fuel droplet evaporation that occurs in a relatively long time as it was shown in [46,47] and can be attributed to the low level of turbulence intensity in these zones. It is worth noting that these kind of cooling profiles have already been observed on a same fuel atomizer by performing multi-band LIF thermometry on fuel droplets [104]. In the region between the two reaction zones (Zone C), the mean temperature is constant and equal to $331 \pm 2 \text{ K}$. This equilibrium temperature corresponds to the wet-bulb temperature of n-heptane in these conditions. A similar value was also obtained by Letty et al. [16] for the same fuel, but for a different flame geometry. This temperature is clearly below the boiling temperature ($T_b = 370 \text{ K}$), as it has also been reported by [105] for acetone droplets in a reacting stream. Close to IRZ, the mean temperature profile shows a sudden rise in temperature across the mean flame brush represented by the mean progress variable.

5.3 Flame structure

The local properties have just been defined, we will now describe the flame structures found in our configuration.

5.3.1 Inner Reaction Zone (IRZ)

Instantaneous snapshots of OH-PLIF at 10 Hz in a vertical cross section are reported in Fig. 5.10 and illustrates the Inner Reaction Zone topology. The IRZ structure is strongly wrinkled and located along the shear layer created by the air co-flow discharging into the ambient air. Additionally, the inner reaction zone is characterized by a strong OH gradient indicating that combustion occurs in a partially premixed regime with a

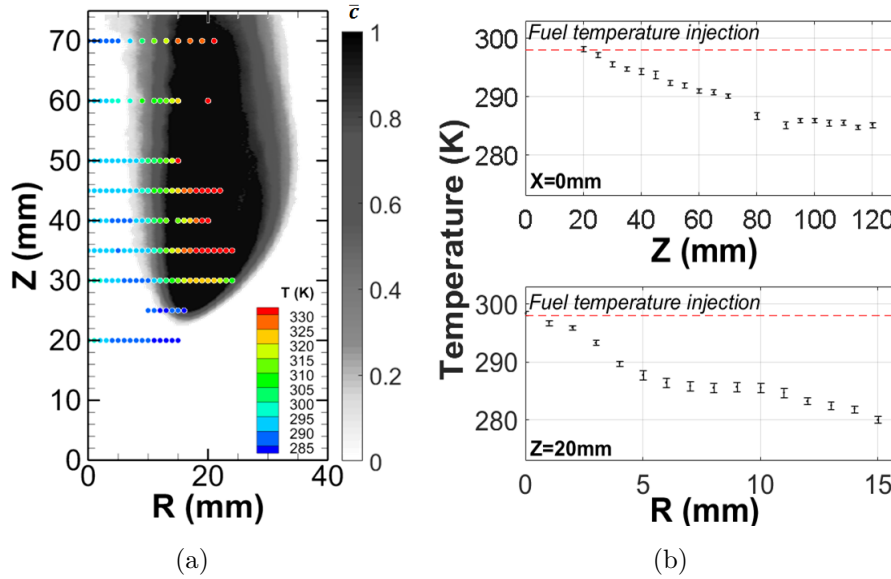


Figure 5.9: (a) Evolution of mean droplet temperature and mean progress variable maps \bar{c} (b) Axial and radial profiles of mean temperature in the mixing zone below the stabilization point (bottom) and along the centerline axis (top). The errors bars indicate the RMS of measurement.

flame propagation mechanism [18]. In the central part of the spray (Zone A), the mixing between small droplets ($D_{10} < 20 \mu m$) and the air co-flow generates a very lean region below the flammability limit ($\phi = 0.58$ [18]) of *n*-heptane in these conditions. The radial position of the *IRZ* corresponds to a region where the local equivalence ratio is slightly higher than along the centerline ($R = 0$ mm) due to the presence of larger droplets when R is increasing. The *IRZ* is then located in a very lean region of the flow and submitted to strong velocity fluctuations. Consequently, the *IRZ* is strongly disturbed (momentum and mass transfer) and wrinkled by local velocity gradients and frequent events of transient phenomena such as local extinctions are observed. These local extinctions are illustrated by holes in OH-PLIF video given as supplementary material 2 and will be investigated in more details in the following section.

5.3.2 Outer Reaction Zone (ORZ)

Fig. 5.10 displays some instantaneous images of OH radical obtained by OH-PLIF at low repetition rate [17]. Fuel droplets both in non-reactive zones (spray exit, mixing zone) and in reactive zones (zones C and ORZ) can be easily identified by Mie scattering during the acquisition. The ballistic trajectories of large inertial droplets lead to have droplets in zone C, where the high temperature implies to increase the evaporation rate and to generate a gaseous fuel reservoir. Despite there are few big droplets ($D_{10} > 30 \mu m$) coming to the outer region of the spray, the droplet evaporation rate implies the production of fuel vapor until reaching an equivalence ratio higher than $\phi = 1.8$ [18]. Moreover, it was shown in

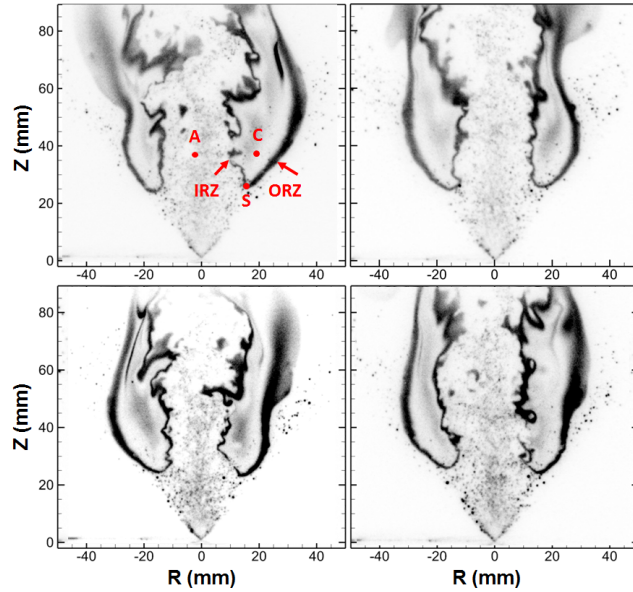


Figure 5.10: Selected images of OH-PLIF images at low repetition rate 10 Hz [17]

a similar configuration, studied by Ma et al. [106], that the CO formation (in zone C) comes from fuel thermal decomposition and incomplete hydrocarbon combustion. The chemical reactions occur during the incomplete hydrocarbon combustion, also produce CO_2 and H_2O , which implies to have the fuel mass fraction $Y_f < 1$ and mixture fraction $\xi_{st} < \xi < 1$ in zone C . The air entrainment is shown in Fig. 5.11(a), where streamlines are represented with the velocity magnitude. The streamlines are uniform far away from the air jet, and diverge close to the ORZ with a stagnation point located in average at $R = 37$ mm and $Z = 52$ mm. At this stagnation point, flow trajectories are separated: one move towards the leading edge and the second one towards the top of the flame. It is worth noting that the quiescent surrounding air is accelerated towards the air co-flow exit and reaches $1 \text{ m}\cdot\text{s}^{-1}$ just below the flame leading edge. The entrainment of the surrounding air reacts with the gaseous fuel reservoir in a diffusion-like outer flame front (ORZ), where a stoichiometric line is present and located between the rich (burned gases) and lean (fresh gases) sides. Compared to the IRZ , ORZ is less wrinkled, more stable, thicker, and characterized by a smoother OH gradient. Figure 5.11(b) summarizes the ORZ structure. The structure of this diffusion flame therefore depends on the ratios of molecular diffusion and chemistry time scales [107]. Then, any changes in local fuel composition (local mixture fraction) will modify the thickness of the mixing zone and the reaction rate.

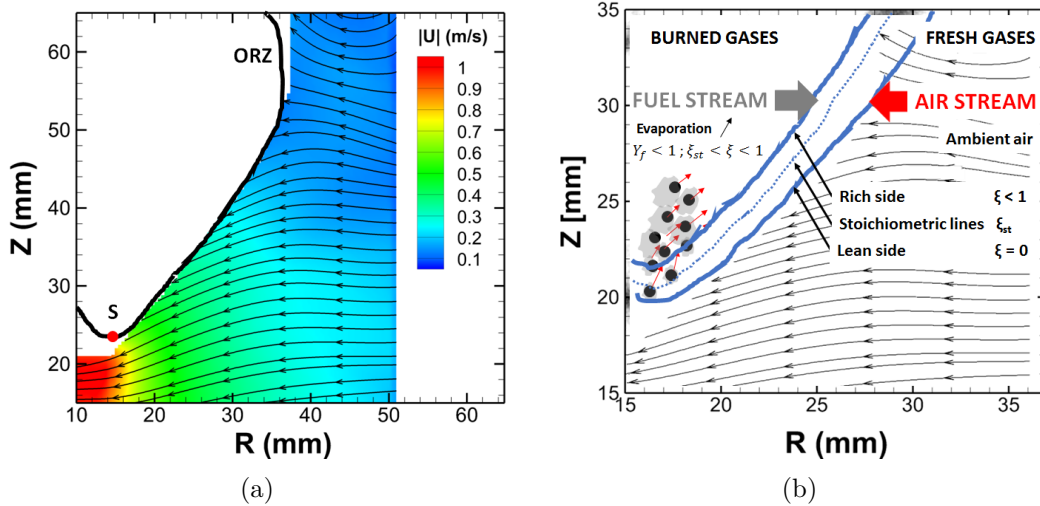


Figure 5.11: (a) Spatially averaged ORZ position (black lines obtained with OH-PLIF measurements) and air entrainment streamlines with the norm of velocity ($|U| = \sqrt{U^2 + V^2}$) obtained with HS-PIV-(B) configuration). (b) Schematic representation of ORZ : Generic structure of a laminar diffusion flame

5.4 Stabilization of the flame base

The mechanism for stabilizing a spray flame can be carried out in several ways. First the flame can be stabilized by a recirculating flow obtained by a rotating air inlet (air co-flow swirling). The hot gas recirculation ensures an activation of the reaction. Several works [6, 108, 109] study this type of flow, particularly in terms of the influence of the spray on the structure of the flame. Moreover, these studies provide a very complete database which allows a comparison with the numerical simulation and thus validate the different models. An other approach can be the stabilization by a pilot flame. In this configuration, the main flame is stabilized by a very small flame, called a "pilot flame", generally a gaseous and premixed flame, which continuously activates the reaction in the incoming cold fuel. Gounder et al. [31] recently studied the influence of fuel volatility, co-flow velocity, as well as the properties of drops as the diameter on an academic burner stabilized by a pilot flame. Finally, Marley et al. [25, 26] and Ge et al. [110] have studied a configuration in which the flame is lifted and stabilizes naturally in a non-recirculating flow. The authors have shown that in this configuration, the stabilization mechanisms are very sensitive to fluctuations in air co-flow velocity. These studies are close to our configuration and an analogy can be made with the stabilization mechanisms occur in a triple flame. Triple flames correspond to the stabilization zone of a diffusion flame between two parallel streams of cold oxidizer and fuel, initially separated by a splitter plate. The flame is stabilized in a flow when its propagation speed is able to be sustained by the local flow velocity [107]. However, the stabilization mechanisms of a lifted spray jet flame are very complex and are conditioned by the droplet convection-vaporization, the flow

aerodynamics and the chemical reaction budgets. For this specific operating condition, the flame is lifted and stabilized around $R = 15.5 + / - 3mm$ and $Z = 24 + / - 3mm$. Each square in Fig. 5.12 corresponds to the leading edge location extracted from the 500 OH-PLIF images.

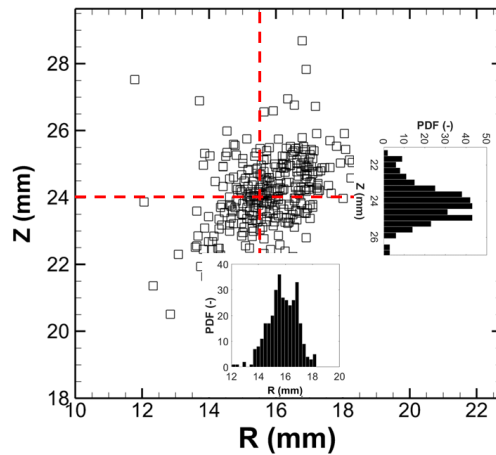


Figure 5.12: Positions of the flame base

This position presents a favorable condition to sustain a stable reaction: the turbulence is low and there is enough fuel vapor available fed by the evaporation of large inertial droplets. This mechanism can be justified with the result obtained by Shum-Kivan et al [18] in a common paper presented in the last symposium of combustion. Indeed, the collaboration with the CERFACS laboratory allow to identify more precisely the stabilization mechanisms in a spray jet flame. Figure 5.13 shows an instantaneous field of gaseous equivalence ratio near the leading edge with an isocontour of zero flame displacement speed S_d defined as in [63]. The leading edge is positioned, where the exact balance between the turbulent burning velocity and the downstream convective velocity (zero flame displacement) is observed. Moreover, figure 5.13 suggests a strong correlation between the position of the leading edge and the gaseous equivalence ratio field. At the stabilization point (S), the gaseous equivalence ratio varies between 0.4 and 1.4 whereas 1 mm upstream (S'), the local mixture is clearly too lean to allow the flame propagation.

5.5 Fuel droplets temperature conditioned by the distance to the flame front

In order to go further in the analysis of the fuel droplet temperature behavior near the inner reaction zone and of droplet/flame front interactions, the I-GRT and OH-PLIF techniques are coupled together. Therefore, simultaneous and instantaneous measurements of flame front structure and fuel droplet temperature are provided.

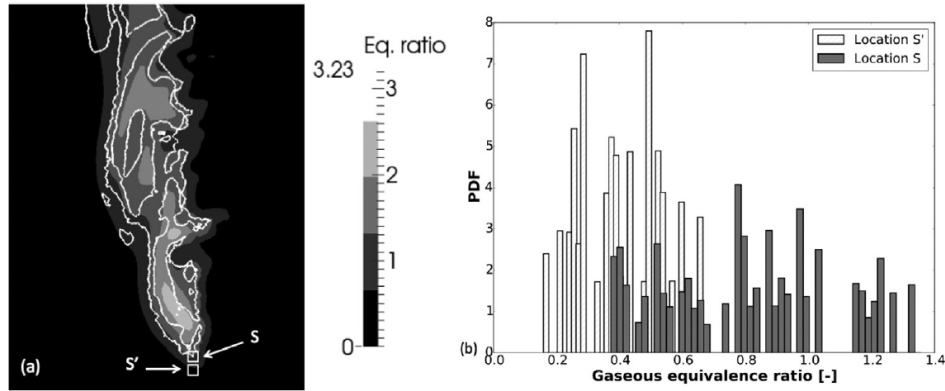


Figure 5.13: Right: Instantaneous field of gaseous equivalence ratio with an isocontour of zero flame displacement speed in a vertical cut, obtained from LES. Left: PDF of gaseous equivalence ratio at two locations (S) and (S'), from LES [18].

The validation of this technique is done by a direct comparison with the C-GRT results. First, in order to validate the I-GRT technique, the I-GRT measurements are averaged over 100 instantaneous recordings, and directly compared to the data obtained by C-GRT (Fig. 5.14). A very good agreement is found for all the radial positions in fresh gases, in flame flapping zone or in burnt gases and especially for the regions far from the mean inner reaction zone, which demonstrates the performance of the I-GRT technique and the robustness of the inversion method.

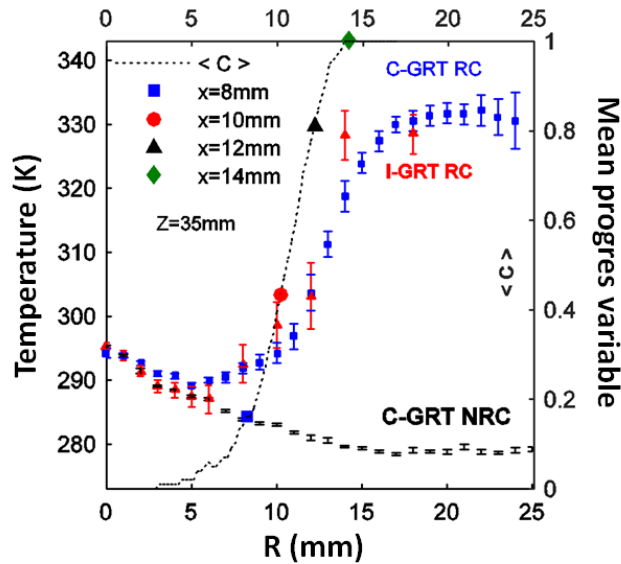


Figure 5.14: Radial profiles of the mean temperature obtained by C-GRT for the non-reactive case (black) and for the reactive case (blue squares) across the flame front at $Z=35$ mm. For comparison, the mean temperature obtained by averaging instantaneous measurements by I-GRT is also reported (red triangles). The errors bars indicate the RMS of measurement.

In a second step, the results are analyzed along a radial profile ($Z = 35$ mm), and

the mean fuel droplet temperature conditioned by the distance (d_f) between the probe volume of GRT and the flame front is reported in figure 5.15.

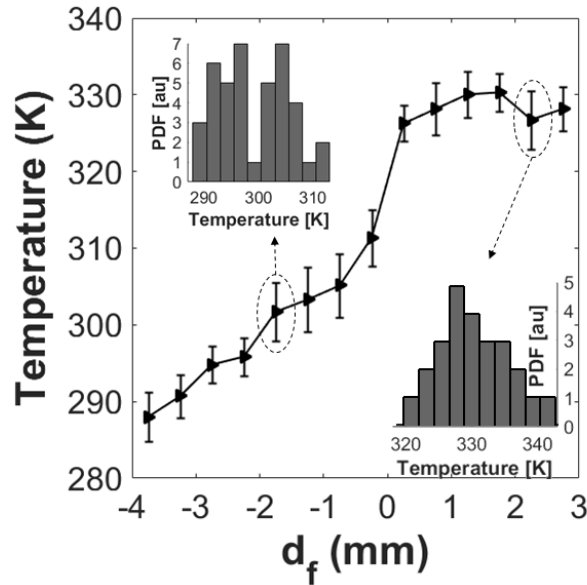


Figure 5.15: Mean droplet temperature conditioned by the distance to the flame front along the axial position $Z=35$ mm and associated PDF of temperature. The error bar indicates the RMS of the distribution.

The specific value $d_f=0$ represents the position of the instantaneous flame front, whereas the negative and positive values of d_f concern the fresh and burnt gases, respectively. 1000 instantaneous rainbow images are recorded for each of the 4 radial positions indicated in Fig. 5.15 across the mean inner reaction zone ($X=8, 10, 12$ and 14 mm). Each triangle in 5.15 results from data conditioning from all these 4 radial positions. The bin width is fixed to 0.5 mm and it is equal to the spatial resolution of the I-GRT in the OH-PLIF plane. Since temperature measurements are taken in the space referential of the flame, figure 5.15 shows a much steeper gradient across the flame front. The temperature of fuel droplets in the burnt gases remains constant even for small distances d_f meaning that the fuel droplets reach the wet-bulb temperature very quickly and, thus, validate the assumption made previously concerning the temperature homogeneity within the fuel droplet for GRT measurements. In the fresh gases, a slight increase of the temperature is observed when reducing the distance d_f . For these locations, the probability density function (PDF) of fuel droplet temperature is rather bimodal, indicating the existence of cold and of heated-up droplets. An additional conditioning can be done by considering not only the distance to the flame front, but also the radial location of the measurement volume (figure 5.16). Indeed, in the fresh gases and near the flame front, the fuel droplet temperatures are different for each radial station at a constant distance d_f . This can be illustrated for the distance $d_f = -1.75$ mm, where the mean temperature is equal to 297 K and 305 K when the measurement volume is located at $X=10$ mm and $X=12$ mm,

respectively. Indeed, for the same distance to the flame front, the droplet temperature is different according to the “origin and history” of the droplets.

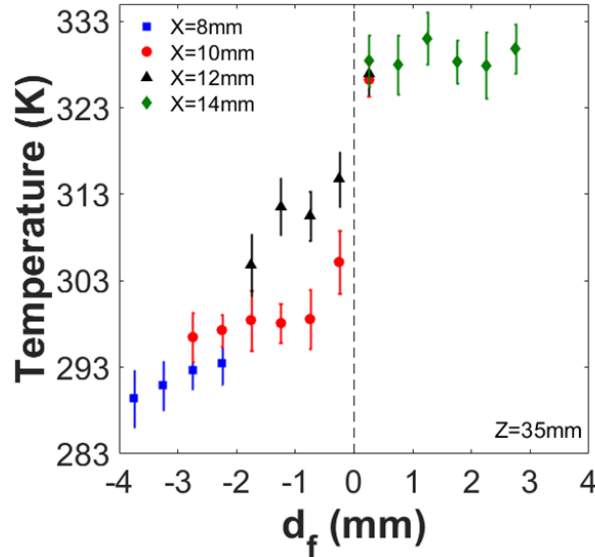


Figure 5.16: Mean droplet temperature conditioned by the distance to the flame front along the axial position $Z=35$ mm, for different radial measurement positions ($X=8$, 10, 12 and 14 mm).

For each measurement in the burnt gases ($d_f > 0$), the droplet temperature is constant and equal to 331 ± 2 K. Even for different absolute positions of the measurement volume, the same temperature is reached after the droplets have crossed the flame front. For negative distances to the flame front in figure 5.16, different plateaus associated to different mean droplet diameters (5.5) are observed, grouping the different temperature measurements for each absolute position of the measurement volume. This means that there is a higher probability to find hot droplets within the measurement volume at greater radial positions (closer to the mean flame) even for the same relative distance from the measurement volume to the instantaneous flame front. Nevertheless, these temperature measurements are product of an integration of the contributions of all droplets contained in the instantaneous measurement volume (cold and hot droplets). Indeed, due to the turbulent movement of the inner reaction zone, some droplets that are seen in the measurement volume may have already crossed the flame front at a lower axial location, entering and exiting the hot region (5.17). In this experimental configuration, the diameter, the velocity and the trajectory of droplets depend on their position in the spray. This means that for each absolute position of the measurement volume, the droplets have personal characteristics and a personal history. This interpretation clearly shows that the origin of droplets and their history are a key parameter to determine the fuel droplets temperature as a function of instantaneous flame front distance.

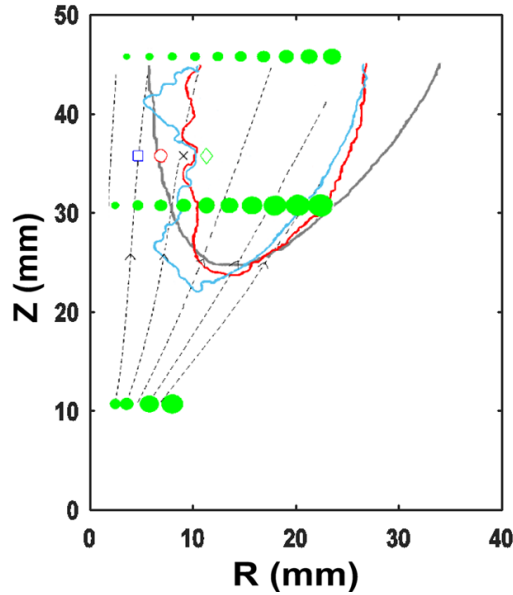


Figure 5.17: Radial evolution of mean droplet diameter (green circles) at different axial stations and their mean trajectory for reactive condition (dashed line). Two instantaneous flame front are plotted (red and blue lines) with the averaged progress variable $\langle \bar{c} \rangle = 0.5$ (gray line).

5.6 Conclusion

The lifted spray flame features a double reaction zone structure, with an inner, lean premixed flame mostly fed by small droplets concentrating in the center region, and an outer diffusion flame burning the fuel vapor produced by the larger droplet evaporation in the burnt gas region between the two flames with the surrounding air. This fuel vapor also feeds a secondary diffusion flame, located very close to the inner premixed flame and burning the remaining oxidizer. A close look at the flame base shows that it is located around stoichiometric conditions, ie., where the flame speed is fastest. Flame stabilization is therefore driven to first order by the droplet spatial distribution and their evaporation rate. The fuel droplet temperature is first analyzed by Continuous Global Rainbow Refractometry (C-GRT), which provides quantitative measurements in mixing and reactive zones. In the mixing zone, the fuel droplet temperature decreases to a lower equilibrium temperature close to 284 K along the centerline. Between the two reaction zones, the evaporation process occurs at an equilibrium temperature (331 K) lower than the fuel boiling temperature. In a second step, I-GRT is coupled to OH-PLIF to provide a conditional averaged measurement of fuel droplet temperature by the relative position of the measurement volume to the flame front (d_f). The profile across the flame front presents a step gradient that allows distinguishing the temperature of droplets situated in the burnt gases and in the fresh gases. The present results reveal a bimodal shape of the fuel temperature distribution close to the flame front. This is mainly due to the contribution of droplets located in fresh gases as well as the contribution of

droplets that could have already crossed the flame front. One of the fundamental aspects to consider in turbulent two-phase combustion is the strong interactions between the chemical reactions, the turbulence and the droplets, which occur during the evaporation and combustion processes. Indeed, the simulation of these configurations is a complex task since it requires at least an accurate prediction of the fuel vapor, directly obtained through the evaporation model, and a detailed description of the combustion reactions able to predict the different modes of combustion [111]. This chapter is a preliminary description of the different zones of the Jet Spray Flame and it illustrates the strong interactions between large inertial droplets and the leading edge revealing also some local extinctions in the IRZ and on the flame leading edge. The timescale for turbulence and chemistry are very small and require accurate experimental data through high-speed measurements in order to analyze the transient phenomena that occur in a spray jet flame. This is the subject of the chapter6.

Chapter 6

Flame dynamics and local extinctions

Contents

6.1	Position of local extinctions	102
6.2	Analysis of joint measurements of HS-OH-PLIF and HS-PIV	103
6.2.1	Flame-turbulence interactions	103
6.2.2	Droplet-flame interactions	107
6.3	Conclusion	109

We were able to show in previous chapters (1,2,5), that the typical double flame structure is very complex and depends on the local properties of the dispersed and carrier phases. The chapter 1 demonstrates that although numerical simulation is a valuable tool to tackle these different interactions between liquid and gas phases, the method needs to be validated through reliable experimental studies. With the improvement of the high repetition rates, high speed diagnostics can resolve temporarily the scalars in turbulent flows. These efforts have yielded a greater understanding of the turbulent flame dynamics by tracking the temporal evolution of transient phenomena such as local extinction, auto-ignition and turbulence-chemistry interactions [?, 78, 112, 113]. However, an insight on the mechanisms that control the flame dynamics and the transient phenomena such as extinction or re-ignition in two-phase flows is still under progress due to the measurements complexity in spray combustion. Despite the recent works on the application of high speed diagnostics in spray combustion [6, 103], accurate experimental data on transient phenomena such as local extinction mechanisms in real and representative two-phase flow configurations are still challenging. In the current chapter, the CRSB database is improved with temporal and spatial measurements of the flame front and its associated velocity field. The focus is placed on the transient phenomena that occur in a spray jet flame and, in particular, on the mechanisms governing the local extinctions. The objective

of this chapter is to extend experimentally the knowledge of turbulence-flame interactions and droplet-flame interactions by combining two high-speed optical diagnostics. Special attention is given to the investigation of local flame perturbation due to the large inertial droplets.

6.1 Position of local extinctions

Along this study, OH-PLIF signal is used as a marker of the reaction zones since disruptions in continuous OH fronts correlate well with local flame front extinctions [114]. Here, the different zones of local flame extinction are marked in Figure 6.1 where they are superimposed with the mean OH-PLIF image. These markers represent the position (R, Z) of local flame extinction appearance extracted from time series of HS-OH-PLIF images. One can notice three different zones of local extinctions associated with three different flame structures. First, local flame extinctions are observed in the *IRZ* (red deltas) in axial regions from $R = 10$ and $R = 15$ mm for different heights above 27 mm. These local extinctions occurs the most frequently in a region where the lean partially vaporized premixed flame front is submitted to intense local strain. Occasionally, some local extinctions occur close to the flame leading edge (blue triangles). This zone is characterized by large droplets ($D_{10} > 30 \mu m$) with a mean velocity equal to $10 m.s^{-1}$. At this location, the local turbulence intensity is moderate, and the extinction is therefore mainly controlled by droplets-flame interactions. The third zone concerns the *ORZ*, where the large initial droplets expelled from the pressure injector cross the flame leading edge and are still present when they interact with the *ORZ*. The perturbations between large droplets and *ORZ* (which are not extinctions) are observed in the green delimited region in Fig. 6.1.

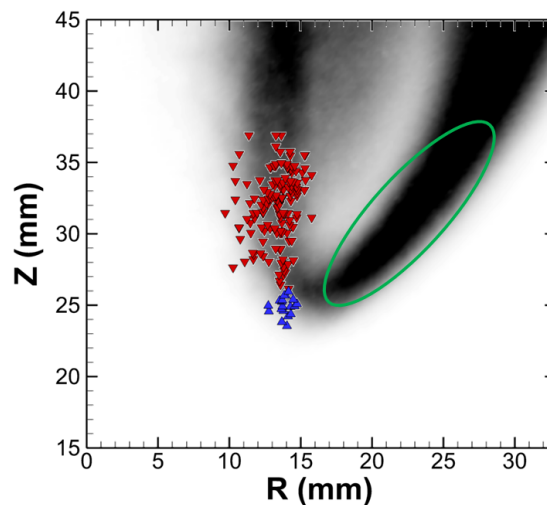


Figure 6.1: Mean OH-PLIF with extinction points

In summary, three regions of transient phenomena are observed in the spray jet flame and defined here for subsequent analysis with more details:

- (i) Extinctions in the IRZ far away from the flame leading edge: flame-turbulence interactions.
- (ii) Extinctions in the IRZ close to the flame leading edge: droplets-flame interactions.
- (iii) Perturbations in the ORZ: droplets-flame interactions.

6.2 Analysis of joint measurements of HS-OH-PLIF and HS-PIV

6.2.1 Flame-turbulence interactions

Figure 6.2 presents a sequence of flame extinction in the *IRZ* illustrated by OH-PLIF images superimposed with the corresponding velocity fields obtained by HS-PIV. Note that the velocity vectors are overlaid with the instantaneous strain rate of flow and computed as $\sigma = (\sum E_{ij}^2)^{\frac{1}{2}}$, where E_{ij} is estimated by $E_{ij} = \frac{1}{2}(\partial_j v_i + \partial_i v_j)$, the 2D strain rate tensor. The maximum value of σ is around 5000 s^{-1} and appears intermittently in the flow region interacting with the *IRZ*. These large scales of velocity fluctuations are created by the velocity gradients in the shear layer between the co-flow and the ambient air (Supplementary Materials, SM2). Figure 6.2 highlights that the flame front thinning and wrinkling are caused by a high strain rate ($\sigma > 5000 \text{ s}^{-1}$) in *IRZ* region. From $t = 0.0 \text{ ms}$ to $t = 0.8 \text{ ms}$ the OH signal in the flame front becomes thinner and thinner. The extinction event is observed on the HS-OH-PLIF images at $t = 0.8 \text{ ms}$, which correspond to a position $R = 12 \text{ mm}$ and $Z = 35 \text{ mm}$. The local extinction seems to appear when the flame front is too fine to support a high stretch rate. Then, with the local extinction in the *IRZ*, a gap is produced and causes a hole separating the inner flame front in two reaction zones. The hole and the local *IRZ* are convected downstream due to the mean air velocity field. The hole propagation rate is not constant and depends on the local turbulent flow. Note that with these operating conditions (air: 6 g.s^{-1} ; fuel: 0.28 g.s^{-1}) a local extinction in the *IRZ* cannot cause a global extinction of the flame.

Figure 6.3 presents a schematic representation of the turbulence-flame interactions in the *IRZ*. Close to the injector when the co-flow is discharging in the quiescent air, large coherent and intense turbulence structures are created by the mean velocity gradient. They are large enough to go far out into the co-flow and into zone (*C*) and then to induce a strong large scale mixing between fuel droplets, vapor and air. Then, this local heterogeneous and turbulent mixture interacts with the reaction zone and disturb the flame front by wrinkling processes. In the hot region close to the *IRZ* the kinematic viscosity changes approximately by a factor of 20 from fresh to burned gases. Even if the flow is laminarized by the higher viscosity close to the *IRZ*, the flame is disturbed by the

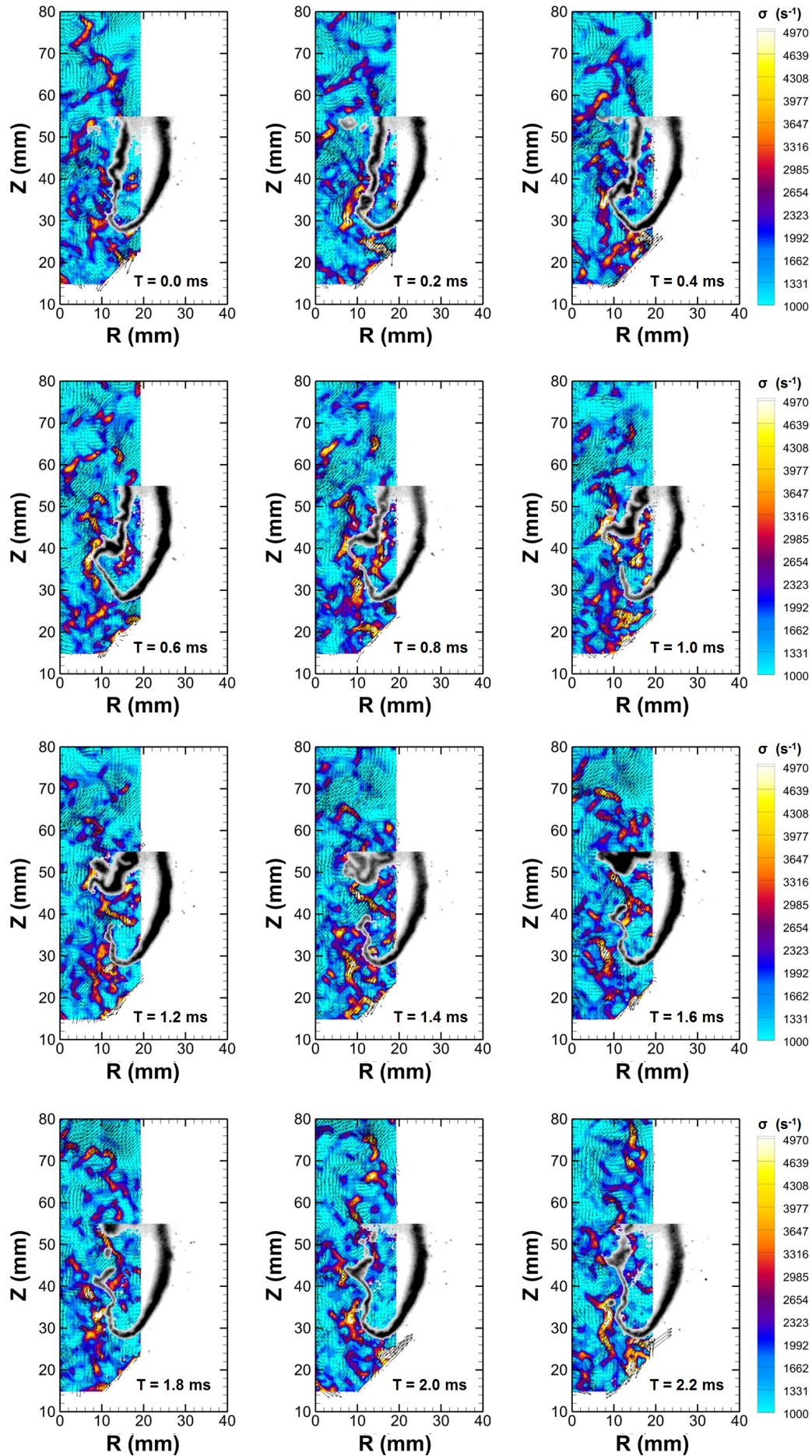


Figure 6.2: HS-OH-PLIF series images overlaid with the fluctuation velocity field and the strain rate (SM3)

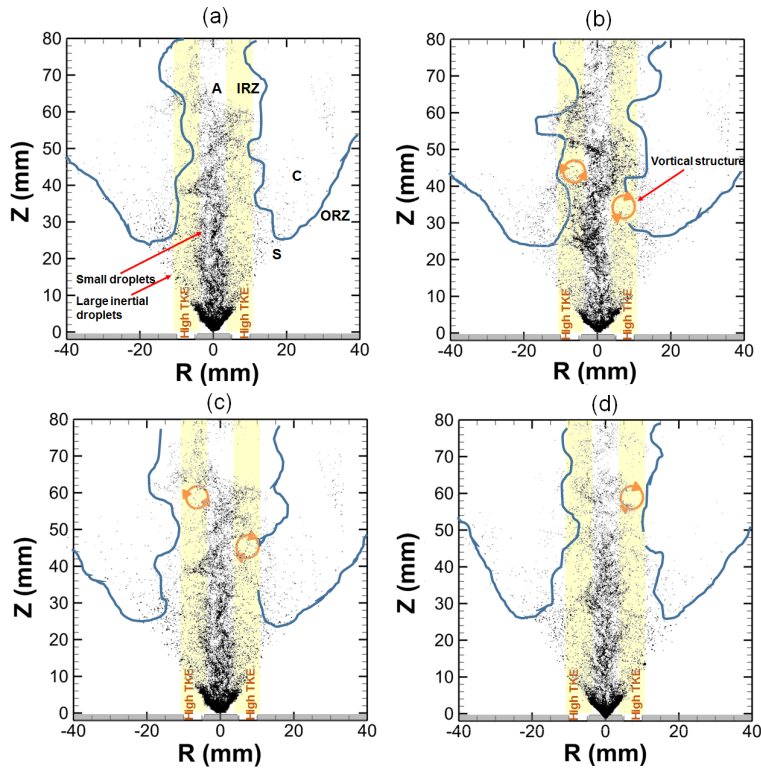


Figure 6.3: Schematic representation of the extinction mechanisms in the inner reaction zone.

flow aerodynamics. When local strain rate associated with local equivalence ratio exceeds a critical value, local flame extinction occurs and is convected downstream by the flow field. Indeed, recent study [115] demonstrates that during flame-vortex interactions, the flame can locally extinguish when the flow exceed a critical extinction strain rate. The main difference with local extinction with gaseous flames [116, 117] lies on the presence of small fuel droplets near the reaction zone which can enhance fuel heterogeneities or quickly evaporate when crossing the flame front. Franzelli et al. [118] has shown that local extinctions occurring in spray jet flame may also be induced by local fuel depletion.

To validate the strong aerodynamic effect on local extinction mechanisms in the IRZ, caused by local velocity gradients and lean mixtures, an extinction frequency analysis is applied to different HS-OH-PLIF measurements. An analysis region with a probe located in the mixing region in the vicinity of the reaction zone ($R = 14 \text{ mm}$ and $Z = 30 \text{ mm}$) is used to determine the temporal apparition of extinctions. In Fig. 6.4(a), Df represents the distance between the probe and the flame front position, extracted from OH-PLIF images by the data processing explained in Appendix. The specific value $Df = 0$ corresponds to the position of the instantaneous flame front when the IRZ is located at the same position as the probe, whereas the negative and positive values of Df imply a flame-probe distance located in the fresh and burnt gases, respectively. The values of $Df > 10 \text{ mm}$ correspond to the distance between the probe and the ORZ. This

occurs when there is a local extinction in the IRZ. The temporal evolution of Df has a so-called telegraphic shape, alternating $Df > 10 \text{ mm}$ and $Df \simeq 0 \text{ mm}$ values. The power spectral density function (PSD) of the temporal evolutions of Df are reported in Fig. 6.4(b). A strong peak around 80 Hz is clearly visible, repeatable, indicating periodic flame extinction phenomenon. These measurements have been performed three times separated by several weeks. It can be observed that for the red and blue lines, the PSD show a strong peak around 80 Hz whereas for the third acquisition (green) a peak at around 80 Hz is still observed but with a more broadened shape.

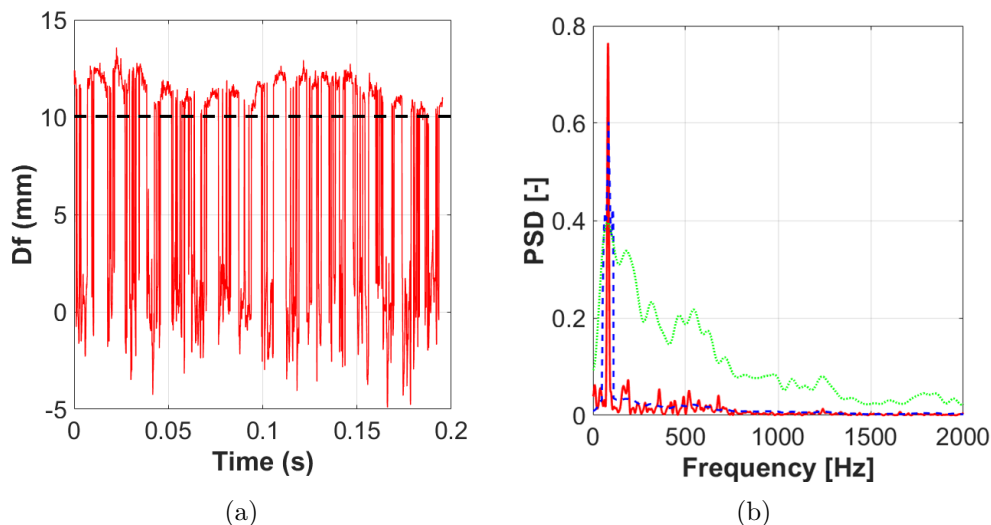


Figure 6.4: Profile at $R = 16 \text{ mm}$ and $Z = 30 \text{ mm}$. (a) Extinction occurrence temporal analysis. (b) Extinction occurrence frequency analysis

The frequency analysis of the large-scales of turbulence seems relevant for the understanding of the extinction mechanisms and it is now discussed. From high-speed PIV measurements, a temporal velocity signal is extracted at $R = 13 \text{ mm}$ and $Z = 30 \text{ mm}$ located in the shear layer (region A). The integral of the auto-correlation function of these velocity fluctuations is then determined and is equal to 12.2 ms. The latter represents the temporal integral length scale of the turbulence at this location, where local flame extinctions occur. It represents a measurement of the longest time that the velocity fluctuation remains autocorrelated being, hence, representative of coherent large structures in the flow. In this case it is equivalent to a frequency of 82 Hz. This value is similar to the flame extinction occurrence underlying that flame extinction in IRZ is mainly controlled by flame/turbulence interactions. Indeed, in the mixing zone of the flame (zone A), the lean mixture is very close to the flammability limit [18] and the local flame strain rate induced by the large structures of the shear layer will exceed locally and periodically the extinction strain rate of the IRZ.

6.2.2 Droplet-flame interactions

Extinctions in the leading edge

As already seen in the previous section, the small droplets mainly stay in the cold central zone, where they evaporate slowly and never cross the flame front. On the contrary, large inertial droplets ($D_{10} > 30 \mu m$) move to the external part of the spray crossing the flame base and reaching the hot region. Figure 6.5 presents a local extinction event in the leading edge caused by a large droplets. At $t = 0.2$ ms, a large droplet (yellow circle) crosses the leading edge. 0.1 ms after, a hole is produced corresponding to a local flame extinction.

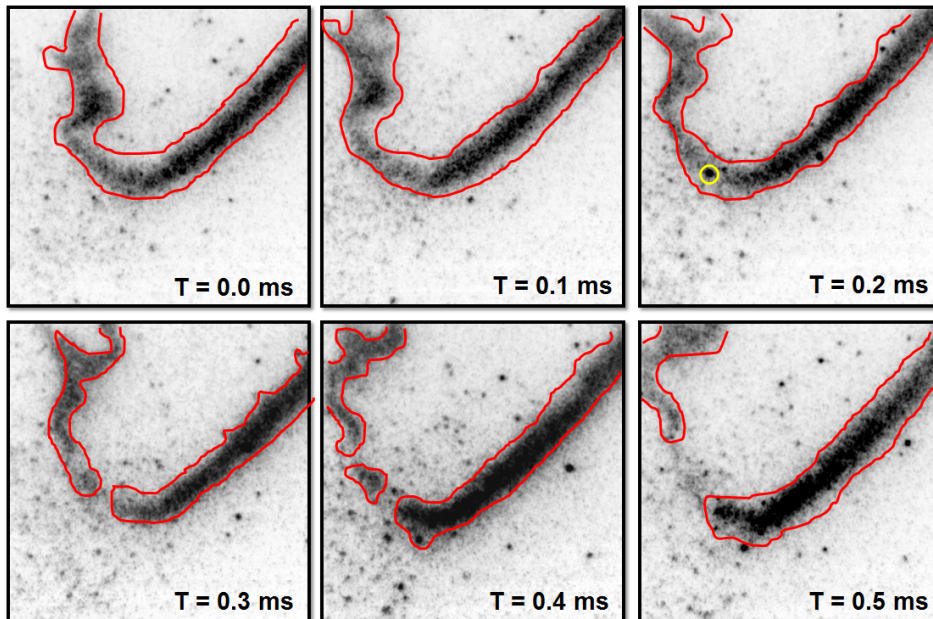


Figure 6.5: HS-OH-PLIF images - time separation = 0.1 ms. Extinction in the leading edge due to the droplet-flame interactions.

Previous numerical studies [119, 120] suggest that the droplet-flame interaction mechanisms, in a partially premixed flame, should be related to a thermal disturbance and to a modification of the local mixture. Indeed, Nakamura and Akamatsu [119] show that the energy exchange between droplets and gaseous phase may disturb the reaction rate. The temperature of droplets is much lower than of the gaseous phase, acting as a sink term for the chemical reactions. The intermittent passage of large droplets in the leading edge induces a locally high strain rate due to the droplet motion, which can reduce the reaction rate [121–123]. When crossing the flame, fuel droplet temperature increases up to a wet-bulb temperature [17], which remains lower than the fuel boiling temperature. In addition, the high burned gas temperature leads to a strong fuel evaporation rate and a large values of Y_f gas around the droplets. The local extinction in the leading edge can be explained by the droplet temperature in this region ($T_{droplet} \ll T_{flame}$) and the mixture around the droplet, which is very rich and outside the flammability limits.

Perturbations in the ORZ

Figure 6.6 presents HS-OH-PLIF images separated by 0.1 ms, where two big droplets (red circles) cross the zone C with a slip velocity of $\approx 7m.s^{-1}$. Further downstream, droplets that have survived the leading edge move towards the ORZ, where they disturb the flame front. Indeed, after the passage of the drops, a local perturbation located in the wake can be easily identified.

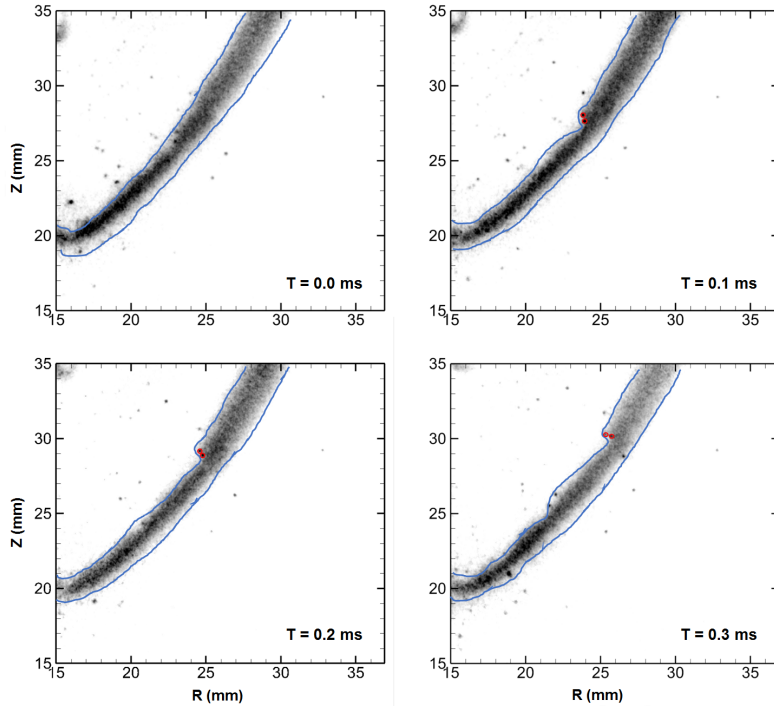


Figure 6.6: HS-OH-PLIF images - time separation = 0.1 ms. Perturbations in the outer reaction zone (ORZ) due to the droplet-flame interactions.

Figure 6.7(a) presents a schematic representation of the droplet-flame interaction. As described in the previous section, large droplets cross the leading edge and continue to evaporate in zone C . The strong thermal exchange leads to a fast evaporation regime resulting in an increase of the gaseous fuel mass fraction and, hence, a droplet diameter reduction. However, bigger droplets can reach until the ORZ and induce local perturbations in the reaction zone, as it can be seen in HS-OH-PLIF images (Fig. 6.6). Figure 6.7(b) shows the schematic evolution of radial profiles for the fuel and oxygen mass fractions and the temperature along the dashed line represented in Fig. 6.7(a). In the burned gases, zone C , a lot of species are present and imply gaseous fuel mass fraction $Y_f < 1$. However, close to the droplet, the pure fuel vapor generated by the evaporation leads to increase the fuel mass fraction until to reach $Y_f = 1$ near the liquid interface. The Y_f profile shows a strong negative gradient due to the diffusion of the pure fuel vapor towards the burned gases. The droplet evaporation decreases the surrounding temperature due

to the heat latent absorption. From the burned gases, the temperature decreases until to reach the wet-bulb temperature inside the droplet. Verdier et al. [17] have recently shown that the wet-bulb droplet temperature is around 330 K in zone *C*. The strong thermal exchange between the high surrounding temperature and the droplets leads to an increase of the gaseous fuel mass fraction around the droplets and a decrease of the temperature. This process generates interactions with the local location of the stoichiometric mixture fraction line. The droplet-flame mechanism in ORZ is related to a cooling effect (strong gradient between the droplet and the flame temperature $T_d \ll T_f$) and local increase of the mixture fraction around the droplet.

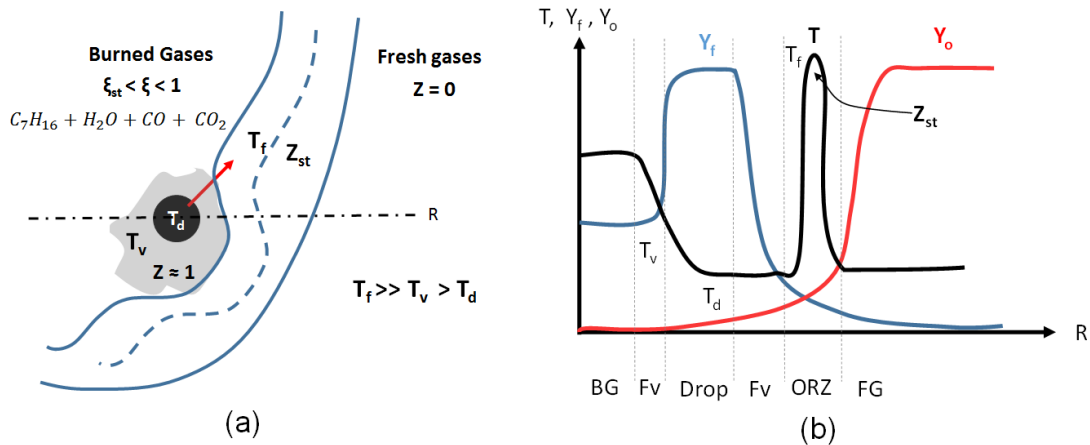


Figure 6.7: (a) Schematic representation of the droplet-flame interactions. (b) Schematic representation of a radial profile for the fuel and oxidant mass fraction and temperature in different regions. Burned Gases (BG), Fuel vapor (Fv), Drop, ORZ and Fresh Gases (FG) are respectively the burned gases, the fuel vapor, the droplet, the outer reaction zone and the fresh gases.

In most cases, the droplets disturb the flame front but no extinctions can be observed, compared to the premixed flame zone (IRZ). Furthermore, the perturbation time is shorter than the local extinction duration in IRZ. In the ORZ, the turbulence intensity is very low and combustion occurs in diffusion regime, which prevents the amplification of the perturbation caused by the droplets.

6.3 Conclusion

In this chapter, a detailed experimental study of turbulence-droplet-chemistry interaction events in an *n*-heptane spray jet flame has been presented. The sequences of the simultaneous high-speed measurements allow to follow the evolution of non-stationary and local extinction events with sufficient spatial and temporal resolution. The flame exhibits a double structure with inner and outer reaction zones, where fuel droplets are still present and interact with the reaction zones. Three different flame zones exhibit three

different mechanisms of droplet-turbulence-flame interactions. First, periodic local flame extinctions are observed in the IRZ downstream the leading edge for axial stations above $Z=27$ mm. These local extinctions occur in a region where the lean partially vaporized premixed flame front is submitted to intense local strain rate induced by the shear layer. This extinction mechanism is associated to flame-turbulence interactions since most of the small droplets within this region have been rapidly evaporated at the entrance of the reaction zone. The second mechanism is related to the droplet-chemistry interactions occurring at the flame leading edge and leading less frequently to local flame extinctions. Indeed, these zones are characterized by low turbulence intensities and the big droplets, which have a low temperature, act as a heat sink for the flame front, which finally extinguishes due to the cooling effect. Finally, the third mechanism is also associated to the droplet-flame interaction mechanism but occurring in the ORZ. The largest droplets flying to the ORZ evaporate quickly in the burnt gases region producing large amount of fuel vapor surrounding the droplet. They may interact with the diffusion flame front where a strong decrease of the OH is observed around the droplet during its trajectory. If no local extinction is observed, a strong modulation of OH signal indicate a local decrease of flame heat release.

Chapter 7

Comparisons Simulations / Experiments

Contents

7.1	Experimental and numerical analysis of a turbulent spray flame structure	113
7.1.1	Numerical setup	113
7.1.2	Non reacting case	116
7.1.3	Reacting case	119
7.1.4	Effect of the evaporation model and the chemistry	124
7.2	6th Workshop on measurement and computation of Turbu- lent Spray Combustion (TCS6)	125

Accurate modeling of spray combustion is currently one of the key issues in gas turbine simulations. The interaction between the turbulent flow, the fuel droplet dispersion and evaporation, and the heat released by combustion leads to complex flame structures [12], characterized by important mixture heterogeneity and various combustion modes, from fully premixed to purely diffusion regimes. This has been highlighted by Jenny et al. [124] that provide a recent review of computational model developments relevant for turbulent dilute spray combustion. The presence of droplets poses also a difficulty to experiments, although several classical and new techniques can perform accurate and reliable measurements. Many experimental works have been undertaken on spray flames, ranging from the simplest configuration of a single burning droplet to more complex spray burners. Experimental measurements can provide relevant databases that can be used for the understanding of the physical phenomena and for numerical models validation. However, only a partial understanding of these multiple interactions can be extracted experimentally and, thus, must be completed jointly with the numerical simulations. These joint approaches are efficient strategies and a so-called virtuous circle that can improve both

experimental and numerical tools, and the understanding of the coupled physical phenomena.

The main objective of this Chapter is to illustrate the interest of the joint analysis between numerical and experimental approach, in the framework of a Spray Jet Flame configuration. The added values of these joint studies can be summarized as follow:

- The first step of the joint approaches concerns the validation of the numerical simulation by a direct comparison with mean and RMS data (carrier and dispersed phases, flame structure, ...). This final comparison has a sense only if the boundary conditions are well characterized by the experiments in terms of spray angle, droplet size distribution, velocities, etc. The more accurate the boundary conditions, the more efficient the comparison. Through this comparison, all the sources of uncertainties from the experiments and from the simulations are taken into account simultaneously.
- The second step is associated to the improvement of the experimental set-up and optical diagnostics in the objective of LES model validation. Indeed, the results of step 1 can highlight some hard points and specific needs to improve the LES models. New set of experiments or new experimental configurations can be developed to bring these informations.
- The last step is related to the benefits that simulations can bring to the experiments. LES simulations can provide an extensive database in which most of the parameters are unaccessible to the experiments. Using all these data from experiments and simulations will improve the knowledge on the spray combustion. Moreover, in some cases, LES can call to question the experimental results, which is necessary to perform better experiments and obtain reliable experimental database.

This chapter is divided into two different parts that highlight the joint experimental and numerical analysis that have been made along the thesis according to efficient collaborations with different laboratories. The results of the collaboration with CERFACS is redrawn in the first part and corresponds to the content of a joint paper presented at the last Symposium of the Combustion Institute [18]. The second part of this chapter concerns a more general collaboration with different laboratories in the framework of the 6th Turbulent Spray Combustion workshop in which the CORIA Rouen Spray Burner (TCS6 2017) was a target test case.

7.1 Experimental and numerical analysis of a turbulent spray flame structure

This section presents a combined experimental and numerical study of the CORIA Rouen Spray Burner [18]. A quantitative comparison between Large Eddy Simulation (LES) coupled to Discrete Particle Simulation (DPS) for the dispersed phase confirms the capability of LES to reproduce the gaseous and liquid flow structure in both non-reacting and reacting cases with good accuracy. The lifted stabilized spray flame exhibits a complex shape due to interactions between turbulence, chemistry and evaporation. A detailed analysis shows that both partially-premixed and diffusion flames are present, depending on the capacity of droplets to evaporate. Furthermore, an attempt is made to identify the processes leading to two-phase flame stabilization. In addition to the content of the paper [18], the droplet temperature results are also described and compared.

7.1.1 Numerical setup

A numerical study is performed using LES of fully compressible, multi-species, reacting turbulent flows, together with Discrete Particle Simulation (DPS). Simulations are performed with the AVBP code, a massively parallel solver co-developed by CERFACS and IFPEN [125]. It solves the full compressible Navier Stokes equations on unstructured grids using explicit high order numerical schemes, here the two-step, 3^{rd} order in space and time Taylor-Galerkin scheme of [126]. Gas phase boundaries are treated according to the Navier Stokes Characteristic Boundary Conditions formalism [127].

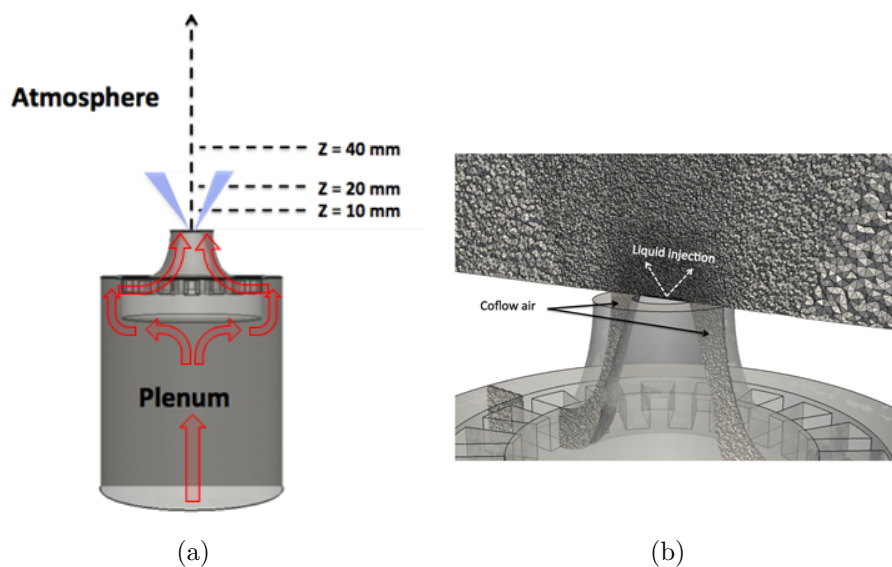


Figure 7.1: (a) View of the main part of the computational domain. (b) View of the mesh in a vertical cut.

Figure 7.1 shows the computational domain used for the simulation. It includes the inlet pipe, the plenum and the injection veins leading to a large cylindrical box ($R = 200$ mm and $Z = 300$ mm) representing the atmosphere. The obligation to put boundary conditions in the simulation requires to enlarge the domain, but increasing the number of cells involves a longer calculation time. To optimize the calculation time, the experimental result of air entrainment was useful to chose the good domain size. The geometry contains 53 millions tetrahedral cells corresponding to 9 millions nodes. It has a smallest cell size of 0.2 mm and is refined both in the near fuel injector region and in the zone where the opening jets are localized. The experimental results in terms of the flow aerodynamics allow us to refine in this critical region. Indeed, the annular air co-flow discharging into the ambient air creates a shear layer, which is important to capture the flame-turbulence interactions.

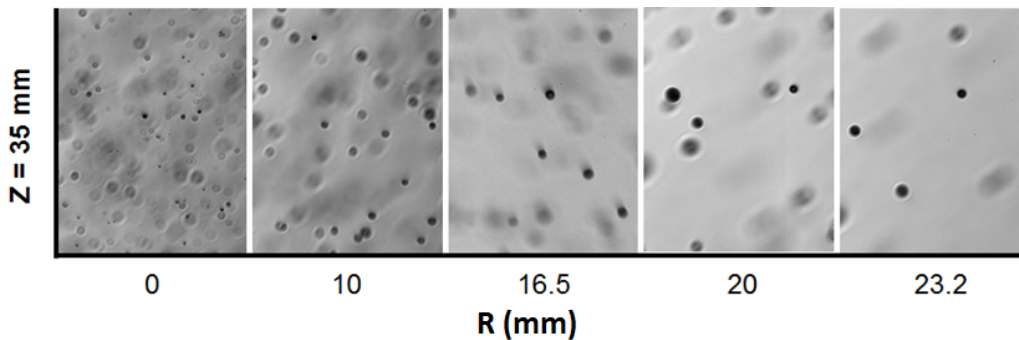


Figure 7.2: Shadowgraphy images for radial profile at $Z=35$ mm.

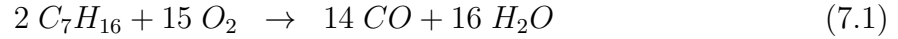
The PDA results give information about the droplet size distribution, which is essential for modeling the dispersed phase and liquid fuel injection. The small droplet size, in the range $1-60 \mu\text{m}$ enables to apply the point source approximation. The spray is also assumed sufficiently diluted, ie., with a volume fraction $\alpha_l < 0.01$, to neglect collisions. Indeed, the shadowgraphy images obtained experimentally show that spray can be considered as dilute (fig. 7.2). This figure illustrates the droplet concentration in a probe volume positioned at different radial stations for $Z = 35$ mm. Despite there are more droplets in the center, the spray can be considered as dilute. Furthermore, droplets are only subjected to Stokes drag force, other forces being negligible in this case, with drag coefficient obtained by the Schiller-Neumann correlation [128]. The evaporation model is the one proposed by Abramzon and Sirignano [53]. The two-way coupling between the liquid and the gaseous phase is ensured by a first order interpolation between the droplet location and the grid nodes.

Liquid injection is modeled using the Fuel Injection Method by Upstream Reconstruction (FIMUR) previously proposed by [129]. This method enables to circumvent the

atomization issue, which is still today out of reach in LES of complex two-phase reacting flows, by injecting an already formed spray with velocity and size distributions determined from global and geometrical characteristics of the injector. This model was successfully applied to several turbulent spray configurations, predicting spray velocity and size distributions in excellent agreement with experimental measurements downstream the injector [130]. Indeed, the characteristic diameter of the droplet distribution after primary and secondary break-up are needed. The experimental results are needed to put in data FIMUR. Strong exchanges with CERFACS were set-up to obtain and give the most appropriate initial conditions for the simulation. Indeed, it was important to keep in mind that FIMUR is a way to bypass the simulation of the atomization process. This implies that differences are unavoidable for heights close to the burner outlet. Indeed, the liquid sheet will not be simulated by the LES, which implies that during these first three millimeters the comparison will not be relevant. The limit of this model in reacting conditions comes from the fact that the evaporation of the drops will be faster for low axial heights for the simulation than for the experiment. Indeed, FIMUR injects drops at the exit of the burner which will experience a strong interaction with the co-flow of air. However, the LES today is forced to use this type of tool. It is therefore necessary to provide experimental results as close as possible to the burner outlet. In the following the parameters given by the experiments are expressed:

- The half spray angle: From spray images obtained by shadowgraphy and by the Mie scattering of the droplets with a green laser allow to extract the opening angle of the spray. To be consistent with the fact of the atomization is a chaotic process, an average of angle was performed on 20 images (shadowgraphy + Mie diffusion).
- The orifice radius is also a critical parameter in FIMUR and it was obtained from a microscope.
- The pressure drop coefficient was fixed by the CERFACS.
- The Rosin Rammler distribution is an important parameter injected in FIMUR and depends on the experimental results. In this spray configuration, a decrease on the PDA validation was observed below $Z = 10$ mm and it becomes unsatisfactory below $Z = 7$ mm in the dense region of the spray. To be consistent with the validation criteria, only the results for axial station equal to $Z = 10$ mm are used to built the Rosin Rammler distribution used in FIMUR.

The *n*-heptane oxidation chemistry is described by a two-step global scheme (*2S_C7H16_DP*) built in [9] using the same methodology as proposed in [131] to correctly reproduce the laminar flame speed and the adiabatic temperature for a wide range of operating conditions. It comprises six species and two reactions, the irreversible *n*-heptane oxidation into CO and the $CO - CO_2$ equilibrium (Eq.7.2).



Its validity has been assessed by comparison with a detailed mechanism [132] on a series of laminar premixed at ambient conditions. A very good agreement is obtained in the range $\phi = 0.4 - 1.5$ in terms of both laminar flame speed and adiabatic temperature, the mean relative errors being 3% and 4% respectively. The experimental OH-PLIF experiments are used to refine the mesh in the zone where the flame is present. This mesh refinement allows us to fully resolve the flame front and neglect the sub-grid scale wrinkling.

7.1.2 Non reacting case

Experimental and numerical non reacting two-phase flow results are first compared to assess the two-phase flow dynamics. The comparison is also used to prove the ability of the LES to predict the non reacting conditions of a complex spray.

Carrier phase:

Figure 7.3 shows the gaseous mean and root mean square (RMS) axial velocity profiles along the radial direction at three different distances from the injector ($Z = 10, 20$ and 40 mm). The agreement between LES and measurements is very good for the mean values (Fig. 7.3a). In particular, the double peak near the injector corresponding to the accelerated air coming from the co-flow, is well captured. Further downstream, the co-flow air jets merge to form a unique larger jet with a flat axial velocity profile. RMS values are also in good agreement (Fig. 7.3b) and are maximum in the mixing region of the jet, with a maximum intensity of 30%. Concerning the carrier phase, the mean and RMS velocities are perfectly predicted by the LES. There was no hard point for this comparison. Note that, the RMS values predicted by the LES are slightly lower than experimental results. In addition, it is important to note that the simulation provides information at the burner outlet that the experiment cannot obtain because of the presence of the liquid sheet. Indeed, the negative axial velocity at $R = 0$ mm shows the existence of a small recirculation zone just behind the injector.

The air injection system generates radial velocities (7.4), approximately 10 times smaller than the axial velocities at $Z = 10$ mm, and rapidly decreasing down to zero at $Z = 40$ mm. The agreement between simulation and experiment is again very good for both the mean and RMS values. Note that contrary to the mean values, the fluctuations of the radial and axial velocity are of the same order of magnitude, as they both result from the turbulence generated by the air jet.

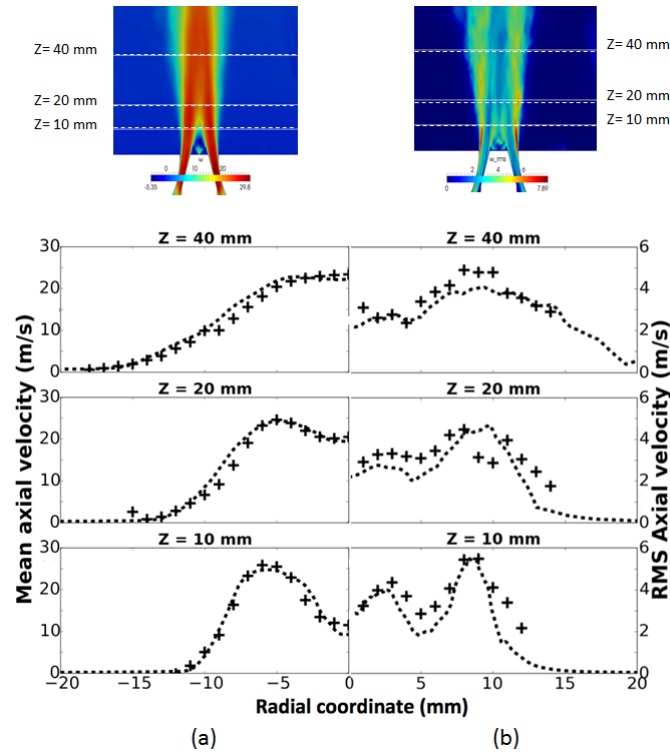


Figure 7.3: Radial profiles of (a) mean axial velocity and (b) RMS axial velocity at $Z = 10, 20$ and 40 mm for the carrier phase. (+) Exp; (-) LES.

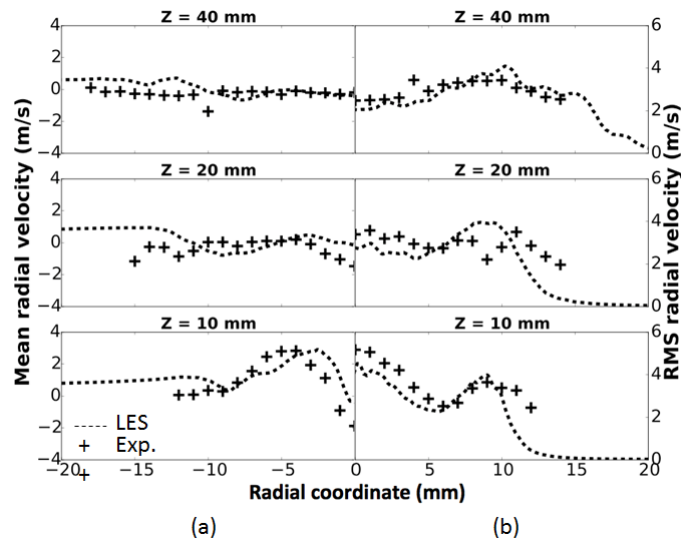


Figure 7.4: Radial profiles of (a) mean radial velocity and (b) RMS axial velocity at $Z = 10, 20$ and 40 mm for the carrier phase. (+) Exp; (-) LES.

Dispersed phase:

The same comparisons are now made for the dispersed phase. In order to make these results statistically comparable, LES analysis uses a control volume of the same size as the PDA probe, and only experimental results respecting the LES detectability (rating count > 100 droplets/s) are plotted. Figures 7.5a and 7.5b show the axial and radial

velocity profiles for the spray along the radial direction at the same axial locations as before. Experimental points represent mean and RMS values while numerical results correspond to all the droplets tracked during the calculation time. Droplets are sorted into three diameter classes, namely: $0-15 \mu m$, $15-35 \mu m$ and $35-60 \mu m$. A fairly good agreement is observed between experiment and LES, showing that the spray distribution is well reproduced. Velocity profiles are quite similar to the gaseous ones. Large inertial droplets are found on the external part of the spray whereas small droplets are entrained by the air co-flow and concentrate near the spray axis. This is clearly visible on Fig. 7.6 which displays the droplet size radial distribution at the same axial positions. Most discrepancies between the velocity profiles appear for large droplets and are probably due to a lack of statistical convergence due to their low number in the simulations.

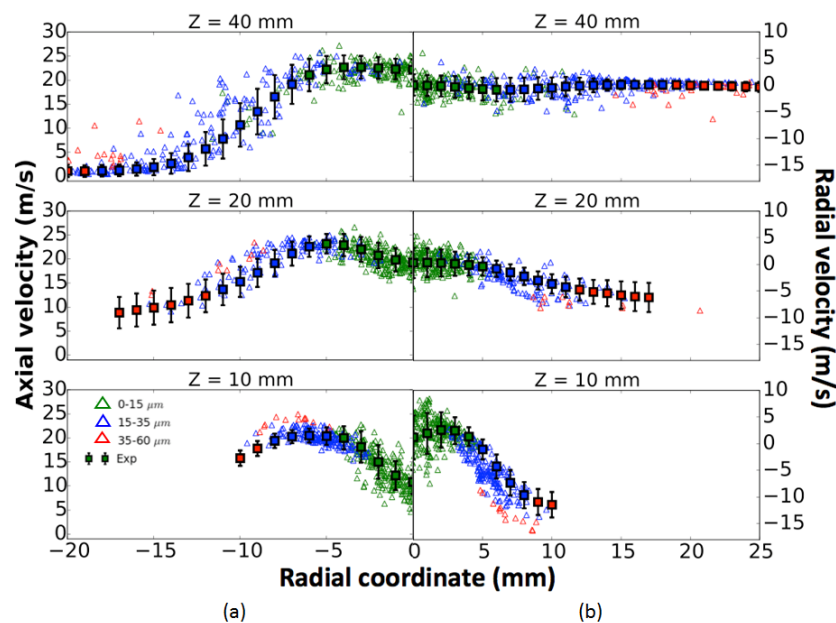


Figure 7.5: Mean components of fuel droplet (a) axial velocity (b) radial velocity separated in three size-classes. \triangle represent the $[0 - 15] \mu m$ group, \triangle the $[15 - 35] \mu m$ group, \triangle the $[35 - 60] \mu m$. Error bars are proportional to measured RMS values.

Figure 7.7 presents the mean fuel droplet temperature obtained by simulation (black \square) and experiments (red $+$). Note that, to be consistent with the experimental GRT results, the simulated fuel droplet temperature profiles are weighted by the following equation: $D_p^{7/3}$, where D_p is the droplet diameter. Figure 7.23 displays the radial profile of the mean fuel droplet temperature for experiments (GRT) and simulations in non reacting conditions. The deviation between the predicted and measured profiles is found to be considerably significant. GRT results indicate that the liquid fuel droplet temperature is close to the fuel injection temperature at $R = 0$ mm, and decreases from 298 K to 279 K. This cooling profile is observed for each axial station ($Z = 20, 30$ and 40 mm) on the experimental results. However, the fuel droplet temperatures calculated by the LES are strongly different. Indeed, the fuel droplet temperature profile seems to be constant at a

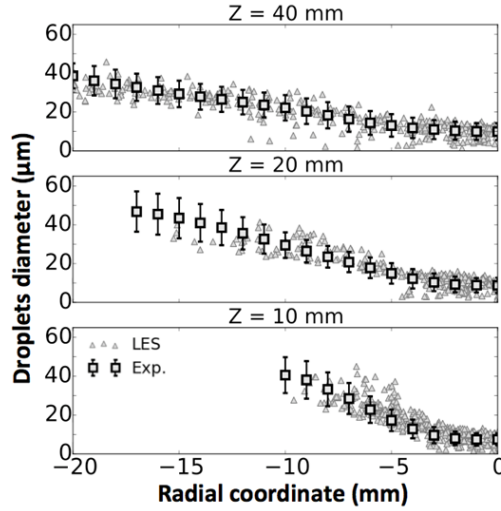


Figure 7.6: Radial profiles of droplet diameter at $Z = 10, 20$ and 40 mm for the carrier phase. (\square) Exp with error bars; (\triangle) LES.

temperature equal to $T = 281$ K. Figure 7.7 shows that for the largest droplets located at radial stations where $R > 12$ mm, the fuel temperature obtained by the resolution of the Abramzon-Sirignano evaporation model is in agreement with the result obtained by GRT. In this part of the spray, the number density of large droplets is very small and the assumption of isolated droplet without interactions with its neighbors (made in the evaporation model) is acceptable, and give the same temperature results compared to the experiments. However, in the center of the spray ($R \approx 0$ mm) where small droplets are present with an elevated number density, the fuel droplet temperature prediction by LES is in disagreement with GRT result. In region where fuel droplet density is high, the interaction between the droplets must be taken into account for the calculation of the fuel droplet temperature. It is worth noting that similar temperature profiles have already been observed on the same fuel atomizer by performing multi-band LIF thermometry experiments on fuel droplets ([104]).

7.1.3 Reacting case

Flame shape

Figure 7.8 shows instantaneous visualizations of the flame in a vertical cross section both from experiments and LES. The overall shape of the flame is very similar in both cases: the spray flame is lifted and stabilized downstream the injector. It exhibits two branches corresponding to an inner and an outer flame front sharing a common flame base (S). Fig. 7.9 shows an instantaneous field of C_7H_{16} mass fraction. The maximum of fuel vapor is observed between the Inner Reaction Zone (B1) and in the Outer Reaction Zone (B2) that develop downstream the leading edge. In the central cold air jet region (A), the quantity

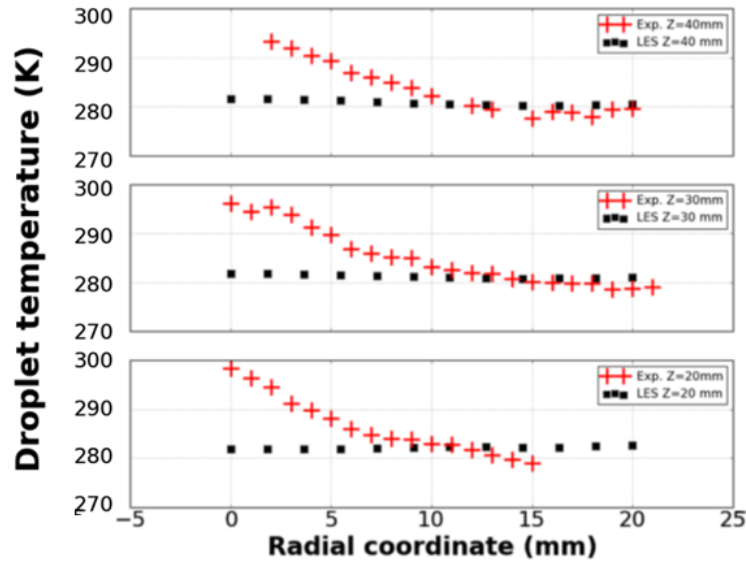


Figure 7.7: Radial profiles of fuel droplet temperature at $Z = 20, 30$ and 40 mm. (+) Exp; (\square) LES.

of fuel vapor is low. The droplets of the spray which undergo evaporation in this region are indeed very small and represent a small part of the spray in terms of mass. This leads to the formation of a lean fuel mixture. The mixing is enhanced by the turbulence which is maximum on the shear layers of the jet enabling the development of a wrinkled inner flame front around this partially premixed region. The wrinkled shape of the Inner Reaction Zone is not only generated by the turbulence but also by local variations of mixture fraction. Since, the flame structure is well predicted by the LES, a joint effort can be made on the identification of the different combustion regimes encountered in the Inner Reaction Zone and in the Outer Reaction Zone.

Combustion regimes

It is expected that droplet evaporation leads to local fuel inhomogeneities and also induces both premixed and non-premixed burning modes. The combustion regime may be characterized with the Takeno flame index [133] in Fig. 7.10, where positive (respectively negative) values indicate premixed (respectively non-premixed) combustion. A complex flame structure is revealed, which exhibits combined premixed and diffusion modes. The inner flame region exhibits a positive flame index meaning that it behaves like a premixed flame. In this region, the high level of turbulence and evaporation of the small droplets leads to a partially premixed mixture. The outer flame front exhibits a diffusion like combustion regime with a very low level of turbulence. A diffusion flame appears also between the inner premixed flame front and the burnt gases of region (C). This kind of double structure is a characteristic of spray flames [134] and its exact structure will be detailed hereafter. Note that some pockets of diffusion flames detached from the inner

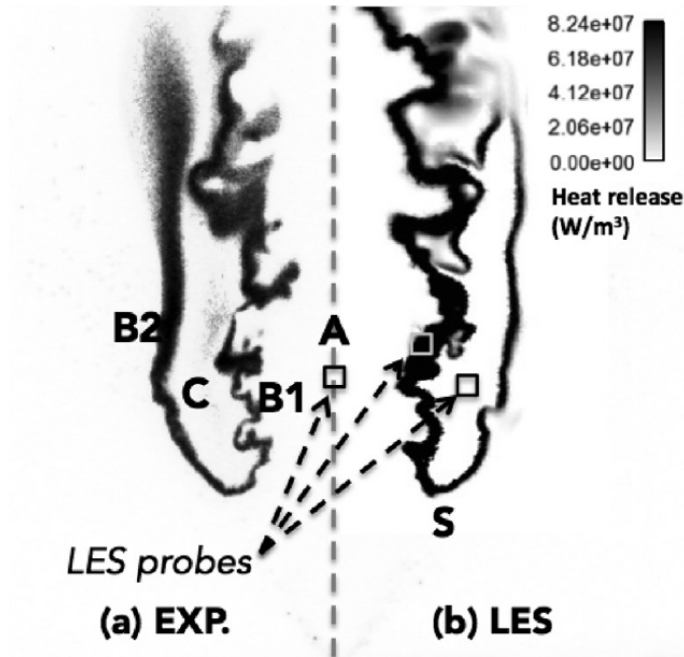


Figure 7.8: Instantaneous visualization of the spray jet flame. LES: heat release field. EXP: OH-PLIF image

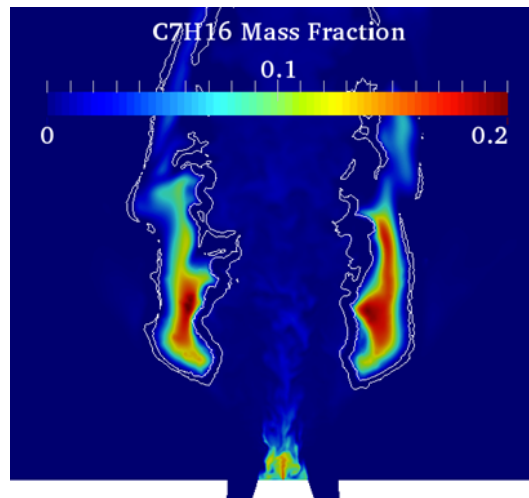


Figure 7.9: Instantaneous field of fuel vapor with an isocontour of heat release extracted from LES

reaction zone are also observed experimentally and numerically.

To further analyze the flame structure, a scatter-plot of temperature in the mixture fraction space along a vertical plane is shown in Fig. 7.11. The mixture fraction is defined as in [135] and does not account for liquid fuel. Note that points are differentiated by the Takeno flame index with only reactive regions represented. The outer diffusion flame (B2) is distinguished from the diffusion flame attached to the inner reactive zone using its spatial location. As expected, diffusion flames and maximum temperature mostly occur

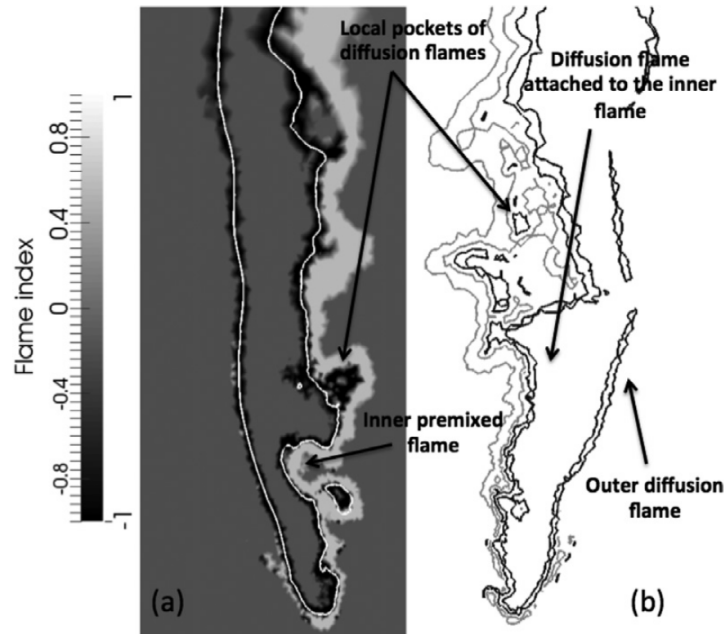


Figure 7.10: (a) Field of Takeno flame index, with isoline of stoichiometric mixture fraction (white). (b) Isolines of Takeno index, corresponding to premixed flames (grey, Takeno=1) and diffusion flames (black, Takeno=-1), obtained from LES

around stoichiometric conditions ($Z_{st}=0.062$). The outer diffusion flame (B2) shows little dispersion, consistently with the weak turbulence intensity at the flame location. The inner premixed branch (B1) fed by region (A) burns in mostly lean conditions. Finally, the diffusion flame attached to the inner reaction zone seems to behave like the outer diffusion flame.

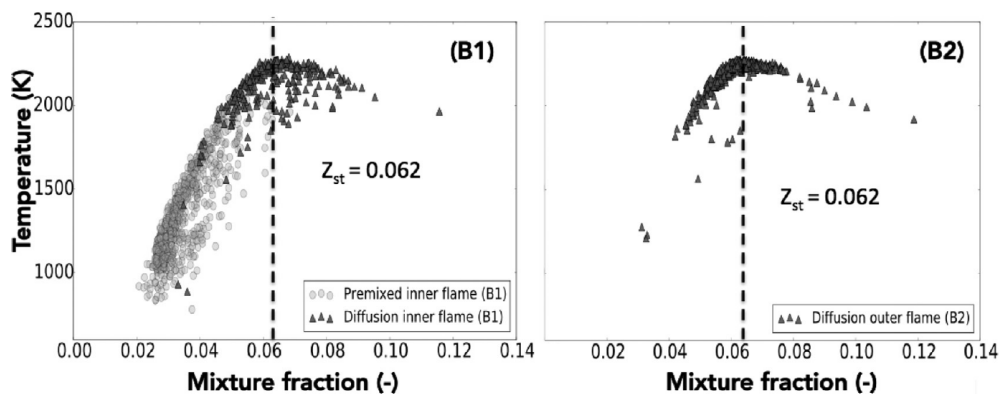


Figure 7.11: Scatter-plot of temperature versus mixture fraction in a vertical plane, obtained from LES. [18]

To better understand the flame structure, Fig. 7.12 shows instantaneous radial profiles (obtained from LES) of fuel vapor and oxidizer mass fractions, equivalent fuel mass fraction Y_{fl} and heat release normalized by its maximum value on the profile, at $Z = 30$ mm. Starting from the center of the jet, the cold mixture of air and fuel vapor, with slowly

evaporating droplets (A) is found and feeds the lean premixed flame (B1) that burns all the fuel. Fuel droplets evaporate very fast in the reaction zone (B1), increasing locally the total equivalence ratio above the lean flammability limit. The remaining air then reacts with the fuel vapor that diffuses from the fuel-rich, hot region (C), forming the diffusion flame very close to the flame (B1). Almost all droplets evaporate in region (C), from which oxygen has almost fully disappeared, which explains that no combustion occurs in this zone. Then the fuel vapor of (C) burns with the outer air in a purely diffusion flame (B2).

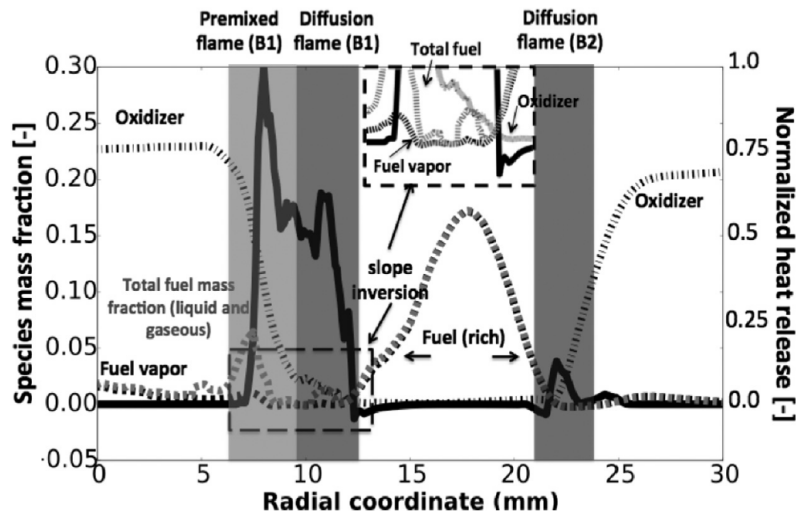


Figure 7.12: Instantaneous radial profiles across the flame at $Z = 30$ mm: (solid line) Normalized heat release; (dashed black) Fuel vapor and (dashed gray) total fuel mass fraction (vapor + liquid); (dash-dot) Oxidizer mass fraction. [18]

Stabilization of the flame base

Figure 7.13(a) shows the equivalence ratio near the stabilization point with an iso-contour of zero flame displacement speed S_d defined as in [127]. Zero flame displacement speed indicates an exact balance between the turbulent burning velocity and the downstream convective velocity, and characterizes flame stabilization. In the flame base region, it appears that the iso-contour perfectly matches with regions close to unity gaseous equivalence ratio, suggesting a strong correlation between the position of the flame base and the gaseous equivalence ratio field. This observation is confirmed by fig. 7.13(b) which shows the PDFs of equivalence ratio at the stabilization point and 1 mm upstream. At the stabilization point, the gaseous equivalence ratio varies between 0.4 and 1.4 whereas just below, the mixture is clearly too lean to allow propagation. This means that in this spray flame configuration, the flame stabilization is mainly controlled by the amount of fuel vapor available, and that the position of the flame base is dictated by the stoichiometric, fastest flame front as the result of the balance between the flame displacement speed and the droplet evaporation rate. Moreover, the mechanisms involved seem to be analogous

to those found in the triple flame without the poor branch due to lack of fuel vapor in upstream premixed zone.

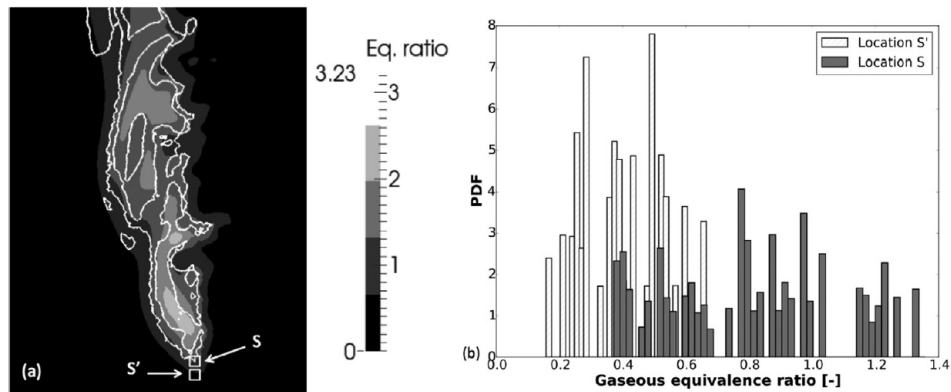


Figure 7.13: (a) Instantaneous field of gaseous equivalence ratio with an isocontour of zero flame displacement speed in a vertical cut, obtained from LES; (b) PDF of gaseous equivalence ratio at two locations (S) and (S'), from LES. [18]

Note that the liftoff distance of the LES is shorter than the measured one. A possible explanation of this difference may come from the simplified 2 steps chemistry and/or the evaporation model. This will be discussed in the following section.

7.1.4 Effect of the evaporation model and the chemistry

The two-step global scheme ($2S_C_7H_{16}_DP$) used as the combustion model in this simulation could explain the underestimated location of the leading edge. Shum-Kivan [136] performed a new simulation but with a detailed chemistry provided by the Anatically Reduced Chemistry (ARC) methodology. The latter contains 24 transported species, 32 species in quasi steady state and 217 reactions [136]. In this configuration, it seems that the detailed chemistry does not modify the the stabilization height. More details can be found in [18].

The evaporation model has been modified to illustrate the impact on the flame liftoff height. In a recent conference paper, Noh et al. [137] illustrate the effect of three evaporation models (classical rapid mixing, Abramzon-Sirignano and Langmuir-Knudsen) on the flame liftoff height for the same experimental configuration. The authors show that all the models capture very well the formation of the double reaction zones and the global flame structure, but clear differences become visible in terms of the flame liftoff height (Fig. 7.14). These preliminary results highlight the sensitivity of flame response to fuel droplet interactions with the evaporation model.

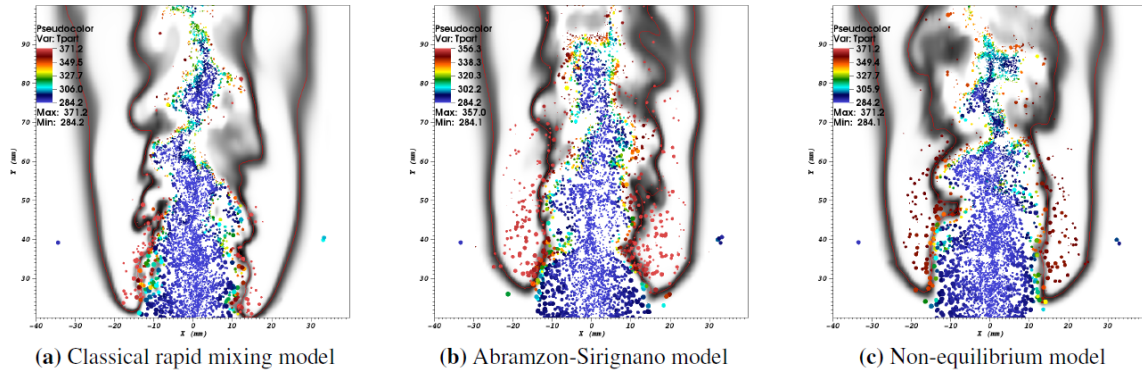


Figure 7.14: Contour plots of the simulated OH mass fraction together with an isoline of the stoichiometric mixture fraction highlighted in red lines and the corresponding instantaneous droplet motions. Color map indicates the droplet temperature while droplets are scaled with their sizes.

7.2 6th Workshop on measurement and computation of Turbulent Spray Combustion (TCS6)

The aim of this workshop is to stimulate progress in the understanding of turbulent spray combustion by organizing focused discussions on open problems and promising new initiatives and collaborations in this area. The workshop links recent developments in studies of dispersed multiphase flow and combustion. The intention is to have interactive discussions between participants. Invited lectures, given by experts in the field of turbulent spray combustion (one experimental and one computational), initiate discussions, whereas participants have the opportunity to present their work in contributed poster presentations. An important aspect of this workshop is the round-table discussions, which focuses on the assessment of state-of-the-art and on initiation of future collaborations in experimental as well as computational techniques in spray combustion. It is the intention to define some target test cases, for which experimental databases will be developed and on which modeling and numerical algorithm issues will be tested.

In preparation of the workshop a special effort is made to collect and compile the best possible experimental datasets useful for model validation. The databases remain available for use afterwards and, in a number of cases, are suitable for inclusion in the ERCOFTAC wiki. A special effort has been made to create a database that can be read by the entire scientific community. During the last TCS, three experimental facilities were used as target test cases:

- Sydney University spray burner. Many studies issued from the Sydney University burner [30, 31] present a comprehensive mapping of the flow and droplet fields in turbulent non-reacting as well as in reacting dilute spray jets of acetone and ethanol fuels. The burner is designed in such way that the boundary conditions are characterized with sufficient details and the stability limits of the flames are known. The

flow is intentionally simple so that attention is shifted to the study of flow–droplet interactions with and without heat release. Velocity, turbulence and droplet size data are measured using a conventional LDV/PDA system. Laser-induced fluorescence (LIF) is employed to image the hydroxyl radical OH which marks the existence of hot regions or reaction zones and used to study the turbulent spray flames approaching extinction. Sequences of conditions are investigated to resolve the effects of increasing the droplet loading (at a fixed carrier flow rate, where the carrier is air) and the effects of increasing the carrier velocity (at a fixed liquid flow rate).

- Cambridge University swirling spray burner [6]. The Cambridge Swirl Flame is meant to study finite-rate kinetic effects in spray combustion, in configurations of direct relevance to gas turbine combustors. Confined short turbulent swirling *n*-heptane spray flames, stabilized on an axisymmetric bluff body in a square enclosure, have been examined close to the blow-off limit and during the extinction transient with OH chemiluminescence and OH-PLIF. The comparison of flames of different canonical types in the same basic aerodynamic field provides new insights on the relative blow-off behavior. The flame structure has been examined for conditions increasingly closer to blow-off.
- Coria Rouen Spray Burner (CRSB). This is the database obtained along this thesis. This burner reports experimental studies [17] where flame structure, flow topology, fuel droplet temperature and local extinction mechanisms of *n*-heptane spray flames are investigated. The burner consists of an annular non-swirling co-flow of air that surrounds a central hollow-cone spray injector, leading to a lifted spray flame. The experiments include measurements of droplet size and velocity by Phase Doppler Anemometry (PDA) and fuel droplet temperature by GRT, flame structure by High-Speed Planar Laser Induced Fluorescence of OH radical (HS-OH-PLIF) simultaneously recorded with the velocity fields of the reactive flow obtained by High-Speed Particle Image Velocimetry (HS-PIV). These new results on fuel droplet temperature, local extinction of spray flames and droplet-flame interactions will also strengthen the CORIA Rouen Spray Burner (CRSB) database for the improvement of evaporation and combustion models for reacting sprays.

In the following section, only the comparison and discussion between simulations and experiments in the CRSB target test case are presented. The goal of this discussion is to highlight the diversity of the models to describe the chemistry and the evaporation of the fuel droplets, and to demonstrate their influence on the results of the simulations. The comparison is made on the velocity profiles of the carrier and dispersed phases, the mean diameter of fuel droplets, the mean temperature of fuel droplets and flame structure. The simulation of CRSB burner was realized by 4 different teams:

- Cerfacs (Toulouse, France) with the AVBP code
- EM2C (Paris, France) with YALES2 code
- Imperial College London (London, England) with BOFFIN code
- TuDelft (Delft, Netherlands) with OpenFOAM

Figure 7.15 shows that regardless of the numerical study, everyone has chosen to adopt an approach based on Lagrangian/Two-way. Atomization and break-up models are adopted by Imperial College whereas fuel droplets are injected directly at the exit of the fuel injectors according experimental fuel droplet size distribution for the last three numerical teams. Concerning the evaporation model used during simulations, the Abramzon-Sirignano’s model is chosen by Cerfacs and Imperial College london, whereas the Ranz-Marshall evaporation model is adopted by EM2C and TuDelft.

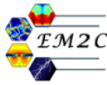
	Approach	Evaporation	Break-Up
	Lagrangian/Two-way	Abramzon-Sirignano	No
	Lagrangian/Two-way	Ranz-Marshall	No
	Lagrangian/Two-way	Abramzon-Sirignano	Stochastic Model
	Lagrangian/Two-way	Modified Ranz-Marshall	No

Figure 7.15: Liquid phase modeling for the different numerical teams.

The different numerical models are reported in Fig. 7.16 for each numerical teams.

The turbulence-chemistry models will not be described in this section. More details can be find in [63]. However, particular attention will be paid in the following sections to the effect of the chemical mechanisms used in LES on the flame structure results. The numerical set-up are described in Fig. 7.17. Clear differences can be observed in the domain size and geometry, and in the number of cells. It is worth noting that air entrainment by the co-flow is not negligible (as it was shown experimentally by high-speed PIV in Chapter 5) in the combustion process and directly affects the Outer Reaction Zone. Changing the width of the computational domain or the boundary conditions will probably have an impact on the LES results.

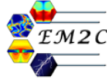
	Turbulence-chemistry interaction model	Chemical Mechanism
	No modelling required due to great refinement of the flame.	Reduced: 24 transported, 32 QSS species, 217 reactions. Obtained using ARC.
	F-TACLES including differential diffusion effects. Flamelet tabulated based on detailed chemistry. Require transport of mixture fraction and progress variable.	Detailed 106 species 1738 reactions POLIMI
	Transported PDF closed using the Eulerian Stochastic Fields Method with 8 fields. Does not require any assumption on combustion regime.	Reduced 22 species 18 reactions <i>Liu et al. 2004</i>
	FGM from steady and non-steady non-premixed flamelets, with presumed beta-PDF.	Skeletal 188 species 939 reactions <i>Lu and Law 2006</i>

Figure 7.16: Combustion phase modeling for the different numerical teams.

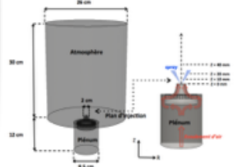
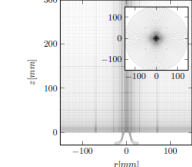
	 		
N cells	53 M tetrahedral cells	5 M hexahedral cells	0.4 M hexahedral cells
Domain size	300 mm X 260 mm	500 mm X 300 mm	400 mm X 300 mm
Plenum	Yes	No	No
Additional Info	Unstructured grid minimum spacing 0.1 mm 	Structured grid Expansion ratio below 10% 	Cylindrical mesh. The cells near the fuel nozzle have a characteristic size of 0.66 mm. An expansion ratio of 1-3% is used.

Figure 7.17: Numerical setup.

Carrier and dispersed phases

A comparison of the simulated and measured mean gas-phase velocity is first performed. The gas phase axial velocity shows a satisfactory agreement, as it is observed in Fig. 7.18. The typical double peak in the velocity is well predicted by all the simulations. However, concerning the RMS of the velocity, the simulations slightly underestimate the velocity fluctuations. Note that in most simulations, the subgrid-scale contribution to the fluctuations is not taken into account in the computation, that explains a lower RMS level in the simulation than in the experiment. The same behavior is observed in fig.7.19, which compares the radial profiles of mean radial velocity for the carrier phase.

The same comparisons are now made for the dispersed phase (Fig. 7.20) and 7.21. A

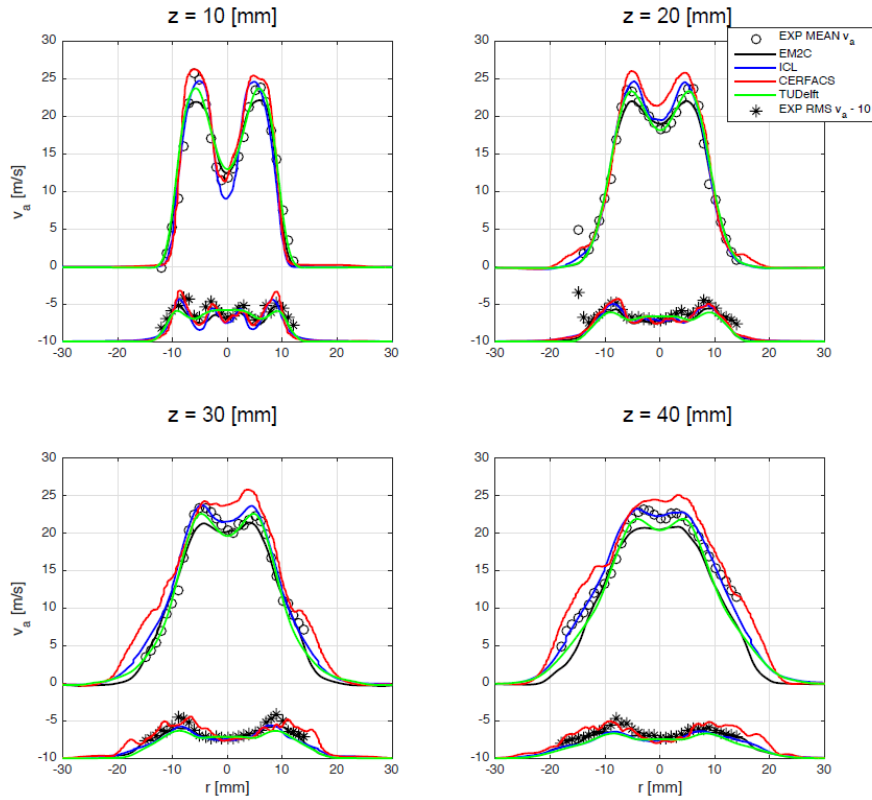


Figure 7.18: Radial profiles of mean axial velocity and RMS at $Z = 10, 20, 30$ and 40 mm for the carrier phase.

fairly good agreement is observed between experiment and LES, showing that the spray distribution is well reproduced. The comparison shows that the liquid phase characterization is more accurate closer to the centerline while larger discrepancies are observed at the edge of the jet.

The comparison of droplet size in terms of mean diameter ($D_{10} = \sum_{i=1}^n \frac{D_i}{N}$) is reported in Figure 7.22.

The hard point of this comparison was found in the fuel droplet temperature measurement. To be consistent with the experimental GRT results, the simulated fuel droplet temperature profiles are weighted by the following droplet diameter: $D_p^{7/3}$. Figure 7.23 displays the radial profiles of the mean fuel droplet temperature for experiments (GRT) and simulations for different axial stations. First, the deviation between the predicted and measured profiles is found to be considerably significant, whatever the simulations. The initial cooling of droplets located in the center of the spray ($R < 10\text{mm}$) is not predicted by the simulations. However, for $Z > 30\text{mm}$ the increase of fuel droplet temperature is observed both experimentally and numerically, but it occurs in a different manner. All the simulations reveal that the increase of fuel droplet temperature is faster than the profile obtained by GRT. These different evolutions can be explained by the different position of the flame leading edge obtained by the simulations. In addition, all the simulations predict a plateau for the fuel droplet temperature in zone C , but with value ranging from

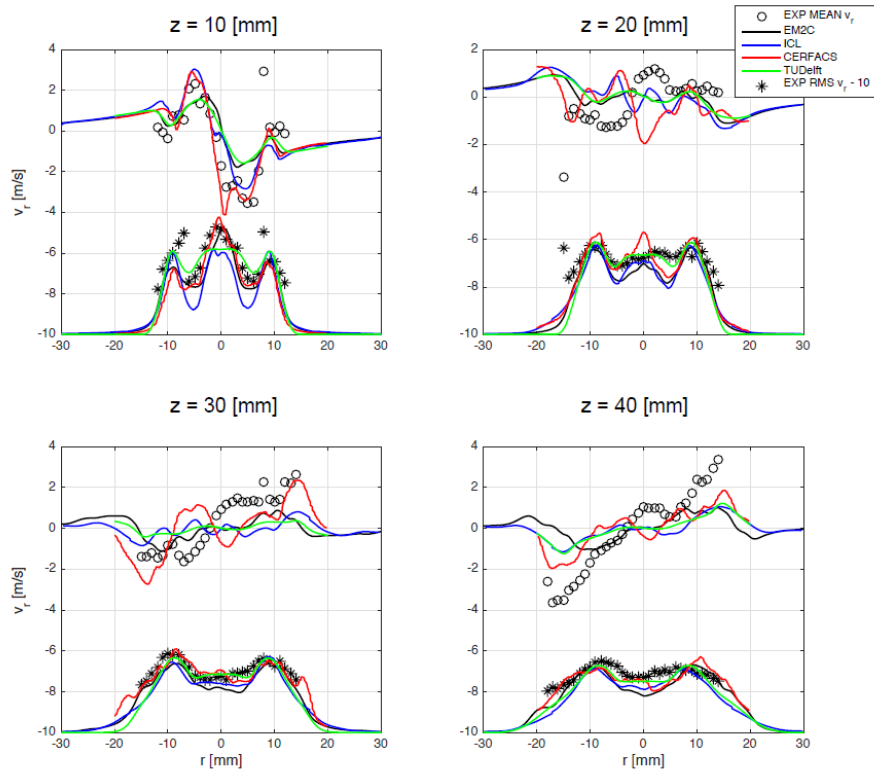


Figure 7.19: Radial profiles of mean radial velocity and RMS at $Z = 10, 20, 30$ and 40 mm for the carrier phase.

350 K to 360 K. No clear correlation with the evaporation model can be made. Moreover, these equilibrium temperatures differ from the experimental one which reaches 331 K. This comparison reveals the high sensitivity of the predicted droplet temperature values to the evaporation model, as it was shown in the reference paper of Miller et al. [7]. However, one strong effort must be also made for the experimental contribution by increasing the level of validity and of confidence of the measurements. These differences justify the necessity to perform additional measurements with fuels characterized by a wide range of boiling temperatures or volatilities (i) to demonstrate the capacity of the GRT technique to discriminate different fuel droplet temperature evolutions even in non-reacting configurations, and (ii) to provide an additional database for LES to extensively test different evaporation models and evaluate their capacity to accurately predict the experimental tendencies.

Flame structure

Figure 7.24 illustrates the instantaneous flame structure obtained by the different numerical teams. First, the two reaction zones are predicted by all the models. However, some important differences with the OH experimental images can be observed, especially in the shape of the outer reaction zone. Indeed, all simulations predict the behavior of this specific combustion regime, but a singularity is found between $Z = 30$ and 40 mm, for the Cerfacs and EM2C simulations. This may be due to the size of the physical domain

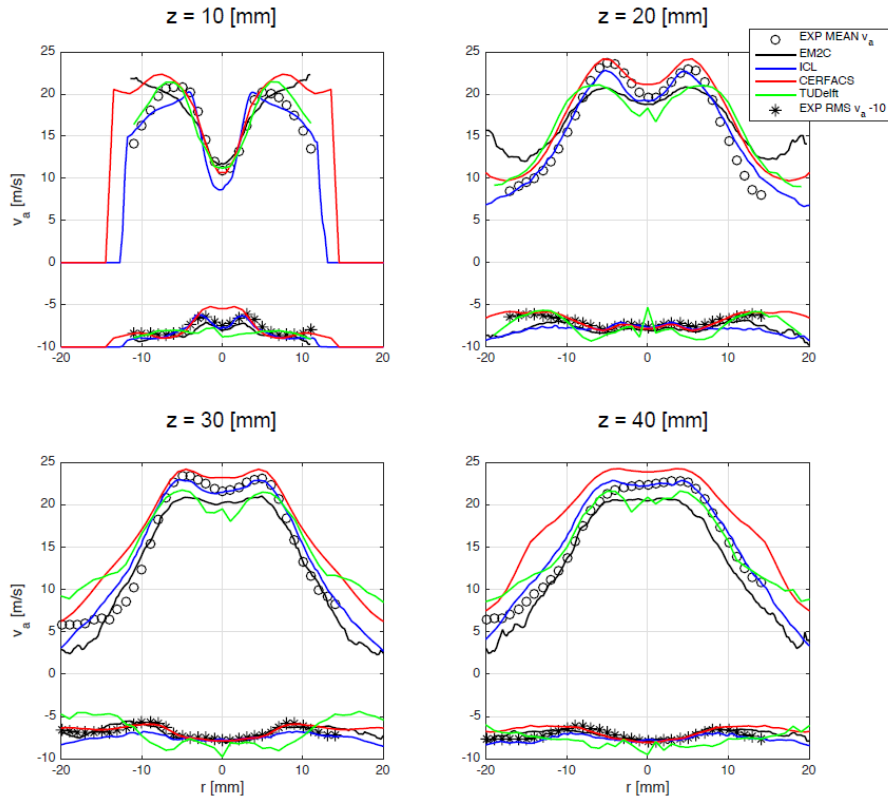


Figure 7.20: Radial profiles of mean axial velocity and RMS at $Z = 10, 20, 30$ and 40 mm for the dispersed phase.

which is larger for Imperial College and may capture the entire recirculation zone in the ambient air. The latter directly controls the location of the ORZ. Therefore, reducing the width of the computational domain alters the shape of the ORZ.

Figure 7.25 presents a comparison between the simulations and the experiment for the mean OH results and a global good agreement can be found. However, The width of zone C as well as the amplitude of the IRZ wrinkling may change significantly between all the results and the experiments. It seems also that the quality of the mesh and the evaporation model have a strong impact on the structure of the flame. Moreover, in most of the simulations the lift-off height is underestimated compared to the experimental results. The investigation is still in "work in progress", but it appears that the combustion model does not influence the height of the flame stabilization whereas the evaporation model does so. (Figure 7.14).

The effort must be done in the next step on the local description of local reaction structures, and on the interactions between turbulence, reaction zone and fuel droplets. From this analysis, the importance of the turbulent combustion models and chemistry should be highlighted. Thanks to this first participation in the 6th TCS workshop, the discussions are now open and collaborations are established to continue to improve our knowledge on spray combustion.

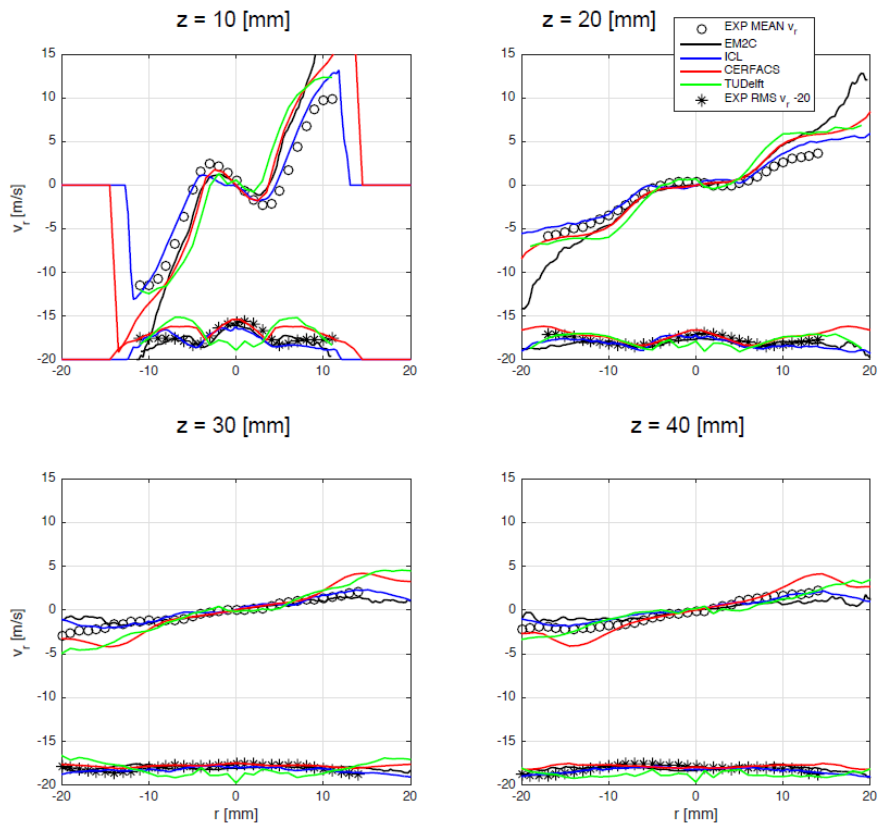
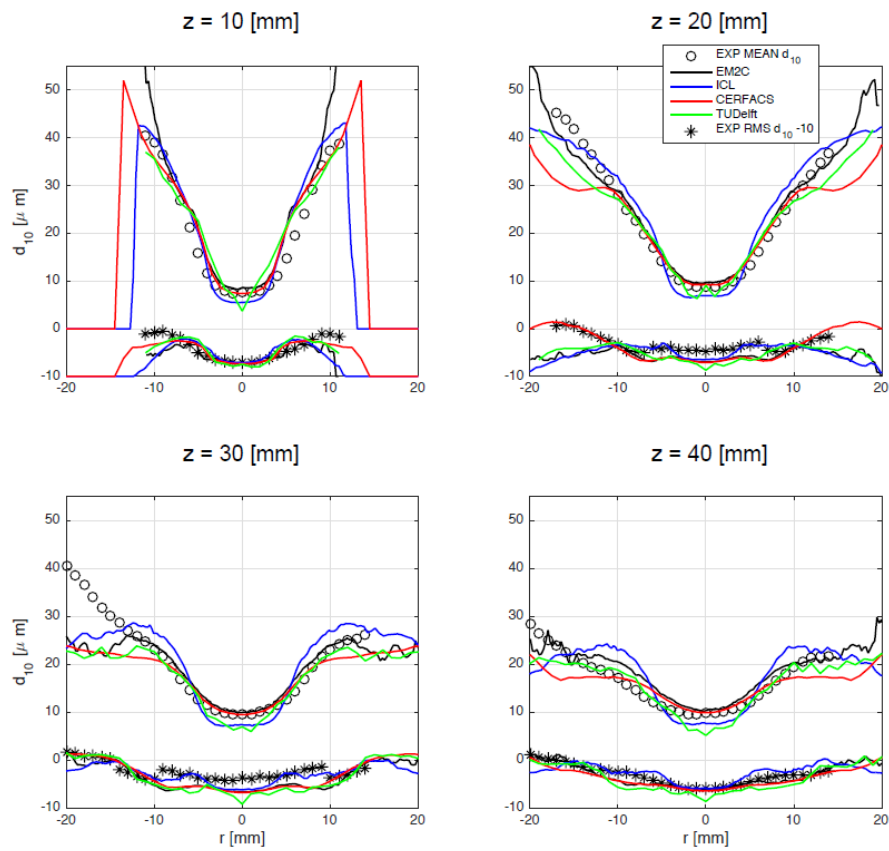


Figure 7.21: Radial profiles of mean radial velocity and RMS at $Z = 10, 20, 30$ and 40 mm for the dispersed phase.

Figure 7.22: Radial profiles of mean droplet diameter (D_{10}) at $Z = 10, 20, 30$ and 40 mm.

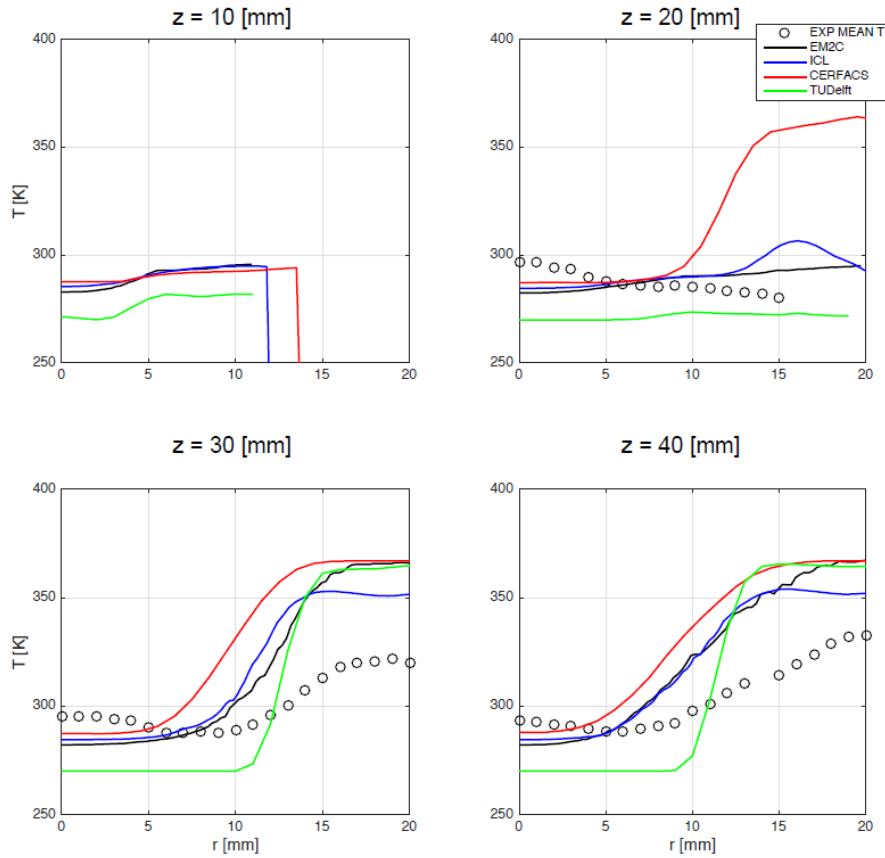


Figure 7.23: Radial profiles of mean droplet temperature at $Z = 10, 20, 30$ and 40 mm.

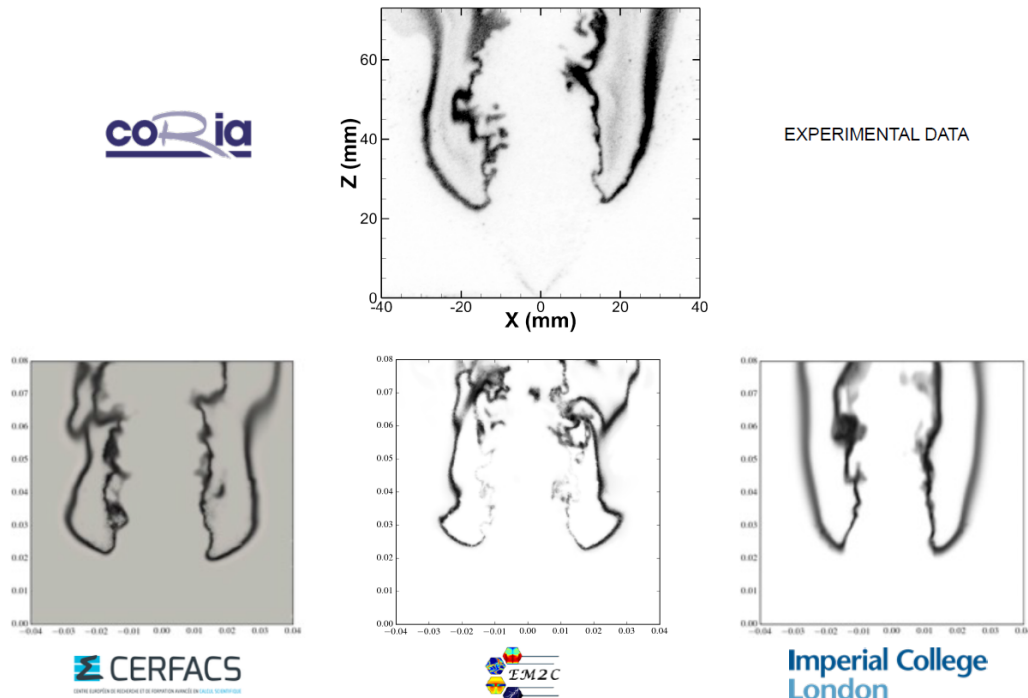


Figure 7.24: Comparison of OH-PLIF images between experiment and numerical results

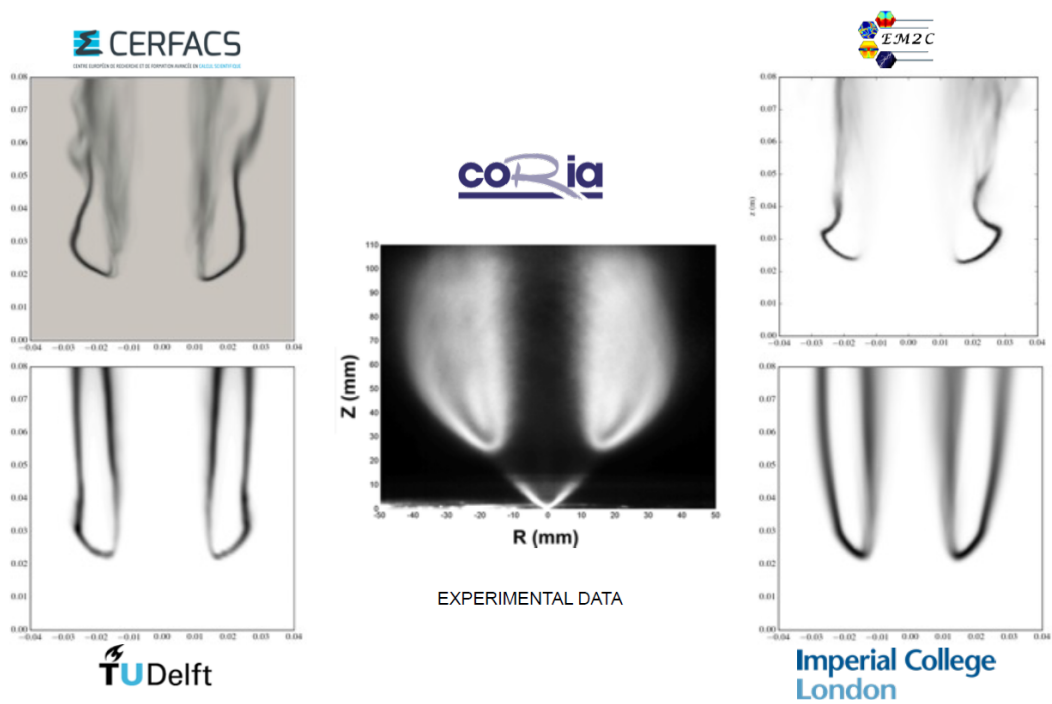


Figure 7.25: Comparison of the mean OH-PLIF images between experiment and numerical results

Chapter 8

Conclusion and Perspectives

Contents

8.1 Conclusion	137
8.1.1 Characterization of non-reactive conditions	138
8.1.2 Characterization of reactive conditions	138
8.1.3 CRSB - Flame Data Base	140
8.2 Perspectives	140
8.2.1 Database extension	140
8.2.2 Improvement of GRT technique	141
8.2.3 Extension of the experimental conditions	142

Aviation has fundamentally transformed society over the past 40 years. The growth of air traffic over the last 20 years has been spectacular, and will continue in the future. Although the combustion chamber has been the subject of numerous studies to improve, in particular, the performance of propulsion systems, today the standards are increasingly drastic and pressure to reduce the NO_x emissions continues. To meet these objectives, it is important to improve the theoretical knowledge on two-phase flow combustion in order to improve the aircraft engine in terms of pollutant emissions. This thesis deals with the experimental study of a spray jet flame at constant pressure, under weakly turbulent and lean flow conditions.

8.1 Conclusion

This work, carried out within the framework of a part of the ANR TIMBER project, aims to improve the understanding of two-phase flow combustion, as well as to produce an efficient and original database for the validation of the models used in LES. The use of high-performance optical diagnostics made possible to obtain numerous experimental

data on the carrier and dispersed phases as well as on the flame structures. Joint studies with different numerical results have allowed us to deepen our knowledge about spray flames. In the following, the main conclusion about this spray jet flame is given.

8.1.1 Characterization of non-reactive conditions

The first part of this work consisted in establishing the non reacting properties of the carrier phase and the dispersed phase. PDA was used to extract the properties of fuel droplets (size and velocities) and to define the level of turbulence in the carrier phase. The novelty of the results in non reacting conditions lies on the application of a Global Rainbow Refractometry technique to measure the fuel droplet temperature evolution along the evaporation process. The main features of the non reacting flow are now given:

- **Carrier phase:** The annular air co-flow surrounding the fuel atomizer is injected at a bulk velocity of $21m.s^{-1}$. Further downstream, it merges to form a unique larger jet with a flat axial velocity profile. The air injection system generates radial velocities, approximately 10 times smaller than the axial velocities at $Z = 10$ mm, and rapidly decreasing down to zero at $Z = 40$ mm. Moreover, the annular air co-flow discharging into the ambient air creates a shear layer at the interface between the high air co-flow velocity and the ambient air, inducing a high level of turbulence with large scale structures. The turbulent kinetic energy does not follow the same pattern as the axial velocity, with peaks diffusing radially with increasing axial stations.
- **Dispersed phase:** Fuel is injected by a pressurized fuel injector that expels the droplets with a strong radial velocity component forming a hollow cone of an 80 degree opening. Large inertial droplets are found on the external part of the spray whereas small droplets are entrained by the air co-flow and concentrate near the spray axis. The fuel droplet temperature is close to the fuel injection temperature at $R = 0$ mm, and decreases radially from 298 K to 279 K. This decrease of temperature is observed for each axial station ($Z = 20, 30$ and 40 mm). This cooling effect results from the evaporation process that occurs along the droplet trajectories taking relatively long time to reach their final temperature.

8.1.2 Characterization of reactive conditions

The second phase of this work is dedicated to the characterization of the Jet Spray Burner in reactive conditions, in terms of flame structure, flow topology and local extinction mechanisms. The droplet size and velocity are obtained by Phase Doppler Anemometry (PDA) whereas the flame structure is investigated by High-Speed Planar Laser Induced

Fluorescence of the OH radical (HS-OH-PLIF) simultaneously recorded with the velocity fields of the reactive flow, obtained by High-Speed Particle Image Velocimetry (HS-PIV).

- **Flame structure:** The lifted spray flame features a double reaction zone structure, with an inner lean premixed flame mostly fed by small droplets concentrating in the center region, and an outer diffusion flame burning the fuel vapor produced by the larger droplet evaporation in the burnt gas region between the two flames with the surrounding air. This fuel vapor also feeds a secondary diffusion flame, located very close to the inner premixed flame and burning the remaining oxidizer. The flame base shows that it is located around stoichiometric conditions, ie., where the flame speed is the fastest. Flame stabilization is therefore driven to first order by the droplet spatial distribution and their evaporation rate.
- **Fuel droplet temperature:** The GRT technique was also successfully applied in reactive conditions and allowed to bring new information regarding the thermodynamic behavior of fuel droplets along their trajectories across the flame front. This technique was first applied with a continuous laser (C-GRT) to extract temporally averaged values of fuel droplet temperature according to the methodology developed initially by Letty et al. [16]. However, this technique was extended to measure instantaneous and local fuel droplet temperatures by using a pulsed laser, in order to improve the knowledge of the droplet evaporation in reacting conditions. Therefore, conditional averaged measurements of fuel droplet temperature according to the distance of flame front were reported for the first time by coupling instantaneous GRT (I-GRT) with OH-PLIF. The dataset provided here offered the opportunity to validate evaporation models at low and high gas temperatures, since evaporation models have been shown to differ significantly from each other when calculating the steady state droplet temperature and when evaluating the droplet heating time. Indeed, it was found in the experiments that between the two reaction zones, the evaporation process occurred at an equilibrium temperature (331 K) lower than the fuel boiling temperature, while for numerical results the evaporation process occurs closer to the boiling temperature. These results contribute to improve scientific knowledge on several steps of two-phase flow combustion, including heat and mass transfer of fuel droplets, fuel vapor production and repartition.
- **Flame extinctions analysis:** Simultaneous HS-OH-PLIF and HS-PIV recordings were used to characterize the dynamics of extinction and non-stationary events in the spray jet flame which underline different mechanisms of droplet-turbulence-flame interactions. In the inner reaction zone, the local flame extinctions were mainly controlled by the shear layer induced by the co-flow and the fuel-air heterogeneities

due to the evaporation of small droplets in the vicinity of the flame front. The large scales of turbulence in the shear layer play a significant role in the dynamics of these extinctions. A mechanism related to the droplet-chemistry interactions occurs at the flame leading edge and occasionally produces a local flame extinction. Indeed, this zone is characterized by low turbulence intensities and large droplets, which have a low temperature and act as heat sinks for the flame front. Therefore, occasional local extinctions occur here due to the cooling effect. It is also found that the large inertial droplets penetrate the lower part of the inner front reaching the burned gases, where they evaporate rapidly. They also disturb the outer reaction zone due to their low temperature and the rich mixture in their wakes.

8.1.3 CRSB - Flame Data Base

The third part of this work was to provide an original database suitable for numerical modeling to predict non-stationary events such as local flame extinction in spray flames and the influence of the evaporation model on the fuel droplet temperature. An effort on the construction of the database allowed to deliver results usable by the whole scientific community. The different laboratories (CERFACS, EM2C, IMPERIAL COLLEGE and TU Delft) were invited to share this database in order to conjointly evaluate the importance of model choices in LES results. A detailed comparison was made between numerical and experimental results. The simulation strategy strongly affects the results whether in flow properties or flame structure. However, the global shape of the flame is predicted by all simulations, but the hard point concerns the fuel droplet temperature, where strong disagreements were observed between experimental and numerical results. From this perspective we can show the interest of the development of joint studies to develop and validate new evaporation models.

8.2 Perspectives

8.2.1 Database extension

The first part concerns the extension of the database with additional measured quantities. The expertise of the CORIA laboratory on the development of CO-PLIF (PhD Thesis Pierre Malbois) and NO-PLIF (PhD Thesis Erwan Salaün) for high pressure aeronautical combustion could be used and applied to the burner CRSB. This would provide additional information on the pollutant formation mechanisms in two-phase combustion, especially in different flame structures where droplets/flame interactions are strongly different. Currently Dr. Mulla is performing simultaneous OH-PLIF and NO-PLIF measurements on the same burner. Figure 8.1 shows an average of 1500 instantaneous images of *NO* concentration. The black lines correspond to the mean flame front position. *NO* concentration

towards the premixed branch is in the range of 25-35 ppm, and it is very close to the previous Cantera simulations. Moreover, the peak of NO is well aligned with the diffusion branch.

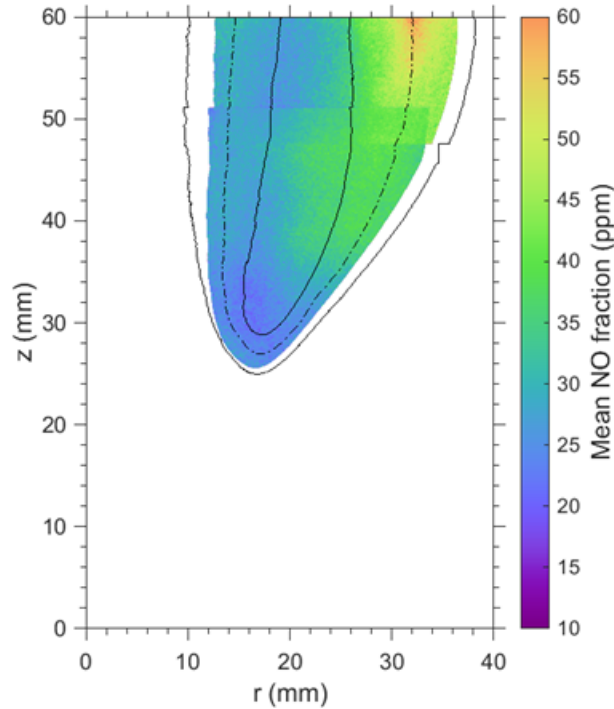


Figure 8.1: Mean NO concentration with the mean flame front position (black lines)

Gas phase temperature measurements are also of interest and this could be achieved by the CARS technique. The latter is under development in CORIA laboratory and it could be applied to bring fundamental knowledge on the evaporation process. Finally, the characterization of the boundary conditions of fuel droplets injection is a critical issue since it directly conditions the success of the numerical simulation. This requires the measurement of the liquid fluxes or the liquid mass fraction of fuel. Some preliminary works with ballistic imaging or holography indicate some promising results.

8.2.2 Improvement of GRT technique

The second part is dedicated to the improvement of the GRT technique. Some strong differences between experimental and numerical results on fuel droplet temperatures were observed along this work. A special effort in the quantification of the experimental uncertainties must be made. This could be achieved by performing new set of measurements by C-GRT on different fuels from volatile fuels (ethanol or acetone) to non-volatile fuels (n-decane or n-dodecane) to study the effect of fuel volatility on the droplet evaporation process in reactive and non-reactive conditions. The extension of the I-GRT technique coupled with PDA for velocity/temperature/size conditional statistics could be also very interesting for the improvement of evaporation models.

8.2.3 Extension of the experimental conditions

In this work, only one operating condition was studied. It was fixed from the stability study of the burner, and the mass flow rate was kept constant for all experiments. It was demonstrated that the local extinctions occurring in the IRZ were mainly due to the strong interaction between the turbulence and the flame front. By varying the mass flow rate of the co-flow, it would be interesting to see if the local extinctions are still present, and if the mechanism of extinction is similar.

Appendix

Appendix A

Analysis of ignition probability and carrier and dispersed phases in non reacting conditions

Currently lean combustion is considered as a promising strategy to achieve the pollutant emissions reduction targets. In lean configuration, the combustion is more susceptible to instabilities, blow-off and complicating ignition. In actual aeronautical combustion chamber, the ignition spark is generally achieved by surface spark-plugs, which is not an optimal position regarding the local thermodynamics and aerodynamics properties. The main conclusions of Birch et al. [138] and Ahmed et al. [139] are that ignition is a stochastic phenomenon and successful ignition depends on many parameters such as the local turbulence intensity and the flammability factor. Some recent LES of spark ignition have been performed in aeronautical combustion chamber to improve the ignition performance for different initial flow conditions. The presence of droplets in spray combustion involves more complex physical phenomena including atomization, dispersion, evaporation and combustion, which generally take place simultaneously or within very small regions in the combustion chambers. Several studies on spray ignition [?, 140–143] have been carried out, including some in more complex aeronautical configuration, such as the pioneer experiments and LES in linear [144, 145] and annular combustion chambers [146, 147].

In a general manner, the ignition process in aeronautical engines can be divided into four steps: (1) spark corresponding to the energy deposition; (2) flame kernel propagation and spreading; (3) flame stabilization on one injector; (4) injector-to-injector flame propagation. Sometimes a missed ignition is observed, even with a sufficient energy supply at phase (1). Phase (2) appears to be a critical step because the flame kernel will be exposed to very different local properties of the flow, which may be adverse or favorable for its survival. The complexity of real aeronautical configurations implies to study the effect of local properties on ignition probability on canonical flame configurations. These

latter present the essential feature of very well defined boundary conditions. Although numerical simulation is a valuable tool to tackle these different interactions between liquid and gas phases, the methods need to be validated through reliable experimental studies. Therefore, accurate experimental data on liquid and gas properties along the evaporation and ignition steps are needed and are still challenging.

In the current study, the CRSB database is completed with spatial measurements of the ignition probability obtained by laser-induced ignition, in order to accurately control the amount of deposited energy and the spark location within the combustion chamber. In this work, spray droplet dispersion, size and velocity, and carrier phase velocity are obtained by Phase Doppler Anemometry (PDA). These local flow properties in non reacting conditions are then analyzed to understand the ignition probability map obtained through a probabilistic approach varying the spark location inside the spray. The objective of this work is to fully describe the local properties of the non reacting flow to extend the knowledge of the main parameters influencing the spray ignition.

A.1 Optical diagnostics

A.1.1 Phase Doppler anemometry (PDA)

Droplet size and velocity are obtained by a commercial PDA system (DANTEC) operating in DUAL mode. The dispersed phase is measured in non reacting condition in order to characterize the droplets properties and the aerodynamic in a spray jet flame before the ignition. An argon laser provides green (514.5 nm) and blue (488 nm) beams. Beam spacing is 50 mm; transmitting and receiving lenses focal lengths are 350 mm and 310 mm, respectively. Due to technical reasons, the off-axis angle of the receiving optics is 50 degrees (in front scattering position), not far from the Brewster angle which, in parallel polarization, enhances the refracted light detection over the reflected light, reducing the trajectory and slit effects. The measurement volume can be approximated by a cylinder of 120 μm in diameter and 200 μm in length. At each measurement location, data sampling is rather limited to 40,000 droplets or to 30 s of measuring time, allowing converged statistics of size-classified data. Due to the spray structure and particle density distribution, the measurements are not possible below $Z = 10\text{mm}$. Indeed, validation levels decrease below 70% for axial stations lower than $Z = 10\text{mm}$ while, downstream, validation of the PDA signals presents values of about 90%. This is mostly due to an increase in droplet concentration. DUAL PDA mode measures droplet diameter following two orthogonal directions which are compared in the phase plot before a droplet is validated (spherical validation). Spherical validation is not significantly affected above $Z = 5\text{mm}$. Shadowgraphy images confirm that there is no ligaments present for $Z > 3\text{mm}$. Provided that this PDA configuration only measures simultaneously in 2 dimensions (relative to the laser

position), axial and radial velocities are measured simultaneously for each point. Besides the spray characterization, the carrier phase velocity is also investigated by seeding the co-flow with $2.5\mu\text{m}$ olive oil droplets. Statistics of size-classified velocities presented in the next figures are calculated when more than 500 droplets have been recorded.

A.1.2 Ignition: spark induced by laser

The mixture was ignited by a laser-induced spark in a selected location (Fig.A.1) using a focused 532 nm laser beam. The experimental setup is composed notably, by a convergent lens of 200 mm focal length and is similar to the one used in [148]. A chopper was used to operate in a single-shot mode. The energy of the laser pulse was controlled and adjusted through the use of a coated variable dielectric attenuator (Laser Optik, Ref. 1Q2) without modifying the Q-switch delay in order to keep the physical beam properties constant. The energy deposited is calculated from the incident energy and transmitted energy by two precision laser pyroelectric Energy Meters (EM,Ophir: PE-25). To ensure a full dynamic range of ignition probability in this work, the deposited laser energy was fixed to 160 ± 5 mJ and kept constant. The spark position was varied through a mesh of 200 interrogation points. For each spark position, 30 independent ignition tests were performed and ignition probability (P_{Ign}) in each point was calculated dividing the number of successful events by the total test number. The number of trials $N = 30$ result in a maximum standard deviation σ of 9% according to the expression Eq.A.1:

$$\sigma = \left(\frac{P_{Ign}(1 - P_{Ign})}{N} \right)^{1/2} \quad (\text{A.1})$$

To make the experiment repeatable, a Labview program permitted precise a control of the parameters and axiomatization of the process, triggering a spark only when the nominal conditions were reached. Time between each sparks is estimated at 5s.

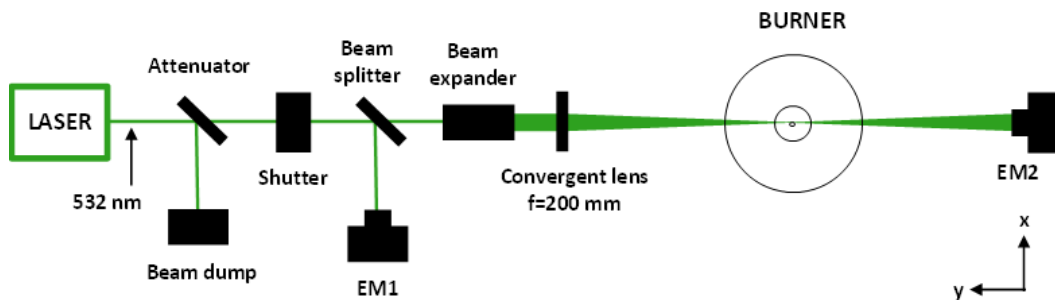


Figure A.1: Optical arrangement for laser induced spark ignition measurements. The mesh is symmetric and just one side is represented here.

High speed visualization

The use of high-speed diagnostics is essential in order to understand the mechanisms involved in flame expansion, stabilization or extinction. High-speed ignition sequence recording was performed for different spark position in the burner. A high-speed camera running at 10 kHz (Phantom V2512, 1280x1280 pix²) recorded the entire spontaneous flame emission from the front of view, and a second one at 4 KHz (Photron SA1, 1024x1024 pix²) captured the top view of the flame. Consequently, it is possible to analyze the 3D temporal evolution of the kernel trajectories.

A.2 Results and discussion

A.2.1 Flow aerodynamics - carrier phase

Figure A.2(a) presents a map of the norm of velocity ($|U| = \sqrt{U^2 + V^2}$) of the carrier phase. Two important features are illustrated in the velocity fields. Consistent with the earlier works [27,32,103], the mean axial co-flow velocity provides two peaks at the exit of the injector. The Bluff-Body configuration leads to have a recirculation zone downstream to the fuel injector with axial velocity around $U_z = -5 \text{ m.s}^{-1}$ (not presented in this figure). Further downstream ($Z > 25 \text{ mm}$), the co-flow air jets merge to form a larger jet with a flat axial velocity profile. Note that the air co-flow jet also generates radial velocities, approximately 5 times smaller than the axial velocities at $Z = 10 \text{ mm}$, which rapidly decrease down to zero at $Z = 25 \text{ mm}$.

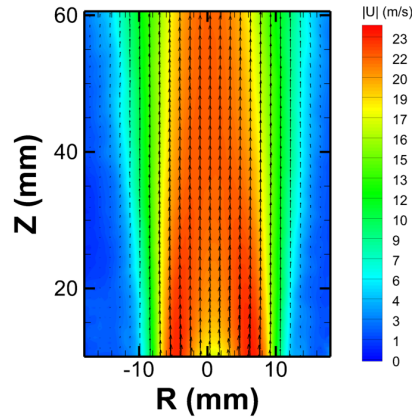
Magnitude of velocity fluctuations is represented in Fig. A.2(b) in terms of the turbulent kinetic energy k . Isotropy along the two directions perpendicular to the Z-axis is assumed and turbulent kinetic energy (k) is calculated following Eq. A.2.

$$k = \frac{1}{2} \left(\overline{(u'_z)^2} + 2 * \overline{(u'_r)^2} \right) \quad (\text{A.2})$$

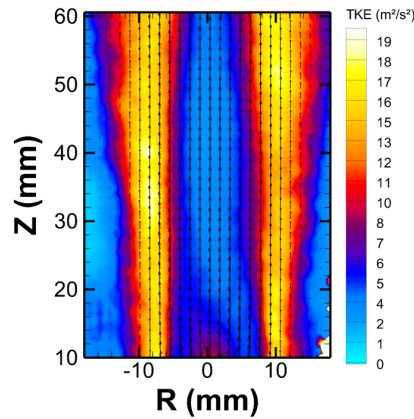
The annular air co-flow discharging into the ambient air creates a shear layer at the interface between the high air co-flow velocity and the ambient air inducing turbulence with large scale structures. The turbulent kinetic energy does not follow the same pattern as the axial velocity, with peaks diffusing radially with increasing axial stations.

A.2.2 Flow aerodynamics - dispersed phase

The fuel spray presents a heterogeneous distribution, with droplet sizes ranging from 2 to 80 μm . Figure A.3(a) displays the radial profile of the mean Sauter Mean Diameter (SMD) for four axial stations ($Z = 16, 25, 35$ and 45 mm). The SMD shows higher values at the borders of the spray ($\approx 52 \mu\text{m}$) and lower values at the center ($\approx 13 \mu\text{m}$). The



(a)



(b)

Figure A.2: (a) Norm of the air velocity with vector field. (b) Turbulent kinetic energy of the air in non reacting conditions

atomization process involving in pressurized atomizer leads to expel the droplets with a strong radial velocity component forming a hollow cone of 80 degree opening. The smallest droplets resulting from the liquid jet breakup are responsive to the air velocity and follow the flow due to associated small Stokes number. However, larger droplets follow ballistic trajectories and are characterized by higher Stokes number, which makes them less sensible to the co-flow. The evaporation process leads to reduce the droplet diameter until to reach a small Stokes number. For a given radial position, the different axial SMD values slightly decrease by the evaporation process. However, this evolution is not present at the centerline ($R = 0$ mm), where SMD values increase with higher Z positions. Indeed, this particular pattern is represented in fig. A.3(b), where three pdf

of droplet sizes are plotted for three axial station ($Z = 7, 35$ and 45 mm). Increasing the value of Z influences the quantity of large drops in the center of the spray. In this situation, the smaller droplets return in the center of the spray by a entrainment process for axial stations upper than 40 mm.

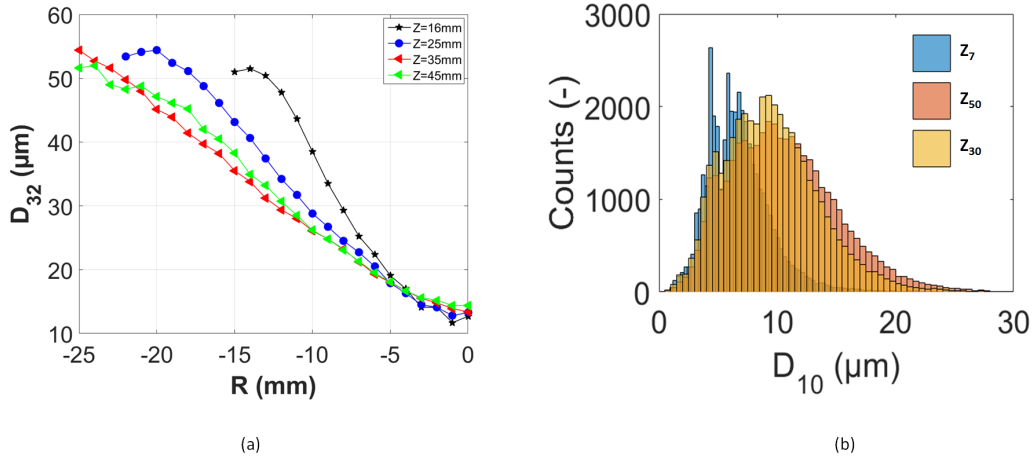


Figure A.3: (a): Fuel droplet Sauter mean diameter D_{32} in non reacting condition at $Z = 16, 25, 35$ and 45 mm). (b) PDF of droplet size for three axial station $Z = 7, 30$ and 50 mm at $R = 0$ mm.

To illustrate the characteristics of the droplets behavior, the mean and RMS of the axial and radial velocity components of different droplet size-classes at four axial stations, $Z = 16, 25, 35$ and 45 mm, are shown in Fig. A.4. The class width was chosen to be $10 \mu\text{m}$. The behavior of the $60\text{-}70$ size group is very close to that of the $50\text{-}60$ group but, since they contain less droplets, they are not presented. Values for the last two groups ($30\text{-}40, 50\text{-}60$) are not shown in the central region because less than 500 droplets were detected per point. The carrier phase velocity profiles are also superimposed.

Figure A.4(a) presents the axial velocity for droplet size-classes at four axial stations. At $Z = 16$ mm the four groups have appreciable axial velocities and depend on the radial position in the spray. In the center, small droplets follow perfectly the axial air velocity (small Stokes number). However, in the shear layer generated by the co-flow, the larger droplets have a lower velocity than for the air co-flow, approximately $5 \text{ m}\cdot\text{s}^{-1}$ less. At $Z= 25$ mm, the small droplets located in the center of the spray accelerates until to reach the air bulk velocity equal to $21.5 \text{ m}\cdot\text{s}^{-1}$. The spray broadens due to injection system and large droplets are now present for higher radial position. This large droplets decelerate until to reach a low velocity close to $1 \text{ m}\cdot\text{s}^{-1}$. From $Z = 45$ mm the set of size-classes follow the air flow and present a flat axial velocity profile. Concerning the radial component, Fig.A.4(b) shows that droplets are ejected from the nozzle with strong radial velocities. The large droplets follow more ballistic trajectories and continue to have radial centrifugal velocities until $Z = 45 \text{ mm}$. Figure A.5 displays the droplet velocity fluctuations. Small droplets are more affected by the shear layer and the large turbulent structures generated

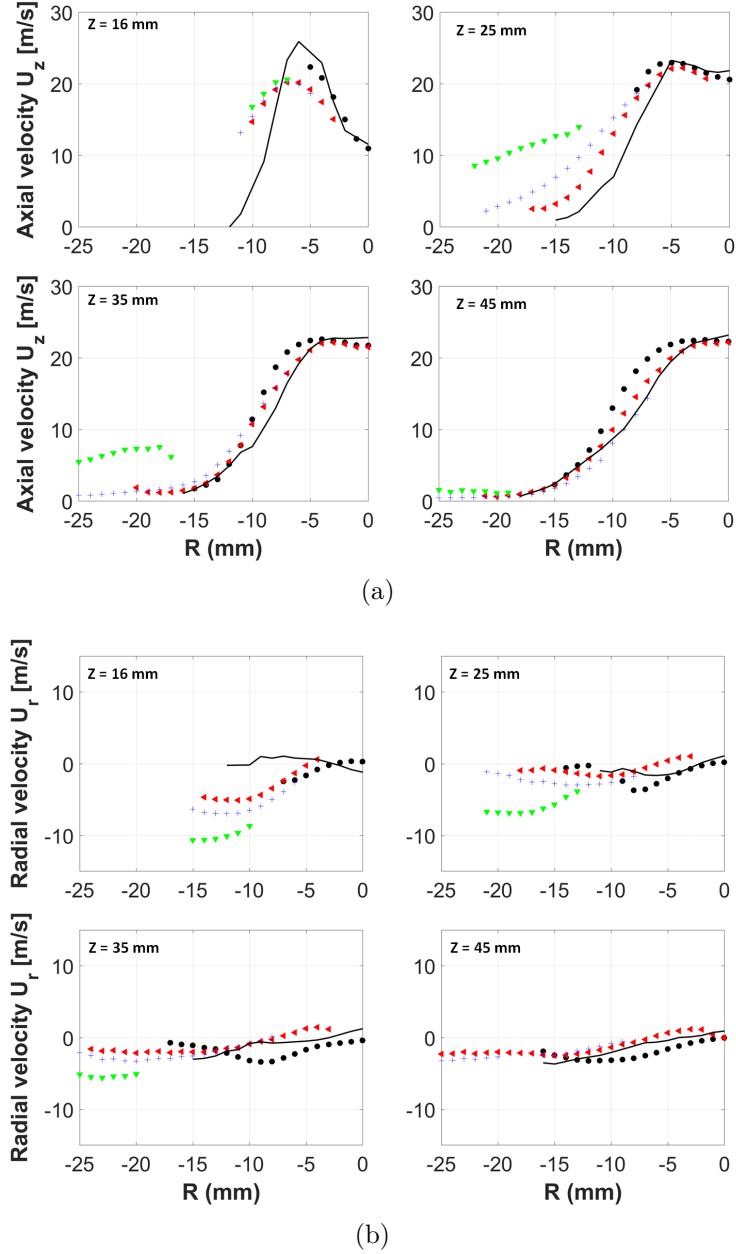


Figure A.4: Mean components of fuel droplet velocity in non reacting conditions separated in four size-classes obtained with PDA configuration. \circ represent the $[0 - 10] \mu m$ group, \triangleleft the $[20 - 30] \mu m$ group, $+$ the $[30 - 40] \mu m$ and ∇ represent the $[50 - 60] \mu m$. Black lines represent the Air velocities profiles. (a) Axial velocity. (b) Radial velocity

by the air jet. Near the radial station $R = -9 \text{ mm}$, in the region where the turbulent kinetic energy is maximum and for axial stations where large turbulent scales are fully developed, the RMS for radial velocities is maximum.

A.2.3 Time scale analysis

The following discussion is based on single droplet theory and the inter-droplet interaction effects are neglected. Urzay [149] propose a formulation to estimate the vaporization time:

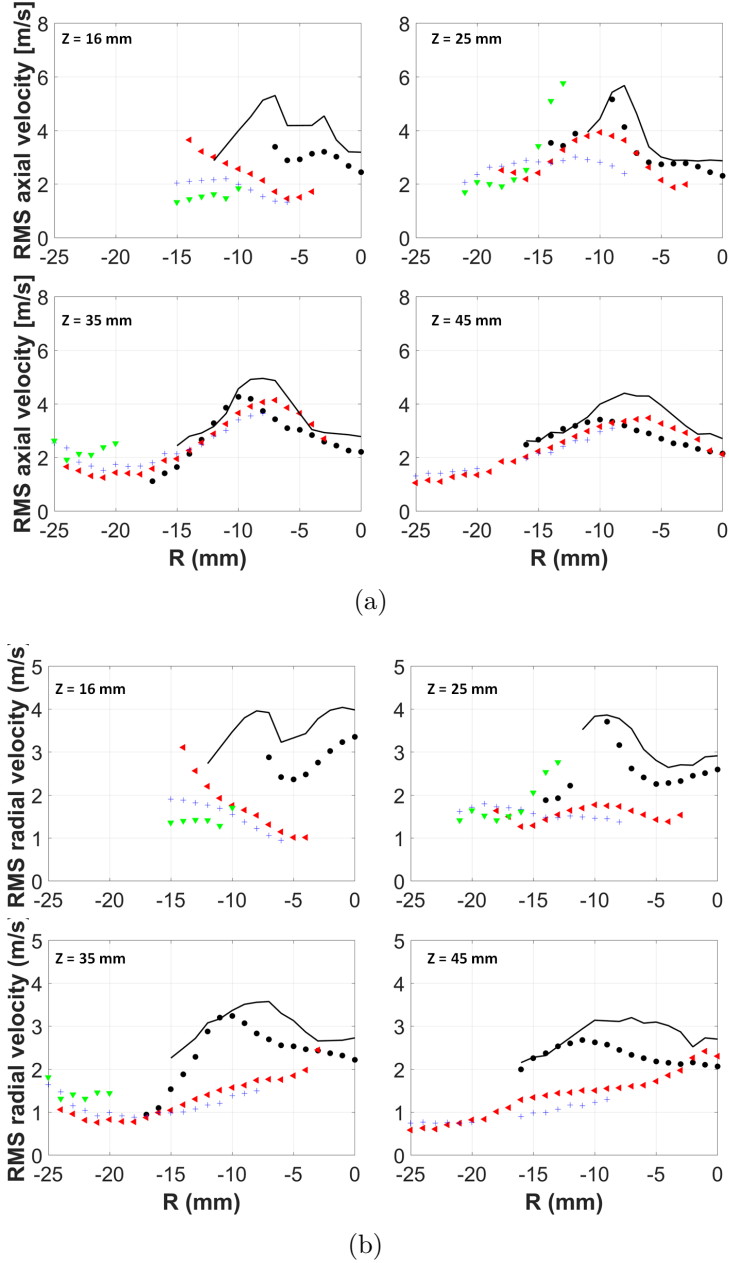


Figure A.5: RMS components of fuel droplet velocity in non reacting conditions separated in four size-classes obtained with PDA configuration. \circ represent the $[0 - 10] \mu\text{m}$ group, \triangleleft the $[20 - 30] \mu\text{m}$ group, $+$ the $[30 - 40] \mu\text{m}$ and ∇ represent the $[50 - 60] \mu\text{m}$. Black lines represent the Air velocities profiles. (a) Axial velocity. (b) Radial velocity

where ρ is the density for droplet and the air and D_t is the thermal diffusivity for the surrounding air.

$$t_v = \frac{\rho_{droplet}}{\rho_{gaz}} \times \frac{D_{droplet}^2}{D_t} \quad (\text{A.3})$$

In this study, the physical properties of the air surrounding the droplet is kept constant and equal to 293 K. From the Eq.A.3, the evaporation rate (\dot{m}_{vapor}) can be estimated with

the droplet volume and density. Indeed, the quantity of vapor produced by the evaporation process is estimated with the following equation:

$$\dot{m}_{vapor} = \frac{V_{droplet} \cdot \rho_{droplet}}{t_v} = \frac{\pi \times D_{droplet}^3 \times \rho_{droplet}}{6 \times t_v} \quad (\text{A.4})$$

Equation A.4 is an estimation of the maximum fuel vapor which can be produced during the evaporation process. Figure A.6 displays the results of the evaporation rate calculated by Eq. A.4 for axial and radial position in spray. Along the centerline, the evaporation rate increases slowly with Z whereas in the spray borders, the evaporation rate is maximum. This region correspond to the largest droplets, obtained by the atomization process. Assuming that all this vapor is available, ignition will be very sensitive to the initial spark position, especially in the region of steep gradient of evaporation rate.

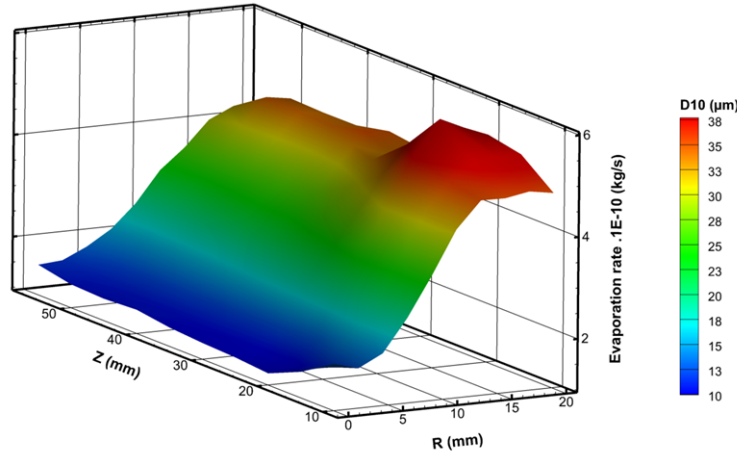


Figure A.6: Representation of evaporation rate (\dot{m}_{vapor}) as a function of axial and radial position. The surface is colored by the mean droplet diameter obtained by the PDA measurements.

A.2.4 Ignition probability

Ignition probability was evaluated as a function of the spark location through the laser-induced ignition experiment. The ignition probability corresponds to the probability of a flame kernel to develop, move and become a stabilized flame. The amount of deposited energy was chosen in order to create a flame kernel everywhere within the mesh so that the kernel probability defined by [150] is unity everywhere. Figure A.7 presents the ignition probability map of the CRSB burner and reveals that ignition becomes an impossible task in the center of the spray. In this region, a flame kernel never evolves into a stabilized flame. The probability increases dramatically with radial distance until to reach a plateau of maximum ignition probability ($P_{ign} = 1$).

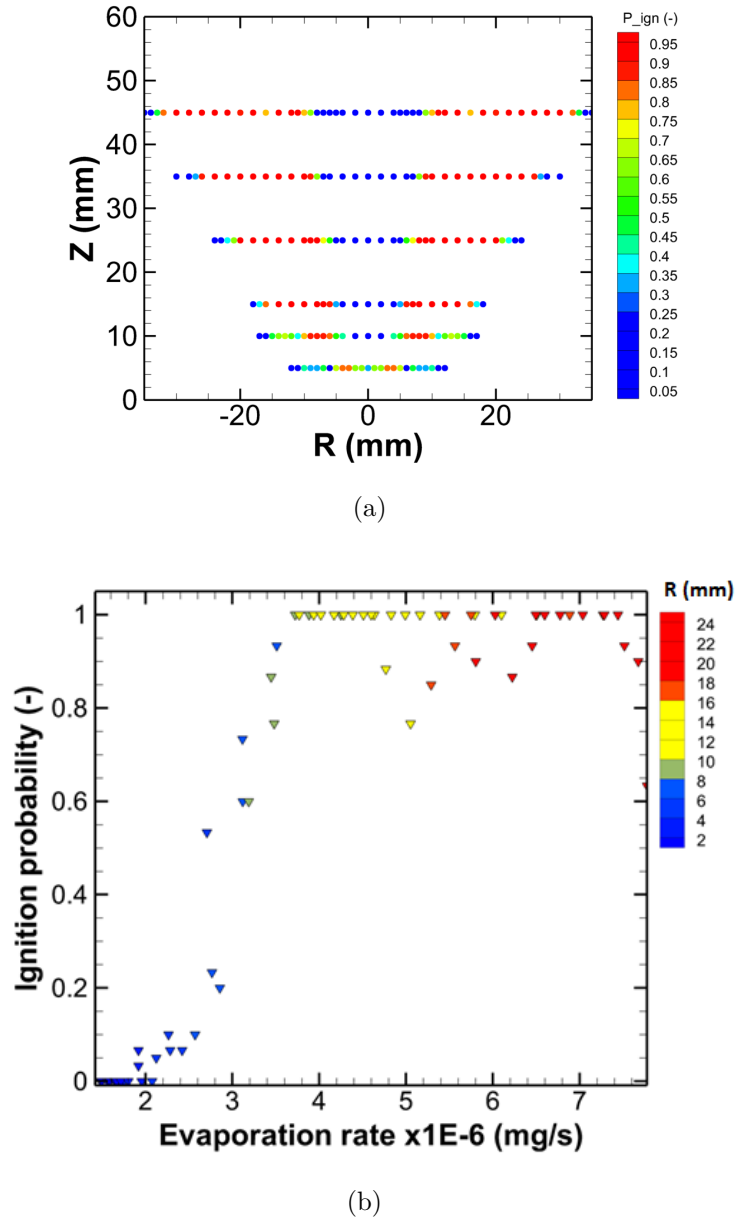


Figure A.7: (a) Ignition probability map with the iso-line $P_{ign} = 0.5$, which correspond to the line with a ignition probability to have 50% of successful ignition.. (b) Ignition probability plotted as a function of evaporation rate and each points are colored by the radial position.

Figure A.7 presents the ignition probability as a function of the evaporation rate estimated by Eq.A.4. Each points are colored by the radial position, where blue color is representative to the the small droplets located in the center, whereas the red color represents the large inertial droplet located in the spray border. The low ignition probability $P_{ign} < 0.2$ corresponds to the central part of the spray, where the mixing between small droplets ($D_{10} < 20 \mu m$) and the air co-flow generates a very lean region very close to the flammability limit ($\phi = 0.58$ [18]) of *n*-heptane. In the spray border the evaporation rate is higher and allows the flame kernel development to reach a stabilized flame. There is a

steep growth in probability from $R \approx 6$ to $R \approx 16$ mm and correspond a zone where the evaporation rate is expected to strongly increase. In addition, turbulent kinetic energy and turbulent mixing of fuel vapor from rich to lean zones are also responsible for the increase of ignition probability when increasing radial locations.

A.2.5 Flame propagation mechanisms

The flame kernel propagation from the spark to the stabilized flame is a complex process that is controlled by many parameters, such as the local turbulence intensity and the fuel vapor distribution. In this paper only the mechanism to obtain a stabilized flame is discussed. The flame kernel extinction is also driven by complex mechanisms but are not studied here. The following figures A.8 and A.9 present an ignition sequence, where spark is located at $R = 15$ mm and $Z = 35$ mm. The flame front is tracked by two cameras, one recorded in the front of view (Fig.A.8) and the second one in the top of view (Fig.A.9). We recall that this work is focused on examination of phase 2 of ignition, this implies that phase 1 is guaranteed.

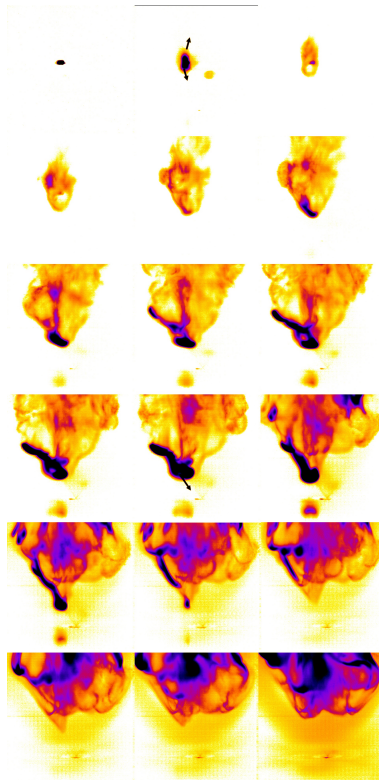


Figure A.8: High-speed recording of flame kernel development from side view. The ignition location is $R = 15$ mm and $Z = 35$ mm, where ignition probability $P_{ign} = 1$.

The first recorded stage in Fig.A.8 shows that the kernel after the spark have smooth curves and remains without wrinkles in the reacting fronts. The flame kernel undergoes an evolution towards the bottom of the burner but also towards the top of the spray. The flame propagation follow the spray border until to reach low axial station $Z \approx 10$ mm.

Then the flame front positioned in the spray border goes up until to reach the axial position correspond to the leading edge of the flame at $R = 15.5 \pm 3 \text{ mm}$ and $Z = 24 \pm 3 \text{ mm}$ [17,18].

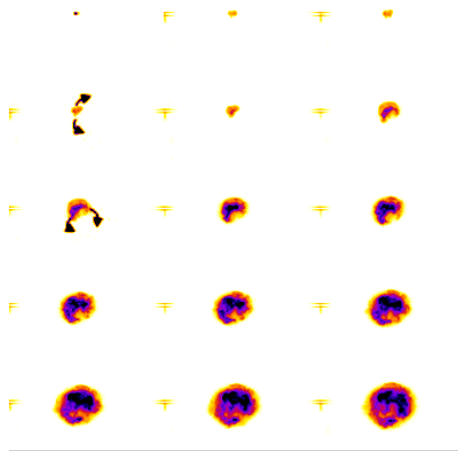


Figure A.9: High-speed recording of flame kernel development from top view. The ignition location is $R = 15 \text{ mm}$ and $Z = 35 \text{ mm}$, where ignition probability $P_{ign} = 1$.

Concerning the recording on the top of view, the kernel grows in the shape of a ring. The flame continues to propagate along the edge of the spray until to reach the merging point. The flame propagation is piloted by the equivalence ratio. The flame does not propagate in the spray center and follows the region where large droplets are present and lead to the fuel vapor production necessary for the flame propagation.

A.3 Conclusion

In this paper, a detailed experimental study of ignition probability in an *n*-heptane spray jet flame has been presented. The results in CRSB burner in non reacting condition reveal strong variations in properties of dispersed phase. The fuel spray shows a complex heterogeneous distribution, with droplet sizes ranging from 2 to 60 μm and velocities from 0 to 22 m.s^{-1} . Concerning the carrier phase, the annular air co-flow discharging into the ambient air creates a shear layer at the interface between the high air co-flow. A simple analysis of the evaporation rate underlines the strong heterogeneous distribution of fuel vapor distribution. The probabilistic approach allow to obtain the ignition probability map inside the CRSB burner. It was found that ignition probability is maximum in region of spray where big droplets are present and where evaporation rate is maximum. The low evaporation rate in the spray center prevents the flame propagation (low ignition probability) and forces the flame to propagate along the spray border, where local equivalence ratio is important and sufficient to allow the flame propagation. A steep gradient in the ignition probability map between the spray centerline and the spray border is directly correlated with the evaporation rate estimation distribution. The flame kernel propagation

and development was studied through high speed visualization. Regardless the position of the spark in region where $P_{ign} = 1$, the flame kernel development follow the same pattern imposed by the amount of fuel available in the spray borders.

Appendix B

Publications and Conferences

Publications

A. Verdier, J. Marrero Santiago, A. Vandel, G. Godard, G. Cabot, B. Renou (2017) Local extinction mechanisms analysis of spray jet flame using high speed diagnostics. *Combustion and Flame*.

A. Verdier, J. Marrero Santiago, A. Vandel, S. Saengkaew, G. Cabot, G. Grehan, B. Renou (2017) Experimental study of local flame structures and fuel droplet properties of a spray jet flame. *Proceedings of the Combustion Institute*.

J. Marrero-Santiago, A. Verdier, C. Brunet, A. Vandel, G. Godard, G. Cabot, M. Boukhalfa, B. Renou (2017) Experimental study of aeronautical ignition in a swirled confined jet-spray burner, GT2017-64476. Accepted in *Proceedings of the ASME Turbo Expo 2017. Journal of Engineering for Gas Turbines and Power*.

F. Shum-Kivan, J. Marrero Santiago, A. Verdier, E. Riber, B. Renou, G. Cabot, B. Cuenot (2017) Experimental and numerical analysis of a turbulent spray flame structure. *Proceedings of the Combustion Institute*.

International conferences

A. Verdier, J. Marrero-Santiago, A. Vandel, G. Godard, G. Cabot, B. Renou (2017) Experimental analysis of ignition probability and local flow properties in a spray jet flame. 4e Colloque INCA, Paris, France, 18-19 October 2017.

A. Verdier, J. Marrero-Santiago, A. Vandel, G. Godard, G. Cabot, B. Renou (2017) Dynamics and local extinction mechanisms of a spray jet flame using high speed diagnostics. 8th European Combustion Meeting, Dubrovnik, Croatia, 18-21 April 2017.

A. Verdier, J. Marrero Santiago, A. Vandel, S. Saengkaew, G. Cabot, G. Grehan, B. Renou (2016) Experimental study of local flame structures and fuel droplet properties of a spray jet flame. 36th International Symposium in Combustion, Seoul, Korea, July 31 – August 5, 2016.

A. Verdier, Javier Marrero Santiago, Alexis Vandel, Gilles Godard, Gilles Cabot, Mourad Boukhalfa, Bruno Renou (2016) High-speed OH-PLIF measurements to study the flame dynamics and the flame-droplet interactions on a spray jet flame. 27th Annual Conference on Liquid Atomization and Spray Systems (ILASS - Europe), Brighton, September 4 - 7, 2016.

A. Verdier, Javier Marrero Santiago, Alexis Vandel, Sawitree Saengkaew, Gilles Cabot, Gerard Grehan, Bruno Renou (2016) Experimental study of fuel droplet temperature along the combustion process in a spray jet flame. 27th Annual Conference on Liquid Atomization and Spray Systems (ILASS - Europe), Brighton, UK, September 4 – 7, 2016.

A. Verdier, J. Marrero Santiago, A.Vandel, G.Godard, G.Cabot, M.A. Boukhalfa and B.Renou (2016) Experimental study of local extinction mechanisms on a spray jet flame. 18th International Symposium on the Application of Laser and Imaging Techniques to Fluid Mechanics, Lisbon, Portugal, July 4 – 7, 2016

A. Verdier, J. Marrero, A. Vandel, S. Saengkaew, G. Cabot, G. Grehan, M. Boukhalfa, B. Renou, C. Gobin and G. Godard (2015) Experimental characterization of fuel droplet temperature in a spray jet flame. European Combustion Meeting, Budapest, Hungary, 1 April 2015.

F. Collin-Bastiani, J. Marrero-Santiago, A. Verdier, A. Vandel, G. Cabot, E. Riber, B. Renou, B. Cuenot. On the extinction and ignition mechanisms along the ignition events in the KIAI spray burner. A joint experimental and numerical approach. 4e Colloque INCA, Paris, France, 18-19 October 2017.

J. Marrero-Santiago, A. Verdier, A. Vandel, G. Godard, G. Cabot, B. Renou (2017). Spray ignition and local flow properties in a swirled confined spray-jet burner: experimental analysis. 28th Annual Conference on Liquid Atomization and Spray Systems (ILASS - Europe), Valencia, Spain, September 6 – 8, September 2017.

J. Marrero-Santiago, A. Verdier, C. Brunet, A. Vandel, G. Godard, G. Cabot, M. Boukhalfa, B. Renou (2017) Experimental study of aeronautical ignition in a swirled confined jet-spray burner, GT2017-64476. American Society of Mechanical Engineering (ASME) TURBO EXPO 2017, Charlotte, North Carolina, 26-30 June 2017.

Javier Marrero Santiago, Antoine Verdier, Gilles Godard, Alexis Vandel, Gilles Cabot, Mourad Boukhalfa, Bruno Renou (2016) Experimental study of airflow velocity, fuel droplet size-velocity and flame structure in a confined swirled jet-spray flame. 27th Annual Conference on Liquid Atomization and Spray Systems (ILASS - Europe), Brighton, UK, September 4 – 7, 2016.

J. Marrero Santiago, A. Verdier, G. Godard, A. Vandel, G. Cabot, M. Boukhalfa and B. Renou (2016) Experimental study of laser ignition probability, kernel propagation and air and fuel droplet properties in a confined swirled jet-spray burner. 18th International Symposium on the Application of Laser and Imaging Techniques to Fluid Mechanics, Lisbon, Portugal, July 4 – 7, 2016.

References

- [1] A. L. Sánchez, J. Urzay, and A. Liñán. The role of separation of scales in the description of spray combustion. *Proceedings of the Combustion Institute*, 35(2):1549–1577, 2015.
- [2] J. Ebner, P. Schober, O. Schafer, R. Koch, and S. Wittig. Modelling of shear-driven liquid wall films: effect of accelerated air flow on the film flow propagation. *Progress in Computational Fluid Dynamics, an International Journal*, 4(3-5):183–190, 2004.
- [3] T. Lancien, K. Prieur, D. Durox, S. Candel, and R. Vicquelin. Large eddy simulation of light-round in an annular combustor with liquid spray injection and comparison with experiments. *Journal of Engineering for Gas Turbines and Power*, 140(2):021504–021514, 2017.
- [4] D. Barre, L. Esclapez, M. Cordier, E. Riber, B. Cuenot, G. Staffelbach, B. Renou, A. Vandel, L. Y. M. Gicquel, and G. Cabot. Flame propagation in aeronautical swirled multi-burners: Experimental and numerical investigation. *Combustion and Flame*, 161(9):2387–2405, 2014.
- [5] S. H. Starner, J. Gounder, and A. R. Masri. Effects of turbulence and carrier fluid on simple, turbulent spray jet flames. *Combustion and Flame*, 143(4):420–432, 2005.
- [6] D. E. Cavaliere, J. Kariuki, and E. Mastorakos. A comparison of the blow-off behaviour of swirl-stabilized premixed, non-premixed and spray flames. *Flow, Turbulence and Combustion*, 91(2):347–372, 2013.
- [7] R. S. Miller, K. Harstad, and J. Bellan. Evaluation of equilibrium and non-equilibrium evaporation models for many-droplet gas-liquid flow simulations. *International Journal of Multiphase Flow*, 24(6):1025–1055, 1998.
- [8] S. Wong and A. Lin. Internal temperature distributions of droplets vaporizing in high-temperature convective flows. *Journal of Fluid Mechanics*, 237:671–687, 1992.
- [9] D. Paulhiac. *Modelisation de la combustion d’un spray dans un brûleur aéronautique*. Thesis, Université de Toulouse.

- [10] H. H. Chiu, H. Y. Kim, and E. J. Croke. Internal group combustion of liquid droplets. *Proceedings of the Combustion Institute*, 19(1):971–980, 1982.
- [11] R. Borghi. The links between turbulent combustion and spray combustion and their modeling. *International Symposium on Transport Phenomena in Combustion*, 127:1–18, 1996.
- [12] J. Reveillon and L. Vervisch. Analysis of weakly turbulent dilute-spray flames and spray combustion regimes. *Journal of Fluid Mechanics*, 537:317–347, 2005.
- [13] P. Xavier. *Investigation of flame stabilization mechanisms in a premixed combustor using a hot gas cavity-based flame holder*. Thesis, INSA de Rouen.
- [14] S. Saengkaew. *Study of spray heat up : On the development of global rainbow techniques*. Thesis, Université de Rouen and Université Chulalongkorn, Bangkok.
- [15] K. Anders, N. Roth, and A. Frohn. Influence of refractive index gradients within droplets on rainbow position and implications for rainbow refractometry. *Particle and Particle Systems Characterization*, 13(2):125–129, 1996.
- [16] C. Letty, B. Renou, J. Reveillon, S. Saengkaew, and G. Gréhan. Experimental study of droplet temperature in a two-phase heptane/air v-flame. *Combustion and Flame*, 160(9):1803–1811, 2013.
- [17] A. Verdier, J. Marrero-Santiago, A. Vandel, S. Saengkaew, G. Cabot, G. Grehan, and B. Renou. Experimental study of local flame structures and fuel droplet properties of a spray jet flame. *Proceedings of the Combustion Institute*, 36(2):2595–2602, 2017.
- [18] F. Shum-Kivan, J. Marrero Santiago, A. Verdier, E. Riber, B. Renou, G. Cabot, and B. Cuenot. Experimental and numerical analysis of a turbulent spray flame structure. *Proceedings of the Combustion Institute*, 36(2):2567–2575, 2017.
- [19] P. Malbois, E. Salaun, F. Frindt, G. Cabot, B. Renou, F. Grisch, L. Bouheraoua, H. Verdier, and S. Richard. Experimental investigation with optical diagnostics of a lean-premixed aero-engine injection system under relevant operating conditions. *Conference paper – ASME*, pages GT2017–64484, 2017.
- [20] A. Jameson. *Time dependent calculations using multigrid, with applications to unsteady flows past airfoils and wings*. Fluid Dynamics and Co-located Conferences. American Institute of Aeronautics and Astronautics, 1991. doi:10.2514/6.1991-1596.
- [21] D. Lathouwers and J. Bellan. Modeling of dense gas–solid reactive mixtures applied to biomass pyrolysis in a fluidized bed. *International Journal of Multiphase Flow*, 27(12):2155–2187, 2001.

-
- [22] S.B. Pope. *Turbulent flows*. 2000.
- [23] P. Goix, C.F. Edwards, A. Cessou, C.M. Dunskey, and D. Stepowski. Structure of a methanol/air coaxial reacting spray near the stabilization region. *Combustion and Flame*, 98(3):205–219, 1994.
- [24] D. Stepowski, P. Goix, and A. Cessou. Simple description of the combustion structures in the stabilization stage of a spray jet flame. *Atomization and Sprays*, 9(1):1–27, 1999.
- [25] S. K. Marley, E. J. Welle, K. M. Lyons, and W. L. Roberts. Effects of leading edge entrainment on the double flame structure in lifted ethanol spray flames. *Experimental Thermal and Fluid Science*, 29(1):23–31, 2004.
- [26] S. K. Marley, K. M. Lyons, and K.A. Watson. Leading-edge reaction zones in lifted-jet gas and spray flames. *Flow Turbulence and Combustion*, 72(1):29–47, 2004.
- [27] G. Cléon, D. Honoré, C. Lacour, and A. Cessou. Experimental investigation of structure and stabilization of spray oxyfuel flames diluted by carbon dioxide. *Proceedings of the Combustion Institute*, 35(3):3565–3572, 2015.
- [28] M. Massot, M. Kumar, M. D. Smooke, and A. Gomez. Spray counterflow diffusion flames of heptane: Experiments and computations with detailed kinetics and transport. *Proceedings of the Combustion Institute*, 27(2):1975–1983, 1998.
- [29] M. Mikami, Y. Mizuta, Y. Tsuchida, and N. Kojima. Flame structure and stabilization of lean-premixed sprays in a counterflow with low-volatility fuel. *Proceedings of the Combustion Institute*, 32(2):2223–2230, 2009.
- [30] A. R. Masri and J. D. Gounder. Turbulent spray flames of acetone and ethanol approaching extinction. *Combustion Science and Technology*, 182(4-6):702–715, 2010.
- [31] J. D. Gounder, A. Kourmatzis, and A. R. Masri. Turbulent piloted dilute spray flames: Flow fields and droplet dynamics. *Combustion and Flame*, 159(11):3372–3397, 2012.
- [32] Hugo Correia R., Mark J. T., E. H. van Veen, and D. Roekaerts. Spray flame structure in conventional and hot-diluted combustion regime. *Combustion and Flame*, 162(3):759–773, 2015.
- [33] H. Correia Rodrigues, M. J. Tummers, E. H. van Veen, and D. Roekaerts. Effects of coflow temperature and composition on ethanol spray flames in hot-diluted coflow. *International Journal of Heat and Fluid Flow*, 51:309–323, 2015.

- [34] R. Yuan, J. Kariuki, A. Dowlut, R. Balachandran, and E. Mastorakos. Reaction zone visualisation in swirling spray n-heptane flames. *Proceedings of the Combustion Institute*, 35(2):1649–1656, 2015.
- [35] C. Letty. *Etude d'une flamme en V diphasique: Approches expérimentale et numérique*. Thesis, INSA de Rouen.
- [36] C. K. Law. Recent advances in droplet vaporization and combustion. *Progress in Energy and Combustion Science*, 8(3):171–201, 1982.
- [37] W. A. Sirignano. Fuel droplet vaporization and spray combustion theory. *Progress in Energy and Combustion Science*, 9(4):291–322, 1983.
- [38] G. Williams. *Combustion theory*. 1985.
- [39] K. Harstad and J. Bellan. Evaluation of commonly used assumptions for isolated and cluster heptane drops in nitrogen at all pressures. *Combustion and Flame*, 127(1):1861–1879, 2001.
- [40] S. S. Sazhin. Advanced models of fuel droplet heating and evaporation. *Progress in Energy and Combustion Science*, 32(2):162–214, 2006.
- [41] S. S. Sazhin, W. A. Abdelghaffar, P. A. Krutitskii, E. M. Sazhina, and M. R. Heikal. New approaches to numerical modelling of droplet transient heating and evaporation. *International Journal of Heat and Mass Transfer*, 48(19):4215–4228, 2005.
- [42] G. M. Faeth. Spray combustion phenomena. *Proceedings of the Combustion Institute*, 26(1):1593–1612, 1996.
- [43] M. Sommerfeld and H. H. Qiu. Experimental studies of spray evaporation in turbulent flow. *International Journal of Heat and Fluid Flow*, 19(1):10–22, 1998.
- [44] T. Li, K. Nishida, and H. Hiroyasu. Droplet size distribution and evaporation characteristics of fuel spray by a swirl type atomizer. *Fuel*, 90(7):2367–2376, 2011.
- [45] J. R. Yang and S. C. Wong. An experimental and theoretical study of the effects of heat conduction through the support fiber on the evaporation of a droplet in a weakly convective flow. *International Journal of Heat and Mass Transfer*, 45(23):4589–4598, 2002.
- [46] C. Maqua, G. Castanet, F. Grisch, F. Lemoine, T. Kristyadi, and S. S. Sazhin. Monodisperse droplet heating and evaporation: Experimental study and modelling. *International Journal of Heat and Mass Transfer*, 51(15):3932–3945, 2008.

-
- [47] T. Kristyadi, V. Deprédurand, G. Castanet, F. Lemoine, S. S. Sazhin, A. Elwardany, E. M. Sazhina, and M. R. Heikal. Monodisperse monocomponent fuel droplet heating and evaporation. *Fuel*, 89(12):3995–4001, 2010.
- [48] Halter F. Lalonde A. Gökalp I. Chauveau, C. An experimental study on the droplet vaporization: effects of heat conduction through the support fiber. *Conference paper ILASS*, 2008.
- [49] C. Chauveau, X. Chesneau, and I. Gökalp. High pressure vaporization and burning of methanol droplets in reduced gravity. *Advances in Space Research*, 16(7):157–160, 1995.
- [50] J. R. Yang and S. C. Wong. On the discrepancies between theoretical and experimental results for microgravity droplet evaporation. *International Journal of Heat and Mass Transfer*, 44(23):4433–4443, 2001.
- [51] H. Nomura, Y. Ujiie, H. J. Rath, J. Sato, and M. Kono. Experimental study on high-pressure droplet evaporation using microgravity conditions. *Proceedings of the Combustion Institute*, 26(1):1267–1273, 1996.
- [52] G. Castanet, L. Perrin, O. Caballina, and F. Lemoine. Evaporation of closely-spaced interacting droplets arranged in a single row. *International Journal of Heat and Mass Transfer*, 93:788–802, 2016.
- [53] B. Abramzon and W. A. Sirignano. Droplet vaporization model for spray combustion calculations. *International Journal of Heat and Mass Transfer*, 32(9):1605–1618, 1989.
- [54] G. F. Yao, S. I. Abdel-Khalik, and S. M. Ghiaasiaan. An investigation of simple evaporation models used in spray simulations. *Journal of Heat Transfer*, 125(1):179–182, 2003.
- [55] D. B. Spalding. The combustion of liquid fuels. *Proceedings of the Combustion Institute*, 4(1):847–864, 1953.
- [56] S. Balachandar and J. K. Eaton. Turbulent dispersed multiphase flow. *Annual Review of Fluid Mechanics*, 42(1):111–133, 2009.
- [57] J. K. Eaton and J. R. Fessler. Preferential concentration of particles by turbulence. *International Journal of Multiphase Flow*, 20:169–209, 1994.
- [58] R. A. Gore and C. T. Crowe. Effect of particle size on modulating turbulent intensity. *International Journal of Multiphase Flow*, 15(2):279–285, 1989.

- [59] F. Zonta, C. Marchioli, and A. Soldati. Direct numerical simulation of turbulent heat transfer modulation in micro-dispersed channel flow. *Acta Mechanica*, 195(1):305–326, 2008.
- [60] S. Elghobashi and G. C. Truesdell. On the two-way interaction between homogeneous turbulence and dispersed solid particles. i: Turbulence modification. *Physics of Fluids A: Fluid Dynamics*, 5(7):1790–1801, 1993.
- [61] K. D. Squires and J. K. Eaton. Particle response and turbulence modification in isotropic turbulence. *Physics of Fluids Dynamics*, 2(7):1191–1203, 1990.
- [62] N Peters. *Turbulent combustion*. Cambridge, cambridge university press edition, 2000.
- [63] T. Poinso and D. Veynante. *Theoretical and numerical combustion*. R.T. Edwards, 2001.
- [64] K. N. C. Bray, P. A. Libby, and M. Champion. *The interaction between turbulence and chemistry in premixed turbulent flames*, volume 40, pages 541–563. Berlin, 1989.
- [65] Damköhler G. Influence of turbulence on flame velocity in gaseous mixtures. *ZH Electrochem*, 1940.
- [66] N. Peters. Turbulent burning velocity for large-scale and small-scale turbulence. *Journal of Fluid Mechanics*, 384:107–132, 1999.
- [67] S. Candel, F. Lacas, N. Darabiha, and J. C. Rolon. Group combustion in spray flames. *Multiphase Science and Technology*, 11(1):1–18, 1999.
- [68] R. Borghi. Turbulent combustion modelling. *Progress in Energy and Combustion Science*, 14(4):245–292, 1988.
- [69] P. Domingo, L. Vervisch, and J. Reveillon. Dns analysis of partially premixed combustion in spray and gaseous turbulent flame-bases stabilized in hot air. *Combustion and Flame*, 140(3):172–195, 2005.
- [70] M. Cordier, A. Vandel, G. Cabot, B. Renou, and A. M. Boukhalfa. Laser-induced spark ignition of premixed confined swirled flames. *Combustion Science and Technology*, 185(3):379–407, 2013.
- [71] A. C. Eckbreth. *Laser diagnostics for combustion temperature and species*. Gordon and Breach Publishers, Amsterdam, The Netherlands, 1996.
- [72] K. Kohse-Höinghaus. Laser techniques for the quantitative detection of reactive intermediates in combustion systems. *Progress in Energy and Combustion Science*, 20(3):203–279, 1994.

-
- [73] F. Grisch and M. Orain. Role of planar laser-induced fluorescence in combustion research. *AerospaceLab*, (1):p. 1–14, 2009.
- [74] K. A. Watson, K. M. Lyons, J. M. Donbar, and C. D. Carter. Scalar and velocity field measurements in a lifted ch₄–air diffusion flame. *Combustion and Flame*, 117(1–2):257–271, 1999.
- [75] P. Baranger. *Techniques d’imagerie quantitatives: fluorescence induite par laser appliquée aux écoulements et aux combustions*. Thesis, Université de Rouen.
- [76] M. Aldén, H. Edner, G. Holmstedt, S. Svanberg, and T. Högberg. Single-pulse laser-induced oh fluorescence in an atmospheric flame, spatially resolved with a diode array detector. *Applied Optics*, 21(7):1236–1240, 1982.
- [77] B. Böhm, C. Heeger, R. L. Gordon, and A. Dreizler. New perspectives on turbulent combustion: Multi-parameter high-speed planar laser diagnostics. *Flow, Turbulence and Combustion*, 86(3):313–341, 2011.
- [78] M. Stöhr, R. Sadanandan, and W. Meier. Experimental study of unsteady flame structures of an oscillating swirl flame in a gas turbine model combustor. *Proceedings of the Combustion Institute*, 32(2):2925–2932, 2009.
- [79] I. Boxx, C. M. Arndt, C. D. Campbell, and W. Meier. High-speed laser diagnostics for the study of flame dynamics in a lean premixed gas turbine model combustor. *Experiments in Fluids*, 52(3):555–567, 2012.
- [80] H. Malm, G. Sparr, J. Hult, and C. F. Kaminski. Nonlinear diffusion filtering of images obtained by planar laser-induced fluorescence spectroscopy. *Journal of the Optical Society of America A*, 17(12):2148–2156, 2000.
- [81] Stanley Osher and James A. Sethian. Fronts propagating with curvature-dependent speed: Algorithms based on hamilton-jacobi formulations. *J. Comput. Phys.*, 79(1):12–49, 1988.
- [82] P. Perona and J. Malik. Scale-space and edge detection using anisotropic diffusion. *IEEE Transactions on Pattern Analysis and Machine Intelligence*, 12(7):629–639, 1990.
- [83] G. Hartung, J. Hult, R. Balachandran, M. R. Mackley, and C. F. Kaminski. Flame front tracking in turbulent lean premixed flames using stereo PIV and time-sequenced planar LIF of OH. *Applied Physics B*, 96(4):843–862, 2009.
- [84] V. Caselles, F. Catté, T. Coll, and F. Dibos. A geometric model for active contours in image processing. *Numerische Mathematik*, 66(1):1–31, 1993.

- [85] C. E. Willert and M. Gharib. Digital particle image velocimetry. *Experiments in Fluids*, 10(4):181–193, 1991.
- [86] A. K. Prasad, R. J. Adrian, C. C. Landreth, and P. W. Offutt. Effect of resolution on the speed and accuracy of particle image velocimetry interrogation. *Experiments in Fluids*, 13(2):105–116, 1992.
- [87] M. Willert M. Raffel and J. Kompenhans. *Particle Image Velocimetry, a practical guide*. 1998.
- [88] A. Cessou and D. Stepowski. Planar laser induced fluorescence measurement of oh in the stabilization stage of a spray jet flame. *Combustion Science and Technology*, 118(4-6):361–381, 1996.
- [89] J. A. Friedman and M. Renksizbulut. Investigating a methanol spray flame interacting with an annular air jet using phase-doppler interferometry and planar laser-induced fluorescence. *Combustion and Flame*, 117(4):661–684, 1999.
- [90] F. Lemoine and G. Castanet. Temperature and chemical composition of droplets by optical measurement techniques: a state-of-the-art review. *Experiments in Fluids*, 54(7):1572, 2013.
- [91] J. P. A. J. van Beeck, D. Giannoulis, L. Zimmer, and M. L. Riethmuller. Global rainbow thermometry for droplet-temperature measurement. *Optics Letters*, 24(23):1696–1698, 1999.
- [92] N. Roth, K. Anders, and A. Frohn. Refractive-index measurements for the correction of particle sizing methods. *Applied Optics*, 30(33):4960–4965, 1991.
- [93] S. V. Sankar, H. Dale, I. Buermann, M. Khalid, and D. B. William. Application of an integrated phase doppler interferometer/ rainbow thermometer/point-diffraction interferometer for characterizing burning droplets. *Proceedings of the Combustion Institute*, 25(1):413–421, 1994.
- [94] S. Saengkaew, T. Charinpanitkul, H. Vanisri, W. Tanthapanichakoon, L. Mees, G. Gouesbet, and G. Grehan. Rainbow refractrometry: On the validity domain of airy’s and nussenzveig’s theories. *Optics Communications*, 259(1):7–13, 2006.
- [95] Buermann D.H. Sankar, S.V. and W.D. Bachalo. Simultaneous measurements of droplet size, velocity, and temperature in a swirl-stabilized spray flame. *International Symposium on the Applications of Laser Techniques to Fluid Mechanics*, 1994.
- [96] P. Briard. *3D characterization of a cloud of particles by Fourier interferometric imaging : 3D relative positions, sizes and refractive indices*. Thesis, INSA de Rouen.

-
- [97] S. Saengkaew, G. Godard, J. B. Blaisot, and G. Gréhan. Experimental analysis of global rainbow technique: sensitivity of temperature and size distribution measurements to non-spherical droplets. *Experiments in Fluids*, 47(4-5):839–848, 2009.
- [98] S. Saengkaew, V. Bodoc, G. Lavergne, and G. Grehan. Application of global rainbow technique in sprays with a dependence of the refractive index on droplet size. *Optics Communications*, 286:295–303, 2013.
- [99] J. A. Adam. The mathematical physics of rainbows and glories. *Physics Report*, 356:229–365, 2002.
- [100] S. Saengkaew, D. Bonin, and G. Grehan. Measurement of droplets temperature by using a global rainbow technique with a pulse laser. *Conference paper – ILASS*, 2010.
- [101] S. Saengkaew, T. Charinpanikul, C. Laurent, Y. Biscos, G. Lavergne, G. and Gouesbet, and G. Gréhan. Processing of individual rainbow signals. *Experiments in Fluids*, 48(1):111–119, 2010.
- [102] J. Wilms. *Evaporation of multicomponent droplets*. Thesis, Universität Stuttgart.
- [103] M. S. Mansour, I. Alkhesho, and S. H. Chung. Stabilization and structure of n-heptane flame on CWJ-spray burner with kHz SPIV and OH-PLIF. *Experimental Thermal and Fluid Science*, 73:18–26, 2016.
- [104] A. Delconte. *Fluorescence induite par laser multibande appliquée à la mesure de température dans les milieux complexes*. Thesis, Université de Lorraine.
- [105] P. Lavieille, F. Lemoine, G. Lavergne, and M. Lebouché. Evaporating and combusting droplet temperature measurements using two-color laser-induced fluorescence. *Experiments in Fluids*, 31(1):45–55, 2001.
- [106] L. Ma and D. Roekaerts. Numerical study of the multi-flame structure in spray combustion. *Proceedings of the Combustion Institute*, 36(2):2603–2613, 2017.
- [107] D. Veynante, L. Vervisch, T. Poinso, L. Linan, and G. Ruetsch. Triple flame structure and diffusion flame stabilization. *Proceedings of the summer Program Center for Turbulence Research, Sanford, Calif, USA*, (1):55–73, 1994.
- [108] J.F. Widmann and C. Presser. A benchmark experimental database for multiphase combustion model input and validation. *Combustion and Flame*, 129(1):47–86, 2002.
- [109] T. Marchione, S. F. Ahmed, and E. Mastorakos. Ignition of turbulent swirling n-heptane spray flames using single and multiple sparks. *Combustion and Flame*, 156(1):166–180, 2009.

- [110] H. W. Ge, I. Düwel, H. Kronemayer, R. W. Dibble, E. Gutheil, C. Schulz, and J. Wolfrum. Laser-based experimental and monte carlo pdf numerical investigation of an ethanol/air spray flame. *Combustion Science and Technology*, 180(8):1529–1547, 2008.
- [111] L. Ma, B. Naud, and D. Roekaerts. Transported pdf modeling of ethanol spray in hot-diluted coflow flame. *Flow, Turbulence and Combustion*, pages 1–34, 2015.
- [112] I. Boxx, C. M. Arndt, C. D. Campbell, and W. Meier. High-speed laser diagnostics for the study of flame dynamics in a lean premixed gas turbine model combustor. *Experiments in Fluids*, 52(3):555–567, 2010.
- [113] C. Abram, B. Fond, A.L. Heyes, and F. Beyrau. High-speed planar thermometry and velocimetry using thermographic phosphor particles. *Applied Physics B*, 111(2):155–160, 2013.
- [114] J. Hult, U. Meier, W. Meier, A. Harvey, and C. F. Kaminski. Experimental analysis of local flame extinction in a turbulent jet diffusion flame by high repetition 2-D laser techniques and multi-scalar measurements. *Proceedings of the Combustion Institute*, 30(1):701–709, 2005.
- [115] M. K. Geikie and K.A. Ahmed. Lagrangian mechanisms of flame extinction for lean turbulent premixed flames. *Fuel*, 194:239–256, 2017.
- [116] P. H. Renard, D. Thévenin, J. C. Rolon, and S. Candel. Dynamics of flame/vortex interactions. *Progress in Energy and Combustion Science*, 26(3):225–282, 2000.
- [117] A. M. Steinberg and J. F. Driscoll. Straining and wrinkling processes during turbulence–premixed flame interaction measured using temporally-resolved diagnostics. *Combustion and Flame*, 156(12):2285–2306, 2009.
- [118] A. Franzelli, B. Vié and M. Ihme. Characterizing spray flame–vortex interaction: A spray spectral diagram for extinction. *Combustion and Flame*, 163:100–114, 2016.
- [119] M. Nakamura, F. Akamatsu, R. Kurose, and M. Katsuki. Combustion mechanism of liquid fuel spray in a gaseous flame. *Physics of Fluids*, 17(12):123301, 2005.
- [120] H. Nomura, M. Hayasaki, and Y. Ujiie. Effects of fine fuel droplets on a laminar flame stabilized in a partially prevaporized spray stream. *Proceedings of the Combustion Institute*, 31(2):2265–2272, 2007.
- [121] X. Mercier, M. Orain, and F. Grisch. Investigation of droplet combustion in strained counterflow diffusion flames using planar laser-induced fluorescence. *Applied Physics B*, 88(1):151–160, 2007.

-
- [122] D. H. Wacks and N. Chakraborty. Flame structure and propagation in turbulent flame-droplet interaction: A direct numerical simulation analysis. *Flow, Turbulence and Combustion*, 96(4):1053–1081, 2016.
- [123] D. H. Wacks, N. Chakraborty, and E. Mastorakos. Statistical analysis of turbulent flame-droplet interaction: A direct numerical simulation study. *Flow, Turbulence and Combustion*, 96(2):573–607, 2015.
- [124] P. Jenny, D. Roekaerts, and N. Beishuizen. Modeling of turbulent dilute spray combustion. *Progress in Energy and Combustion Science*, 38(6):846–887, 2012.
- [125] T. Schønfeld and M. Rudgyard. Steady and unsteady flows simulations using the hybrid flow solver avbp. *Annual Research Briefs*, 37(11):1378–1385, 1999.
- [126] D. Veynante O. Colin, F. Ducros and T. Poinso. A thickened flame model for large eddy simulations of turbulent premixed combustion. *Physics of Fluids*, 12:1843, 2000.
- [127] T. Poinso, D. Veynante, and S. Candel. Quenching processes and premixed turbulent combustion diagrams. *Journal of Fluid Mechanics*, 228:561–606, 2006.
- [128] L. Schiller and A. Nauman. A drag coefficient correlation. *VDI Zeitung*, 77:318–320, 1935.
- [129] M. Sanjosé. *Evaluation de la méthode Euler-Euler pour la simulation aux grandes échelles des chambres à carburant liquide*. Thesis, Université de Toulouse.
- [130] G. Hannebique, E. Sierra, P. and Riber, and B. Cuenot. Large eddy simulation of reactive two-phase flow in an aeronautical multipoint burner. *Flow, Turbulence and Combustion*, 90(2):449–469, 2013.
- [131] B. Franzelli, E. Riber, M. Sanjosé, and T. Poinso. A two-step chemical scheme for kerosene–air premixed flames. *Combustion and Flame*, 157(7):1364–1373, 2010.
- [132] A. J. Smallbone, W. Liu, C. K. Law, X. Q. You, and H. Wang. Experimental and modeling study of laminar flame speed and non-premixed counterflow ignition of n-heptane. *Proceedings of the Combustion Institute*, 32(1):1245–1252, 2009.
- [133] H. Yamashita, G. Kushida, and T. Takeno. *Prog. Astro Aerosp.*, pages 131–193, 1990.
- [134] G. Continillo and W. A. Sirignano. Counterflow spray combustion modeling. *Combustion and Flame*, 81(3):325–340, 1990.

- [135] R. W. Bilger. The structure of turbulent nonpremixed flames. *Proceedings of the Combustion Institute*, 22(1):475–488, 1989.
- [136] F. Shum-Kivan. *Simulation des grandes échelles de flammées de spray et modélisation de la combustion non-prémélangée*. Thesis, Université de Toulouse.
- [137] D. Noh, S. Gallot-Lavallee, W.P. Jones, and S. Navarro-Martinez. Validation of droplet evaporation models for a polydisperse spray in a non-swirling jet flame. *Conference paper - European Combustion Meeting*, 2017.
- [138] A.D. Birch, D.R. Brown, M.G. Dodson, and J.R. Thomas. Studies of flammability in turbulent flows using laser raman spectroscopy. *Proceedings of the Combustion Institute*, 17:307–314, 1978.
- [139] S. F. Ahmed, R. Balachandran, T. Marchione, and E. Mastorakos. Spark ignition of turbulent nonpremixed bluff-body flames. *Combustion and Flame*, 151(1-2):366–385, 2007.
- [140] C. Letty, E. Mastorakos, A. R. Masri, M. Juddoo, and W. O’Loughlin. Structure of igniting ethanol and n-heptane spray flames with and without swirl. *Experimental Thermal and Fluid Science*, 43:47–54, 2012.
- [141] D.R. Ballal and A.H. Lefebvre. A general model of spark ignition for gaseous and liquid fuel-air mixtures. *Proceedings of the Combustion Institute*, 18:1737–1746, 1981.
- [142] K. G. Moesl, K. G. Vollmer, T. Sattelmayer, J. Eckstein, and H. Kopecek.
- [143] A. P. Wandel. Influence of scalar dissipation on flame success in turbulent sprays with spark ignition. *Combustion and Flame*, 161(10):2579–2600, 2014.
- [144] Y. H. Kao, M. Denton, X. Wang, S. M. Jeng, and M. C. Lai. Experimental spray structure and combustion of a linearly-arranged 5-swirler array. (56680):V04AT04A038, 2015. 10.1115/GT2015-42509.
- [145] J. Marrero-Santiago, A. Verdier, C. Brunet, A. Vandiel, G. Godard, G. Cabot, M. Boukhalfa, and B. Renou. Experimental study of aeronautical ignition in a swirled confined jet-spray burner. (50855):V04BT04A020, 2017. 10.1115/GT2017-64476.
- [146] K. Prieur, D. Durox, J. Beaunier, T. Schuller, and S. Candel. Ignition dynamics in an annular combustor for liquid spray and premixed gaseous injection. *Proceedings of the Combustion Institute*, 36(3):3717–3724, 2017.

- [147] E. Machover, E. and Mastorakos. Experimental investigation on spark ignition of annular premixed combustors. *Combustion and Flame*, 178:148–157, 2017.
- [148] B. Cardin, C. and Renou, G. Cabot, and A. M. Boukhalfa. Experimental analysis of laser-induced spark ignition of lean turbulent premixed flames: New insight into ignition transition. *Combustion and Flame*, 160(8):1414–1427, 2013.
- [149] J. Urzay. A revised spray-combustion diagram of diffusion- controlled burning regimes in fuel-spray clouds. *Center for Turbulence Research, Annual Research Briefs* 2011.
- [150] E. Mastorakos. Ignition of turbulent non-premixed flames. *Progress in Energy and Combustion Science*, 35(1):57–97. 0360-1285.